Characterization and Modelling of an Open Cycle CO_2 Transport Refrigeration System

Pierce Kennedy B. Eng., M. Eng.

A thesis submitted to Dublin City University in partial fulfilment of the requirements for the degree of

Doctor of Philosophy

Supervisors:

Dr. Harold Esmonde

Dr. Paul Young

School of Mechanical and Manufacturing Engineering

Dublin City University

June 2018

I hereby certify that this material, which I now submit for assessment on the programme of study leading to the award of Ph. D is entirely my own work, and that I have exercised reasonable care to ensure that the work is original, and does not to the best of my knowledge breach any law of copyright, and has not been taken from the work of others save and to the extent that such work has been cited and acknowledged within the text of my work.

Signed: _____

ID No.: 99284111

Date:

Acknowledgments

I would like to thank my supervisors Dr. Harry Esmonde and Dr. Paul Young for the guidance and support over the course of this project. Their assistance and encouragement over the years has been greatly appreciated. I would like to thank Thermo King and the individuals, Ken Gleeson, John Gough and Bernd Lipp, for the resources they have provided towards the this project and for their confidence in allowing me to the time to complete it.

I would also like to thank Casey Briscoe, Bill Mohs, Scott Munns and Wayne Donnellan for the valuable insights they gave me into modelling techniques and the physics of refrigeration systems without which this project would not have been possible.

I need to give a special mention to my wife Sinead for putting up with me for the past 8 years, for her understanding, support, encouragement and love, and to my son, Cathal, for keeping everything in perspective.

Finally I would like to acknowledge the funding provided for the project by Ingersoll Rand International Ltd.

Table of Contents

List of Abbreviations

AMCA	Air Movement and Control Association
ARB	Air Resource Board
ATP	Agreement on the International Carriage of Perishable Foodstuffs
BPR	Back Pressure Regulator
CFD	Computational Fluid Dynamic
DLL	Dynamic Link Library
EAIT	Evaporator Air Inlet Temperature
EAOT	Evaporator Air Outlet Temperature
ERIT	Evaporator Refrigerant Inlet Temperature
EROT	Evaporator Refrigerant Outlet Temperature
ECIP	Evaporator Coil Inlet Pressure
ECOP	Evaporator Coil Outlet Pressure
EEV	Electronic Expansion Valve
EEVIP	Electronic Expansion Valve Inlet Pressure
ETV	Electronic Throttling Valve
GWP	Global Warming Potential
HDV	Heavy-duty Vehicle
HFC	Hydro-fluorocarbon
HMI	Human Machine Interface
LEZ	Low Emission Zone
LMTD	Log Mean Temperature Difference
NER	Normalized Error Residual
NO_x	Nitrous Oxides
NRMM	Non-road Mobile Machinery
NTU	Number of Transfer Units
MRE	Mean Relative Error
PAF	Performance Adjustment Factor
PED	Pressure Equipment Directive
PI	Proportional Integral
PM	Particulate Matter

PWM	Pulse Width Modulation
RAM	Random Access Memory
RPM	Revolutions per Minute
TRU	Transport Refrigeration Unit

List of Symbols

A	Area	m^2
AS	Surface Area	m^2
C	Thermal Capacitance	$W\ s\ K^{-1}$
C_p	Specific Heat	$kJ\ kg^{-1}\ K^{-1}$
D	Pipe Diameter	m
e	error	-
f	forcing function	-
h	refrigerant enthalpy	$kJ\ kg^{-1}$
K	gain in the pseudo-state equations	-
k	Thermal Conductivity, Sample time	$W\ m^{-1}\ K^{-1}$
L	Length	m
m	Mass	kg
$\dot{m}$	*Mass flow rate of CO_2*	*$kg\ s^{-1}$*
n	number of samples	-
P	Pressure	kPa
Pr	Prandtl number	-
Q	Heat Transfer Rate, Volumetric Flow Rate	$W, m^3\ s^{-1}$
Re	Reynolds Number	-
S	Slip Ratio, Nucleate boiling suppression factor	-
SG	Specific Gravity	-
T	Temperature	°K
U	Heat transfer coefficient	$kW\ m^{-2}\ K^{-1}$
V	Volume	m^3
x	Refrigerant Quality	-
X	State Vector	-

Z	Coefficient Matrix	-
α	refrigerant heat transfer coefficient	kW m^{-2} K^{-1}
γ	Void fraction	-
ε	Evaporator effectiveness	-
ζ	Normalized length of the two-phase region	-
ρ	Density	kg m^{-3}

List of Subscripts

c	cold
cb	convective boiling
exp	experimental
f	Fluid
g	Gas
h	hot
in	Inlet
out	Outlet
l	liquid
min	minimum
nb	nucleate boiling
ref	Refrigerant
RMS	root mean square
SH	Superheated
sim	simulation
TP	Two-phase
v	vapour
wall	tube wall
wet	on the wet perimeter

List of Figures

List of Tables

Abstract

Characterization and Modelling of an Open Cycle CO_2 Transport Refrigeration System

Pierce Kennedy

Transport refrigeration units are in widespread use and are vital to global logistical infrastructure. In their most common form they are diesel powered but these units face an uncertain future with the upcoming introduction of low emission zones in major cities such as Paris and London. Although going largely unnoticed an alternative unit described as an open cycle CO_2 system has been available that does not require diesel power and can freely enter low emission zones. In this dissertation, such a system is examined experimentally and modelled for the first time in literature, using the switched moving boundary technique.

An experimental system is developed on which both static and dynamic tests are performed. Measurements are taken of the relevant air and refrigerant temperatures, the refrigerant pressures, the mass flow rate of CO_2 and the cooling capacity of the system. A method of measuring the two-phase zone length within the evaporator coil with temperature measurements along the length of the coil is presented. The utility and efficiency of the system are examined in detail using the above measurements. The superheat control is identified as an issue.

A switched moving boundary model is adapted to work with an open cycle CO_2 system and refined using the static and dynamic pull-down results from the experimental testing. Additions to the base model include a superheated only representation in the evaporator, the use of a dynamic link library (DLL) to call fluid property routines, a model of the back pressure regulator, the addition of pressure drop into the evaporator model and a new calculation for the refrigerant outlet temperature. The final model is validated against typical customer operating modes at both a fresh set-point of 0°C and a frozen set-point of -25°C. In general good correlation between the experimental results and the model outputs are seen with the exception being the periods where the EEV is closed in cycle sentry control with fans off. The model is subsequently used to design new control parameters for superheat control with good results.

Chapter 1 Introduction

1.1 Challenges of Low Carbon & Low Emissions Transport Refrigeration

The transportation of people and goods around the world face new challenges due to the efforts to decarbonise the world economy to meet the commitments of the Paris climate agreement. Equally challenging is solving the issues of particulate matter (PM) and nitrous oxides (NO_x) in large cities caused primarily by the exhaust emissions of diesel engines. Although the primary focus in tackling these issues so far has been on passenger cars, buses and trucks it will not be long before the focus of legislators widens to include other equipment that use diesel engines such as transport refrigeration units.

To date low emission zones (LEZ's) throughout the world tend to focus on limiting the access of older, more polluting vehicles to city centres [1]. However the recent diesel scandal where Volkswagen was found to be guilty of cheating on emissions testing [2] has lessened the trust in official figures from the standardized emissions tests and made complete bans on diesel engines in LEZ's more likely. Paris, Mexico City, Athens, Madrid and Rome have all made announcements of bans on diesel passenger cars by 2025 and German courts have also ruled that diesel bans can be implemented in Stuttgart and Dusseldorf to combat pollution [3]. While other vehicles have not been included in these bans to date it is only a matter of time before diesel engines in trucks and non-road mobile machinery (NRMM) equipment such as transport refrigeration units (TRU's) will also be excluded from entering city centre areas. London already has an LEZ that targets NRMM vehicles [4] and the EU will introduce new emission standards for NRMM engines from January 2019 [5].

The carbon footprint of TRU's are also under scrutiny along with the heavy-duty vehicles (HDV's) that use them. The European commission is introducing new legislation to monitor and report on the CO_2 emissions from HDV's in January 2019 [6]. The CO_2 emissions from TRU's are not included but more customers are aware of their emissions and the potential for legislation that would affect their equipment in the future. One piece of legislation that has impacted on TRU's indirectly was the introduction of the Fluorinated Greenhouse Gases Regulations (F-gas) in 2014 [7]. While TRU's were not banned from using the refrigerant R404A, the introduction of a quota system for the manufacturers of the refrigerant resulted in a sharp increase in its cost with the

result that the majority of TRU customers in Europe now opt for the alternative R452a refrigerant which has a lower global warming potential (GWP) of 2141. While the GWP of R452a is a substantial improvement over the R404A number of 3922 it is likely that future F-gas legislation will aim for a much lower number such as that used by the MAC directive for air conditioning in passenger cars which has a GWP limit of 150 [8].

Noise emissions are another issue for TRU's as deliveries are often made at night or early in the morning in residential areas. The Netherlands have noise regulations known as PIEK [9], which limit the noise to below 60 dB at 7.5m from the TRU in these cases. The Outdoor Noise Directive, which is the EU legislation that governs noise emissions from TRU's, is also in the process of being revised with more stringent emissions targets expected [10].

The open cycle CO_2 TRU has the potential to solve all of these issues. It has no emissions of PM or NO_x at point of use. It uses a refrigerant with a GWP of 1 and although it emits CO_2 the source of the CO_2 used is a waste product from other industrial processes such as fertilizer and ethanol production so its carbon footprint is limited to the energy required to clean, liquefy and transport it to the point of use. A study of this lifecycle by Engberg et al. [11] showed the carbon footprint to be much less than that of a diesel powered TRU. Noise emissions are also easily controlled as the diesel engine and condenser fans which are the typical noise sources for a diesel TRU are not present. Sufficient muffling of the CO_2 exhaust can result in a unit that can easily meet the stringent requirements of the PIEK noise standard.

1.2 The Open Cycle CO_2 Refrigeration Cycle

The pressure enthalpy (P-H) diagram, Figure 1, shows a standard vapour compression system and an open cycle CO_2 system. As can be seen the open cycle CO_2 system has no compression or heat rejection to the environment in the condenser during operation as this is done industrially on a large scale offline from point of application. There is also no sub-cooling of the refrigerant so the expansion of the refrigerant starts with saturated liquid. Superheating of the refrigerant in the evaporator typically does occur in the open cycle CO_2 system, and can be over a significant percentage of the evaporator coil, but is not necessary for protection of the compressor so can be eliminated if required.

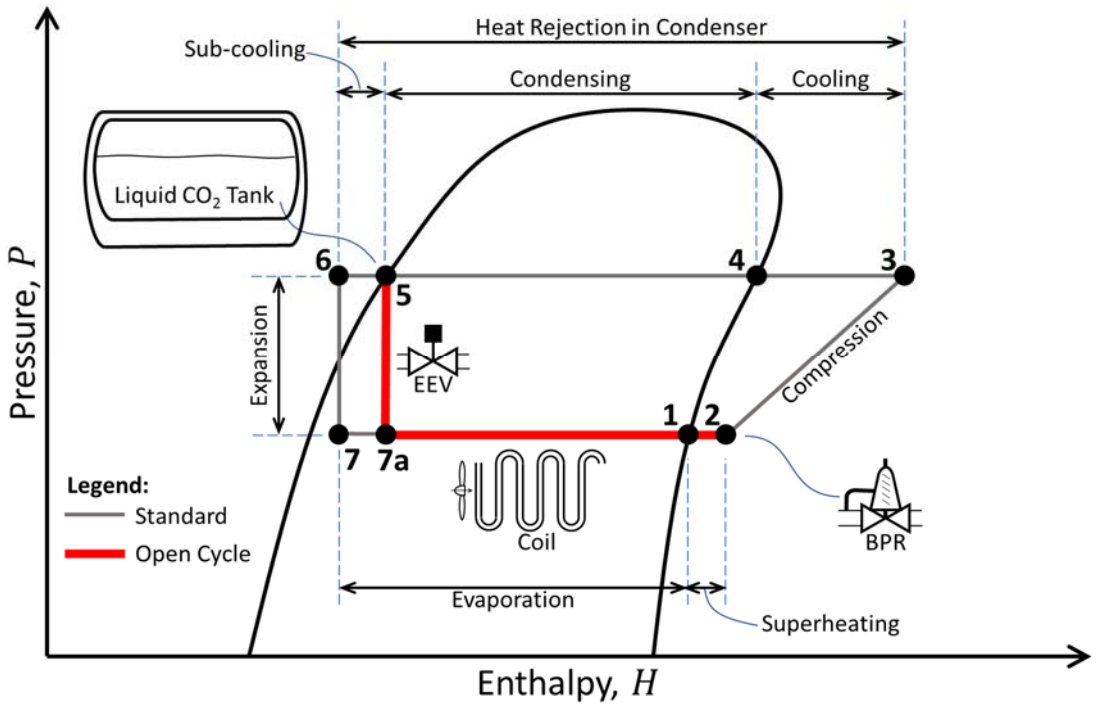

Figure 1: P-H Diagram for Standard Vapour Compression vs. Open Cycle CO_2

1.3 The CryoTech System

The CryoTech open cycle CO_2 refrigeration system used in this study is produced by Thermo King. Two variants are available, the CT-10 unit for rigid truck applications and the CT-15 unit for articulated trailer applications. Both versions use the same S-2 CT and S-3 CT remote evaporator sections and a vacuum insulated CO_2 tank with a capacity of either 330L or 430L. The unit uses hot water when heating or defrosting is required. In a CT-10 this hot water comes from the truck engine coolant circuit and for a CT-15 a small diesel fired burner is used to heat the water. Both the CT-10 and CT-15 are available for single temperature and multi-temperature applications where up to three different temperatures can be maintained within the same cargo box with a remote evaporator in each zone separated by movable insulated bulkheads. For the purposes of this study a CT-15 unit with an S-3 CT remote evaporator and a 330L CO_2 tank were used.

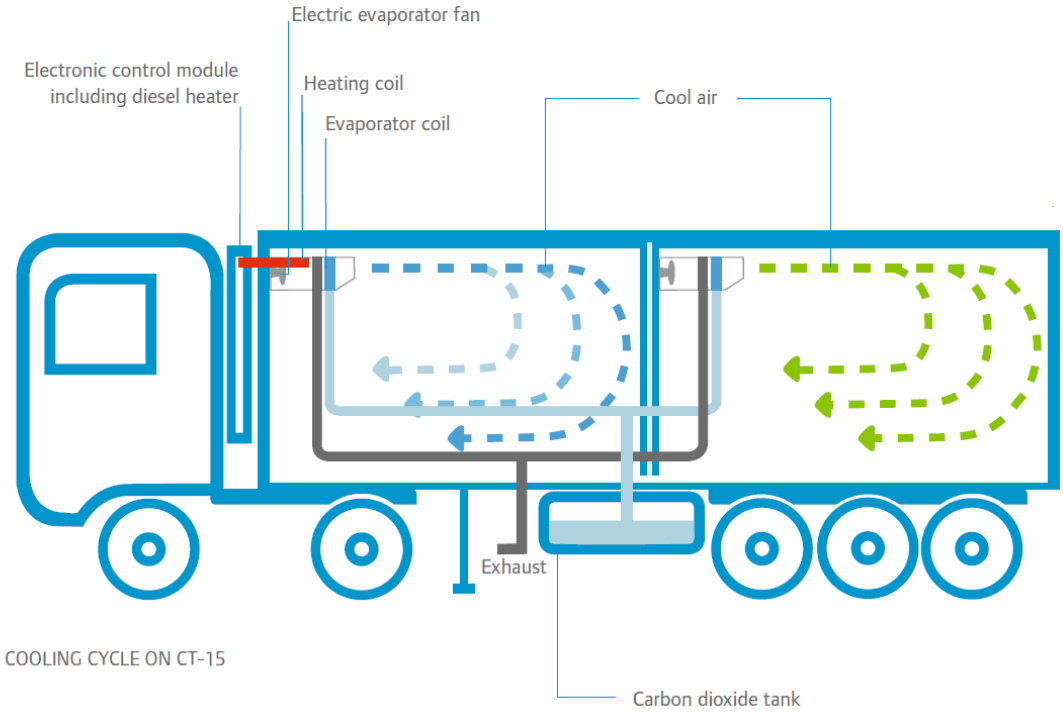

Figure 2: CryoTech CT-15 Multi-temperature System

1.3.1 The S-3 CT Remote Evaporator

The S-3 CT remote evaporator is the larger of the two available with CryoTech systems with a published cooling capacity of 8800W at the ATP (Agreement on the International Carriage of Perishable Foodstuffs) condition of 0°C box temperature and 30°C ambient temperature. It consists of a CO_2 refrigeration circuit containing a CO_2 evaporator coil, a pulse width modulated (PWM) electronic expansion valve (EEV), a back pressure regulator (BPR), a hot water circuit with a hot water coil and valve, a set of three 12 VDC blowers which produce a combined airflow of 2040 m^3 hr^{-1} and a set of sensors which includes an evaporator air inlet temperature (EAIT) sensor, an evaporator air outlet temperature (EAOT) sensor, an evaporator refrigerant outlet temperature (EROT) sensor and a evaporator coil outlet pressure (ECOP) sensor.

The S-3 CT remote evaporator is mounted on the ceiling of a cargo box and draws air up from below across the EAIT sensor before blowing it over the hot water coil and the CO_2 coil. The EAOT sensor is positioned in the outlet airstream of the CO_2 coil.

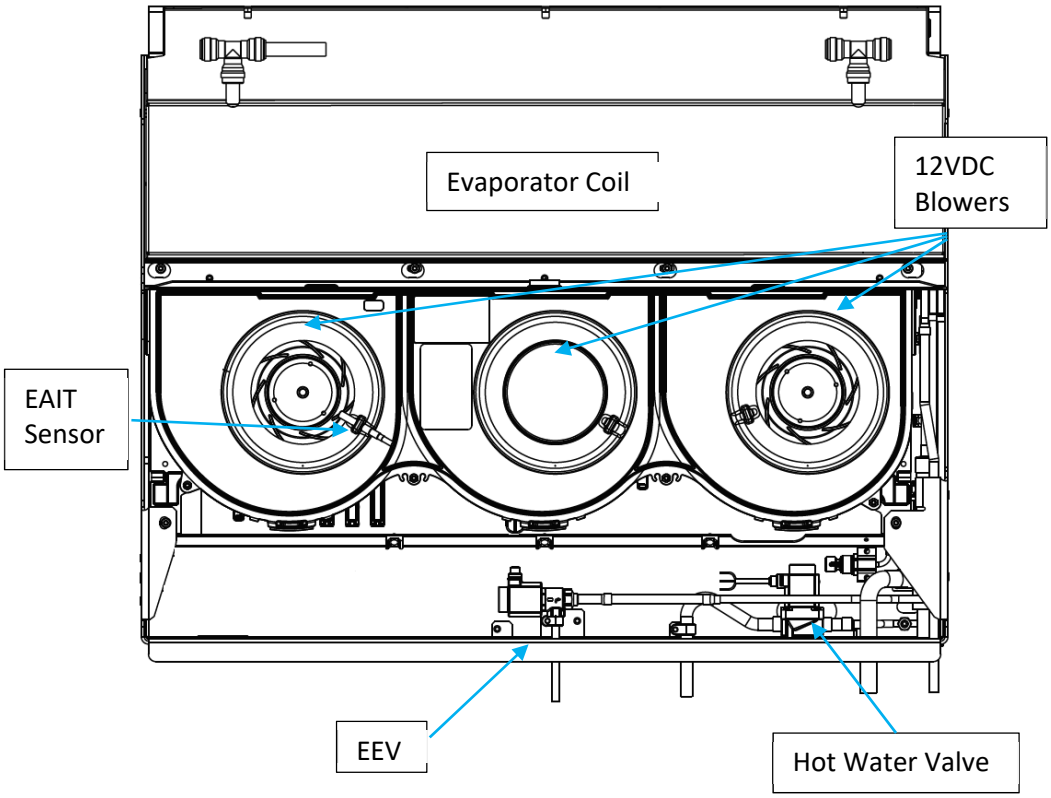

Figure 3: S-3 CT Remote Evaporator

The CO_2 coil is a fin and tube design and has a counter-cross flow configuration where the air flow is perpendicular to the refrigerant flow and the inlet air comes into contact with the refrigerant exiting the coil first, see Figure 4. The coil has a single pass in the refrigerant circuit with 32m of copper piping and 23 u-bends in total. The copper pipe has an inner diameter of 8.125 mm and a wall thickness of 0.7 mm. The total surface area for the copper pipe is 0.69 m^2. The CO_2 coil is four rows deep and six rows high and has a face area of 0.154 m^2. The secondary surface area of the aluminium fins is 6.81 m^2.

The function of the back pressure regulator is to maintain the pressure in the refrigerant circuit of the evaporator coil above the triple point of CO_2 of 517 kPa. It has a nominal setting of 584 kPa.

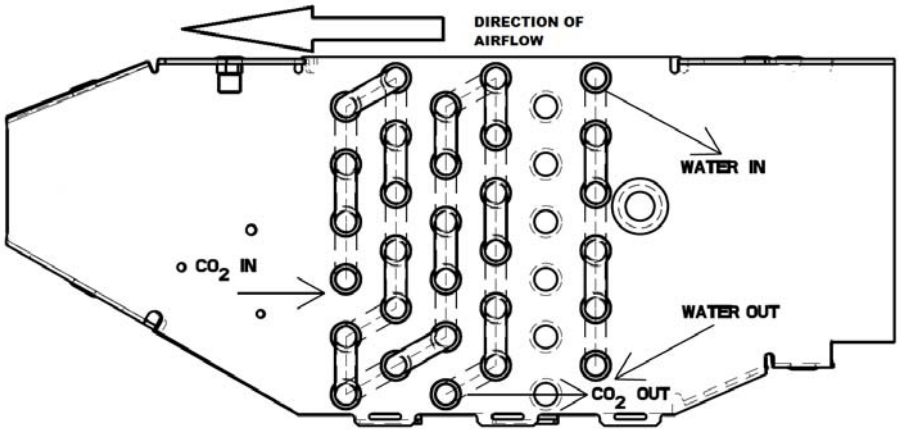

Figure 4: S-3 CT Counter Cross Flow Coil Layout

1.3.2 The CO_2 Tank

The CO_2 tank used in the CryoTech system is a double walled, vacuum insulated stainless steel tank. It is available in 330L and 430L capacity versions. As it is a pressure vessel it is regulated under the pressure equipment directive (PED) and must have safety relief valves as outlined in Figure 5.

The tank is maintained at 1034 kPa by the economizer valve which allows CO_2 vapour to vent at pressures above this setting. Heat leakage into the tank results in boiling of the CO_2 liquid, which at this pressure is at a temperature of -39°C, and results in a loss of approximately 1% of the CO_2 present in the tank over a 24 hour period when liquid CO_2 is not being drawn from the tank.

During installation the remote evaporator is connected to the CO_2 tank with 12.7 mm outer diameter copper piping which is insulated to minimize boiling in the line. When the EEV in the remote evaporator opens, liquid CO_2 is drawn from the bottom of the tank and flows through the piping to the CO_2 coil before being exhausted to atmosphere.

Filling of the CO_2 tank is conducted by a Thermo King CO_2 filling station which pumps the liquid CO_2 into the tank while drawing out the vapour. Filling times are between 10 and 15 minutes to fill a tank from empty depending on tank size and type of fill station.

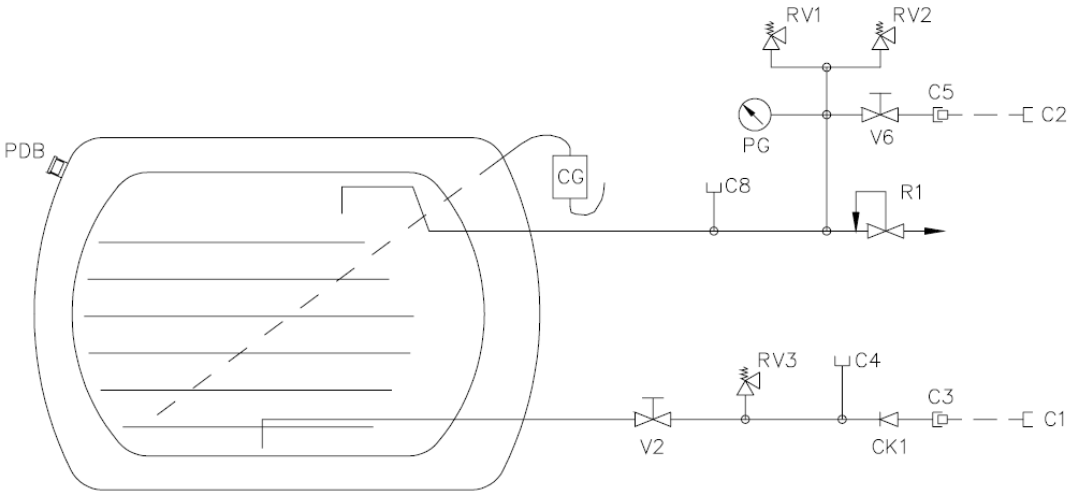

KEY

V2.	Liquid Fill / Decant Valve (1/2" NPT)
V6.	Gas Vent / Trycock Valve (3/4" NPT)
CK1.	Check Valve
PG.	Pressure Gauge
R1.	Economizer (set @ 135 psi)
RV1.	Main Relief Valve – 150 psi
RV2.	Secondary Relief Valve – 150 psi
RV3.	Thermal Relief Valve – 200 psi
PDB.	Safety Disc/Vacuum Pump Down Port
CG.	Contents Indicator/Current Transmitter (Not supplied) – Field Install
C1.	Fill Connector (Not Supplied) – Field Install
C2.	Vent Connector (Not Supplied) – Field Install
C3.	Liquid Fill Piping Connection (1/2" NPT Female)
C4.	Liquid Decant Piping Connection (1/2" NPT Female)
C5.	Gas Vent / Trycock Piping Connection (3/4" NPT Female)
C8.	Pressure Sensing Connection (1/4" NPT Female)
———	Tank Pipework
------	Field Installed Pipework

Figure 5: Vacuum Insulated CO_2 Tank

1.3.3 The System Control

The CryoTech open cycle is controlled by an integrated microprocessor and takes inputs from the user by means of a human machine interface (HMI) on the unit or a telematics device that communicates with the system over a mobile phone network.

Users enter the set-point temperature they need in the cargo box and the system determines whether heating or cooling is required to achieve the set-point temperature. The programmable

range of set-points for the CryoTech system is -40°C to 29°C. Users can also select the type of control they need, continuous or cycle sentry.

Continuous Control

The continuous control mode is designed for customers who have sensitive produce such as flowers or pharmaceuticals where the box temperature must be maintained as close as possible to the set-point temperature and where produce is sensitive to the temperature of the air that is discharged from the evaporator. Options are available for the pull-down to set-point phase which allow for the discharger air temperatures to be controlled to a minimum temperature or for the unit to get to set-point as quickly as possible. The use of these modes may depend on whether the cargo box is loaded or not during this pull-down phase. Once the unit reaches the set-point temperature as determined by the unit temperature sensor, the EEV will start to pulse to maintain the box temperature at that set-point. The evaporator fans will remain on while the unit is turned on in this mode.

Cycle Sentry Control

The cycle sentry control mode is designed for customers who have less sensitive produce such as dairy or frozen goods who wish to minimize their CO_2 consumption. For this mode the pull-down is achieved with the EEV fully open. Once the unit reaches set-point the EEV closes and the box temperature is allowed to increase to a programmable limit above the set-point. The default limit value is 2.2°C. Once the unit sensors indicate that this limit has been reached the EEV opens again and pulls the temperature back down to the set-point. The periods that the EEV is off are known as Null periods and it is possible to program the unit so that the evaporator fans are either off or on during this time.

1.4 Motivation

Despite the fact that open cycle TRU's have been on the market since the late 1990's little study has been completed on these systems. As mentioned in Section 1.1 the carbon footprint benefits over diesel powered TRU's have been established by Engberg et al. [11] and the systems other environmental credentials when it comes to PM, NO_x and noise emissions are self-evident.

However there have been no studies completed on the performance of the system and no attempts to model its characteristics.

This work examines the system in detail with regards to its temperature control, cooling capacity performance and efficiency of CO_2 use. A model of the system is developed with the aim of maximizing the system efficiency and providing a simulation tool for further system enhancement.

1.5 Layout of thesis

The remainder of this work is organized as follows. Chapter 2 is a review of the literature where studies of TRU's of different types are examined along with the modelling techniques which have been employed by others to model refrigeration systems dynamically. Chapter 3 describes the experimental system and the techniques used to investigate the open cycle CO_2 system before presenting the static and dynamic results from the testing. Chapter 4 introduces the base model that was adapted for the open cycle CO_2 system from work on vapour compression systems and uses the static and the dynamic pull-down results to develop the model further to achieve the required accuracy. Chapter 5 presents the validation of the model with the dynamic results from a full set of typical customer control modes and demonstrates improvements to the superheat control which was developed using the model. Chapter 6 discusses the experimental testing, system performance, model accuracy and utility in detail clearly outlining the benefits of the system, its current shortcomings, the good correlation of the model and its usefulness in developing future control and system upgrades. Chapter 7 contains the conclusions and the recommendation for future work.

Chapter 2 Literature review

2.1 Transport Refrigeration

The transport of temperature sensitive goods such as fresh and frozen foods, flowers and pharmaceuticals requires a cargo box that is temperature controlled. In the past the only means to reduce the temperature during transport was to use ice. However when Jones and Numero [12] patented the first transport refrigeration unit in 1942 this changed and allowed for the development of transport refrigeration as we know it today. The most common type of transport refrigeration unit uses a vapour compression cycle to cool a refrigerated box. The compressors for these systems are either driven by the vehicle engine for smaller trucks, by a separate diesel engine for larger trucks, articulated trailers and rail cars or by an electric power source for marine containers.

2.1.1 Alternative Transport Refrigerant Unit's

Other types of TRU's include systems with eutectic plates and those that use cryogenic liquids, either CO_2 or N_2, as a refrigerant in an open cycle exhausting the gas to atmosphere [13]. Open cycle systems were initially developed to spray the cryogen directly into the cargo space, initially with N_2 [14] and later with CO_2 [15]. This method has potential safety issues, as the cryogen replaces the oxygen in the atmosphere inside the cargo space, and performance issues for fresh produce, which requires airflow within the cargo space. None the less commercially available systems using nitrogen were available from BOC in the 1980's in the UK and were again marketed recently in Europe by EcoFridge with enhanced safety measures such as oxygen sensors. Both the safety and performance issue of the spray cryogen systems were resolved by using an evaporator coil instead to expand and contain the cryogen. Again the concept initially used N_2 [16] before extending the concept to CO_2 [17] with the addition of a back pressure regulator to maintain the pressure above the triple point in the coil and prevent dry ice forming. In 1991 Thermo King developed the first commercially available open cycle CO_2 system with an evaporator coil in response to the challenges of phasing out CFC refrigerants due to their ozone depleting effects. However hydro-fluorocarbon (HFC) refrigerants such as R404a were successfully implemented to address this issue and the use of open cycle CO_2 systems have remained a niche product since.

2.1.2 Environmental Impact of TRU's

Recent actions to phase out high GWP HFC refrigerants in an effort to combat climate change and the recent plans by cities such as Paris, Madrid, Copenhagen and London to introduce diesel bans once more brings the importance of this open cycle CO_2 technology to the fore. When compared with alternative low GWP systems that utilize natural gas engines or battery packs the economics and carbon footprint of the open cycle CO_2 system for city distribution offers a viable alternative.

The CO_2 used is a waste product of other industries and is liquefied efficiently at an industrial scale [18] requiring much less energy than would be used by a diesel powered TRU to produce equivalent cooling capacity. As a result these units have extremely low environmental impact emissions as examined by Engberg et al. [11] in a study of the system life cycle emissions, and are recognized by the California Air Resource Board (ARB) as a stepping stone towards zero emissions technology for TRU's [19]. A recent study Rai and Tassou [20] concluded that the production emissions of liquid CO_2 offset the in use benefits of open cycle CO_2 systems but they assumed that the CO_2 was separated from air and failed to consider that the majority of CO_2 is the marketplace is a waste gas from other industries such as ammonia and ethylene oxide production. According to a report by the European Industrial Gas Association [21] over 80% of the CO_2 recovered in Europe is obtained as a waste gas from these types of processes.

To the authors knowledge this is the first detailed analysis of an open cycle CO_2 TRU examining the system performance and efficiency, and the first attempt at modelling the system. For that reason, and because of the similarity of the evaporator coil and valve components, the next sections of the literature review will focus primarily on vapour compression systems with tube and fin heat exchangers.

2.2 Experimental Testing & Model Validation

The purpose of the experimental testing in this study is to characterize the open cycle CO_2 system in terms of performance and efficiency, and to use the results from the testing to validate the dynamic system model that will be developed. The review of the literature in Sections 2.2.1 focuses on experimental testing of TRU's due to the similarities in size, operating conditions and customer duty cycles to open cycle CO_2 systems. Studies of stationary equipment and mobile air conditioning systems were not considered due to the differences in the three parameters listed above. Particular emphasis is placed on measurement parameters that were

needed to characterize the system, how those measurements were taken and at what frequency. Section 2.2.2 then examines how experimental test results were utilized to validate dynamic models and why hard transients, such as system start-up and shut-down, were important to include in the experimental testing.

2.2.1 Experimental Testing on TRU's

All TRU's in Europe are required to undergo refrigeration capacity measurements under the ATP agreement for the international carriage of perishable foodstuffs [22] by an independent test agency. This testing involves using electrical heaters to balance the refrigerant load from the system and hence calculate the refrigeration capacity of the system by measuring the power applied to the heaters and the heat gained through the walls of the cargo box. The testing is done at ambient temperature of 30°C and two cargo box temperatures which are typically -20°C and 0°C. The test requires a stable box temperature and cooling capacity over a period of 3 hours. This long period of stability is difficult for open cycle CO_2 system as the pressure in the tank tends to drop as liquid CO_2 is drawn out. The issue was identified by the French ATP agency Cemafroid after the last ATP testing was performed on the open cycle CO_2 system with alternative proposals being made to the WP11 2014/16 working group in the UN to attempt to address the issue. Work is ongoing to get agreement on this proposal.

Dynamic experimental testing of TRU's in literature is limited. A study by Jia et al. [23] examined co-current flow and counter-flow evaporator coils in a marine container refrigeration unit. They measured refrigerant temperatures, air temperatures, refrigerant pressures and refrigerant mass flow rate but only presented limited data over a period of 250 s for the superheat temperature and air outlet temperature. A change in refrigerant mass flow rate from 73 to 80 g s^{-1} was used to induce a transient response but the effects on the two presented variables were minimal. The logging rate of the data acquisition system was not noted in the study.

Donnellan [24] presented a detailed analysis of defrost strategies and optimization on a TRU. The study included measurements of air temperature, refrigerant temperature, refrigerant mass flow rates, air velocity and refrigerant pressures. The author used both external thermocouples soldered to the tubes and immersion type thermocouples which contacted the refrigerant fluid to take measurements of the refrigerant temperatures. Refrigerant mass flow measurements were carried out using a coriolis mass flow meter. Dynamic test results are presented over a typical customer duty cycle which included the pull-down to the set-point temperature and controlling the temperature at set-point. The data was logged at 15 second

intervals which was sufficient for the defrost study but would be too slow to catch some of the faster dynamics of the refrigerant temperatures and pressures.

Experimental testing on a TRU is presented by Jain [25] as validation of a moving boundary model. Measurements of refrigerant enthalpy, refrigerant mass flow rate, evaporator and condenser temperatures and pressures are given for the system as well as for some sub-components. Both static and dynamic test results are presented but the scope of the dynamic results is limited by the system restrictions and no hard transient results are presented for the validation. For the steady state experimental testing data was sampled every 15 seconds and for transient testing the sampling rate was every 1 second. While the sampling rate for the dynamic testing for this study was faster than the other studies it is likely that some transient effects were still missed. No attempts were made in the studies discussed to determine the speed of transient response for any of the variables that were measured to determine what sampling frequency would be sufficient to capture all the dynamic characteristics.

2.2.2 Validation Testing of Vapour Compression Models

Model validation is the task of assessing if the model outputs agree with experimental data. It is critical for establishing the validity of the model but is often limited to specific variables of interest or missing all together with only comparisons to others models presented [26]. Model validation can be either quantitative where result are compared visually or qualitative where numerical comparisons of the results are presented. The sampling rate used in the experimental testing should be sufficient to capture the dynamic response of all the variables under study otherwise significant transient effects can be missed [26]. Hard transients, which are typically caused by unit start-up or shut-down, are also important to capture as they are difficult to model correctly [27].

A good example of qualitative experimental validation for a switched moving boundary model was presented by Li and Alleyne [28] where comparisons are made to condenser pressure, evaporator pressure, condenser air outlet temperature, evaporator air outlet temperature, evaporator refrigerant outlet temeprature and evaporator superheated temeperature. Hard transients were examined in this case to validate the switched moving boundary model with both start-up and shut-down conditions examined. No quantitative comparison of the results were performed and the rate at which the experimental data was sampled is not mentioned. In similar work by Li [29] the experimental data was sampled at 10 Hz which would be sufficient to capture dynamic transient effects for the data presented.

A qualitative comparison of a moving boundary model was presented by Yao, Wang & Huang [30] with temperatures for the condenser and evaporator along with the evaporator superheat compared. Quantitative analysis was presented using the mean relative error (MRE) given by:

$$MRE = \frac{1}{m}\sum_{i=1}^{m}\frac{\left|\Delta y_{sim} - \Delta y_{exp}\right|}{\left|\Delta y_{exp}\right|} \times 100\% \quad (2.\ 1)$$

where Δy is the variation in the response parameter compared to the initial value, the subscript *sim* refers to the simulation results, the subscript *exp* refers to the experimental results and m is the number of samples. Since the MRE was relative to the initial value it relied on the initial conditions in the model matching the initial conditions in the experimental testing to give a correct values for the absolute error between the simulation and experiment. If the initial conditions don't correlate an offset between the two sets of data will not be captured in the error. Some transient effects were examined where the EEV opening degree was increased by 5% and the evaporator heat load was increased by 0.2 kW but the effects on the measured variables was not large and no hard transients were examined. The sampling rate of the experimental data is not mentioned in the study but the simulation step time is set to 1 second so it is unlikely that the data was sampled any faster. This sampling rate would not be sufficient to capture all the transient effects for the temperatures and pressures under study.

A study by Pangborn et al. [31] showed experimental validation of both switched moving boundary and finite volume models with respect to condenser pressure, evaporator pressure and the full set of temperatures for both the evaporator and condenser. Quantitative analysis was performed using the normalized error residual given by:

$$NER = \frac{\sum_{k=1}^{end}(simulation(k) - experimental(k))^2}{\sum_{k=1}^{end} experimental(k)^2} \quad (2.\ 2)$$

where k is the sample time index. Transient effects were introduced by step changes in the EEV opening by 5% and by changes in the compressor speed from 1200 to 1400 RPM. These changes resulted in significant changes to the measured variables but again no hard transients were examined. Five different runs were completed to examine the noise in experimental results. The same test rig as Li [29] was utlized so the sampling time is likely to have been 10 Hz once again.

All of the studies above which have experimental validation have used a purpose built experimental test rig to provide experimental validation. While the design of these test rigs

allow for purpose built measurement locations they are often simplified systems missing components that are likely to be in commercial systems such as secondary valves. As discussed in Section 2.2.1 Jain [25] performs experimental validation on a commercial TRU. Although step changes in compressor speed and EEV opening are discussed during the work the final system validation is presented with only small changes in these two inputs due to the system restrictions. Quantitative error was evaluated using a root mean squares method:

$$e_{RMS} = \frac{1}{\bar{y}_{measured}}\left(\frac{\left\|y_{measured} - y_{predicted}\right\|}{\sqrt{n}}\right) \quad (2.\ 3)$$

where y was the output and n was the number of samples.

While many of the studies mentioned here display the lengths of the zones within the moving boundary models for the condenser and evaporator, none has attempted to validate the zone lengths experimentally.

2.3 Refrigeration System Models

2.3.1 Modelling Techniques

Modelling of refrigeration systems is generally made up using sub-models of the system components joined together [28,32,33]. For vapour compression systems the main sub-models would include a compressor, a condenser, an evaporator and an expansion valve model. Other components such as heat exchangers, receiver tanks and distributors have also been considered [25]. Models of the refrigerated space such as cargo boxes [29] have likewise been examined. Models can be either empirical, based on physical parameters of the components or be a combination of both. Often a physical model can be tuned with empirical data to give better performance [29,31].

Modelling of refrigeration systems can be broken down into two main categories, static and dynamic modelling. Static modelling concentrates on predicting behaviour of systems at prescribed values of factors such as evaporation temperature, condensation temperature, compressor speed and fan speed. They allow for system components to be sized to meet full range capacity requirements for the system at those predetermined conditions. Outside of the prescribed values the model is less reliable and performance may be less than optimal [34]. Transient effects, which can be significant for changes in compressor speed, fan speed and

expansion valve opening, are also neglected which makes static models unsuitable for developing system control algorithms.

Dynamic models are less common in literature but have become more popular with the increase in cheap computing power and the need for more efficient systems. They are generally physical models so that they can describe the transient system behaviour accurately. The condenser and evaporator coils are commonly modelled dynamically because of their complex, non-linear transient response [25,28,33]. These models tend to be based on mass and energy conservation equations. Computational fluid dynamic (CFD) models have been examined but it has been shown that they are currently unable to model the phase change of the fluid [35]. Two methods which are commonly used are the moving boundary and finite difference methods [26,31,36], see Section 2.3.2.

Other components within dynamic system models are often modelled statically as their response is an order of magnitude faster than the system response and their transient response has a negligible effect on the system response [25]. The expansion valve and the back pressure regulator are such components in open cycle CO_2 systems.

2.3.2 Evaporator and Condenser Coil Dynamic Models

The finite difference method splits up the length of the evaporator or condenser coil into a number of equal lengths and then calculates the changes in the refrigerant properties across each one. The advantages of such an approach are that it can accurately capture the phase transition between the two-phase and superheated regions in the evaporator and the condenser [36]. However it has been shown that at least 7-8 discretization's are needed for accurate results and this results in a computationally intensive model [37]. A more recent study from Pangborn et al. [31] comes to a similar conclusion showing that between 20 and 200 control volumes are needed to give accurate results in a finite difference model.

On the other hand the moving boundary technique has only two regions for an evaporator and three regions for a condenser. The model consists of a two-phase region and a superheated region for the evaporator and a superheated, a two-phase and a sub cooled region for the condenser with a moving boundary that can adjust the length of each of the regions depending on inputs to the models. Stability of the model can be an issue when the length of any of the zones goes to zero as can be the case when the superheated region in the evaporator disappears due to insufficient heat absorption. Various strategies have been employed to deal with this

situation including assuming a constant heat transfer coefficient to eliminate the need for a two zone model [38]. In most other cases a mean void fraction, which describes the ratio of vapour volume to total volume, is used to remove one or more of the zones from the model when needed [39]. However removing zones can cause discontinuities and numerical problems in the model. A novel approach to solve this has been to use pseudo-state variables to describe the inactive zone and allow them to track the output from the active zone to give a smooth transition when the zone once more becomes active [28]. These are known as switched moving boundary models.

Several studies [31,36,40] report that the moving boundary modelling approach has simulation speed advantages over the finite difference technique without significant effects on model accuracy.

2.3.3 Humidity Models

Another important factor for modelling evaporators is that of humidity. Humidity can have a large impact even when air temperature is above freezing. In the early stages of condensation water build up on the surface of the coil can either increase or decrease capacity. Eldredge [41] examines this effect on the air side heat transfer coefficient and gives a variable called the Colburn J factor to improve model accuracy. When frost begins to form on the evaporator coil airflow through the coil can be reduced and this will directly affect the cooling capacity of the system. Iragorry [42] found that frost also acts as an insulator and reduces the capacity of the coil. There are several models in literature, both physical and empirical for frost formation. The majority of the models however are for idealized situation where a flat plate or a cylinder is examined [42]. Tso [43] present a model which does examine a fin and tube evaporator using the finite difference method. The authors acknowledges that this in a complex non-linear problem because of the evaporator geometry and the position of the phase change within the evaporator. Experimental results show up to 20% difference with the model at certain times for the air side pressure drop across the coil. This pressure drop is related to the air flow rate and frost thickness and is a critical factor for the model. Currently it appears that the more complex models of frost formation do not offer sufficient benefits in terms of accuracy to justify the increase in complexity for the evaporator model.

2.4 Heat Transfer Coefficients Models

Both empirical models such as the Gnielinski [44] correlation and semi empirical correlations based on flow pattern maps have been used to predict heat transfer coefficients for refrigeration systems. According to Patino [45] those based on flow pattern maps have proven to be more accurate as they attempt to describe the different types of flow within the two phase region and base the correlations on the physical characteristics of each type of flow. Flow pattern map correlations were originally developed for HFC refrigerants [46] but fluid specific correlations for CO_2 [47,48] were created as it was recognized that the properties of the fluid in the two-phase region was significantly different to HFC refrigerants. According to Thome [49] the heat transfer coefficients for CO_2 can be 2-3 times higher than HFC refrigerants at the same saturation temperatures.

An attempt at a universal correlation for the annular flow region was recently made by Yuan et al. [50] but this still showed significant errors for CO_2 and did not address the other flow regions. Further updates to the flow pattern maps were introduced by Mastrullo et al. [51] which addressed the effects of differences in reduced pressures, the ratio of the pressure of the fluid to its critical pressure, on the transitions from one flow regime to another for both CO_2 and R410a. However no changes were proposed to the heat transfer coefficient equations within the flow regime and the reduced pressure for CO_2 was limited to 0.57 (7°C saturation temperature) whereas the reduced pressure in the open cycle CO_2 system in the current study are as low as 0.1 (-48°C saturation temperature). Studies in literature of heat transfer coefficients for CO_2 appear to be limited to saturation temperatures of -25°C with a reduced pressure of 0.21 so the findings of Mastrullo et al. [51] would suggest that the available correlations will have significant errors for the heat transfer coefficients in the open cycle CO_2 system under study.

2.5 Pressure Drop Models

In the models developed for vapour compression systems an assumption is made that there is negligible pressure drop along the length of the evaporator coil [28,39,52]. This assumption allowed for a significant reduction in the complexity of the model as the effects of momentum can be ignored. While this can be justified for vapour compression systems with short multi-

pass evaporator coils it cannot be assumed to be the case for single pass evaporator coils used in open cycle CO_2 systems where the pressure drop along the length of the coil can be up to 30% of the inlet pressure. This is of particular concern as the outlet pressure of the coil is controlled by the BPR and because the evaporator coil outlet pressure is needed as an input to the BPR when modelling the system.

Qiao et al. [53] do include pressure drop within their models for moving boundary systems. They use assumptions that the pressure drop varies linearly along the length of the two phase zone and that the pressure drop is concentrated at the outlet of the evaporator or at the outlet of each phase to simplify the modelling effort.

Correlations for pressure drop in two-phase flow for CO_2 were typically based on empirical models until Cheng et al. [54] developed a correlation based on a previous flow patent map model for HFC refrigerants. A review of pressure drop correlations by Mastrullo et al. [55] and an experimental study by Wu et al. [56] both conclude that the flow pattern map based model was the most accurate for CO_2 pressure drop.

Most models only consider flow in straight tubes, however the pressure drop in u-bends in the open cycle CO_2 system is an important consideration as there are 23 u-bends along the length of the single pass coil. An extensive review of the literature for two-phase pressure drop in u-bends by Da Silva Lima [57] indicated that pressure drop in u-bends can be between 1 and 7 times higher than pressure drop in straight tubes. The author also noted that the majority of studies were conducted with water and air mixtures, and that the studies that did include refrigerants were limited to flow in the bubby or mist flow regimes. A new pressure drop correlation taking into account the effects of u-bends was presented by Da Silva Lima [57] based initially on the flow pattern map correlation for pressure drop in straight tubes by Moreno Quibén and Thome [58]. This correlation should provide better accuracy for the open cycle CO_2 system which has 23 u-bends in the evaporator coil.

2.6 Superheated Zone Models

When modelling the superheated zone in the evaporator in a moving boundary model the majority of authors [28,52,59] assume that the enthalpy varies linearly along the length of the zone. While this assumption creates little error for systems with short superheated regions, modelling of systems such as the open cycle CO_2 system which have single pass coils with

superheated regions that can span the majority of the coil with higher air inlet temperatures, suffer from this assumption. Huang et al. [60] make use of the ε-NTU method for both the two-phase and single phase regions of their co-axial heat exchanger model that uses a combination of finite volumes and moving boundaries within the segments but only consider steady state conditions. The Log Mean Temperature Difference (LMTD) method [61] can also be used to calculate the inlet the outlet temperatures of the air and refrigerant in an evaporator for steady state conditions. In dynamic models a version of the ε-NTU method has been used to calculate the air outlet temperature [29,52] but the authors used a linear assumption for the refrigerant temperature distribution in the superheated zone.

2.7 Void Fraction Models

The void fraction is the ratio of the tube cross-section filled with vapour to the total cross-sectional area. It is used in the calculation of the two-phase heat transfer coefficients and pressure drop as well as in moving boundary models. Empirical and flow-pattern based models are available in literature to calculate the void fraction. The available flow pattern based models in literature deal for the most part with two-phase condensation [62,63] and those that include evaporation [64] do not include flow patterns such as dry out and mist flow in their flow pattern maps which are critical for two-phase flows at the typical mass flux values in the open cycle CO_2 system.

With regards to empirical models, the model by Zivi [65] uses a slip ratio to specify a velocity ratio between the liquid and vapour phases and has been used extensively in moving boundary models [52,53,59] although McKinley [52] does note that there is no reason the void fraction cannot be calculated by other methods. Void fraction correlations based on flow pattern maps have been used in both two-phase heat transfer coefficients and pressure drop models. The Rouhani-Axelsson drift flux model is the most common version and has been used by Thome et al. [63] for HFC refrigerants, and by Cheng et al. [54] and Kim et al. [66] for CO_2. Empirical models based on the Lockhart–Martinelli parameter [67] are also investigated in several review papers [64,68] with improvements on the base model made by Tandon et al. [69] by combining it with a mass flux term and by Yashar et al. [70] by adding a term based on the Froude number. Both of these are reported by Jassim et al. [64] to show good correlation over a large range of refrigerants but don't seem to be utilized extensively in literature for moving boundary, pressure drop or two-phase heat transfer coefficient models.

A review of void fraction models by Jassim et al. [64] concluded that the Zivi model predicted 78.2% of a database of 5 HFC refrigerants within 10% error bands, models based on the Lockhart–Martinelli predicted 80.3% the database with the 10% error bands and the Rouhani-Axelsson model predicted 88.8% of the same database within the 10% error bands.

2.8 Summary

A review of the current state of the art in terms of open cycle CO_2 systems, experimental testing on TRU's and modelling of vapour compression refrigeration systems has been conducted in this chapter. As mentioned in Section 2.1.2 there has been no experimental analysis or modelling of open cycle CO_2 transport refrigeration systems in the literature to date.

Best practice techniques for the static experimental testing of the open cycle CO_2 system have been identified in the ATP certification testing methodology and issues identified during the certification tests have been highlighted. The necessary temperature, pressure and mass flow rate parameters for characterization of the system have been identified from several studies of dynamic behaviour in similar refrigeration systems. The need for a sufficiently quick logging rate to capture all the transient effects in the experimental data is highlighted and the requirement for start-up and shut-down dynamics in the experimental testing to fully validate the model has been identified. The lack of experimental validation of the length of the two-phase zone has been noted and a methodology for such a measurement for the open cycle CO_2 system will be presented in Chapter 3.

Modelling approaches for vapour compression systems have been examined and the switched moving boundary technique has been identified as a good fit for modelling the open cycle CO_2 system due to its speed advantages over the finite difference method. The detailed aspects of the model such as heat transfer coefficients, pressure drop model, superheated zone model and void fraction will be discussed further during the model development in Chapter 4 when these will be selected based on their applicability to the CO_2 system and their accuracy when compared with experimental results.

Chapter 3 Experimental Testing

As detailed in Chapter 2 no studies in the literature have looked at the performance and efficiency of open cycle CO_2 systems or attempted to model them. The aim of this chapter is to provide the first experimental characterisation of on open cycle CO_2 system and to provide sufficiently varied experimental data for the validation of the model that will be developed in Chapter 4. An experimental test rig will be presented that utilizes test methodologies used for other refrigeration systems identified in Chapter 2, Section 2.2, Page 11 to measure temperatures, pressures and mass flow rates of the air and refrigerant. A new methodology for measuring the length of the two-phase region will be presented to allow for the first validation of this parameter in a moving boundary model. Some issues unique to experimental testing of open cycle CO_2 systems will be discussed.

In the second half of the chapter from Section 3.7 onwards a subset from the total number of static and dynamic experimental results will be presented with analysis of the system characteristics that are identified. The dynamic tests will include typical customer usage which includes hard transients which have been noted as important for including in the validation of the model. Section 3.12 will look at the CO_2 consumption for the different customer duty cycles with analysis of the variations between these modes of operation.

3.1 Experimental Setup

For the experimental testing a test rig was developed using a Thermo King CryoTech CT-15 unit and an S-3 CT remote evaporator to perform static and dynamic tests at different operating conditions. Pictures of the rig are shown below in Figure 6 and Figure 7.

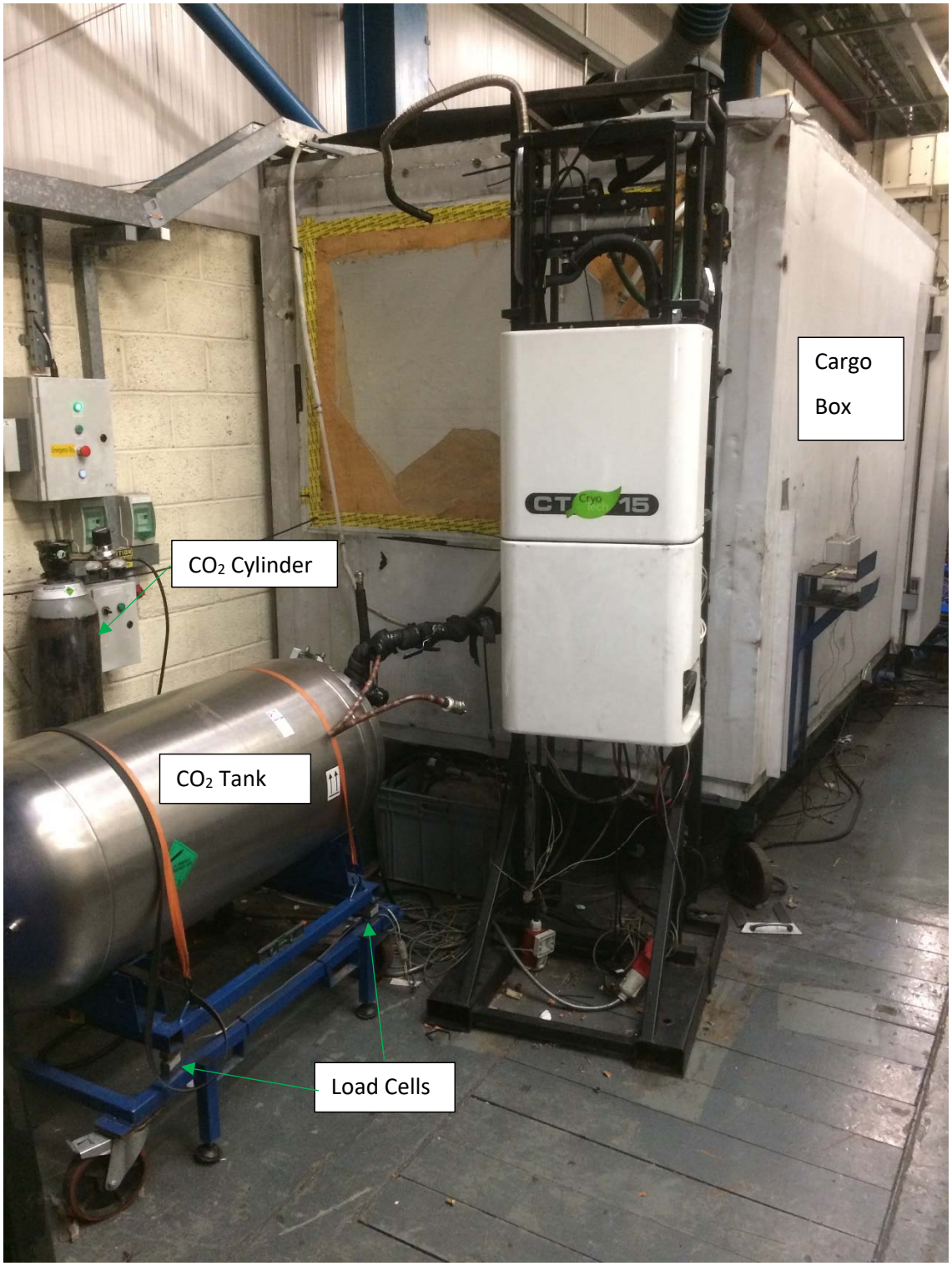

Figure 6: Experimental Test Rig

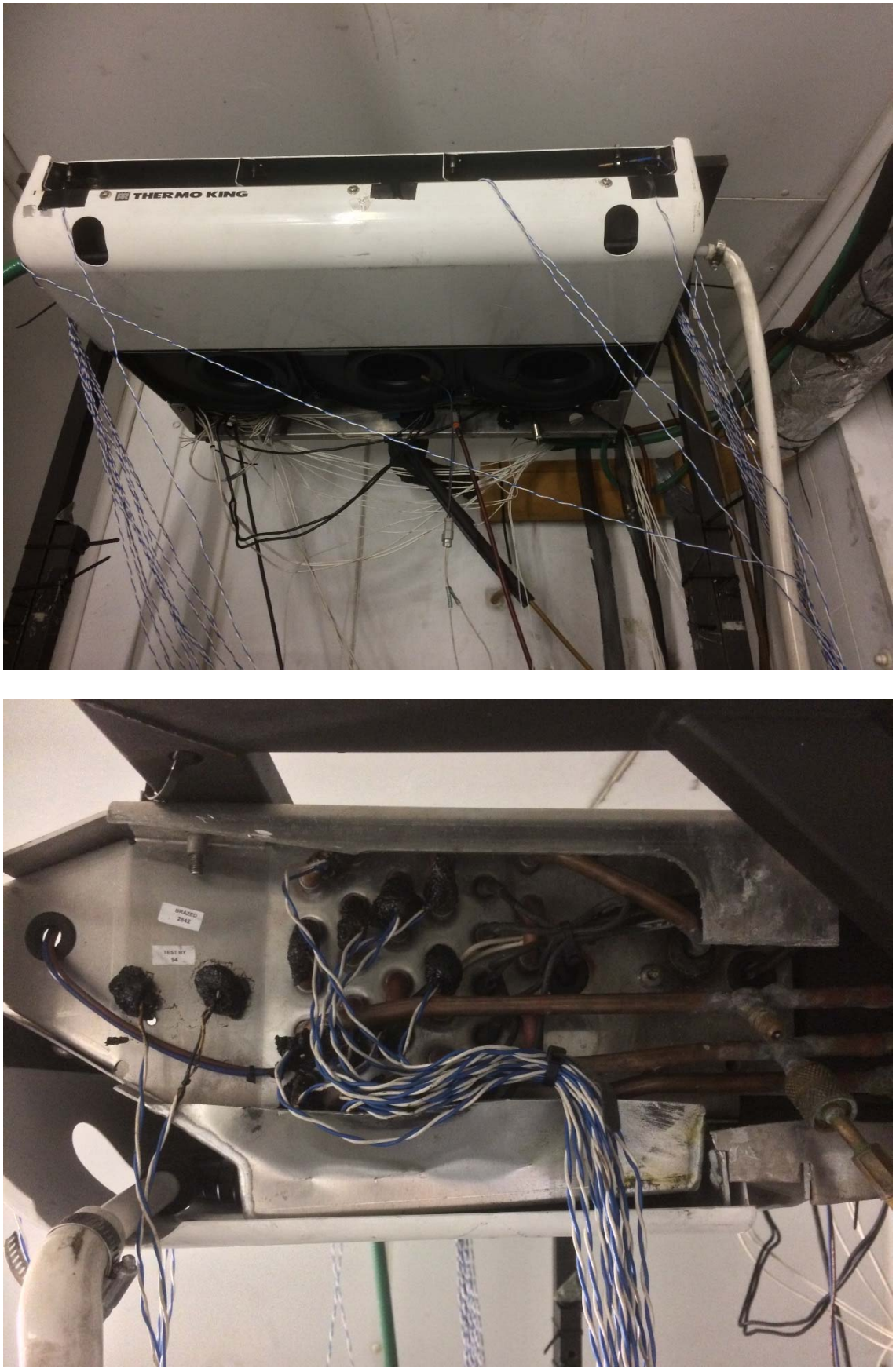

Figure 7: Instrumented S-3 CT Remote Evaporator

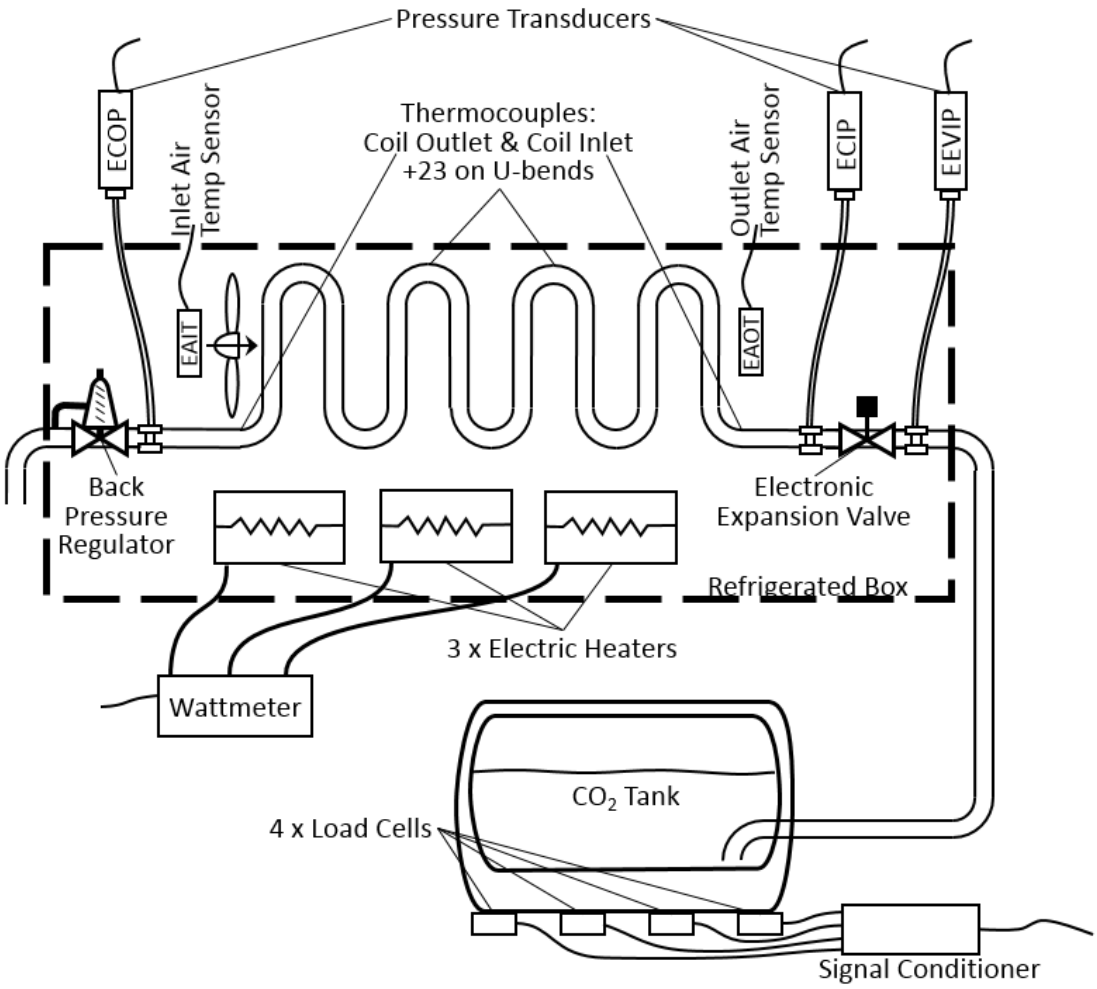

Measurement Equipment				
Measurement Parameter	**Equipment**	**Type**	**Manufacturer**	**Accuracy**
Temperature °C	**Thermocouple**	T-type	Cambridge Refrigeration Technology	±1°C
	Data logger	SCXI 1303	National Instruments	cold junction accuracy of 0.85C
Tank Mass kg	**Load Cells**	LCM101-250	Omega	±0.025Kg each
	Signal Conditioner	TXDIN 1600S	Omega	±5µA
Cooling Capacity W	**Wattmeter**	Digilogic Model DL3-1K5A2-6270	Scientific Columbus	0.1% of reading
Pressure kPa	**Pressure Transducers**	3HMP2-5	Sensata Technologies	±1% of reading

Figure 8: Experimental Test Setup

Thermocouples were added to the exterior of the copper piping to measure refrigeration temperature at the inlet to the coil (ERIT), at each u-bend of the evaporator coil (labelled POS1-23) and at the coil exit (EROT) as shown in Figure 7. Two sets of three thermocouples were also placed in the evaporator air inlet stream (EAIT) and the evaporator air outlet stream (EAOT) to measure average temperature. Pressure transducers were placed before the expansion valve (EEVIP), at the inlet to the coil (ECIP) and after the evaporator coil (ECOP). Four precision load cells were used to measure the mass of the tank and the output of this was used to calculate the mass flow rate of CO_2 ($\dot{m}$) over time. An external cylinder of CO_2 was utilized to maintain the tank pressure close to 951 kPa during the testing. Without this the pressure in the tank tended to drop as the liquid was withdrawn from the tank as the heat gain into the tank was insufficient to keep the pressure at the economizer setting. This pressure drop was especially an issue for the static testing where the cooling capacity of the system was to be measured as these tests required stable conditions over a long period of time with the EEV fully open. The test procedure for the static tests required balancing the cooling against the power from the electric heaters, the heat gain rate of the insulated box and the heat generated by the electric evaporator fans. This method is used for cooling capacity certification testing of transport refrigeration units [22].

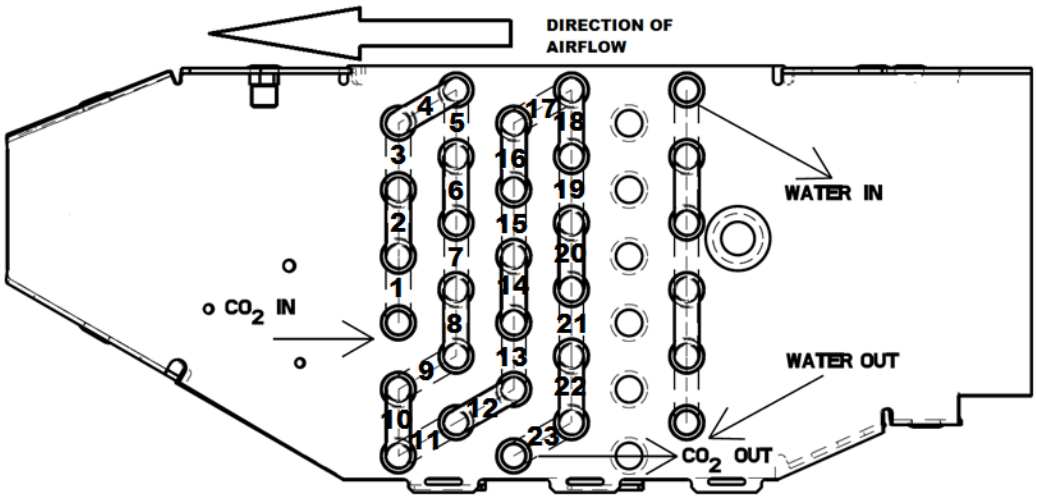

Figure 9: Thermocouple measurement locations (numbered)

All of the sensor data were logged initially at a rate of 1 Hz for the static testing. For the dynamic testing a study was performed to check the velocity of the boundary between the two-phase and superheated regions to determine the logging rate that was needed to accurately capture

the dynamics of the system. It was determined that the fastest transition of the two-phase boundary between two of the temperature measurement points, using the methodology described later in Section 3.8, took 0.7 s. As a result it was decided to log at 14 Hz, a rate that is equivalent approximately 10 times the fastest transition speed, to ensure enough data was available to capture the system dynamics sufficiently. This is in line with the best practice identified in studies in Chapter 2, Section 2.2, Page 11 where 10 Hz was the fastest logging rate used.

For the dynamic testing the control voltage of the EEV was also monitored to capture when the valve was opened and closed. This was needed to characterize the system behaviour when the EEV pulsed for temperature or superheat control. As the data logger was only capable of taking in 0-5 V signals the 12 V applied to the valve was used to switch a relay. A 5 V input into the data logger then indicated the valve was closed and a 1 V input indicated the valve was open.

3.2 Airflow Measurements

The S-3 CT remote evaporators from the CryoTech system utilized three 12V blowers as described in Chapter 1, Section 1.3.1, Page 4. A series of tests were performed on the test rig at box temperatures ranging from -30°C to +30°C to determine the effects of temperature changes and air density change on the airflow of the evaporator. The voltage and current for the fans were measured to determine the power consumed and fan RPM was checked at each measurement point with a handheld tachometer, see Table 1.

Figure 10: Wind-tunnel for Evaporator Airflow Measurement

Table 1: S-3 CT Evaporator Blower Data

Temperature (°C)	RPM Fan 1	RPM Fan 2	RPM Fan 3	RPM Average	Voltage at Fans (V)	Current (A)	Power (W)
28.7	2207	2209	2165	2194	12.19	6.00	219.42
28	2242	2267	2208	2239	12.67	6.37	242.12
27	2230	2258	2198	2229	12.195	6.55	239.51
20	2195	2203	2201	2200	12.2	6.10	223.26
20	2212	2253	2213	2226	12.67	6.45	245.29
21.7	2203	2233	2186	2207	12.18	6.30	230.20
20	2220	2259	2203	2227	12.29	6.60	243.34
20	2206	2242	2186	2211	12.23	6.64	243.74
17.5	2199	2207	2180	2195	12.6	6.50	245.70
18	2208	2230	2180	2206	12.6	6.50	245.70
18.5	2204	2214	2179	2199	12.6	6.50	245.70
10	2175	2198	2179	2184	12.16	6.00	218.88
10	2209	2218	2187	2205	12.67	6.55	249.09
10	2168	2204	2150	2174	12.18	6.40	233.86
10	2208	2227	2167	2201	12.29	6.60	243.34
10	2189	2205	2164	2186	12.246	6.64	243.90
0	2146	2169	2149	2155	12.18	6.00	219.24
0	2177	2213	2173	2188	12.67	6.65	252.89
0	2153	2199	2133	2162	12.18	6.53	238.73
0	2168	2197	2145	2170	12.229	6.53	239.69
-10	2126	2151	2128	2135	12.17	5.60	204.46
-10	2153	2210	2156	2173	12.67	6.76	256.82
-10	2131	2151	2122	2135	12.18	6.73	246.04
-10	2138	2171	2114	2141	12.204	6.86	250.98
-20	2106	2118	2111	2112	12.2	5.60	204.96
-20	2142	2176	2138	2152	12.67	6.86	260.62
-20	2096	2130	2103	2110	12.18	6.77	247.25
-20	2014	2153	2100	2089	12.227	6.97	255.81
-30	2061	2099	2102	2087	12.15	4.30	156.74
-30	2088	2136	2093	2106	12.18	6.87	250.91
-30	2067	2125	2071	2088	12.224	7.12	260.96

The same S-3 CT remote evaporator was then mounted on a wind tunnel which was designed per the AMCA standard [71] for aerodynamic testing of fans. The data from the

Table 1 was then used to calculate the equivalent static pressure for the test rig by matching the current draw and RPM's for the blowers and by monitoring the ambient temperature in which the test was being conducted as shown in Figure 11. This data will be used in Chapter 4

to develop a fan model which can vary the airflow rate depending on conditions such as box temperature, relative humidity and fan RPM.

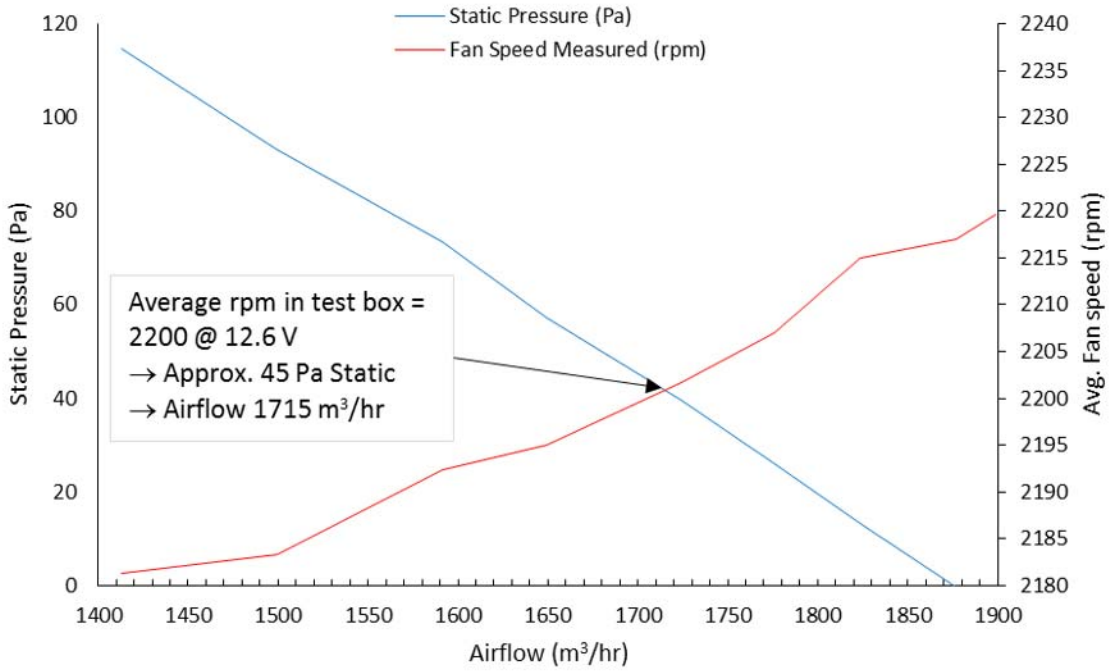

Figure 11: S-3 CT Evaporator Airflow Test @ 18°C

3.3 Effects of Vapour at Inlet to EEV

In general for studies of vapour compression systems [39,52] there is an assumption that the liquid entering the expansion valve is in a sub cooled state. This is achieved through a mixture of drawing liquid off the bottom of a receiver tank and cooling the liquid with the cold suction gases exiting the evaporator by means of a suction line heat exchanger. However for the open cycle CO_2 systems sub-cooled liquid at the EEV is not possible. Although liquid CO_2 is drawn from the bottom of the tank there is generally several meters of piping between the tank and the expansion valve, and a significant temperature difference between the liquid CO_2 temperature of -39°C at 1034 kPa and the average air temperature in the test lab of approximately 30°C, resulting in some boiling of the liquid CO_2 in the piping and consequently an increase in the enthalpy. Sub-cooling the liquid via a heat exchanger is not possible as normally the vapour exiting the evaporator is at a higher temperature than the liquid at the inlet. As a result the insulation of the lines between the tank and the evaporator is very important when minimizing

the amount of vapour present at the inlet to the expansion valve and will be investigated below to see the effect of increasing the amount of insulation has on system characteristics.

The main effects of having vapour at the inlet to the expansion valve were to decrease the mass flow rate through the valve and to increase the enthalpy. The decrease in mass flow rate is due to the increase in the volume of the fluid that is passing through the valve. Liquid CO_2 at 1034 kPa has a density of 1113 kg m^{-3} whereas CO_2 vapour has a density of only 27 Kg m^{-3} at the same pressure [72]. This increases the volume of the fluid substantially for even small increases in the vapour quality. For example a vapour quality increase of 3.5% results in the fluid volume increasing 2.3 times which would result in a 20% reduction in flow rate. The resulting decrease in flow rate produces a proportional reduction in system cooling capacity but cooling capacity per kg of CO_2 remains unaffected. As long as the reduction in cooling capacity is taken into account, adequate sizing of the system can be achieved.

The enthalpy change due to the boiling of the liquid in the tube results in a proportional reduction in the cooling capacity of the system while also producing a reduction of system cooling capacity per kg of CO_2 and is therefore more significant in terms of system efficiency. Any increase due to heat transfer from the piping to the air within the insulated box will contribute to the cooling effect of the system but anything that happens outside the box will be lost cooling potential. Therefore the insulation of the piping between the tank and the insulated box is of highest importance.

A series of tests were carried out within increasing amounts of insulation on the piping between the tank and the expansion valve. Test 1 was a baseline test carried out with a very short length of pipe of 1m between the tank and the expansion valve, and insulated with 100mm thick phenolic insulation with a K-factor 0.02 W m^{-1} K^{-1} where possible. The tank valve manifold was the exception to this due to the difficult geometry and it was insulated with several layers of the 9.5mm thick insulation with the K factor of 0.04 W m^{-1} K^{-1}.

For the baseline test the inlet and outlet pressure of the EEV and the mass flow rate of CO_2 were recorded. The liquid density, ρ_f, at EEV inlet pressure was calculated using *Refprop* with the assumption that there was saturated liquid present. With this data a flow coefficient K_v was calculated using:

$$K_v = \frac{\dot{m}}{\rho_f \sqrt{\Delta P / SG}} \tag{3. 1}$$

where ΔP is the pressure drop across the valve and SG is the specific gravity of liquid CO_2. This baseline test was performed three times to get an average value of 0.0793 for the K_v.

Tests 2, 3 and 4 were all conducted with the standard piping length for the test setup of 7.5m between the tank and the EEV. For Test 2 there was no insulation used. For Test 3 a single layer of 9.5mm thick, 0.0403 W m^{-1} K^{-1} insulation was used between the tank manifold and the EEV, with no insulation on the manifold itself. This is standard practice for installation of these types of systems. Finally for Test 4 all piping from the tank manifold to the evaporator was insulated with 100mm thick phenolic insulation with a K factor 0.02 W m^{-1} K^{-1} and the tank manifold was insulated as per Test 1.

For the Tests 2, 3 and 4 it was assumed that Equation 3.1 was still valid when the CO_2 entering the coil was two-phase and the two-phase density, ρ_{TP}, was back calculated assuming the same value for K_v that was found in Test 1, the measured values for the mass flow rate, $\dot{m}$, and ΔP. With a value for ρ_{TP} it was possible to calculate the void fraction, γ, using:

$$\gamma = \frac{\rho_{TP} - \rho_f}{\rho_g - \rho_f} \tag{3. 2}$$

where ρ_g is the vapour density.

Finally the inlet quality, x, at the EEV was calculated using:

$$x = \frac{\gamma \mu_s}{1 - \gamma(1 - \mu_s)} \tag{3. 3}$$

where μ_s = $(\rho_g/\rho_f)S$ and the slip ratio, S, is taken to be $S = (\rho_f/\rho_g)^{1/3}$ from the Zivi correlation [73].

The average results for Tests 2, 3 and 4 are shown in Table 2. As a result of these tests it was decided to use the highest level of insulation from Test 4 for the experimental set-up to help achieve the closest correlation with the model outputs in Chapters 4 and 5.

Table 2: Refrigerant Quality with varying levels of insulation

Test	**2**	**3**	**4**
Description	No Insulation	Standard Insulation	High Level of Insulation
$\dot{m}$	0.0243	0.0224	0.0238
ΔP	161	133	120
ρ_{TP}	758	786	1114
γ	0.327	0.304	0.109
μ_s	0.0834	0.0813	0.0831
χ	3.9%	3.7%	1.1%

3.4 Measurements of Mass flow rate of CO_2

Typically the mass flow of refrigerant in experimental testing is performed using a mass flow meter as described in several of the experimental studies in Chapter 2, Section 2, Page 11. A coriolis mass flow meter was initial used in the open cycle CO_2 test rig but proved to be inaccurate due to the vapour in the liquid line that is discussed in Section 3.3. As a result a different solution based on measuring the mass of the tank was utilized.

The measurements of the mass flow rate of the CO_2 were taken by measuring the change in mass of the CO_2 tank over time when the EEV was open and there was liquid CO_2 at the EEV. The load cells used were accurate to within ±0.025 kg so with typical flow rates of between 0.02 kg/s and 0.025 kg/s, as seen in Figure 12, it was necessary to take the measurement over a relatively long period of time to get accuracy. For tests where the EEV was pulsing at different duty cycles it was not possible to identify the flow rate for each opening period so it was assumed to be the same as the flow rate measured during the pull-down phase. An example of the measurements taken for pull-downs to a frozen set point of -25°C is shown in Figure 12. The slope of the linear trend line gives the mass flow rate in kg s^{-1} and the R^2 value shows how closely the data matches the linear trend line. From this testing it can also be seen that the initial level of liquid CO_2 in the tank does not affect the accuracy of the measurements.

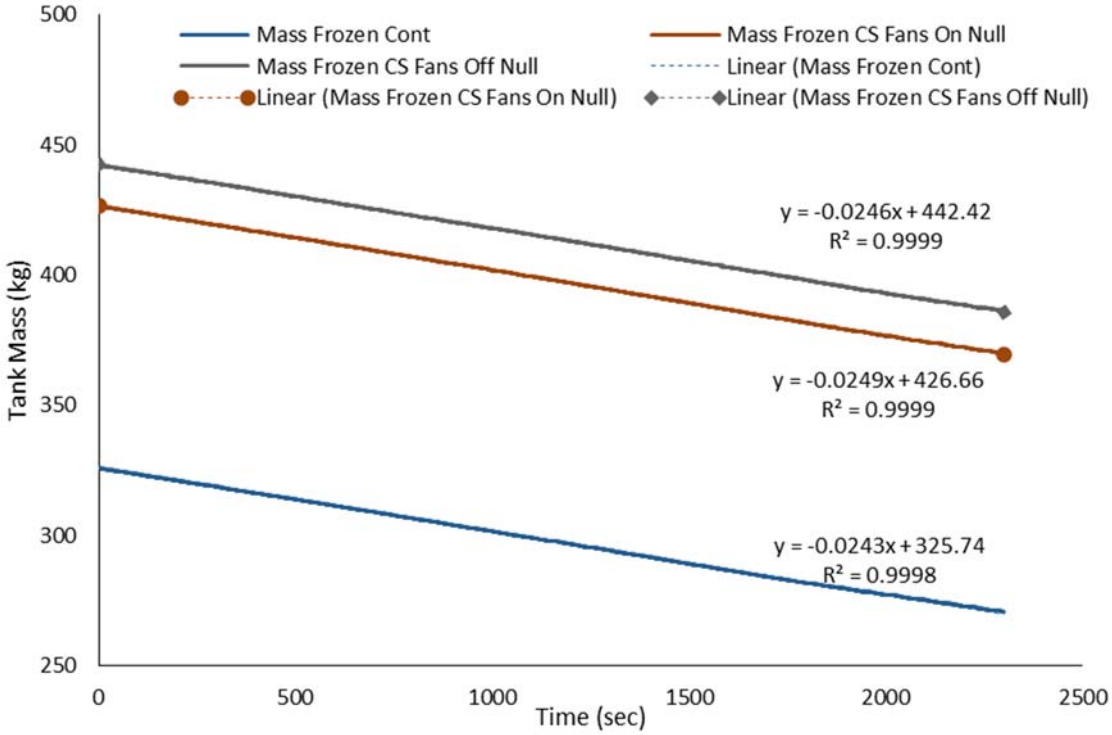

Figure 12: Tank Mass for Pull-downs to -25°C Set-point

3.5 Evaporator Air Outlet Temperature Measurements

A study was conducted to determine the best place to locate the thermocouples for EAOT measurements as it was noted by Pangborn et al. [31] that incorrectly placed measurement for EAOT could results in errors when comparisons are made to simulations. A set of nine thermocouples were used at 30mm, 80mm and 130mm from the face of the coil and along the length of first tube of the refrigeration circuit outlined in Figure 13. The unit was allowed to pull-down with the EEV fully open until the two-phase boundary reached the outlet of the coil as determined by the methodology outlined in Sections 3.6 and 3.8. The mass flow rate of CO_2 was 0.0249 kg s^{-1} during the test.

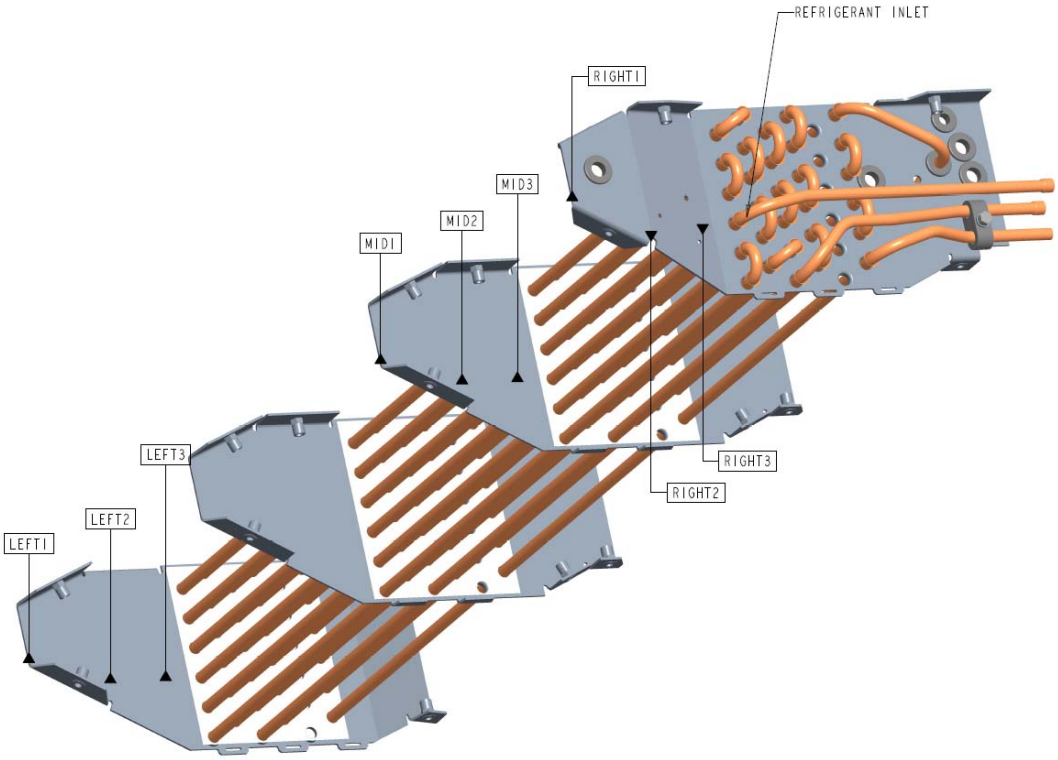

Figure 13: Thermocouple Measurement Locations for EAOT Study

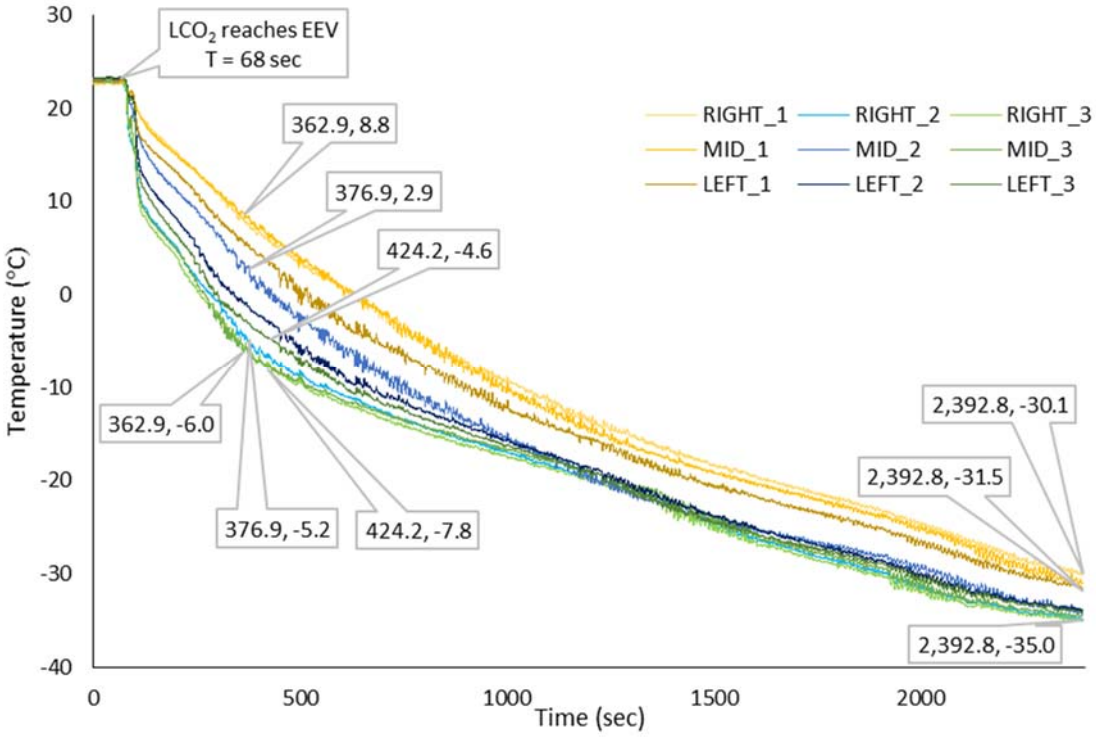

Figure 14: Evaporator Air Outlet Temperature Measurement Location Study Results

The results of this study are presented in Figure 14. It can be seen that there are large deviations in the temperatures measured especially during the initial pull-down period from 68 seconds to 1000 seconds. The largest deviation with increasing distance from the coil occurred at 362.9 seconds where Mid 1, the measurement point the furthest distance away from the coil, was 14.8°C warmer then Mid 3, which was closest to the coil. The largest deviation across the face of the coil occurred shortly afterwards at 376.9 seconds where Mid 2 was 8.1°C warmer than Right 2 which was at the same distance from the face of the coil. After 1000 seconds the deviation in the EAOT measurements for the point at 30mm and 80mm away from the coil decreases substantially. This likely corresponds with the two-phase boundary reaching the end of tube 11 as this is the last tube in the first row of the coil and tubes 10 and 11 are just below tube 1 in the first row, as shown in Figure 9 on Page 26. At the end of the test where the full coil is full of two-phase CO_2 the largest deviation at distances away from the coil is down to 4.9°C on the right side of the coil and the largest deviation across the face of the coil down to 1.4°C at the furthest point from the coil.

For the purposes of comparison with the model developed in Chapter 4 the measurements closest to the coil will be used as these are closest to the simulation output. The deviation across these points is highest at 3.2°C at 424.2 seconds and the deviation reduces to less than 2.1°C from 720 seconds for the remainder of the test. It should be noted that the unit discharge air sensor is placed at the 130mm distance from the coil to best reflect the temperature which will be experienced by the cargo.

3.6 Measurement of two-phase region length for Static Testing

Validation of the normalized length of the two-phase region, ζ, was performed by monitoring the temperatures along the length of the coil. The single pass coil in the S-3 CT evaporator in the open cycle CO_2 system allows for 25 thermocouple measurements positioned at the inlet (ERIT), at the 23 u-bends (labelled POS1-23) and at the outlet (EROT) as outlined in Section 3.1.

Table 3: Thermocouple Measurement Location vs. ζ value

Location	ζ value
ERIT	0
POS 1	0.0417
POS 2	0.0833
POS 3	0.125
POS 4	0.167
POS5	0.208
POS 6	0.250
POS 7	0.292
POS 8	0.333

Location	ζ value
POS 9	0.375
POS 10	0.417
POS 11	0.458
POS 12	0.500
POS 13	0.542
POS 14	0.583
POS 15	0.625
POS 16	0.667
POS 17	0.708

Location	ζ value
POS 18	0.750
POS 19	0.792
POS 20	0.833
POS 21	0.875
POS 22	0.917
POS 23	0.958
EROT	1.000

To determine the value of ζ the temperature at each of the points along the coil were examined and the two-phase boundary was identified by the location at which the temperature oscillations reached the saturation temperature. The rapid decrease in temperature was an indication that liquid CO_2 droplets, which at the saturation temperature were generally much colder than the superheated vapour temperature, had impacted the u-bend and that the refrigerant at this point was in the mist flow region of the flow pattern map, see Figure 15.

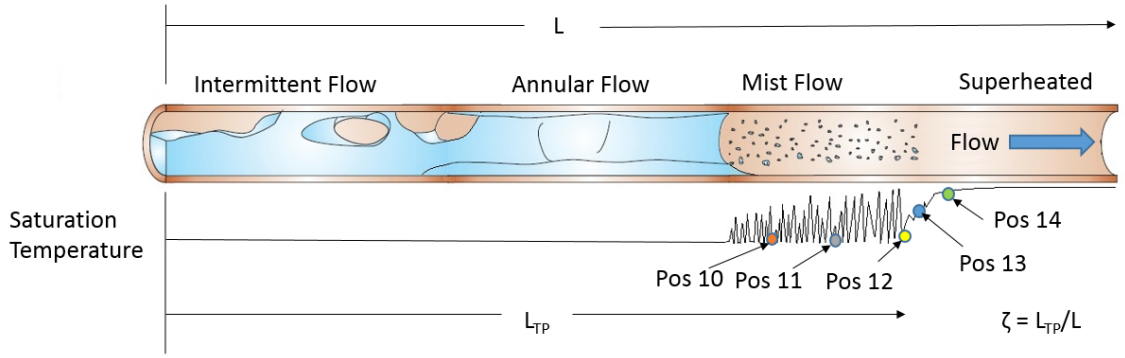

Figure 15: Two-phase flow patterns to Superheated in Evaporator Coil

Figure 15 is an instant in time where the temperature is plotted against the two-phase zone length. Positions 10 and 11 are in mist flow region and since this region only contains droplets of liquid CO_2 the temperature fluctuates back towards the vapour temperature between droplet impacts. Position 12 is the location of the two-phase region boundary where the temperature

fluctuations are just reaching the saturation temperature. For position 13, which is in the superheated region, some temperature oscillation were still present but they do not reach the saturation temperature. Further into the superheated region at position 14 the temperature remain consistently higher with only minor oscillations.

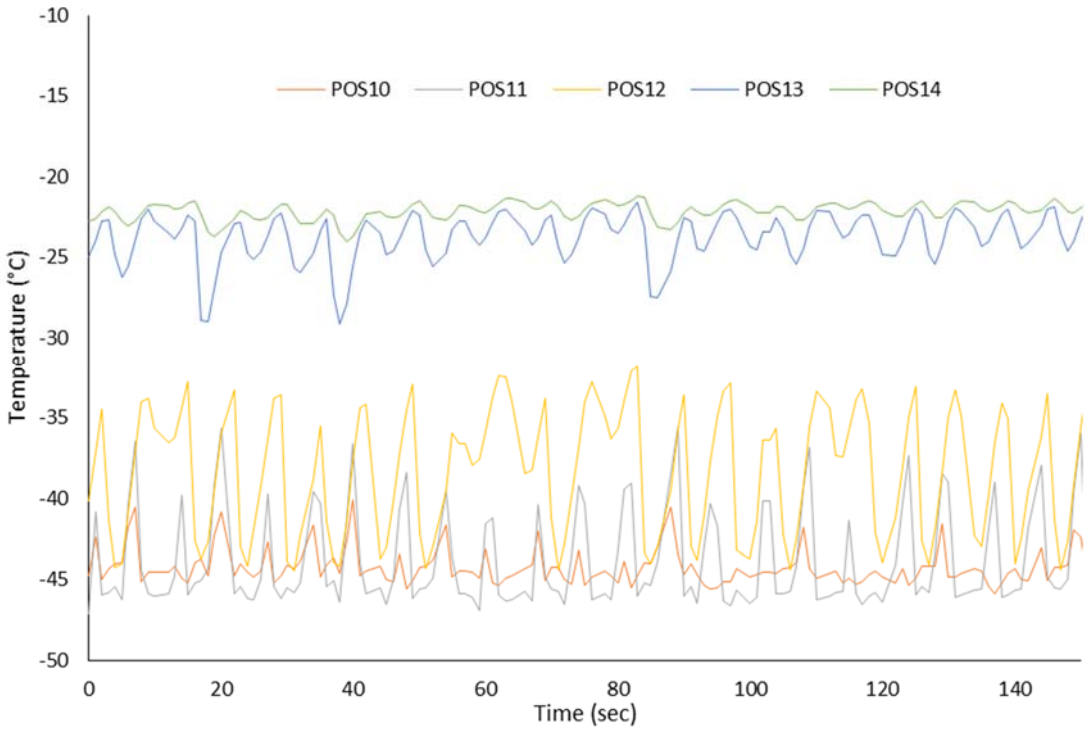

Figure 16: Coil Temperatures for Static Test for -9.5°C Box and Mass flow-rate of 0.0219 kg s^{-1}

Figure 16 shows coil temperature measurements against time for the same measurement points as Figure 15. Position 12, which represents a ζ value of 0.5, has been identified as the location of the two-phase boundary for this test as the temperatures seen for this point fluctuate down as far as the saturation temperature. The temperatures for position 13 are not low enough to indicate that liquid CO_2 is impacting the u-bend walls in this location and for this reason this point has been identified to be in the superheated region. The ζ value is given as ±0.04 as this is the normalized distance between any two measurement points. These measurements are repeated for each of the static tests in the next section.

3.7 Experimental Results for Static Tests

Three static tests were carried out at average box temperatures of 4.4°C, -9.5°C and -13.0°C over a period of 1000 s. Graphs of temperature and pressure measurements are shown in the sections below to demonstrate how well controlled these parameters are. These are followed by a graph of the coil temperatures measurements which indicate the location of the two-phase zone boundary as described in Section 3.6. The mass flow rate of the CO_2 was calculated from the mass of the tank with the method outlined in Section 3.4. The inlet enthalpy was calculated from *RefProp* [72] using the average EEV inlet pressure (EEVIP) and the assumption from Section 3.3 that the inlet quality is 1.1%. To get accurate results all temperatures and pressures should remain constant throughout the test. EAIT and EEVIP were considered to have the biggest impact as they affected the heat transfer and the mass flow rate of CO_2 respectively. The deviations in these temperatures and pressures, and the effects they have on the measurements are described below.

3.7.1 Results at Box Temperature of 4.4°C

For Test 1 EAIT, Figure 17, reduced by 0.07°C on average over the length of the test. This is within the ± 0.5 K that is allowable in the ATP testing procedure [22]. However EEVIP, Figure 18, had a more significant reduction in its average of 22 kPa over the 1000 s. The ATP regulations have no limits with regards to the pressure within the system but as discussed in Chapter 2, Section 2.2.1, Page 12 the changes in pressure are an issue when measuring the cooling capacity of an open cycle CO_2 system. The addition of the external cylinder, as described in Section 3.1, to maintain the pressure was not fully successful in preventing this issue. This drop in inlet pressure into the valve results in a drop in mass flow rate of the CO_2 and a consequent decrease in cooling capacity and the length of ζ. For Test 1 the length of ζ, as demonstrated by the coil temperature measurements in Figure 19, does not vary during the test indicating that the pressure drop in EEVIP is not significant.

The heat added to the box to maintain the EAIT was 7.0 kW. To calculate the cooling capacity of the system for these conditions the heat lost from the box at the ambient temperature of 17.6°C of 405 W and the heat from the evaporator fans of 251 W are summed with the heat added to the box to get the total of 7.7 kW.

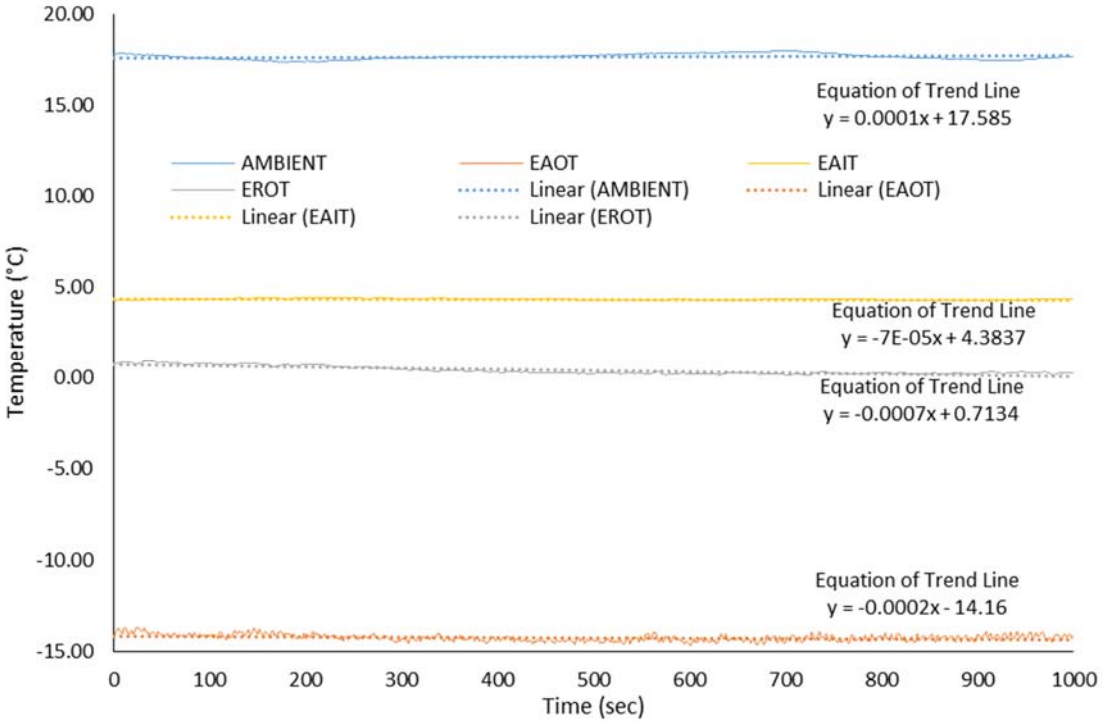

Figure 17: Air and Refrigerant Temperatures for Static Test 1. Box Temperature = 4.4°C, Flow Rate = 0.0215 kg s^{-1}, Inlet Enthalpy = 113.79 kJ kg^{-1}

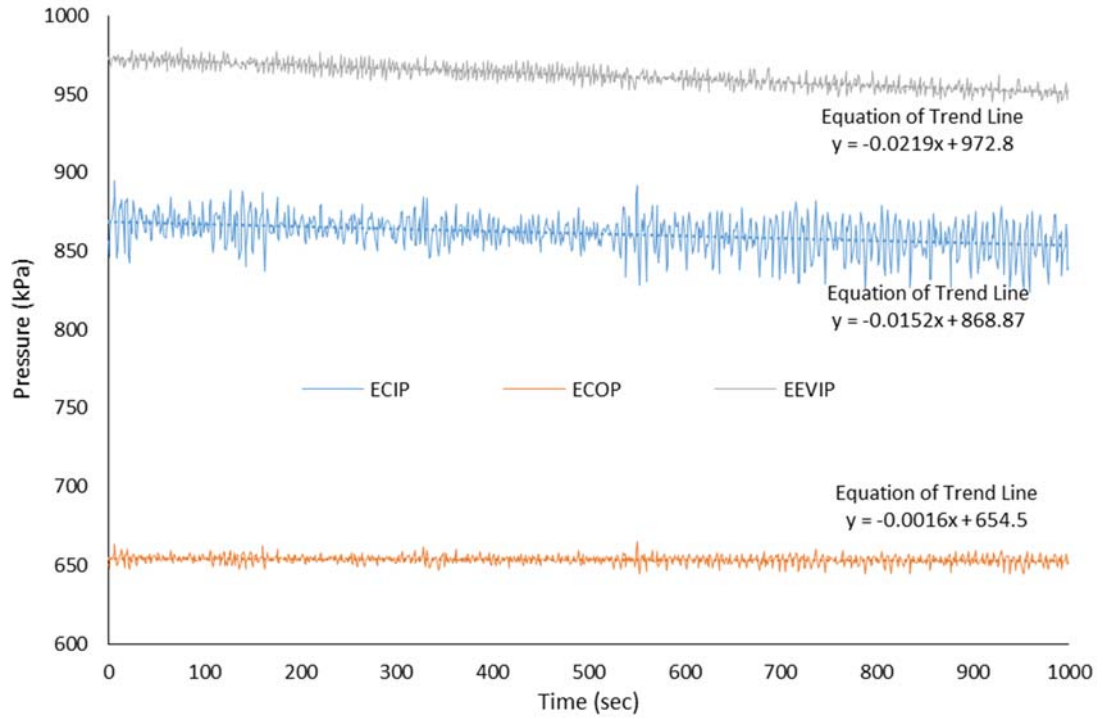

Figure 18: Pressure for Static Test 1. Box Temperature = 4.4°C, Flow Rate = 0.0215 kg s^{-1}, Inlet Enthalpy = 114 kJ kg^{-1}

The coil temperatures surrounding the two-phase boundary are displayed in Figure 19. Measurement point 8 can be identified as the position where the temperatures are reaching the saturation temperature but is still fluctuating as described in Section 3.5. This gives a measurement of a ζ value of 0.33 ± 0.04. An increase in the amplitude of the fluctuations for measurement point 9 and an increase in the average temperature of points 9 and 10 show the effects of decreasing EEVIP over the length of the test.

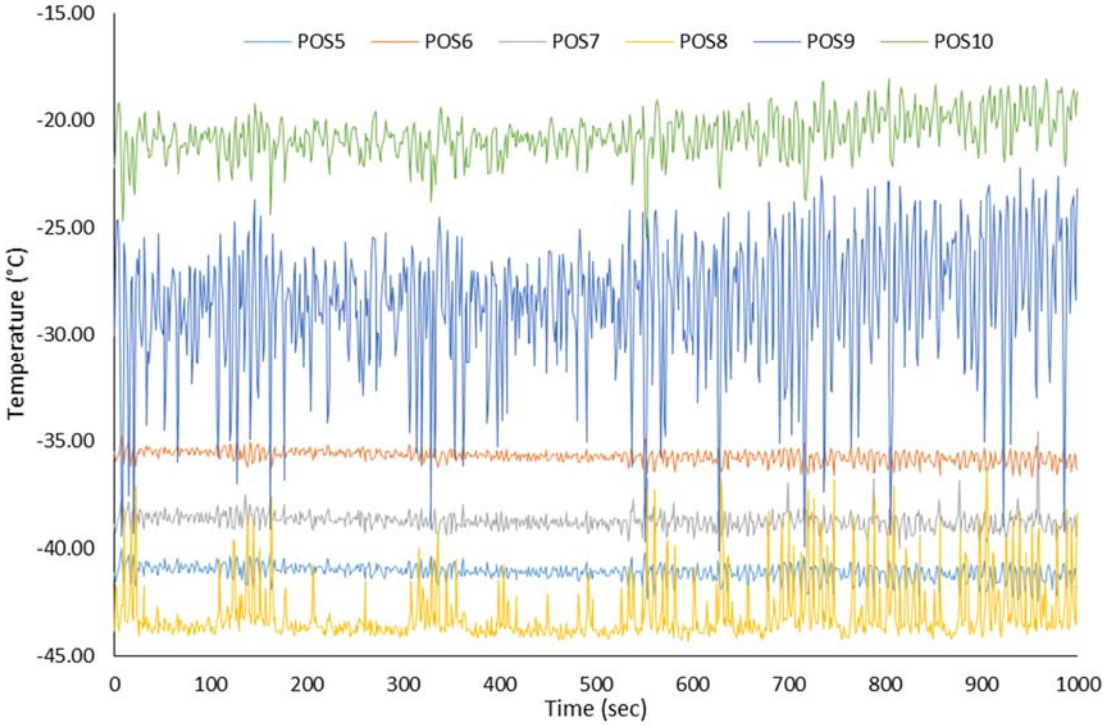

Figure 19: Coil Temperature for Static Test 1. Box Temperature = 4.4°C, Flow Rate = 0.0215 kg s^{-1} Inlet Enthalpy = 114 kJ kg^{-1}

3.7.2 Results at Box Temperature of -9.5°C

For Test 2 EAIT, Figure 20, was once again maintained within acceptable limits with a decrease of only 0.005°C over the length of the test. For this test EEVIP, Figure 21, was also held more constant with a decrease of only 3 kPa in its average over the length of the test. This stability is reflected in the coil temperatures shown in Figure 22 where position 12 is determined to be the location of the two-phase boundary resulting in a ζ value of 0.5 ± 0.04 for this test. The total cooling capacity for this test was calculated to be 8.1 kW.

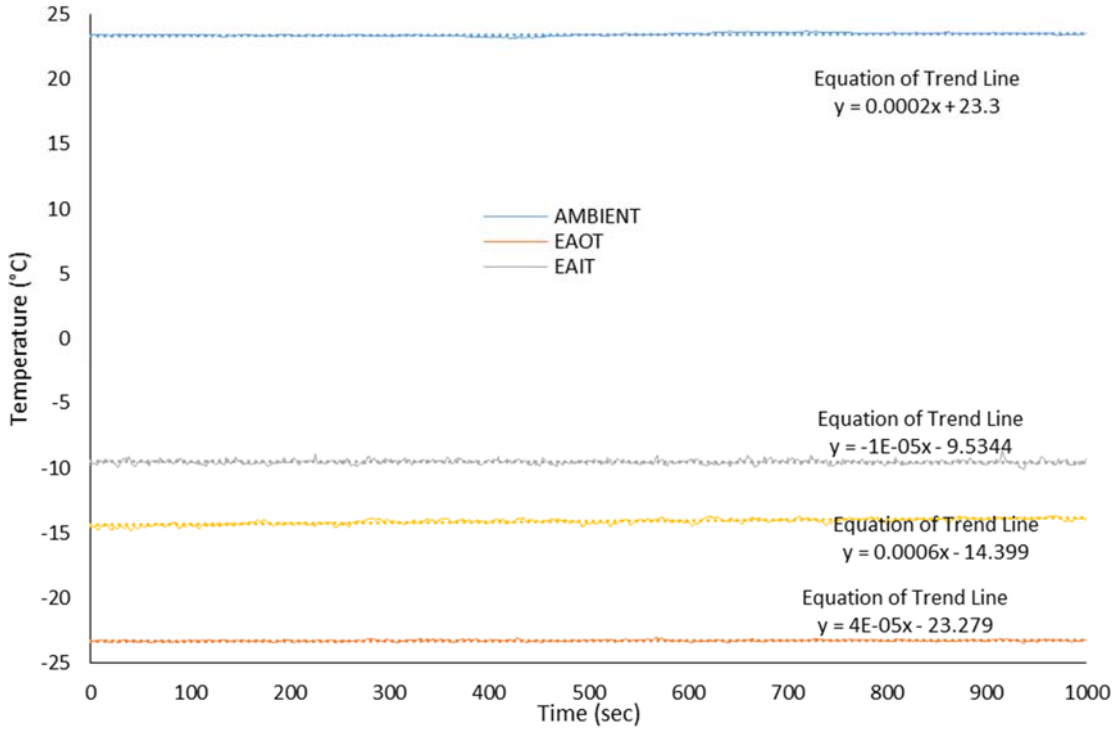

Figure 20: Air and Refrigerant Temperatures for Static Test 2. Box Temperature = -9.5°C, Flow Rate = 0.0219 kg s^{-1}, Inlet Enthalpy = 113 kJ kg^{-1}

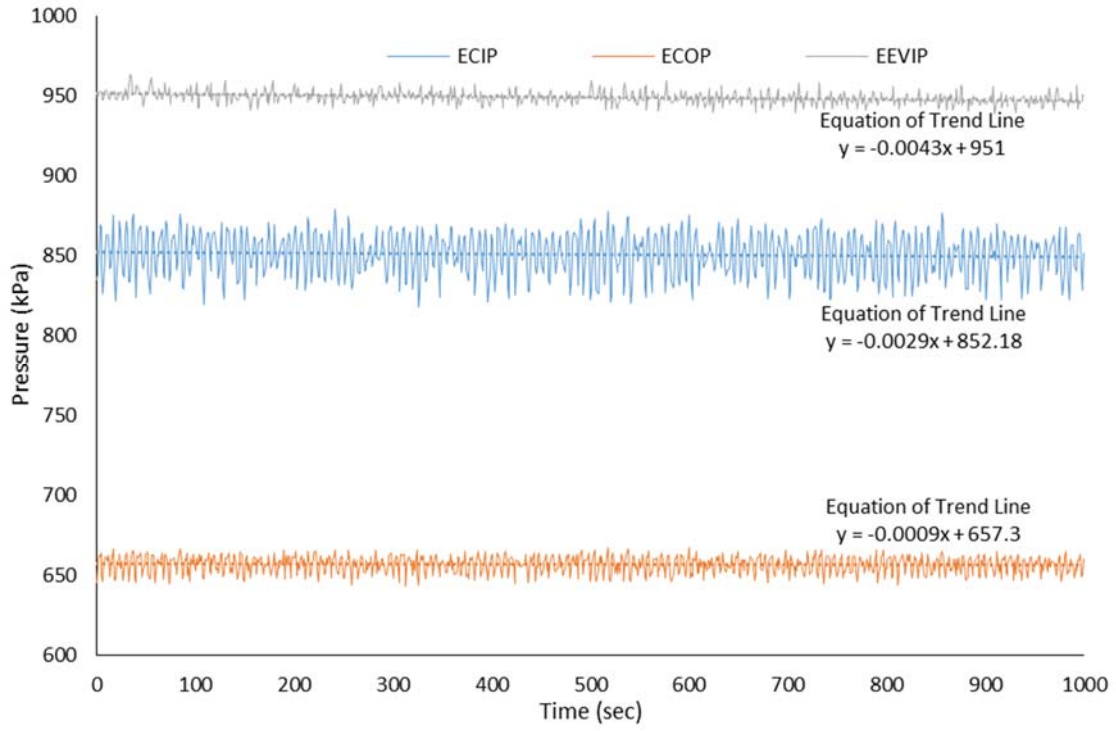

Figure 21: Pressures for Static Test 2. Box Temperature = -9.5°C, Flow Rate = 0.0219 kg s^{-1}, Inlet Enthalpy = 113 kJ kg^{-1}

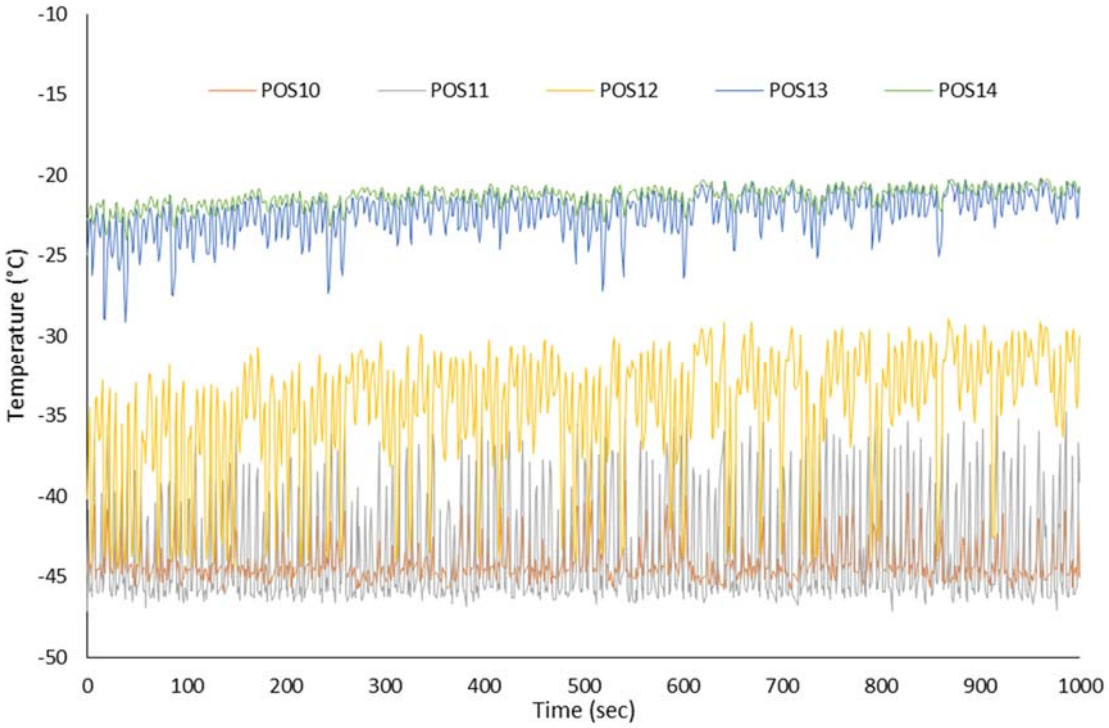

Figure 22: Coil Temperatures for Static Test 2. Box Temperature = -9.5°C, Flow Rate = 0.0219 kg s^{-1}, Inlet Enthalpy = 113.06 kJ kg^{-1}

3.7.3 Results at Box Temperature of -13.0°C

The air temperatures for Static Test 3 are displayed in Figure 23. Although EAIT is once again maintained well with an increase of only 0.002°C over the duration of the test, the ambient temperature outside the box increases by 1.1°C. This has the effect of increasing the heat gained through the walls of the box. Once again EEVIP, Figure 24, decreases over the length of the test by 25 kPa which is significant. These two factors results in significant variation in the coil temperatures seen in Figure 25 and result in boundary moving from position 19 at the beginning of the test to position 17 at the end of the 1000 s. To offset these issues it was decided that taking the static data over a shorter period of time of 400 s when the coil temperatures indicated that the boundary was at position 19 for Test 3. For this data the mass flow rate was calculated as 0.0254 kg s^{-1} which correlates with the higher EEVIP seen during the early portion of the test. The variation in the average for the EEVIP reduces to 11 kPa and the ambient temperature changes reduces to 0.2°C over this shorter duration. The average EAIT remained at 13°C and the inlet enthalpy remains at 116 kJ kg^{-1}. The calculated cooling capacity for the system over the 400 s period was 7.9 kW and the resulting ζ value was 0.79 ± 0.04.

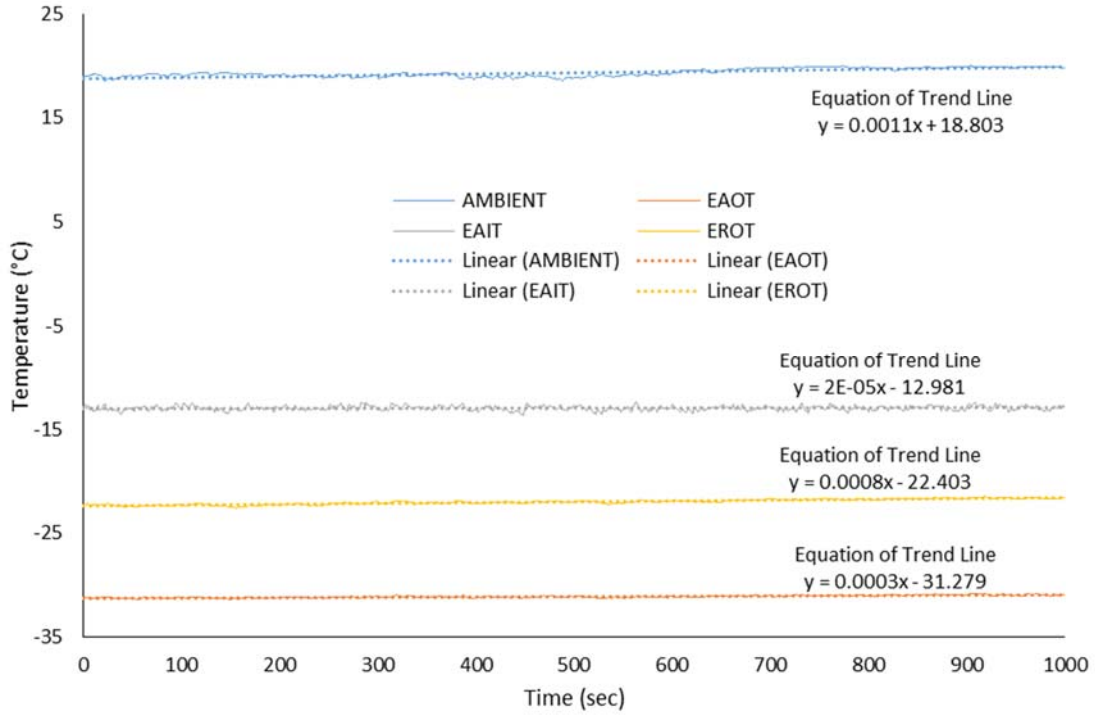

Figure 23: Air and Refrigerant Temperatures for Static Test 3. Box Temperature = -13.0°C, Flow Rate = 0.0248 kg s^{-1}, Inlet Enthalpy = 116 kJ kg^{-1}

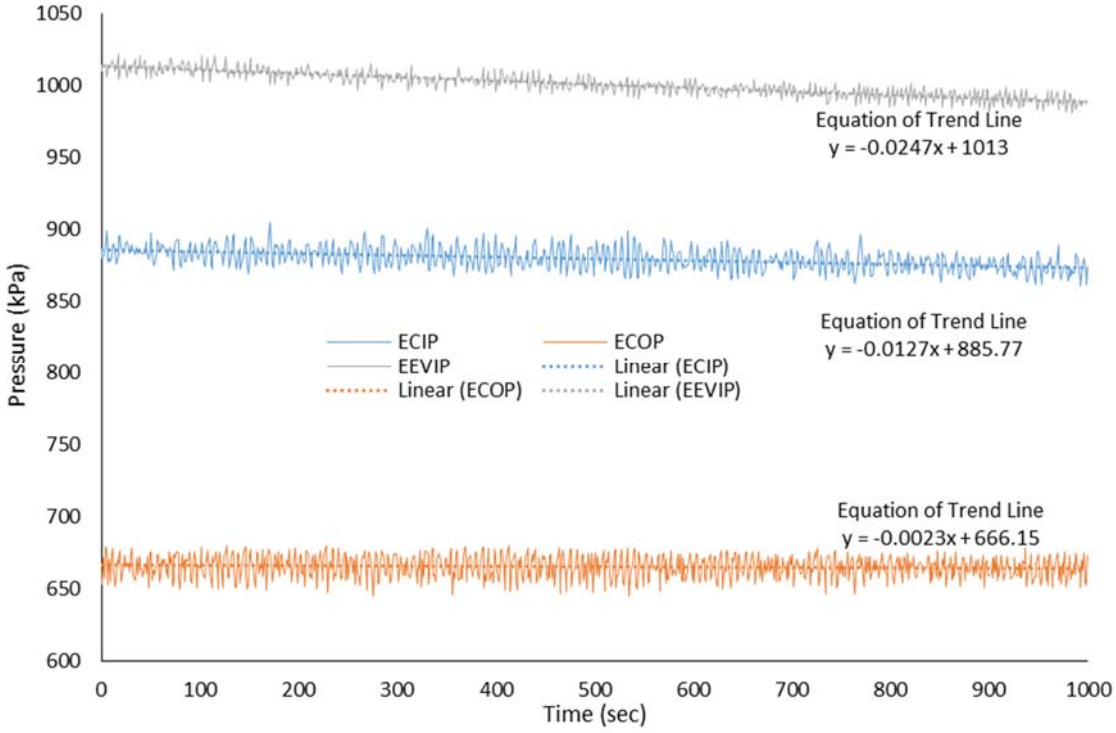

Figure 24: Pressures for Static Test 3. Box Temperature = -13.0°C, Flow Rate = 0.0248 kg s^{-1}, Inlet Enthalpy = 116 kJ kg^{-1}

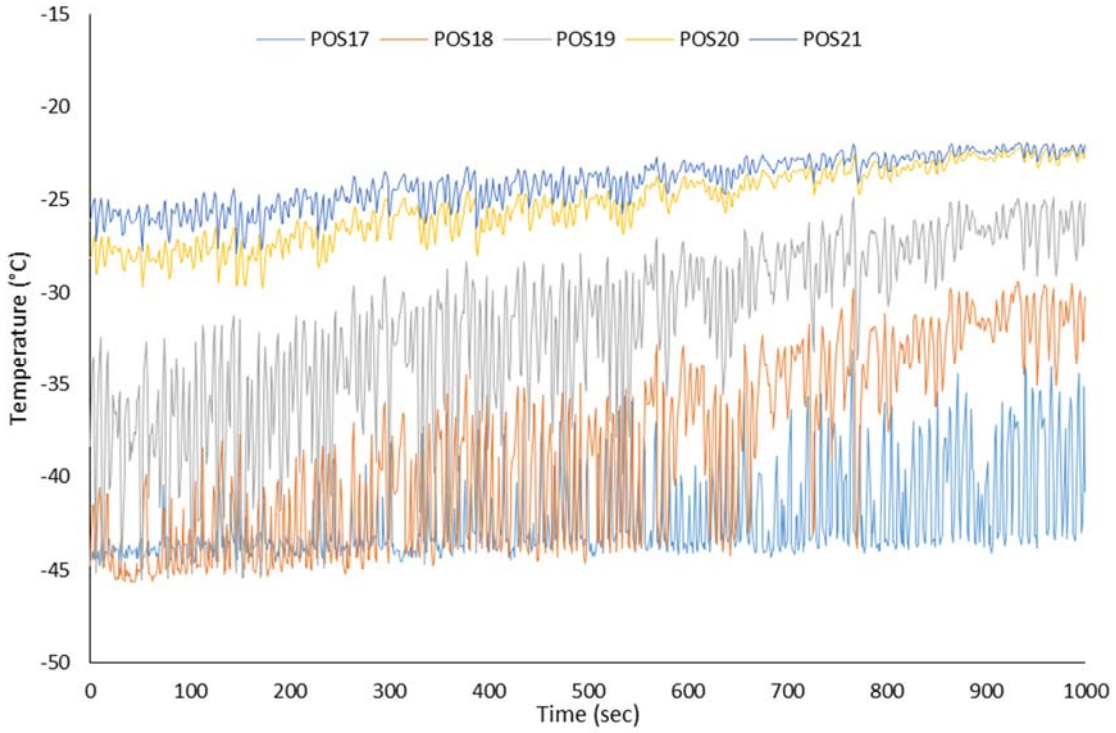

Figure 25: Coil Temperatures for Static Test 3. Box Temperature = -13.0°C,

Flow Rate = 0.0248 kg s^{-1}, Inlet Enthalpy = 116 kJ kg^{-1}

The three static tests above highlight the difficulty of measuring the cooling capacity of the open cycle CO_2 system. Even though the EAIT was kept within acceptable limits for static testing the variations in the system pressures caused stability issues. None the less data was obtained that will be useful for validating the moving boundary model in Chapter 4.

3.8 Measurement of Two-phase Region Length for Dynamic Tests

In dynamic testing as the coil temperatures dropped during pull down it was less clear when the boundary between the two-phase and the superheated refrigerant regions occurred. The temperatures at each point were a lot less stable, exhibiting a gradual decrease in the mean temperature as well as temperature fluctuations due to pressure changes in addition to the temperature changes due to liquid droplets impacting the tube which was the criteria used to identify the two-phase boundary in the static testing. There were also variations in behaviour along the length of the coil and for increasing versus reducing two-phase zone lengths.

3.8.1 Dynamic Pull-downs

During the unit start-up the temperatures at the first number of coil measurement positions changed rapidly in temperature and demonstrate some oscillatory behaviour. During this phase the inlet pressure in the coil was also stabilising and hence had an effect on the temperature measurements. Figure 26 and Figure 27 show the temperature and pressures for the first 160 s after starting the unit at an ambient temperature of 30°C. The first thing to note it that there is a significant delay between the EEV opening at 26.8 seconds and liquid getting to the inlet of the coil at 75 seconds. This is due to the length of the piping between the CO_2 tank and the coil of approximately 7.5m. Secondly it should be noted that the coil inlet pressure takes time to reach equilibrium, as Figure 27 shows, the coil inlet pressure reaches a stable value 94 s after the EEV opens. During this time the temperature of the inlet and points 1 to 3 drop significantly indicating that the two-phase boundary has been reached. However for point 1 in particular the temperature measurements fluctuate and it is difficult to determine at which time the two-phase boundary passes this point. The criteria decided upon to evaluate the data was the time at which the temperature began to decrease and reached the saturation temperature. In Figure 26 this is identified as point T1_C at 105.6 s.

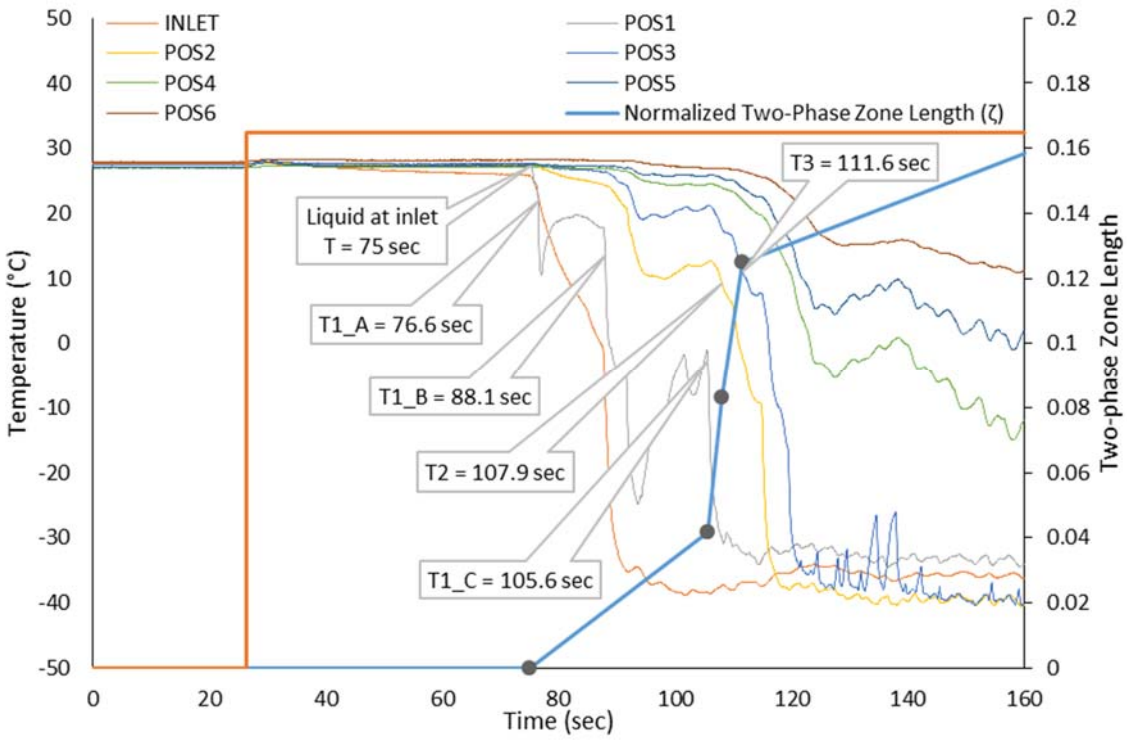

Figure 26: Coil Temperatures and Two-phase Zone Length near Inlet during Start-up

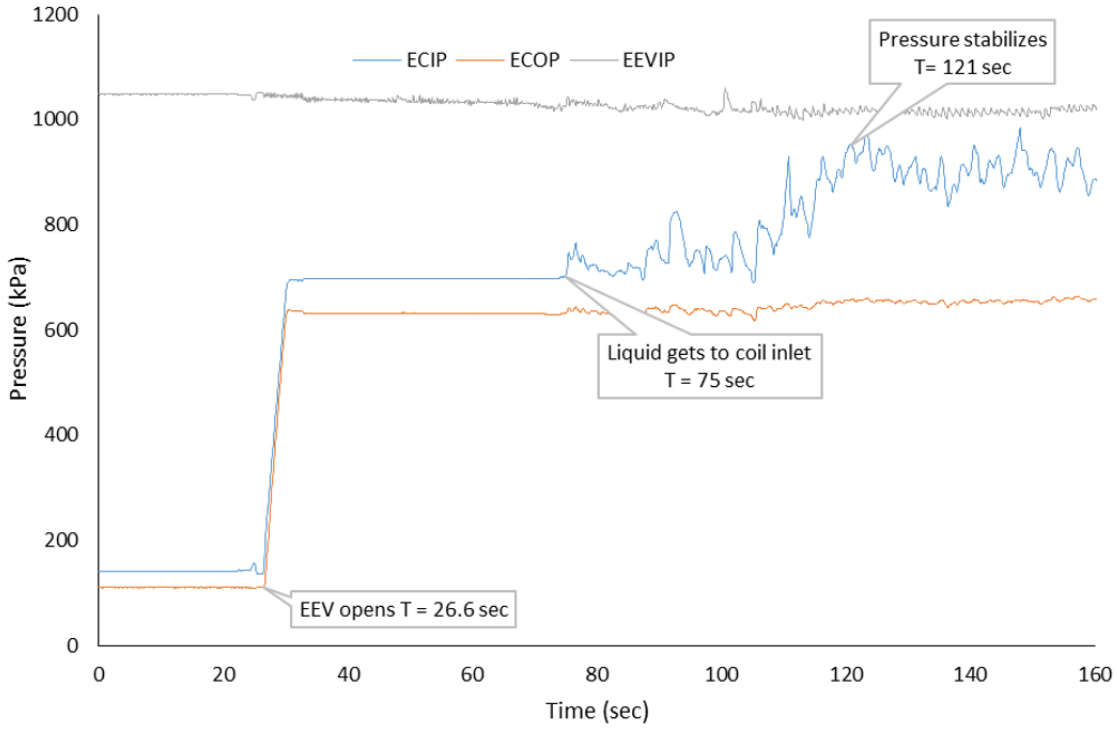

Figure 27: Coil Inlet and Outlet Pressure during start-up

For the middle section of the coil the pressures were relatively stable and the boundary moved at a slower pace. Here it was possible to see behaviour similar to the static tests where temperature fluctuations indicated liquid droplets impacting the tube wall. As the boundary moved closer to the measurement point the minimum temperate of these fluctuations approached saturation temperature and this was identified as the time at which the two-phase boundary reached that point. Following this the temperature fluctuations decreased as more liquid was present in the tube and the two-phase region transitioned towards annular flow. Figure 28 shows temperature measurements for three points near the middle of the coil. As can be seen the times chosen for points 11 and 12 still have some ambiguity but T11_B and T12_B were determined to be the correct times in this case as the earlier points T11_A and T12A had not yet reached the saturation temperature.

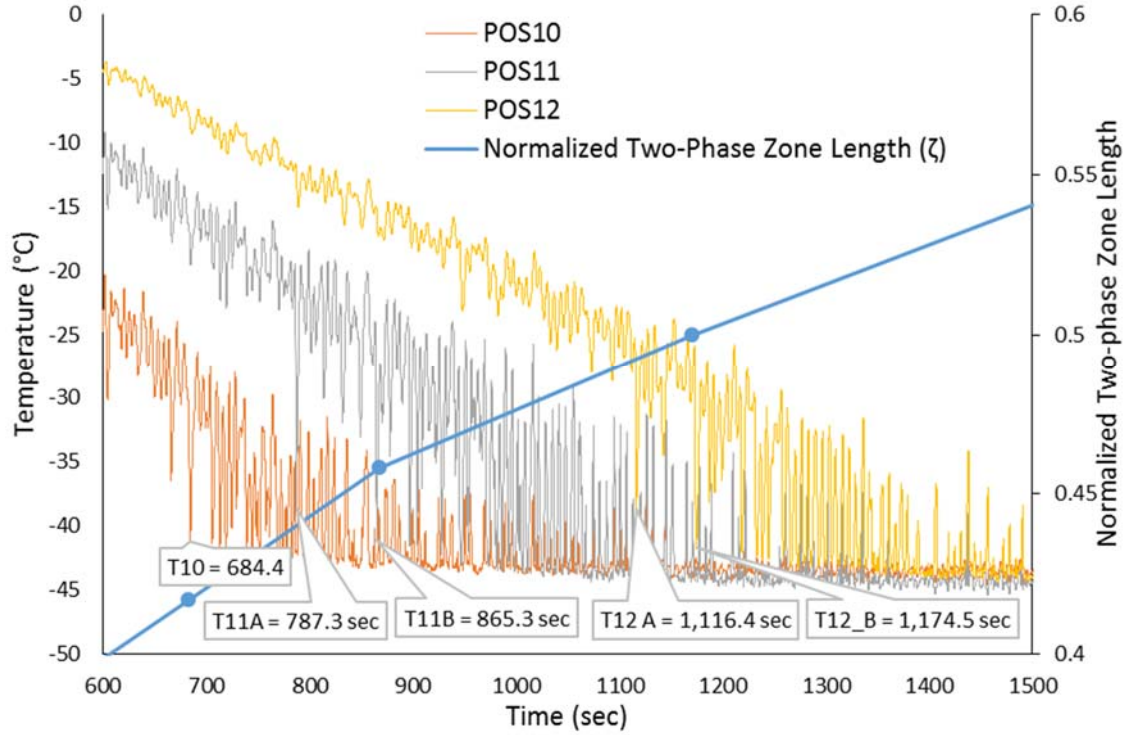

Figure 28: Coil Temperature and Two-phase Zone Length for three consecutive points towards the coil center as the two-phase boundary reaches them

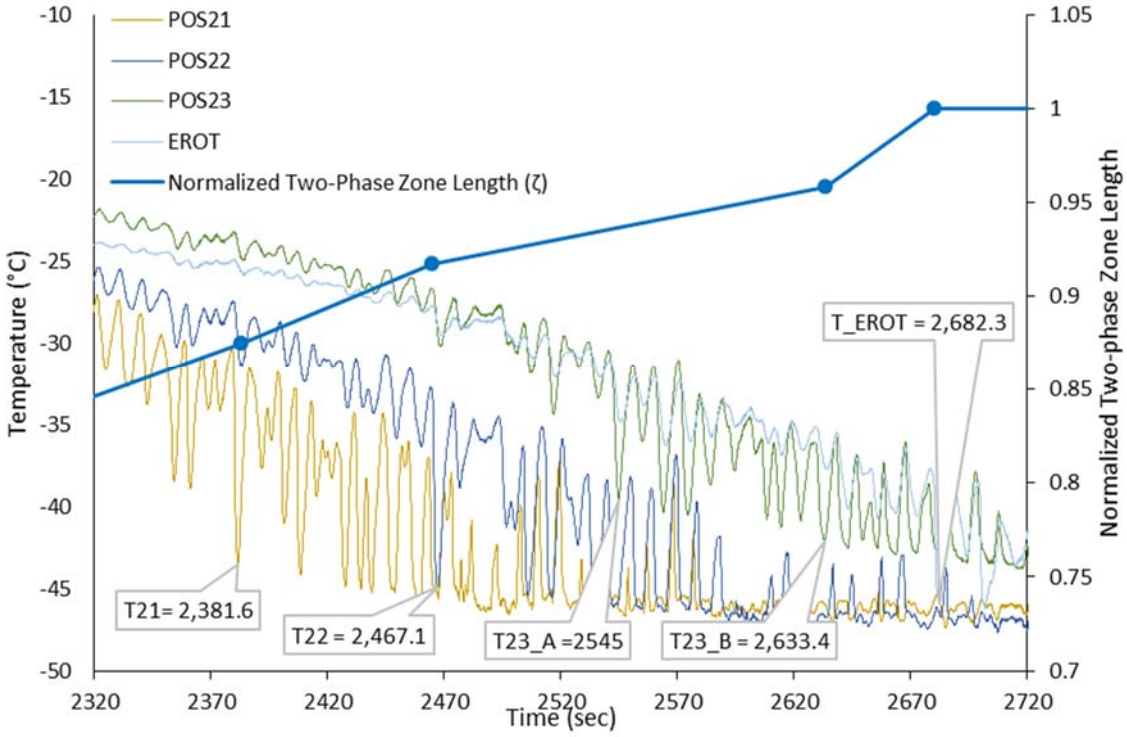

Figure 29: Coil Temperature and Two-phase Zone Length as the two-phase boundary reaches the Coil Outlet

At the outlet of the coil it was sometimes not as clear which point first reached saturation temperature as the difference between the air inlet temperature and the refrigerant temperature had decrease to a level where the fluctuations were hidden in the measurement noise. Temperatures for Point 23 in Figure 29 show this effect. Some inaccuracy in the thermocouple, possibly due to poor soldering onto the copper tube, gives this point a higher saturation temperature than those around it and compounds the difficulty in correctly determining the time at which the two-phase boundary reaches this point. In this case T23_B at 2,633.4 s is determine to be the correct time but a later time could also have been easily chosen.

However for all three cases where the boundary length was increasing the time period of uncertainty was relatively short compared with the time taken for the boundary to move to the adjacent measurement point and the boundary reached each point reduced in series as would be expected.

3.8.2 Shutdown

The case of decreasing two-phase zone length, caused by the closure of the EEV, the EEV pulsing prior to shutdown often resulted in length of ζ being less than unity as is the case in Figure 30 where it is close to position 23. After the EEV closes there is a delay of just under 3 seconds before position 22 and 21 react as the effect of the EEV closing propagate through the length of the coil. There is no discernable time different being the boundary reaching these two points and indeed the time steps to next number of points are very small indicating that the velocity of the two-phase boundary during shut-down is very high. This high velocity continues until the coil is empty of two-phase fluid.

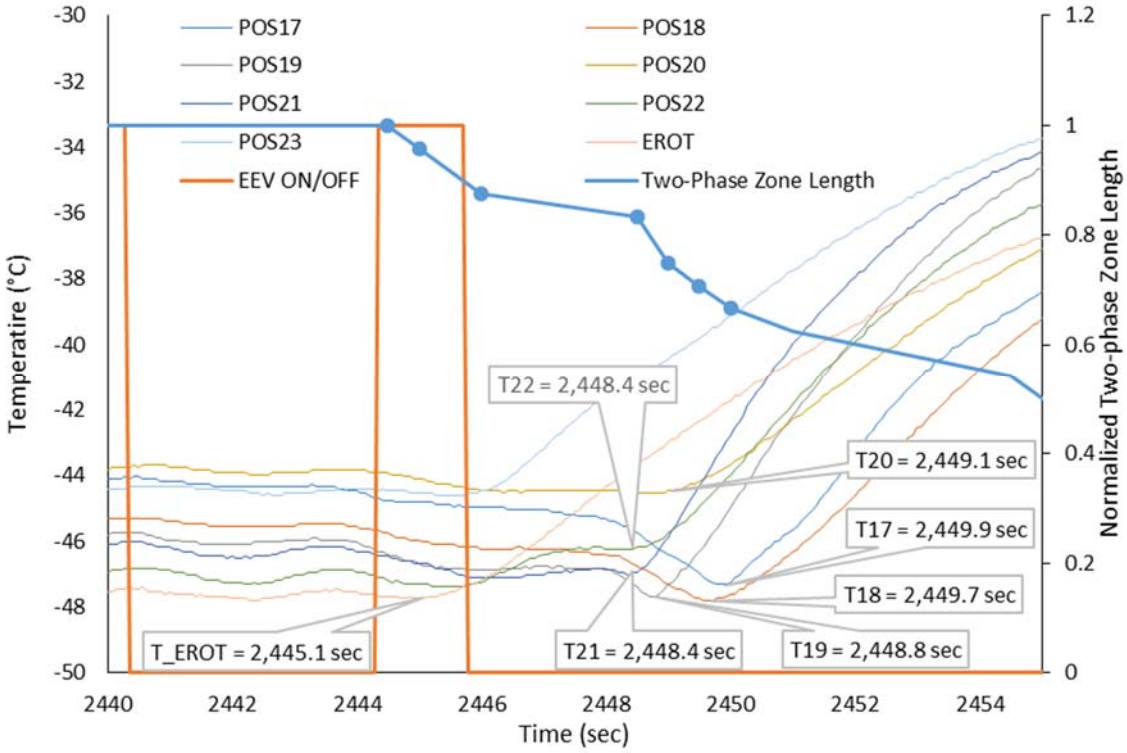

Figure 30: Coil Temperature and Two-phase Zone Length for shut-down

3.8.3 EEV pulsing

The EEV in the open cycle CO_2 system pulses for two reasons, temperature control at set-point during continuous operation and superheated control to maintain the two-phase boundary at a position less than the full length of the coil.

The coil temperatures for superheat control are shown in Figure 31. Once again the delay between the valve closing at 1901.6 seconds and the temperature at the outlet reacting at 1908.5 seconds can be seen. The initial pulse of the valve has an impact on the temperature as far as measurement point 19. This point increases in temperature at 1911.5 sec and begins to return to the saturation temperature three seconds later. This interval is roughly equal to the length of the pulse of 3.1 seconds. The second pulse has a greater effect as the boundary has not yet returned to the end of the coil with temperatures increasing as far as point 17 whereas the third pulse once again only sees temperatures increase as far back as point 19 due to the shorter duration of the 2nd pulse. The boundary does not return to the outlet of the coil until 1957.7 sec, 41.4 seconds after the cycle of pulsing ends with the EEV open. There is some temperature cycling after the 3rd pulse and before the two-phase boundary reaches the end of the coil. This is likely due to the high vapour content in the mist flow region of the two-phase fluid. It can be difficult at times to distinguish between this behaviour and the movements of

the boundary due to valve pulsing. Following the three pulses in this time frame there is a period of valve opening which allows the two-phase boundary to once again return to the outlet of the coil. Ideally this would not occur during superheat control so some improvements in control are obviously needed.

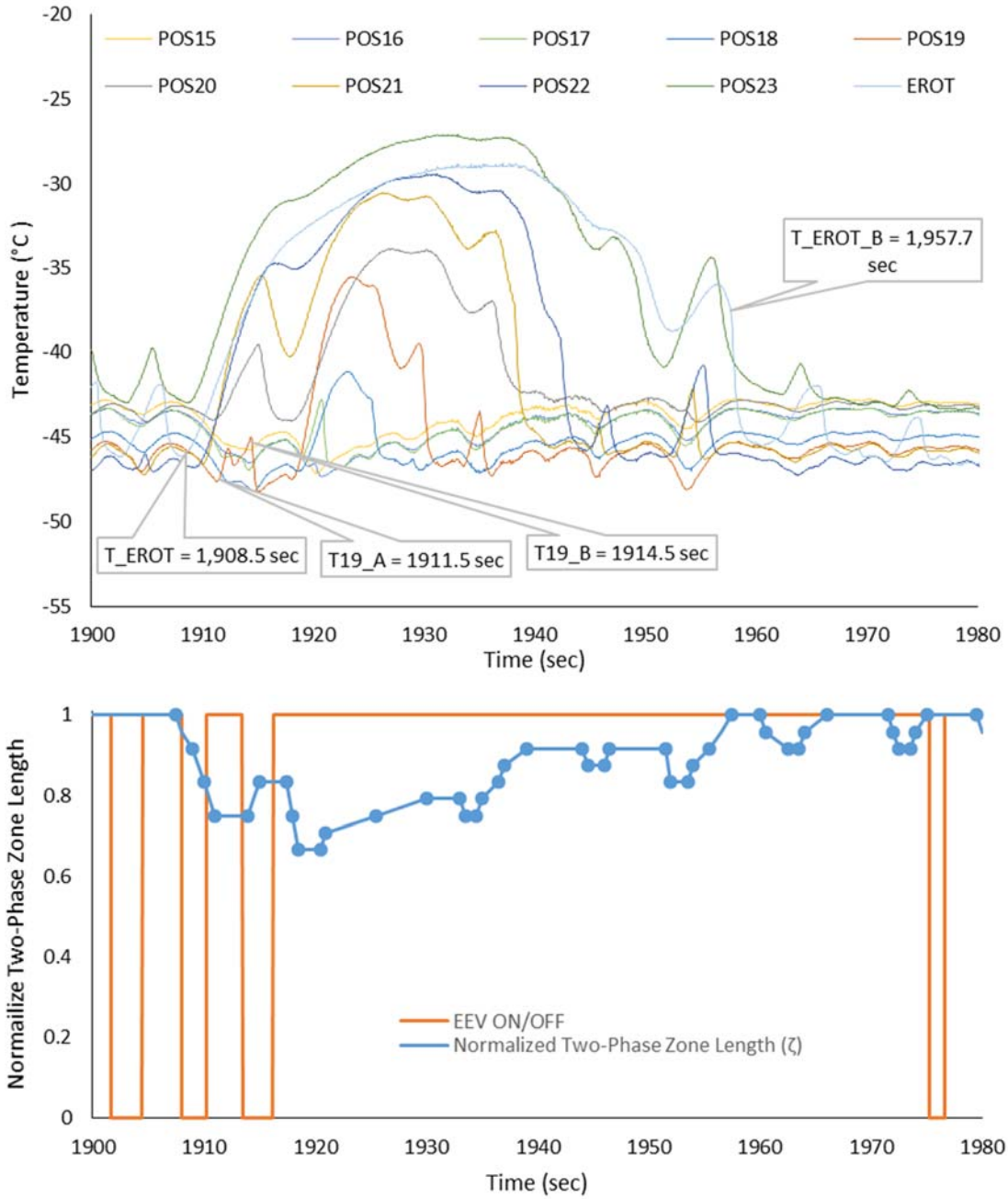

Figure 31: Coil Temperatures and Two-phase Zone Length for Superheat EEV Pulsing

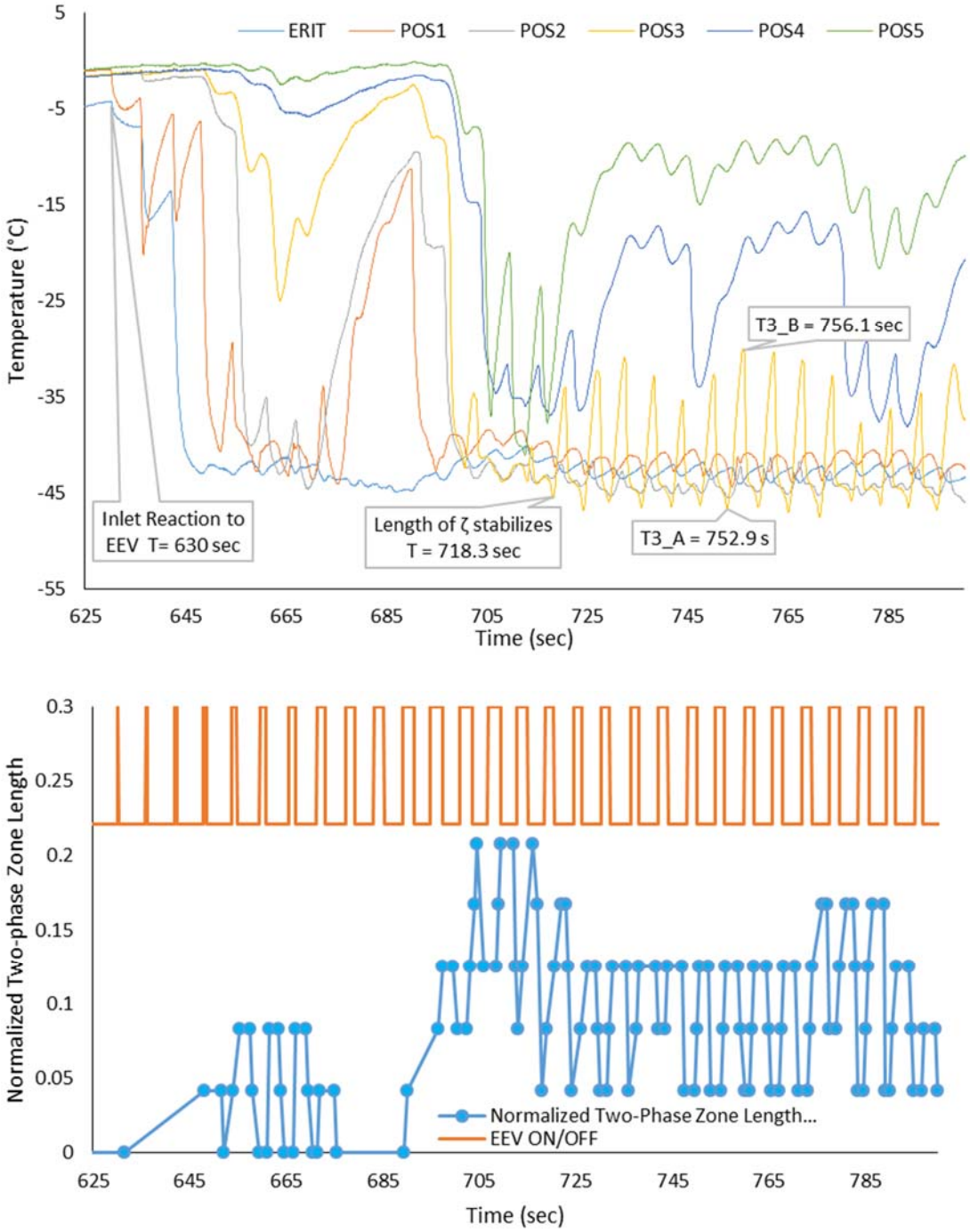

Figure 32: Coil Temperatures and Two-phase Zone Length for Temperature Control EEV Pulsing

Figure 32 shows the coil temperatures for valve pulsing during temperature control. In this case the temperatures at the inlet react instantly to the opening of the EEV as the valve is situated at the inlet to the coil. After the initial opening there is a period of time of 88.3 seconds for the control to stabilize the length of ζ. After this it can be seen that measurements at position 3 have a cyclic behaviour that roughly matches the period of the EEV pulsing. There are also some

reactions to a lesser magnitude from position 2 and occasionally from position 4. Position 5 also reacts but never gets close to the saturation temperature. This reaction of a relativity small number of measurement points would suggest that the control of the length of ζ for temperature control is much better than the control for superheat control.

The methodology described in this section allows for the two-phase zone length to be measured to an acceptable level of accuracy for all the dynamic situations that are likely to be encountered during the normal operation of the open cycle CO_2 system. In doing so it provides the data required for validating this parameter in the moving boundary model in Chapters 4 & 5.

3.9 Experimental Results for Dynamic Pull-down

Typically a pull-down is performed to get EAIT from the ambient temperature to the set-point as fast as possible. This is normally achieved with the EEV fully open until two-phase fluid reaches the coil outlet at which point superheat control would be initiated to limit the exhausting of two-phase CO_2. In this case the EEV is maintained fully open for the duration of the test to examine the system effects without superheat control.

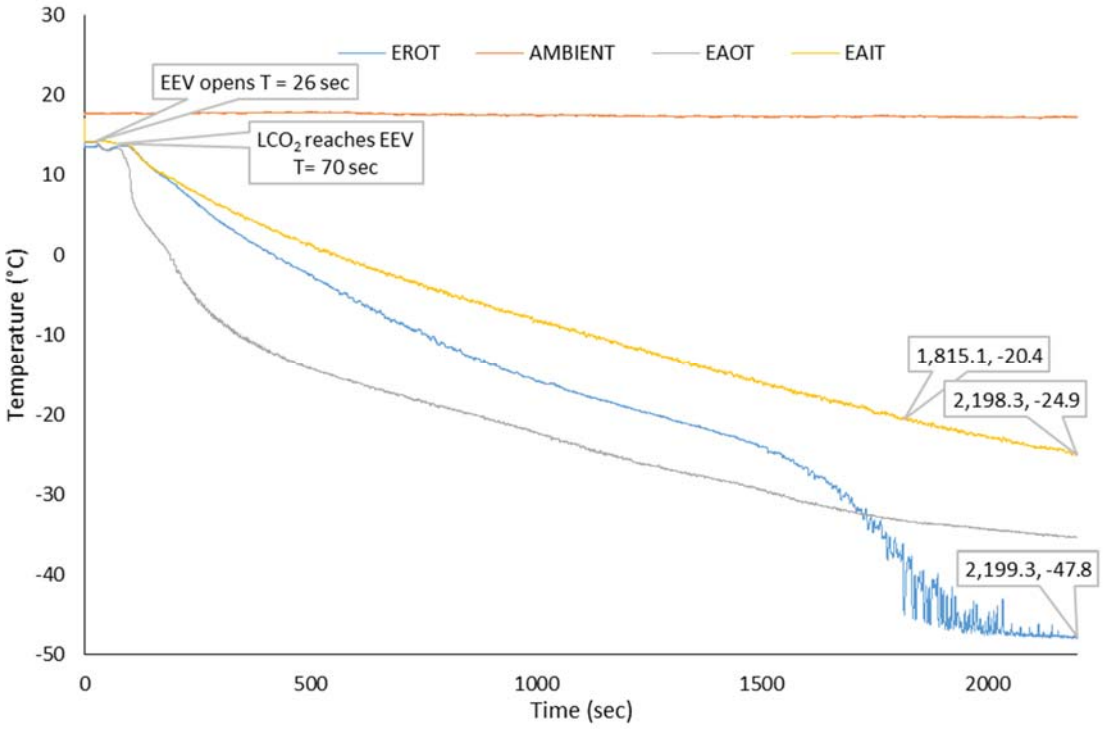

Figure 33: Air and Refrigerant Temperatures for Dynamic Pull-down. Flow Rate = 0.0243 kg s^{-1}, Inlet Enthalpy = 116 kJ kg^{-1}

Figure 33 shows the air and refrigerant temperatures for the dynamic pull-down. The EEV opens at 26 s but there is a delay of 44 s while the liquid refrigerant travels from the CO_2 tank to the EEV and coil inlet before there is any response from the system. EAOT is first to react to the opening of the valve and decreases quicker than EAIT or EROT. After approximately 500 s EAOT is 15°C colder than EAIT and it maintains a similar offset until 1500s where the offset starts to decrease.

EROT on the other hand starts to deviate from EAIT slowly but the rate of change increases until it drop sharply at 1815 s indicating that two-phase refrigerant has reaches the outlet of the coil. EROT then displays a period of high frequency, high amplitude fluctuations which gradually decrease in amplitude and settle at a relatively constant temperature. This period of fluctuations can be linked with the mist flow region of the flow pattern map described in Figure 15 on Page 36 where liquid droplets are impacting the inner wall of the copper tube. As the EAIT temperature decreases the two-phase region at the coil outlet progresses to the annular region in the flow pattern map which gives the consistent temperature seen from 2050 s to the end of the test.

The EROT temperature of -47.8°C at the end of the test is close to the liquid saturation temperatures for the outlet pressure of 665 kPa of -50.6°C. The error between the two can be explained by the measurement of the outside of the copper tube rather than the refrigerant itself and the accuracy of the thermocouples used.

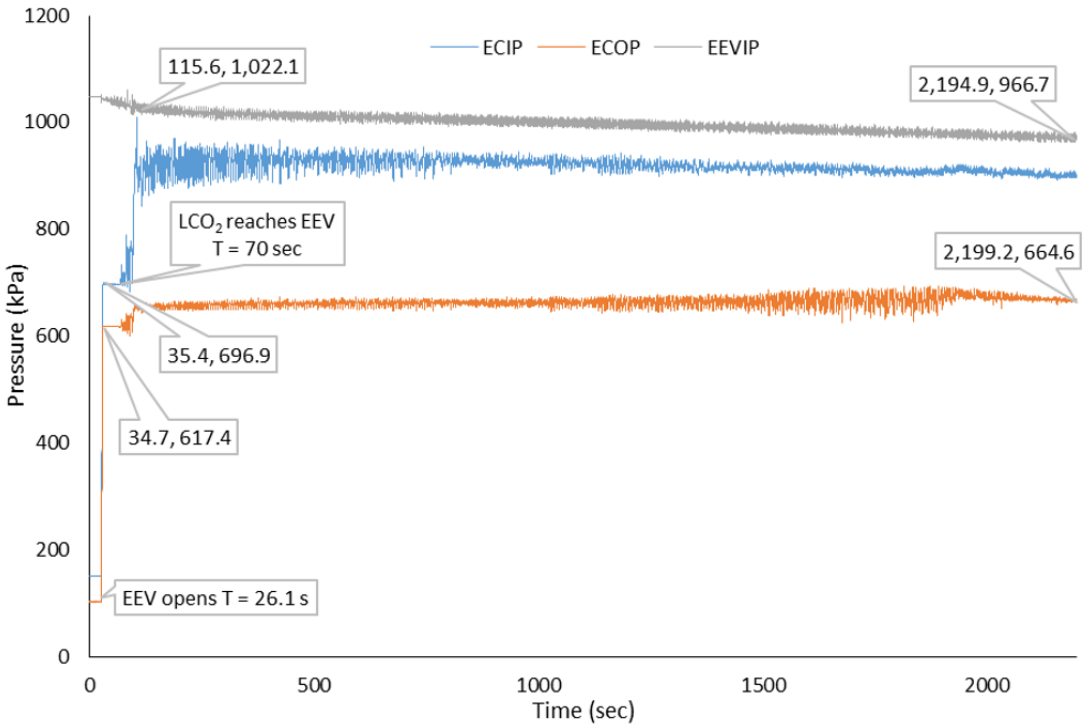

Figure 34: Pressures for Dynamic Pull-down. Flow Rate = 0.0243 kg s^{-1},

Inlet Enthalpy = 116 kJ kg^{-1}

ECIP and ECOP react immediately to the opening of the EEV at 26 s rising to 697 kPa and 617 kPa respectively. However at this point only CO_2 vapour is flowing through the EEV. The main indication that liquid CO_2 has reached the EEV is when ECIP increases and starts to fluctuate at 70 s. Following this it takes ECIP a short time to reach its nominal value of approximately 900 kPa. ECIP displays fluctuations which decrease in amplitude as time progresses. This reduction in amplitude can be linked with the distance of the two-phase boundary from the measurement point. There is a slight decrease in the nominal value of ECIP during the duration of the test which matches the decrease in EEVIP caused by the pressure drop within the CO_2 tank.

ECOP also experiences an increase in pressure once liquid reaches the EEV and settles at 665 kPa after a short period of time. At first there is little fluctuation in the pressure measurement but it increases as the two-phase boundary approaches before decreasing in amplitude once again as the boundary passes and the temperature settles down.

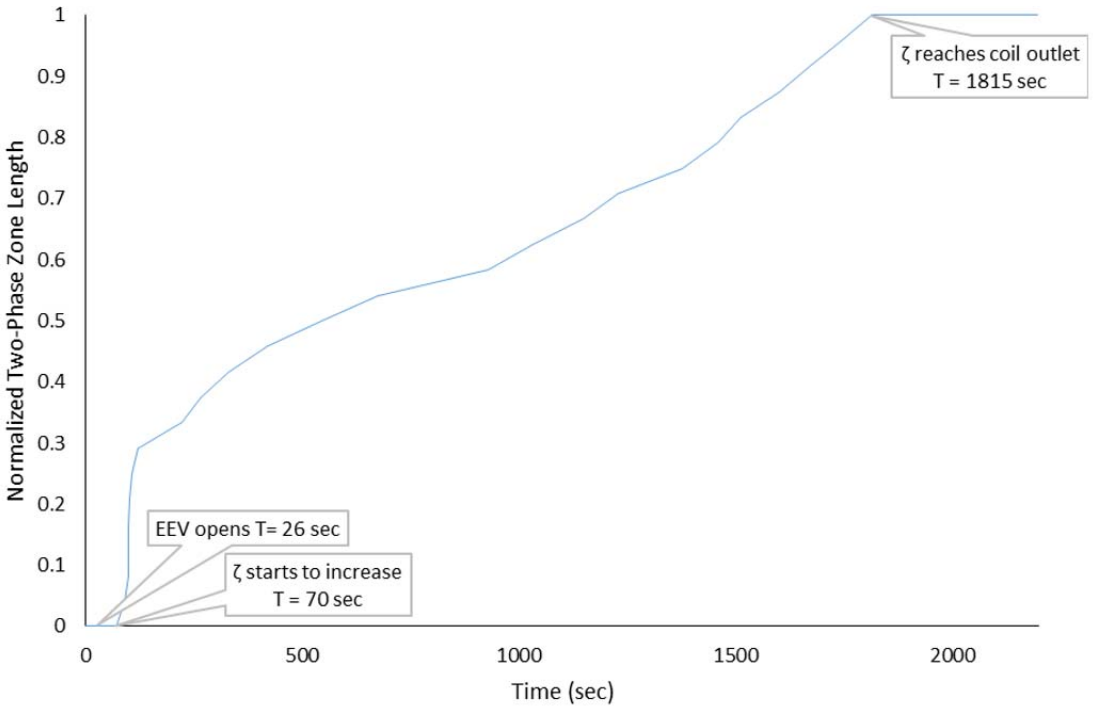

Figure 35: Two-Phase Zone Length for Dynamic Pull-down. Flow Rate = 0.0243 kg s^{-1}, Inlet Enthalpy = 116 kJ kg^{-1}

Figure 35 shows that the two-phase zone length, ζ, starts to increase once the liquid CO_2 reaches the EEV and coil inlet. Initially it increases rapidly as the speed is determined by the fluid dynamics of the two-phase CO_2. At 121 seconds the speed reduces and from then to 1815 seconds the increase in ζ is governed primarily by the heat transfer from the air into the refrigerant. At 1815 seconds ζ reaches the coil outlet and remains there as the EAIT temperature reduces further since the EEV is fully open.

3.10 Experimental Results for Continuous Control

The experimental testing for continuous control was performed at two cargo box temperature, 0°C a typical set-point for transporting fresh goods such as dairy or vegetables, and -25°C which would be a typical set-point used for deep frozen produce such as ice-cream or fish. As outlined in Chapter 1, Section 1.3.4, Page 7, continuous control allows for tight temperature control of the box temperature once the unit has reached set-point and is typically used for cargo which is sensitive to temperature variation.

3.10.1 Fresh set-point

Figure 36 displays the air and refrigerant temperatures for the evaporator coil for the fresh continuous test.

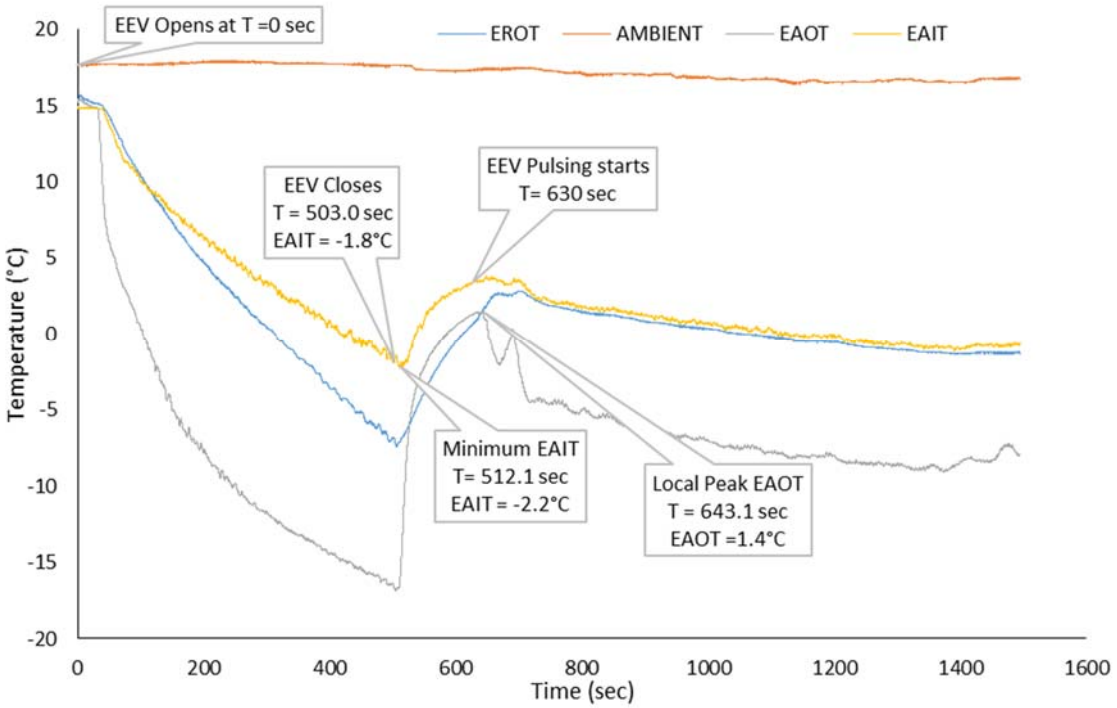

Figure 36: Air and Refrigerant Temperatures for Continuous Control for a 0°C Set-point. Mass flow rate of CO_2 for 100% EEV Duty Cycle: 0.0248 kg s^{-1}

Once again there is a delay in response after the EEV opens due to the length of piping between the tank and the evaporator coil after which the unit operates with a fully open EEV until the EAIT reaches the set-point of 0°C. The EAIT overshoots the set-point slightly as the unit sensor has a slower response than the thermocouples used in the testing and because it takes time for the evaporator coil to empty of refrigerant after the EEV closes. There is an opportunity here to shut off the valve earlier to prevent this overshoot, savings CO_2 and improving the temperature control. After reaching set-point the EEV closes for a period of time. This control is due to a requirement to limit EAOT to 2.2°C below the set-point once the pull-down has been completed to protect the cargo close to the evaporator outlet from freezing. However as can be seen in Figure 36 EAOT goes as high as 1.4°C at 643 seconds into the test so the control of this transition could also be optimized to improve temperature control. At 630 s the EEV starts pulsing to maintain EAIT at the set-point of 0°C. It takes a considerable amount of time to reach the set-

point due to the restriction on the EAOT temperature and it can also be seen that the EAOT exceeds the 2.5°C limit during this period. The primary reasons for this are the difference in the location and response of the unit sensor and the thermocouples for measuring EAOT discussed in Section 3.5. The difference between the two measurements gives an indication of the impact of the location of this EAOT unit sensor on the unit performance.

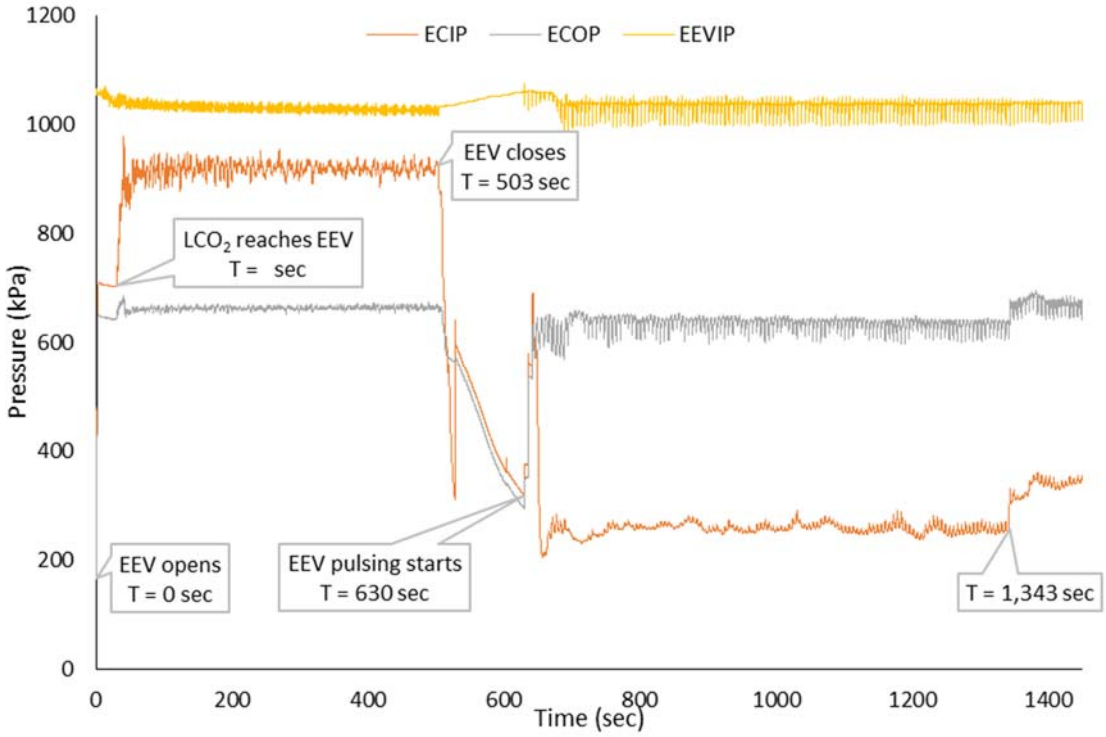

Figure 37: Pressures for Continuous Control for 0°C Set-point. Mass flow rate of CO_2 for 100% EEV Duty Cycle: 0.0248 kg s^{-1}

The pressures for the continuous fresh test are shown in Figure 37. ECIP gives a good indication of when liquid CO_2 reaches the EEV as it initially goes to 700 kPa when vapour is passing through the valve after the EEV opens and then jumps again after 31 seconds to approximately 900 kPa when the liquid arrives. When the EEV closes at 503 seconds there is an immediate reaction from ECIP and ECOP with ECIP briefly spiking below ECOP possibly due to the rapid drop in pressure causing dry ice to form at the inlet to the pressure sensor. When the EEV opens again the pressures increase again but ECIP drops down again to a very low level of 230 kPa at which dry ice would form. Since this is below ECOP and CO_2 is still flowing through the coil this was determined to be a false reading from the pressure sensor likely caused by a partial blockage of the inlet to the sensor caused by dry ice formation. The pulsing of the EEV during superheat

control has the effect of lowering ECOP and causing it, and EEVIP, to cycle at the same frequency as the EEV pulses. After 1,343 seconds an unknown event causing an increase in both ECIP and ECOP. This event is also evident in the length of the two-phase zone in Figure 38 where the length of ζ decreases and to a lesser extent in Figure 36 where the temperature of EAOT increases. A possible cause for the event could be the removal of a partial blockage of the EEV by dry-ice.

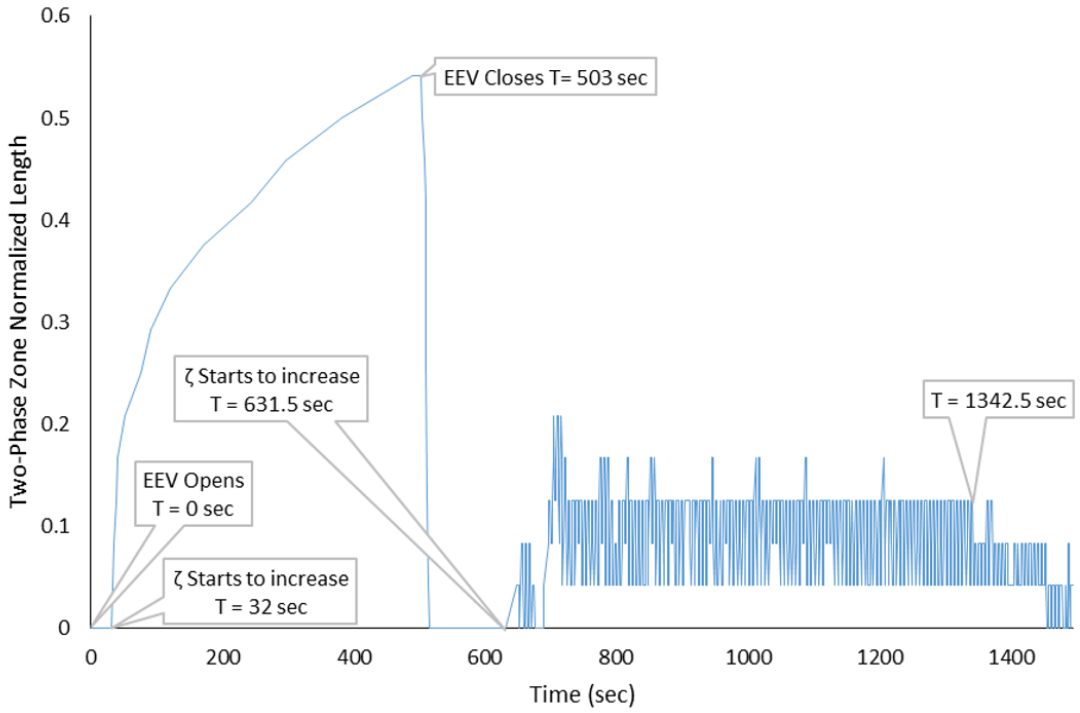

Figure 38: Two Phase Zone Length for Continuous Control for 0°C Set-point. Mass flow rate of CO_2 for 100% EEV Duty Cycle: 0.0248 kg s^{-1}

Figure 38 shows the two-phase zone length, ζ, as measured by the techniques presented in Section 3.8. ζ begins to increase 32 seconds after the valve is opened due to the time it takes for the liquid CO_2 to reach the coil, it then increases to 0.541, which is measurement point 13, before decreasing sharply once the valve is closed again. Once the valve starts pulsing at 631.5 seconds ζ starts to increase before dropping to zero once again. It is likely that this drop to zero is caused by vapour that has built up in the liquid line while the EEV was closed and it is common to all modes after the EEV has been closed for a period of time. The drop to zero is followed by another increase in length and a short period of time where the control stabilizes as EAIT

approaches the set-point again after which the zone length remains around 0.125 until the event mentioned above which causes a pressure increase and a decrease in ζ to 0.083.

3.10.2 Frozen set-point

For the continuous control with a -25°C frozen set-point the initial pull-down is similar to the fresh test but as the temperature drop beyond the fresh limits EAOT drops sharply until it reaches the liquid saturation temperature and pulsing of the valve for superheat control begins, Figure 39. Superheat control continues until the set-point is reached at 2,531 seconds. The slope of EAIT does not appear to reduce significantly during superheat control which indicates that the unit is still operating at close to its maximum performance. Again there is some overshoot of EAIT past the set-point of -25°C and the same control as the fresh condition where the EEV closes for a period before starting to pulse for temperature control at 2,621 seconds. The temperatures take a period of time to settle with EAIT then close to the set-point of -25°C. A decrease in the ambient temperature after 2,253 seconds appears to have no significant effect on the test.

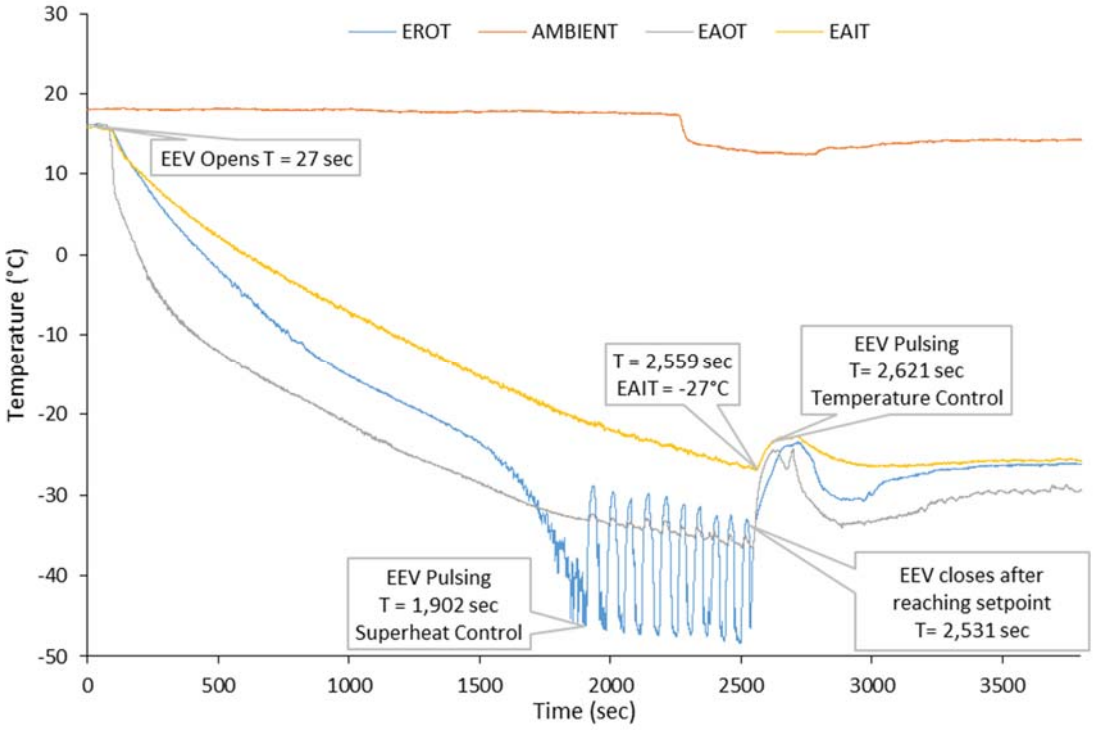

Figure 39: Air and Refrigerant Temperature for Continuous Control for a -25°C Set-point. Mass flow rate of CO_2 for 100% EEV Duty Cycle: 0.0245 kg s^{-1}

The pressure for the frozen test, shown in Figure 40, are again similar to the fresh test for the initial period. It can again be noted that the amplitude of the fluctuation in ECIP decreases and ECOP increases during the pull-down period as ζ progresses along the length of the coil. Once superheat control starts the fluctuations increase and are in phase with the pulsing of the valve and the fluctuation in the EROT. After the valve starts pulsing for temperature control there is an increase in ECIP which is consistent with the increase in EAIT in Figure 39. In this case the ECIP measurements stay above the ECOP measurements and are without the issue identified for the fresh testing in Figure 37.

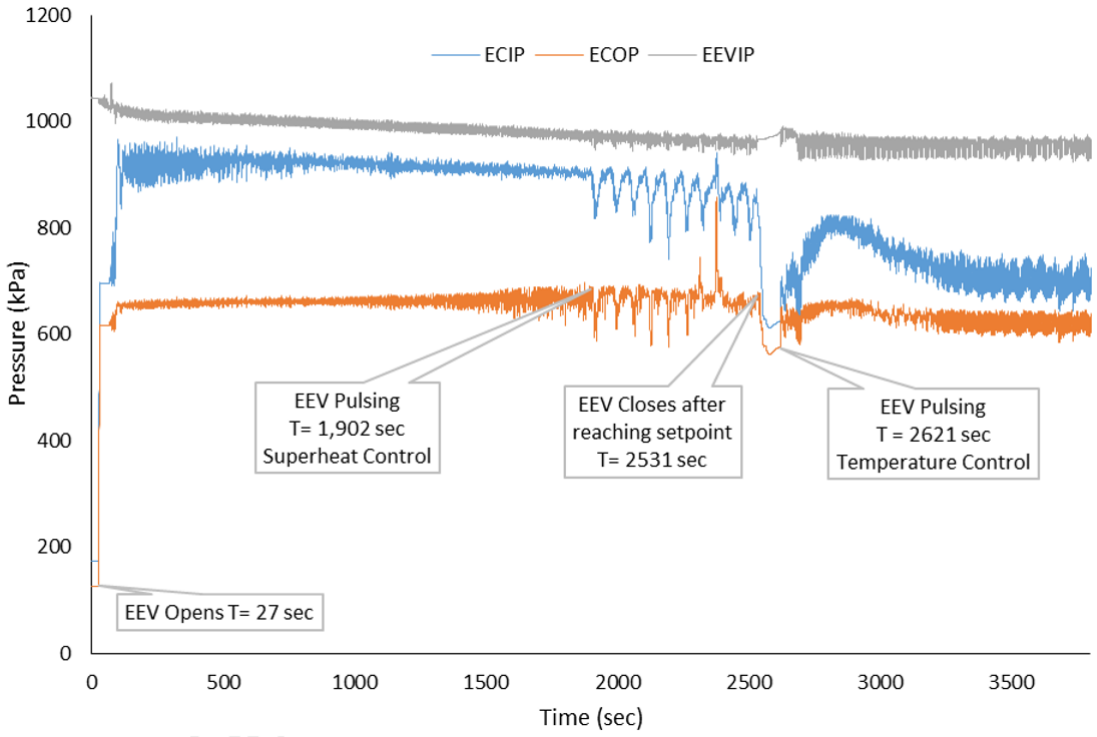

Figure 40: Pressures for Continuous Control for -25°C Set-point. Mass flow rate of CO_2 for 100% EEV Duty Cycle: 0.0245 kg s^{-1}

The measurements of the two-phase zone length, ζ, in Figure 41 show that the two-phase boundary increases rapidly for the initial period of the pull-down after the liquid CO_2 reaches the valve as before until approximately 380 seconds into the test. Between 380 seconds and 1848 seconds when ζ reaches the outlet of the coil, the slope of the ζ curve reduces as heat transfer dominates once again. After the shut-down period ζ begins to increase but drops to zero again similar to the fresh results. Afterwards ζ increases to 0.625 again to bring the EAIT temperature back to the set-point before settling around 0.166. This longer ζ length compared

to the fresh test is needed due to the larger temperature difference between EAIT and the ambient temperature outside the insulated box which results in a larger amount of heat gain into the box. It should be noted that the evaporator coil is oversized for this application with no more than 20% of the coil being used to maintain a -25°C set-point. However the test box is smaller than would be typically used in the field and spare capacity is needed to ensure a fast pull-down of the box temperature to the set-point.

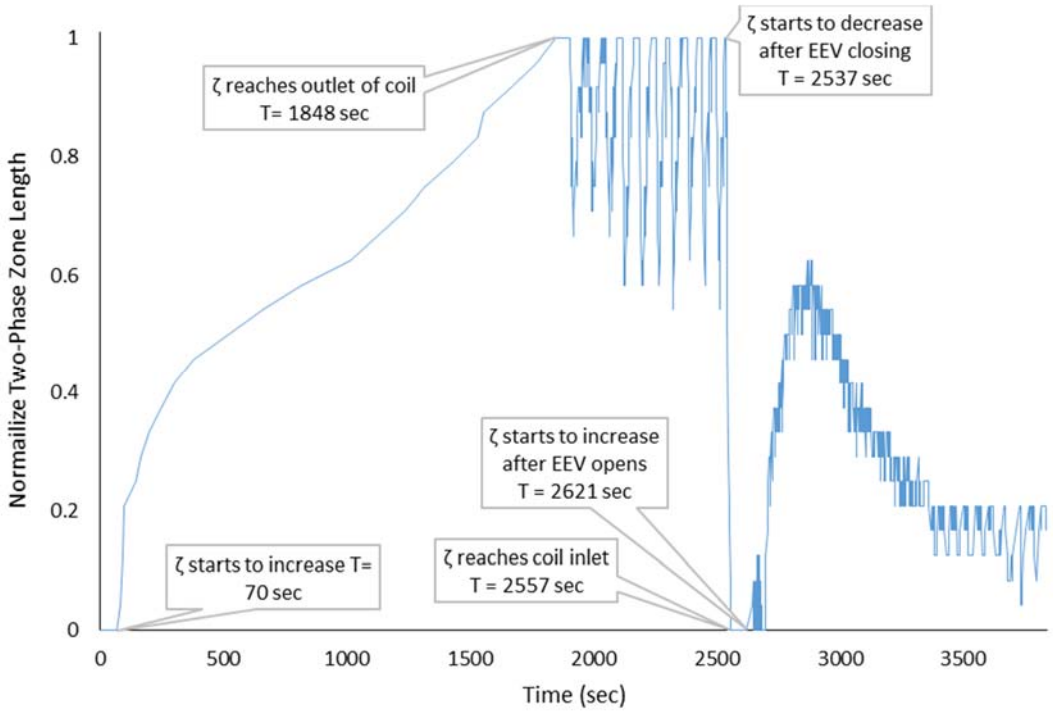

Figure 41: Normalized Two-Phase Zone Length for Continuous Control for -25°C Set-point. Mass flow rate of CO_2 for 100% EEV Duty Cycle: 0.0245 kg s^{-1}

3.11 Experimental Results for Cycle Sentry Control

The experimental testing for cycle sentry control was performed at the same two cargo box temperatures, 0°C and -25°C, as the continuous tests. As outlined in Chapter 1, Section 1.3.4, Page 7, cycle sentry control gets the cargo box to the set-point temperature as quickly as possible and then switches off. The EAIT is allowed to rise until it reaches a switch point 2.2°C above set-point. It then opens the EEV fully again to bring the EAIT back to set-point. It is possible to either keep the fans running during the Null periods to maintain airflow or switch them off

to save CO_2 as desired by the customer. Cycle sentry control is typically used for cargo which is not as sensitive to temperature variation where the customer wishes to minimize CO_2 consumption.

3.11.1 Fresh Set-point with Fans On in Null Mode

The initial pull-down phase for fresh cycle sentry control with fans on in Null, shown in Figure 42, is similar to the pull-down phase for continuous control discussed in Section 3.10.1.

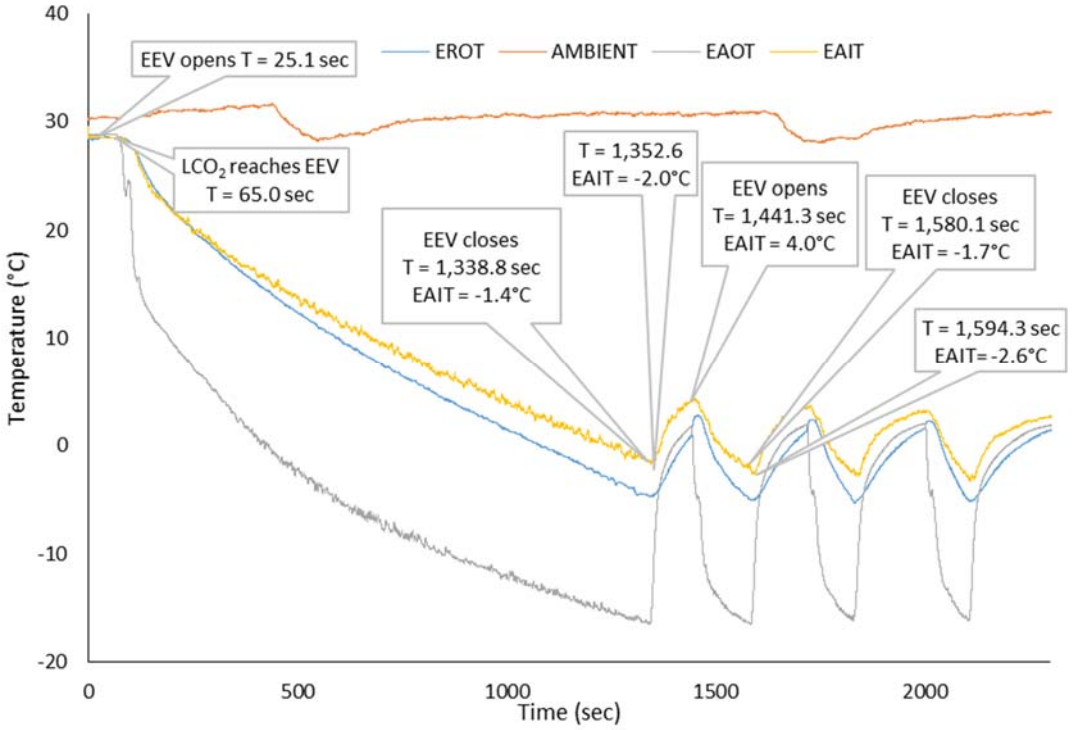

Figure 42: Air and Refrigerant Temperatures for Cycle Sentry Control with fans On in Null for a 0°C Set-point. Mass flow rate of CO_2 for 100% EEV Duty Cycle: 0.0238 kg s^{-1}

Once set-point is reached the EEV closes with the EAIT over-shooting the set-point as before. The length of the Null period is determined by the amount of time is takes for EAIT to reach the switch-point. This temperature rise would be effected by the temperature of the cargo, the condition and size of the cargo box and the temperature difference between the ambient and EAIT. Again EAIT over-shoots the switch-point due to the differences in the dynamics of the thermocouples and the unit controlling sensors. Once the switch-point is reached the EEV opens fully again until EAIT reaches set-point. There is no control based on EAOT for cycle sentry. In

this test the sequence is repeated three times with similar changes in EAIT, EAOT and EROT. Fluctuations in the ambient temperature during the test have no obvious effect on the other temperatures.

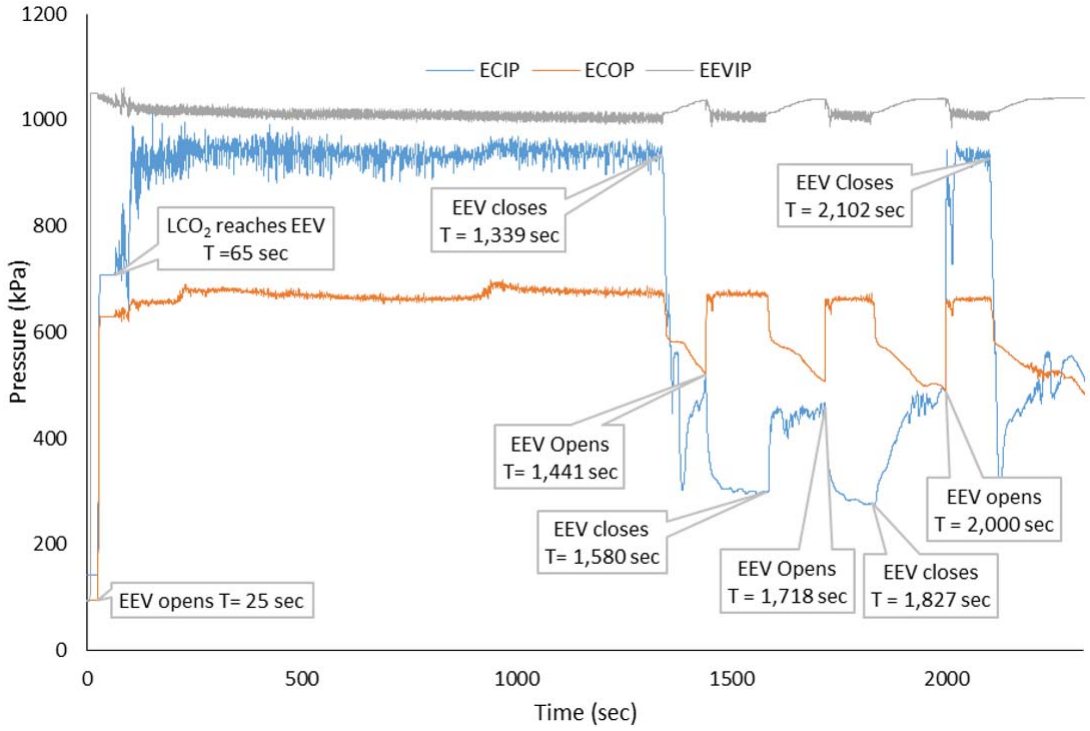

Figure 43: Pressures for Cycle Sentry Control with Fans On in Null for 0°C Set-point. Mass flow rate of CO_2 for 100% EEV Duty Cycle: 0.0238 kg s^{-1}

The pressures for the cycle sentry control with fans running in Null, Figure 43, also show similar behaviour for the initial pull-down as continuous control. The same issue with the ECIP sensor where the value drops below ECOP after the valve closes is displayed although the blockage appears to be dislodged after the EEV opens again at 2,000 seconds. The increases in ECIP during the Null periods may be due to localized boiling of the CO_2 due to the temperature rise.

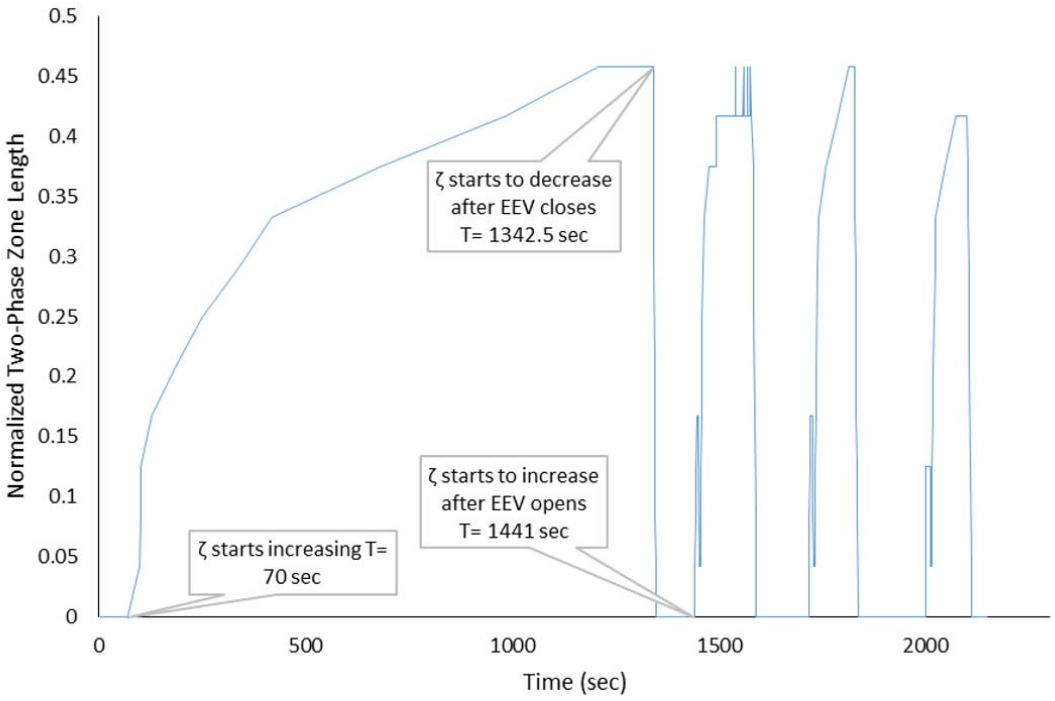

Figure 44: Normalized Two-Phase Zone Length for Cycle Sentry Control with fans On in Null for 0°C Set-point. Mass flow rate of CO_2 for 100% EEV Duty Cycle: 0.0238 kg s^{-1}

The length of the two-phase zone, Figure 44, follows the same pattern for the pull-down phase as the continuous fresh test. ζ goes to zero during the Null periods and returns to broadly the same position each time when EAIT reaches set-point. During the first temperature control period after 1441 seconds ζ displays some oscillations even though the valve is fully open. This may be due to the boundary being close to the measurement point.

3.11.2 Fresh Set-point with Fans Off in Null Mode

For the cycle sentry testing with the fans off in Null mode the initial pull-down was similar to previous tests. However there were significant differences in the system response during the Null periods. As can be seen in Figure 45 there was no overshoot of the EAIT once the EEV closed as there was no airflow to transfer the heat to the air in the cargo box. Instead there is a sharp reduction in EAOT as the static air surrounding the sensor gets rapidly cooled by the coldest section of the coil by the refrigerant circuit inlet. There is also a reduction in EROT as conduction equalizes temperatures along the length of the coil. The time taken for EAIT to reach the switch-point, 412 seconds, is significantly longer than 103 seconds which it took for the cycle sentry test with fans on during Null periods. EAIT starts to increase before the EEV opens at 1,626 seconds as the fan start up 30 seconds before the valve opens. Even after the EEV opens the

EAIT increases by a further 2.1°C to 8.8°C indicating that the average temperature in the cargo box is much higher than the temperature switch point which is set to 2.2°C for this test. EAOT does decrease immediately on opening the EEV but EROT also experiences an increase due to the warmer air blowing over the coil.

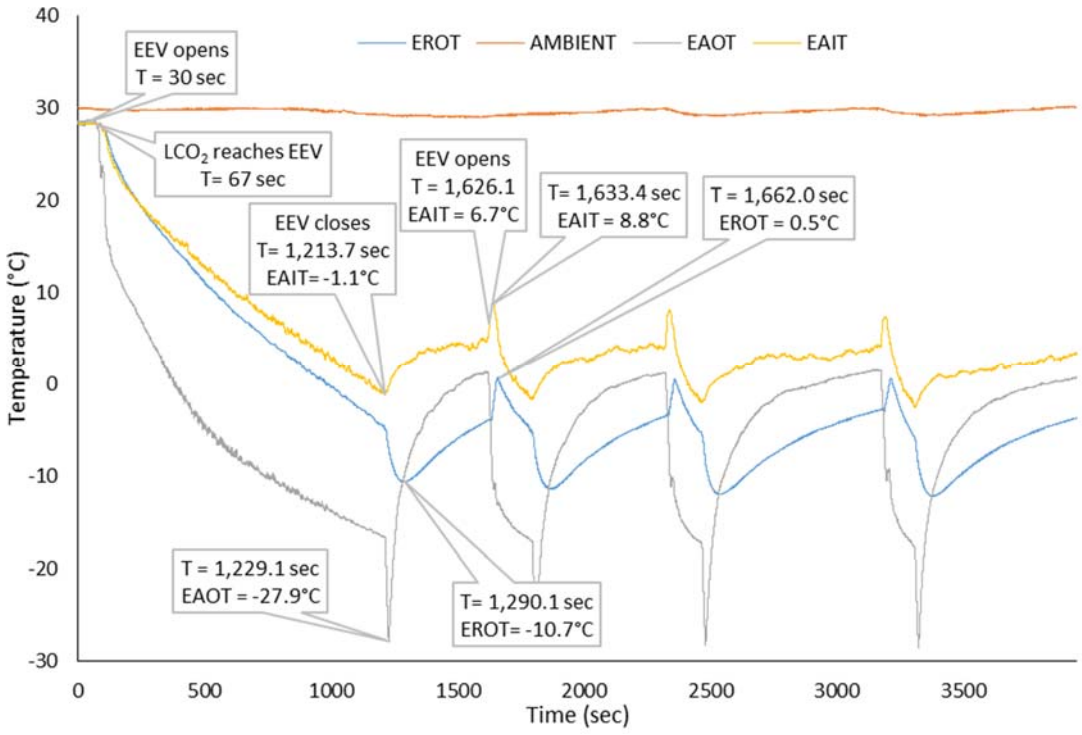

Figure 45: Air and Refrigerant Temperatures for Cycle Sentry Control with Fans Off in Null for a 0°C Set-point. Mass flow rate of CO_2 for 100% EEV Duty Cycle: 0.0236 kg s^{-1}

The pressures in Figure 46 are also unique for the cycle sentry case with fans off in Null. Once the EEV closes both ECIP and ECOP drop in pressure. For three out of the four occurrences ECIP momentarily drops below ECOP before recovering. This appears to be a similar issue with the measurement that was seen in previous tests. Following this both ECIP and ECOP ramp down until the EEV opens again. Each iteration of pull-down and Null mode results in shorter pull-down times and longer Null periods as the items within the cargo box get closer in temperature to the air temperature.

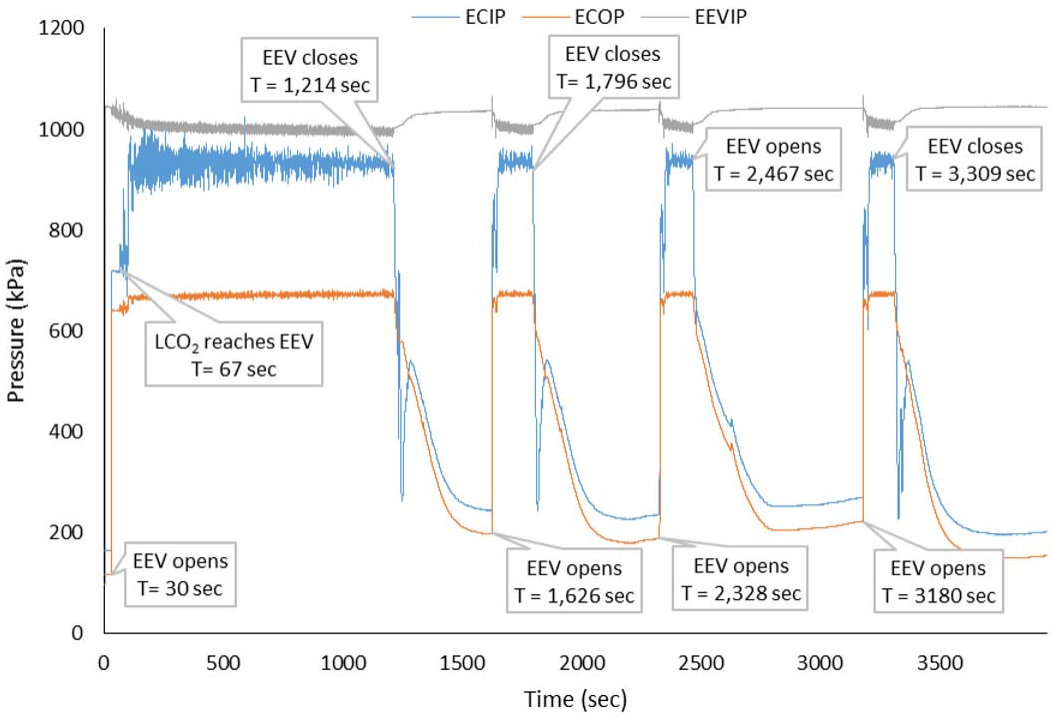

Figure 46: Pressures for Cycle Sentry Control with Fans Off in Null for 0°C Set-point. Mass flow rate of CO_2 for 100% EEV Duty Cycle: 0.0236 kg s^{-1}

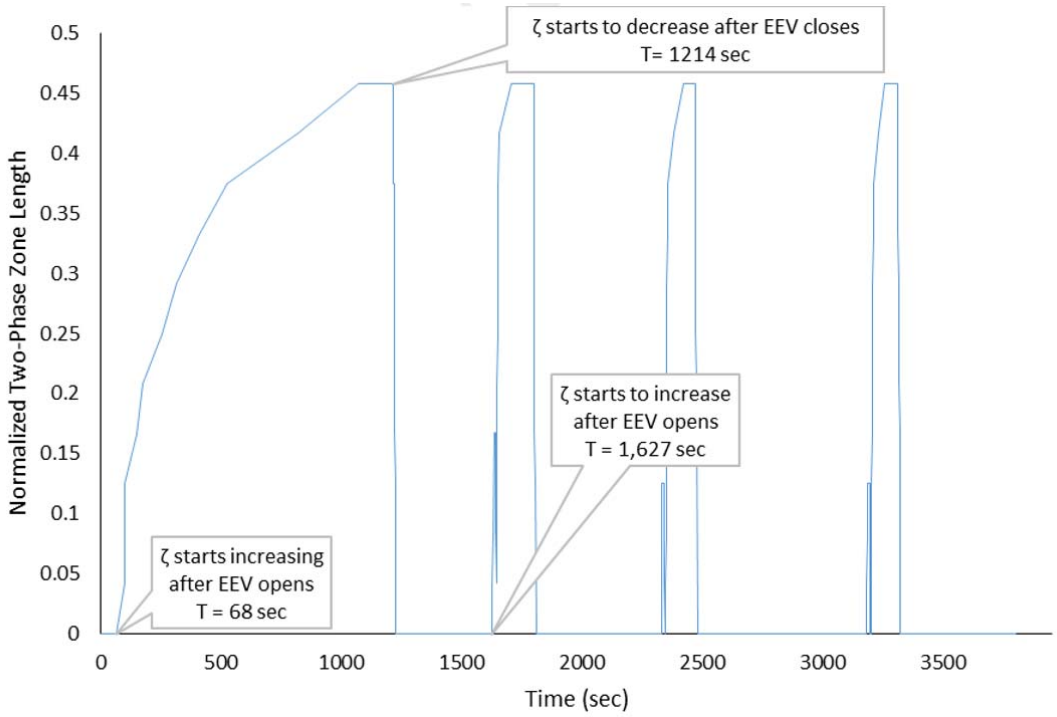

Figure 47: Normalized Two-Phase Zone Length for Cycle Sentry Control with Fans Off in Null for 0°C Set-point. Mass flow rate of CO_2 for 100% EEV Duty Cycle: 0.0238 kg s^{-1}

The length of ζ, shown in Figure 47, does not change significantly between cycle sentry tests with and without airflow in Null mode.

3.11.3 Frozen Set-point with Fans On in Null

The pull-down portion of the cycle sentry frozen test with fans on in Null shows similar behaviour to the continuous test with initial period with the EEV fully open followed by a period of superheat control until the unit reaches set-point and the EEV closes. There is a small amount of overshoot of the EAIT before it starts to increase again during the Null period. EAIT overshoots the restart temperature difference of 2.2°C by 1.8°C before starting to pull-down to the set-point once again. There is a short period of 69 s where the EEV is fully open as the coil fills with two-phase CO_2 before superheat control starts again to bring EAIT to the set-point.

For EROT a sharp increase is noted when the EEV opens again after a Null period. This is due to the sharp increase in pressure that can be seen at this point in Figure 49.

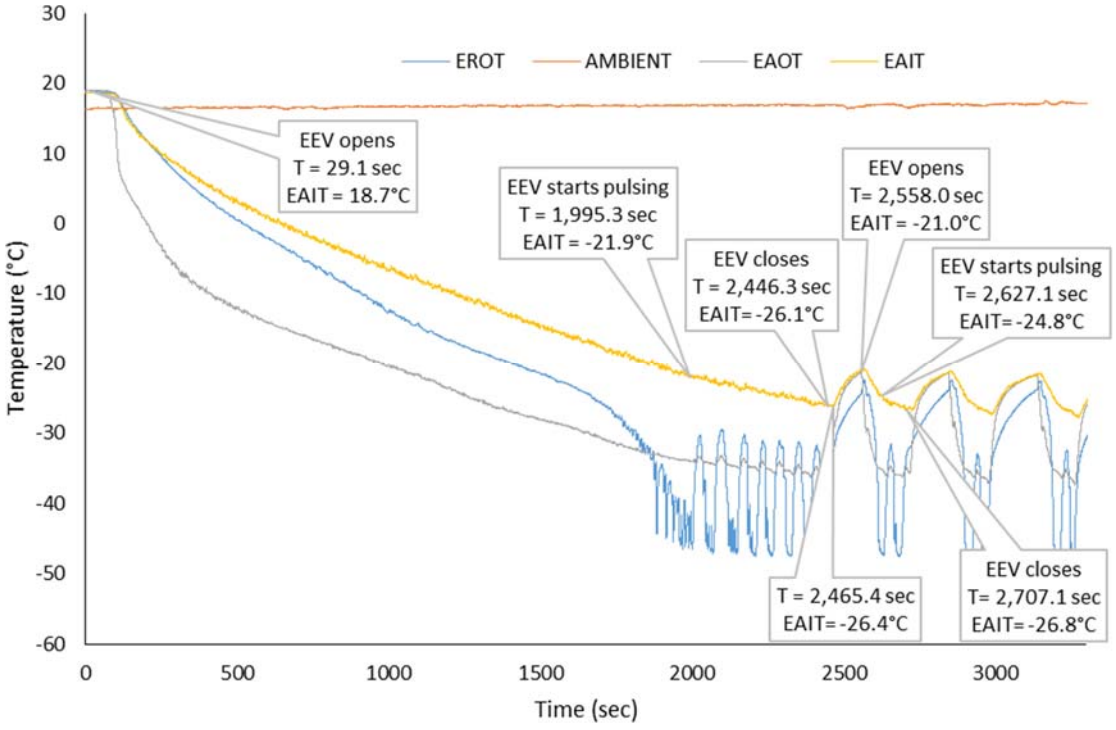

Figure 48: Air and Refrigerant Temperatures for Cycle Sentry Test with Fans On in Null for -25°C Set-point. Mass flow rate of CO_2 for 100% EEV Duty Cycle: 0.0249 kg s^{-1}

ECIP and ECOP also show similar behaviour to the continuous test during the pull-down to set-point. During the Null periods both pressures drop below the BPR setting as the valve does not seal well without flow of CO_2. ECOP recovers for the pull-downs back to set-point but ECIP suffers from the same issues identified in other tests with the sensor being effected by possible blockages of dry-ice.

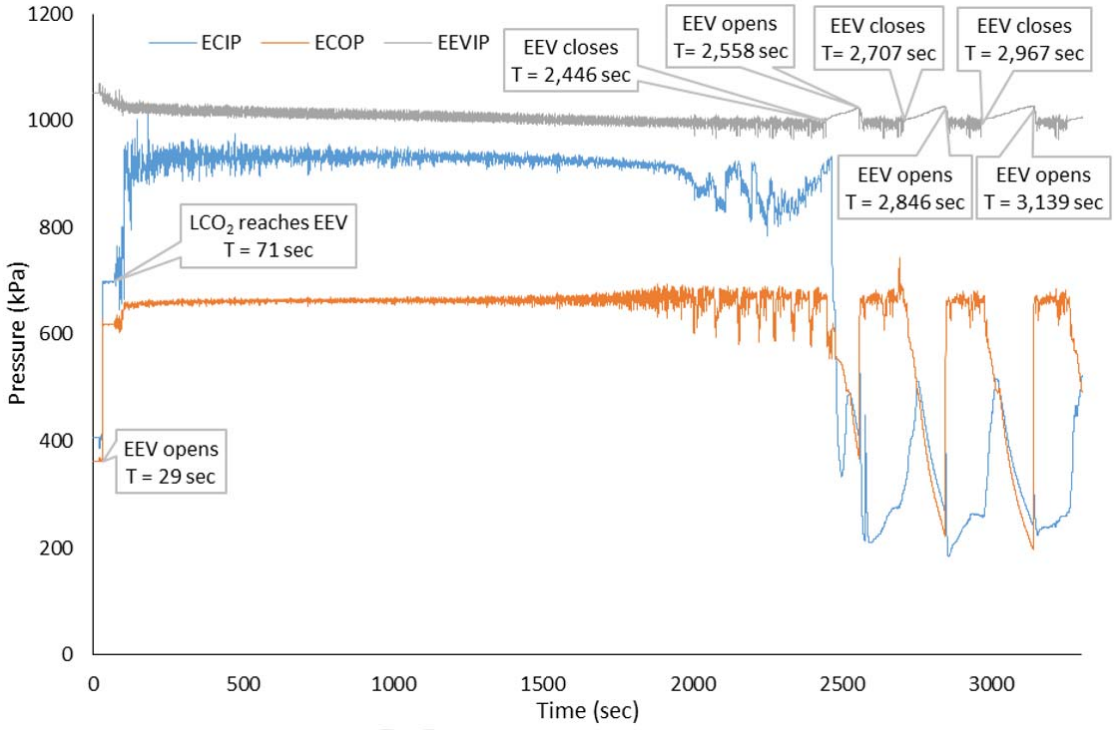

Figure 49: Pressure for Cycle Sentry Test with fans On in Null for -25C Set-point. Mass flow rate of CO_2 for 100% EEV Duty Cycle: 0.0249 kg s^{-1}

The pull-down portion of the ζ graph in Figure 49 is once again similar to the frozen continuous test discussed in Section 3.10.2. There is a steady increasing in ζ length until the two-phase boundary reaches the outlet of the coil, followed by a short period where ζ is equal to 1 before superheat control starts. ζ returns to zero once the EEV closes after EAIT reaches set-point at 2445 seconds. When the EEV opens again at 2558 seconds ζ increases until the two-phase boundary reaches the coil outlet once more. Each of the three pull-downs after Null displayed in Figure 50 show a decrease in the length of ζ during this period which is likely to be linked to vapour build up in the liquid line during the Null periods. Once ζ reaches the coil exit there is a short period of EEV pulsing for superheat control before the EEV closes again when EAIT reaches the set-point.

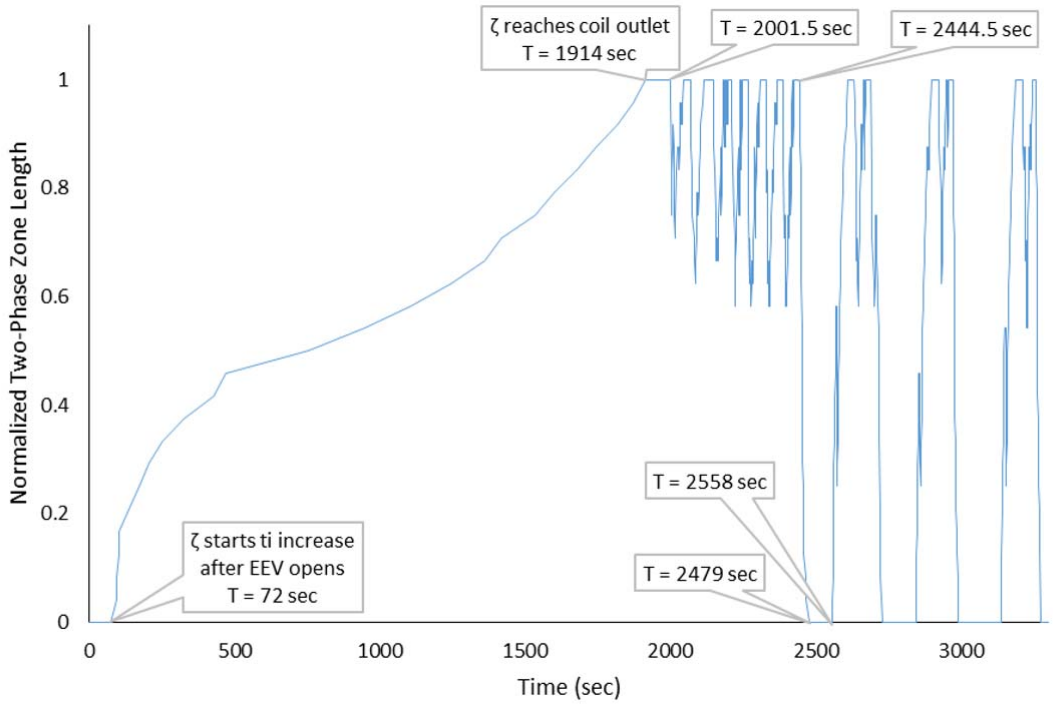

Figure 50: Normalized Two-Phase Zone Length for Cycle Sentry Control with fans On in Null for -25°C Set-point. Mass flow rate of CO_2 for 100% EEV Duty Cycle: 0.0249 kg s^{-1}

3.11.4 Frozen Set-point with Fans Off in Null Mode

The temperatures for the frozen cycle sentry test with fans off in Null, Figure 51, show similar behaviour to the other tests for pull-down and similar behaviour to the fresh cycle sentry test with fans off during the Null period. Once again there is a sharp reduction in EAOT when the EEV closes. It is not as pronounced in this test as EAOT is closer to the liquid saturation temperature. For EROT the temperature drop after the EEV closes is quicker than with the fresh test as the two-phase boundary is very close to the end of the coil. Once again the fans start up before the EEV opens and EAOT increases. When the EEV opens there is a further increase in EAOT due to the pressure rise before the temperature starts to decrease. With such a cold box temperature there is only a short period where the valve is fully open before it starts to pulse due to superheat control. The length of the Null period again substantially exceeds the Null period for the test with fans on in Null due to the lack of heat from the fans and the static air around the EAIT sensor not giving a true reading of the cargo box air temperature. In this test it should be noted that heat mode was used to pull-up the box temperature following a previous test and this is the reason that the EROT, EAOT and EAIT temperature exceed the ambient temperature at the start of the test.

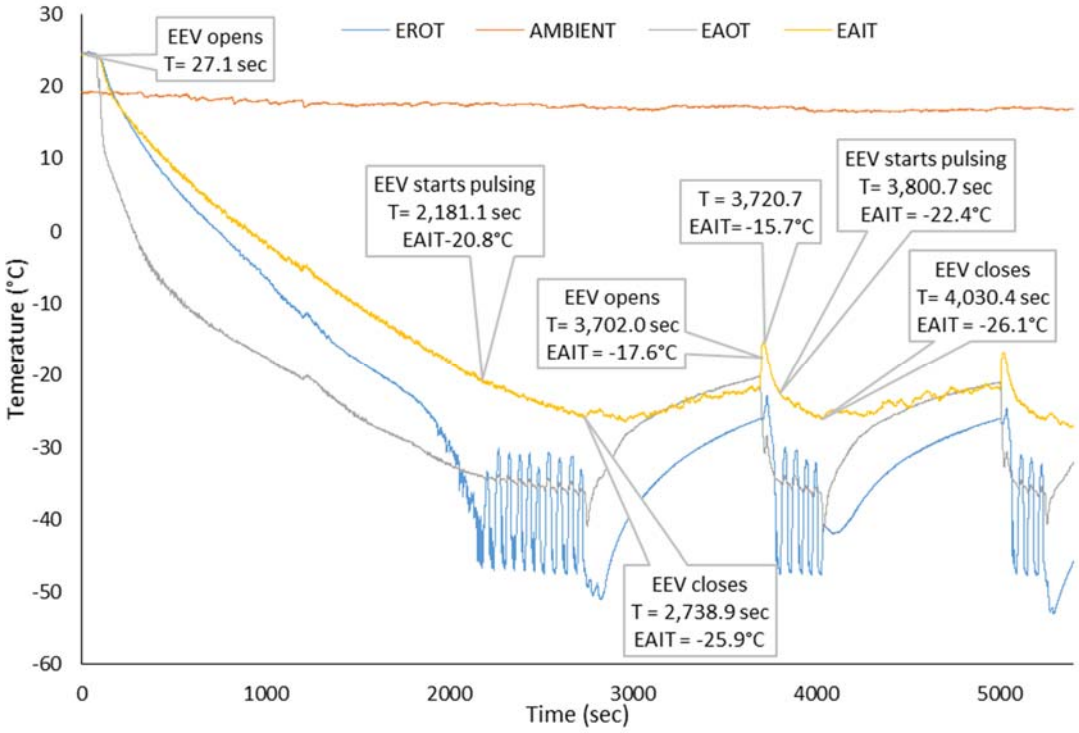

Figure 51: Air and Refrigerant Temperatures for Cycle Sentry Test with Fans Off in Null for -25°C Set-point. Mass flow rate of CO_2 for 100% EEV Duty Cycle: 0.0245 kg s^{-1}

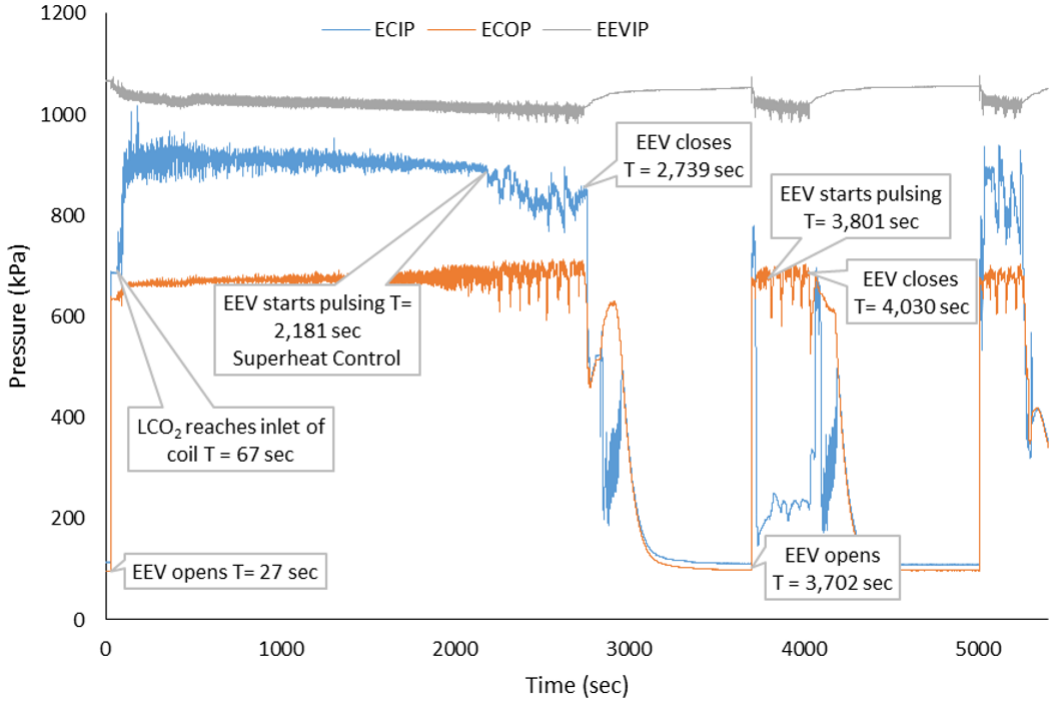

Figure 52: Pressure for Cycle Sentry Test with fans Off in Null for -25C Set-point. Mass flow rate of CO_2 for 100% EEV Duty Cycle: 0.0245 kg s^{-1}

The pressures for the frozen cycle sentry test with fans off in Null are similar to the other frozen tests for the pull-down phase and similar to the fresh cycle sentry test with fans off in Null for the Null period. Again there is an initial drop in both ECOP and ECIP after the EEV closes followed by some fluctuations likely caused by partial blockages of the pressure sensors. After the EEV opens again at 3702 seconds ECIP stay at a low level for the full pull-down to temperature before spiking again once the EEV closes and repeating its previous behaviour. Once again it must be assumed that the inlet to the sensor is being blocked and causing incorrect readings.

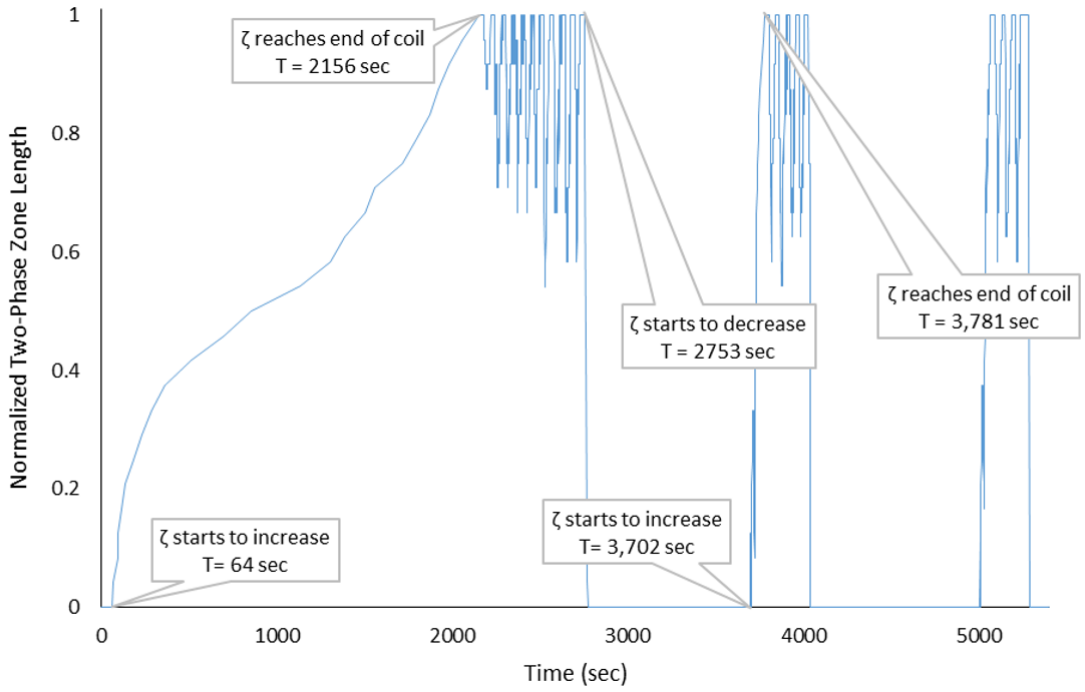

Figure 53: Normalized Two-Phase Zone Length for Cycle Sentry Control with fans Off in Null for -25°C Set-point. Mass flow rate of CO_2 for 100% EEV Duty Cycle: 0.0245 kg s^{-1}

The length of the two-phase zone, displayed in Figure 53, follows similar patterns to those seen in the other frozen cycle sentry test.

This section presents the experimental data for the typical customer operating modes and explains the system characteristics for each variable. This data will be used in Chapters 4 & 5 for validation of the moving boundary model.

3.12 CO_2 consumption comparison for different types of control

A comparison was made of the CO_2 consumption between the different frozen operating modes. Direct comparisons between tests were difficult as the rate of CO_2 consumption was directly related to the ambient temperature which was not under control. The CO_2 tank pressure, which controls the mass flow rate of CO_2, was also a noise factor. The frozen tests presented in Figure 54 were chosen as they were conducted with similar ambient temperatures and flow rates. If mass flow rate of CO_2 and the ambient temperature were consistent between the tests the pull-down portion of each test should take the same time and amount of CO_2. The cycle sentry with fans on in Null test reaches set-point first at 2308 s as it has the lowest ambient temperature and the highest mass flow-rate of CO_2. The continuous test and the cycle sentry with fans off in Null test, which have the same mass flow-rate and similar ambient temperatures, reach their set-points at 2428 s and 2464 s respectively, which is a small difference over a period of the pull-down. There is a small variation of approximately 5% in the amount of CO_2 used to get to the set-point with the cycle sentry with fans on in Null test takes the least amount of CO_2 at 57 kg, the continuous test next at 58 kg and the cycle sentry with fans off in Null taking the most at 60 kg.

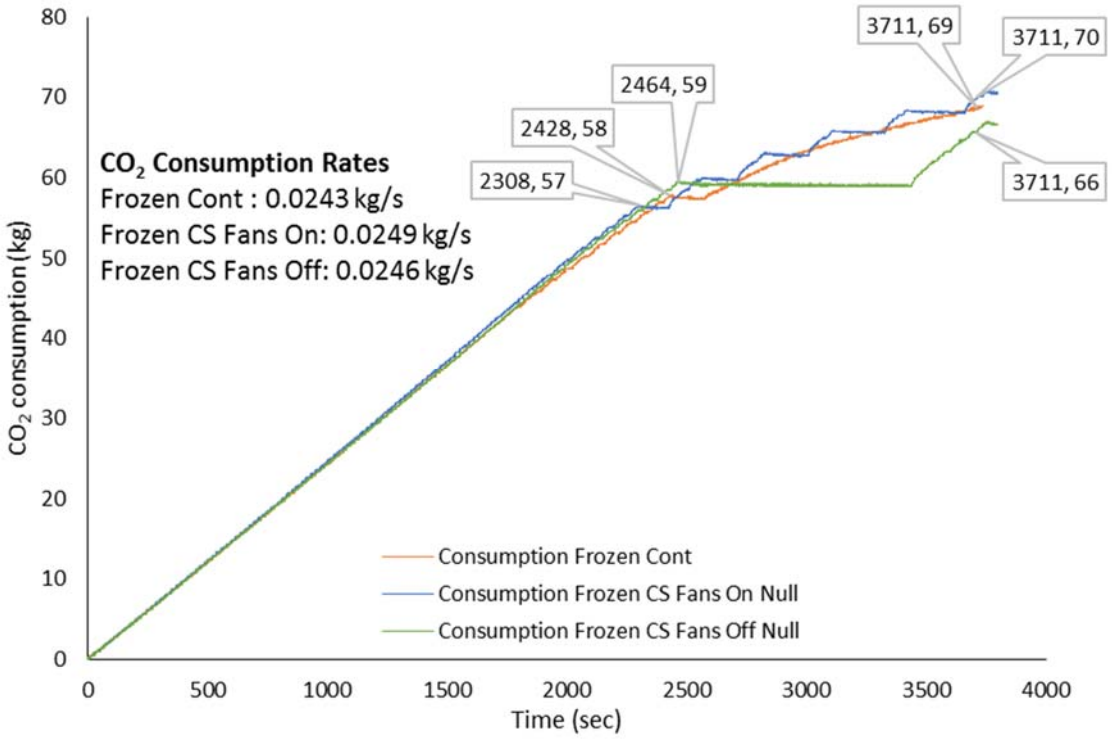

Figure 54: Comparison of CO_2 Consumption for Frozen Operating Modes.

The three tests are then compared again after one cycle of warming to the re-start temperature and pull-down to the set-point. The comparisons are made when the EAIT for all three tests is at -25.7°C as, shown in Figure 55. At this point it can be seen that the cycle sentry with fans on in Null test has now used the most CO_2 at 70 kg, followed by the continuous test at 69 kg with the cycle sentry with fans off in Null test using the least at 66 kg. Figure 55 gives us a good indication as to the reasons for this with the EAIT temperature for the cycle sentry with fans on test overshooting the -25°C set-point on four occasions during this period. The lower ambient temperature that the continuous test experiences is also a factor and it is likely with the same ambient temperatures that the difference between these two tests would be minimal in terms of CO_2 consumption. However the control of EAIT is much better for the continuous test and it is difficult to see the advantage in using the cycle sentry with fans on in Null mode for the open cycle CO_2 system.

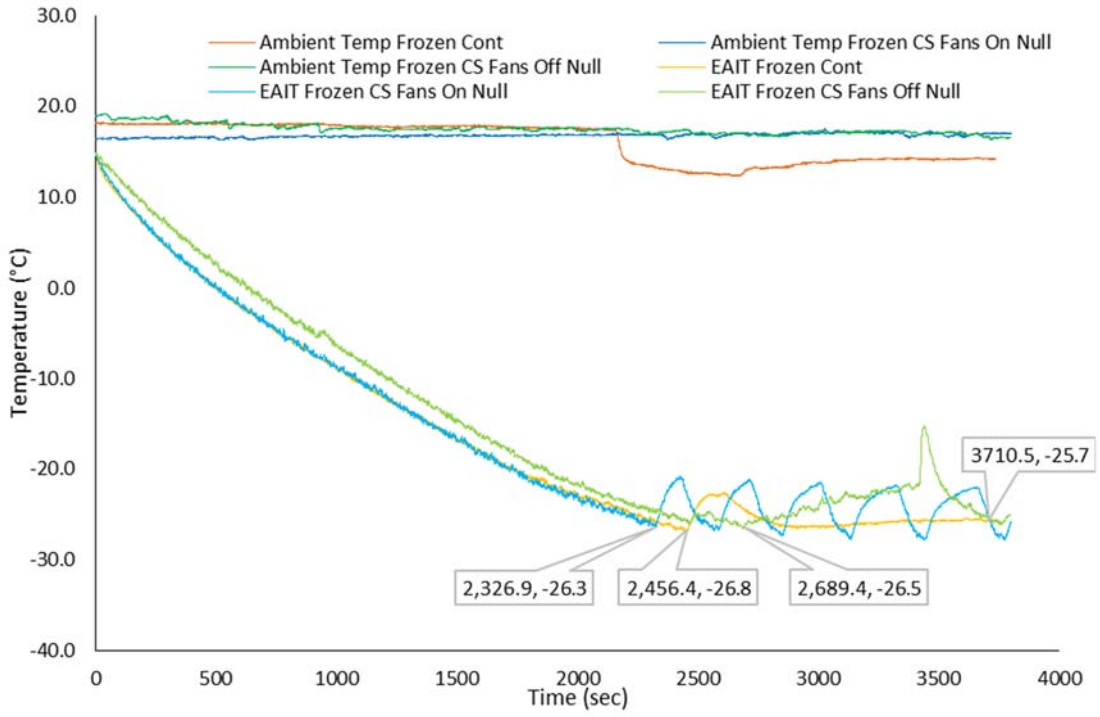

Figure 55: Ambient Temperature and EAIT for CO_2 consumption comparison

The cycle sentry with fans off in Null mode is a different case. There is considerable CO_2 savings in this mode with 43% less CO_2 consumed during the temperature control portion of the test for the cycle sentry with fans off in Null mode when compared with the continuous mode even with the difference in ambient temperatures. This savings is due to the evaporator fans, which

produce 250 W of heat, being off for the majority of this time for the cycle sentry with fans off in Null test. These savings are at the expense of temperature control however with the EAIT temperature reaching 10°C above the set-point temperature for the cycle sentry with fans off in Null test when compared to a temperature deviation of less than 1°C from set-point for the continuous test.

3.13 Summary

This chapter achieves the first two aims outlined for this work in Chapter 1, Section 1.4, Page 8 to experimentally characterize the open cycle CO_2 system and analyse its efficiency in terms of CO_2 consumption.

The experimental set-up that utilized a Thermo King CryoTech open cycle CO_2 system is described and details of the measurements taken on the system are shown. The methodology for determining the airflow from the evaporator fans is demonstrated taking into account the static pressure generated in the cargo box. The effects of vapour in the liquid line from the CO_2 tank are outlined and the measurement method of the mass flow rate of CO_2 is discussed. Additional mapping of the EAOT was performed to analyse the variation in temperature across the face of the evaporator coil and to investigate how quickly the temperatures increase with distance from the coil. Measurements of the two-phase region length were then discussed in detail with a method for measuring the ζ length based on the change in coil temperatures for both static and dynamic tests proposed.

In the second half of the chapter from Sections 3.7 to 3.11 results from the experimental testing are presented for static tests at three box temperatures and for dynamic tests that include a dynamic pull-down, continuous control and cycle sentry control at fresh and frozen set-points. The performance of the open cycle CO_2 system was analysed in terms of temperature control and cooling capacity with these test results. Further analysis on the CO_2 consumption of each operating mode was then presented in Section 3.12.

Chapter 4 Model Development

This chapter presents a switched moving boundary model developed for vapour compression systems and shows how it is adapted for an open cycle CO_2 system. It outlines the basic model before detailing the additions needed for the open cycle CO_2 system. It then uses comparisons with the static and dynamic pull-down results from Chapter 3 to show potential areas of improvement before exploring each model development iteratively with a comparison back to the experimental results. The aim of this chapter is to obtain a model with good correlation to both the static and dynamic pull-down experimental results detailed in Chapter 3.

4.1 Evaporator Coil Model

The approach used to model the evaporator in the open cycle CO_2 system is a switched moving boundary model where the interface between the two-phase and superheated regions in the coil can move along the length of the coil and the model can switch to a single zone two-phase or single zone superheated representation as needed. The model has been adapted for CO_2 from the work done by Rasmussen [39], Li and Alleyne [28] and Fasl [74] on vapour compression systems. The schematic in Figure 56 illustrates inputs, outputs and calculation steps for the evaporator model, indicating how it has been adapted to account for the features of the open cycle system.

The main heat exchanger modelling assumptions made by authors above were retained with the exception of the refrigerant pressure being uniform through the evaporator coil. Those assumption were:

- The heat exchanger is in a single pass cross-flow arrangement
- The refrigerant flow is one-dimensional, compressible and unsteady
- The momentum equation can be neglected
- Conduction along the heat exchanger axis is negligible
- The refrigerant side and air side fin effects are considered

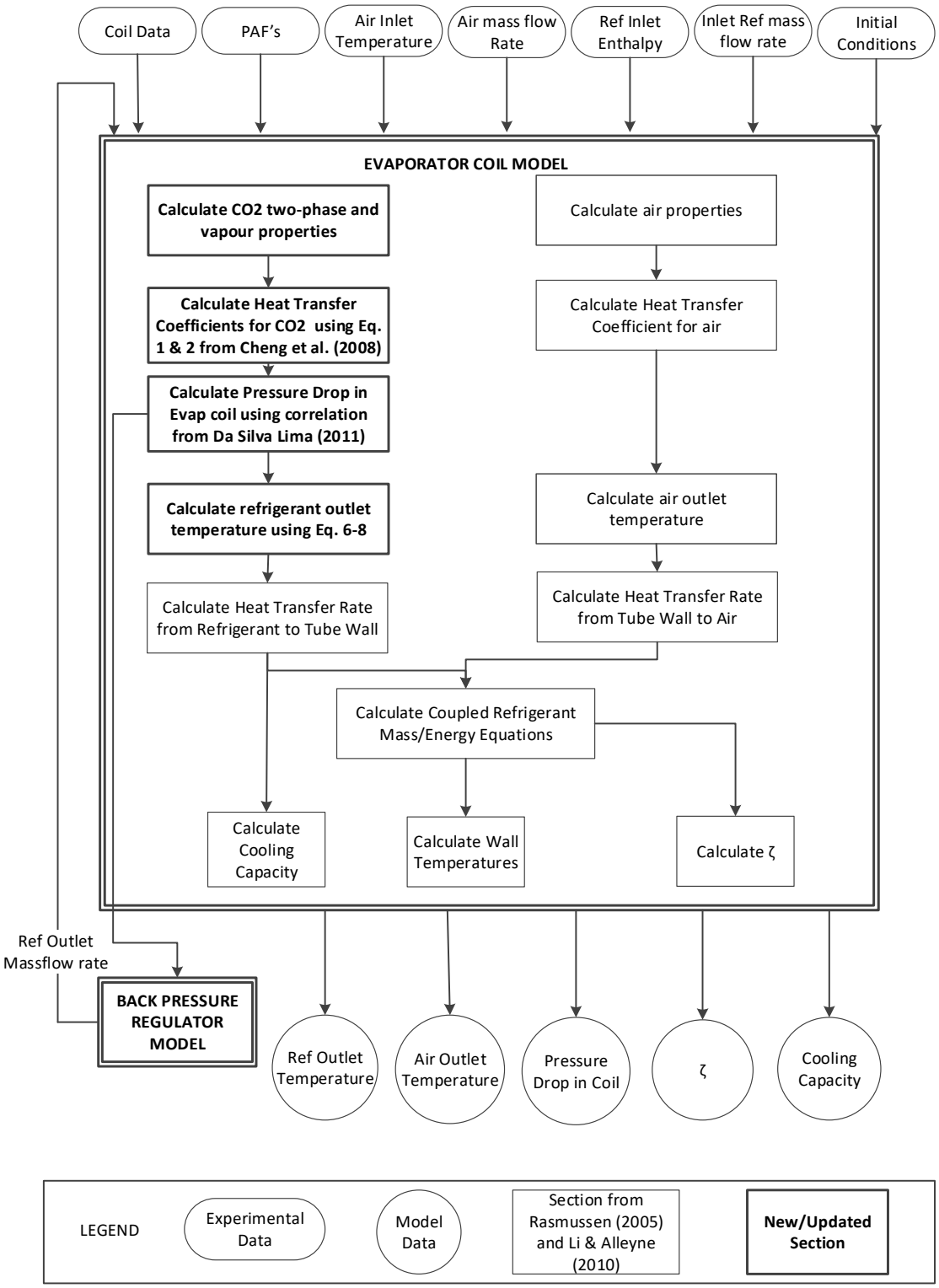

Figure 56: Model Flow Chart

4.1.1 Refrigerant and Air Properties

The method employed by Li [28] to calculate the two-phase and superheated refrigerant properties and the air properties involved creating look-up table which used known parameters such as the refrigerant pressure or the air inlet temperature to reference a table which had been created from *RefProp* [72] for parameters such as the refrigerant density, air density, viscosity and thermal conductivity. Linear interpolation was used between the points on the table. While this strategy was successful for the air properties, and was retained, it proved to be an issue for the refrigerant properties. When calculation were made for refrigerant properties close to the saturation line, the linear interpolation often resulted in values which were not physically possible due to the non-linear changes that occur across the saturation curve. As a result the refrigerant properties were instead calculated with the Ingersoll Rand property routines. These routines use a dynamic link library (DLL) to call a refrigerant model which uses the method employed by Ding et al. [75] to obtain the refrigerant properties from *RefProp* [72].

4.1.2 Coupled Refrigerant Mass/Energy Equations

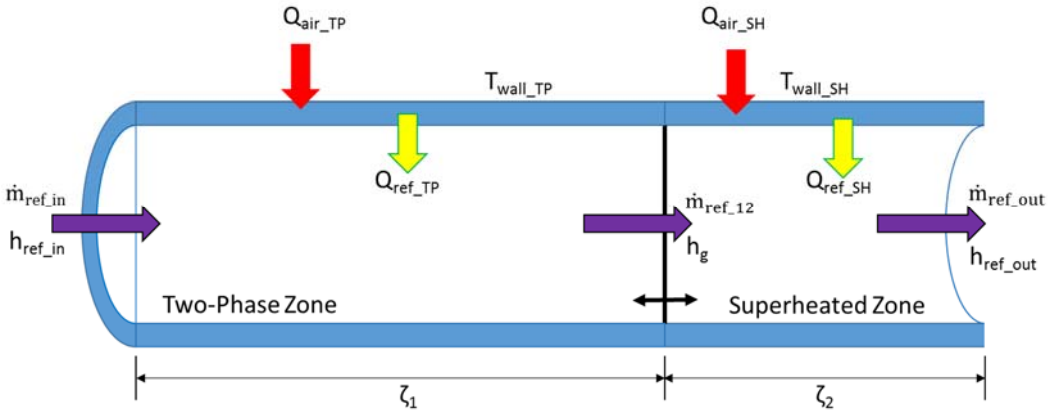

Figure 57: Schematic of Evaporator Model

A schematic of the evaporator coil moving boundary model is displayed in Figure 57 showing the heat transfer from the air to the tube wall and the heat transfer from the wall to the refrigerant for the two-phase and superheated zones as well as the mass flow of the refrigerant through the tube. The boundary between the zones moves along the length of the coil. If ζ_1 goes to zero the model is switched to a superheated only representation. If ζ_1 goes to 1 the model is switched to a two-phase only representation.

From Li [28] the evaporator conditions at each time step are giving by the dynamic state vector:

$$X = [\zeta_1 \; P_{ref} \; h_{SH} \; T_{wall_{TP}} \; T_{wall_{SH}} \; \bar{\gamma}]^T \tag{4. 1}$$

which stays constant for all three model representations described in Sections 4.13, 4.14 and 4.15. State equations are then given by

$$Z(X,u).\dot{X} \; = \; f(X,u) \tag{4. 2}$$

where Z(X, u) and f(X, u) have different coefficient matrices depending on the model representation.

The refrigerant heat transfer from the walls for the two-phase zone is calculated from:

$$Q_{ref\_TP} = \; \alpha_{TP}\zeta_1 AS_{ref}\left(T_{wall\_TP} - T_{ref\_TP}\right) \tag{4. 3}$$

and for the superheated zone from:

$$Q_{ref\_SH} = \; \alpha_{SH}\zeta_2 AS_{ref}\left(T_{wall\_SH} - T_{ref\_SH}\right) \tag{4. 4}$$

The heat transfer from the walls to the air is calculated using the ε-NTU method [61] described in Section 2 and used by Fasl [74]. For the two-phase zone it is given by:

$$Q_{air\_TP} = \; \dot{m}_{air} C_{p\_air} \varepsilon \left(T_{wall\_TP} - \; T_{air\_in\_TP}\right) \tag{4. 5}$$

and for the superheated zone from:

$$Q_{air\_SH} = \; \dot{m}_{air} C_{p\_air} \varepsilon \left(T_{wall\_SH} - \; T_{air\_in\_SH}\right) \tag{4. 6}$$

where

$$\varepsilon = 1 - e^{-NTU} \tag{4. 7}$$

and

$$NTU = \frac{\alpha_{air} AS_{air} \zeta}{\dot{m}_{air} C_{p\_air}} \tag{4. 8}$$

A correction is made to the calculations presented by Fasl [74] where ζ_1 or ζ_2 is multiplied by AS_{air} in equation 4.8 to calculate the correct area of the zone in question rather than it being used as a multiplier in equations 4.6 and 4.7.

The state equations for the average wall temperatures in each zone are given by:

$$\frac{dT_{wall\_TP}}{dt} = \frac{1}{\zeta_1}\left[\frac{-Q_{ref\_TP} - Q_{air\_TP}}{C_{p\_wall} m_{wall}} + \left(T_{wall1} - T_{wall\_TP}\right)\frac{d\zeta_1}{dt}\right] \tag{4. 9}$$

$$\frac{dT_{wall\_SH}}{dt} = \frac{1}{\zeta_2}\left[\frac{-Q_{ref\_SH} - Q_{air\_SH}}{C_{p\_wall} m_{wall}} + \left(T_{wall\_SH} - T_{wall1}\right)\frac{d\zeta_1}{dt}\right] \tag{4. 10}$$

where the transported temperature, T_{wall1}, is determined by boundary movement.

$$\begin{aligned} If\ \frac{d\zeta_1}{dt} < 0, T_{wall1} = T_{wall_{SH}} \\ If\ \frac{d\zeta_1}{dt} \geq 0, T_{wall1} = T_{wall\_TP} \end{aligned} \tag{4. 11}$$

In the case where there is only a superheated region equation 4.9 is replaced by

$$\frac{dT_{wall\_TP}}{dt} = K\left(T_{wall\_SH} - T_{wall\_TP}\right) \tag{4. 12}$$

and in the case where there is only a two-phase region equation 4.10 is replaced by

$$\frac{dT_{wall\_SH}}{dt} = K\left(T_{wall\_TP} - T_{wall\_SH}\right) \tag{4. 13}$$

4.1.3 Evaporator Two-Phase and Superheated Two-zone representation

For the refrigerant side of the model the two-phase zone equations, derived by applying the mass and energy conservation laws, are:

$$\frac{d\zeta_1}{dt} + \frac{\zeta_1}{\rho_{TP}}\frac{\delta\rho_{TP}}{\delta P}\frac{dP}{dt} + \frac{\zeta_1}{\rho_{TP}}\frac{\delta\rho_{TP}}{\delta\bar{\gamma}}\frac{d\bar{\gamma}}{dt} + \frac{\dot{m}_{12}}{\rho_{TP}V_{ref}} = \frac{\dot{m}_{ref\_in}}{\rho_{TP}V_{ref}} \tag{4. 14}$$

$$\left[\frac{\delta h_{TP}}{\delta P} - \frac{1}{\rho_{TP}}\right]\frac{dP}{dt} + \frac{\delta h_{TP}}{\delta\bar{\gamma}}\frac{d\bar{\gamma}}{dt} + \frac{h_g - h_{TP}}{\rho_{TP}V_{ref}\zeta_1}\dot{m}_{12} = \frac{Q_{ref\_TP} + \dot{m}_{ref\_in}(h_{in} - h_{TP})}{\rho_{TP}V_{ref}\zeta_1} \tag{4. 15}$$

and the superheated equations are:

$$\frac{d\zeta_1}{dt} - \frac{\zeta_2}{\rho_{SH}}\frac{\delta\rho_{SH}}{\delta P}\frac{dP}{dt} - \frac{\zeta_2}{\rho_{SH}}\frac{\delta\rho_{SH}}{\delta h_{SH}}\frac{dh_{SH}}{dt} + \frac{\dot{m}_{12}}{\rho_{SH}V_{ref}} = \frac{\dot{m}_{ref_{out}}}{\rho_{SH}V_{ref}} \tag{4. 16}$$

$$-\frac{1}{\rho_{SH}}\frac{dP}{dt} + \frac{dh_{SH}}{dt} - \frac{h_g - h_{SH}}{\rho_{SH}V_{ref}\zeta_2}\dot{m}_{12} = \frac{Q_{ref_{SH}} - \dot{m}_{ref_{out}}\left(h_{SH} - h_g\right)}{\rho_{SH}V_{ref}\zeta_2} \tag{4. 17}$$

The derivative of the mean void fraction, $\bar{\gamma}$, is given by:

$$\frac{\delta\bar{\gamma}_{tot}}{\delta P}\frac{dP}{dt} - \frac{d\bar{\gamma}}{dt} = K_{\gamma}(\bar{\gamma} - \bar{\gamma}_{tot}) \tag{4. 18}$$

4.1.4 Evaporator Two-Phase One-zone representation

When ζ go 1 the superheated region is removed from the model. In practice this occur when the air temperature decreases or the refrigerant mass flow rate increases and there is insufficient heat transfer between the refrigerant and the air. To prevent instability pseudo-state equations are used to track the inactive dynamic states of the superheated zone to the active two-phase zone. These are given by:

$$\frac{dh_{SH}}{dt} = K_h\left(h_g - h_{SH}\right) \tag{4. 19}$$

Since ζ_1 is now stable at its maximum value

$$\frac{d\zeta_1}{dt} = 0 \tag{4. 20}$$

As a result the two-phase refrigerant mass and energy equations become:

$$\frac{\zeta_1}{\rho_{TP}}\frac{\delta\rho_{TP}}{\delta P}\frac{dP}{dt} + \frac{\zeta_1}{\rho_{TP}}\frac{\delta\rho_{TP}}{\delta\bar{\gamma}}\frac{d\bar{\gamma}}{dt} = \frac{\dot{m}_{ref\_in} - \dot{m}_{ref\_out}}{\rho_{TP}V_{ref}} \tag{4. 21}$$

and

$$\left[\frac{\delta h_{TP}}{\delta P} - \frac{1}{\rho_{TP}}\right]\frac{dP}{dt} + \frac{\delta h_{TP}}{\delta\bar{\gamma}}\frac{d\bar{\gamma}}{dt} = \frac{Q_{ref\_TP} + \dot{m}_{ref\_in}(h_{in} - h_{TP}) - \dot{m}_{ref\_out}(h_{out} - h_{TP})}{\rho_{TP}V_{ref}\zeta_1} \tag{4. 22}$$

4.1.5 Evaporator Superheated One-Zone Representation

When ζ_1 goes to zero the two-phase zone is removed from the model. This can occur during start-up before the EEV is opened or anytime the EEV is closed for a sufficient period of time. Again pseudo state equations are used to track the dynamic states of the two-phase zone to the active superheated zone. These are given by:

$$\frac{d\zeta_1}{dt} = K_\zeta(0.001 - \zeta_1) \tag{4. 23}$$

and

$$\frac{d\bar{\gamma}}{dt} = K_\gamma(0.999 - \bar{\gamma}) \tag{4. 24}$$

As a result the superheated refrigerant mass and energy equations become:

$$\frac{\delta\rho_{SH}}{\delta P}\frac{dP}{dt} + \frac{\delta\rho_{SH}}{\delta h_{SH}}\frac{dh_{SH}}{dt} = \frac{\dot{m}_{ref\_in} - \dot{m}_{ref\_out}}{\zeta_2 V_{ref}} \tag{4. 25}$$

$$-\frac{1}{\rho_{SH}}\frac{dP}{dt} + \frac{dh_{SH}}{dt} = \frac{Q_{ref_{SH}} + \dot{m}_{ref_{in}}(h_g - h_{SH}) - \dot{m}_{ref_{out}}(h_{SH} - h_g)}{\rho_{SH} V_{ref}\zeta_2} \tag{4. 26}$$

4.1.6 Switching criteria for evaporator model

The switching from a two-zone two-phase and superheated zone model to a two-phase only model occurs when ζ_2 is smaller than a minimum value and the value of ζ_2 is decreasing

$$\zeta_2 < \zeta_{min} \tag{4. 27}$$

$$\frac{d\zeta_1}{dt} > 0 \tag{4. 28}$$

The switching from a two-zone two-phase and superheated zone model to a superheated only model occurs when ζ_2 is smaller than a minimum value and the value of the mean void fraction $\bar{\gamma}$ is increasing.

$$\zeta_1 < \zeta_{min} \tag{4. 29}$$

$$\frac{d\bar{\gamma}}{dt} > 0 \tag{4. 30}$$

For this work the value of $\zeta_{min}$was chosen to be 0.005.

The switch from the one-zone two-phase only model to the two-zone model occurs when the mean void fraction $\bar{\gamma}$ is increasing and the amount of vapour in the normalized zone length is greater than the minimum value

$$\zeta_1(\bar{\gamma} - \bar{\gamma}_{tot}) > \zeta_{min} \tag{4. 31}$$

$$\frac{d\bar{\gamma}}{dt} > 0 \tag{4. 32}$$

The minimum value should be chosen in this equation to be at least the same as Equation 4.27 to provide a hysteresis effect and prevent rapid switching back and forth between the modes.

The switch from the one-zone superheated only model to the two-zone model occurs when the two-phase zone density is greater than the saturated vapour density and the mass flow rate of refrigerant is greater than zero.

$$\rho_{TP} > \rho_g \tag{4. 33}$$

$$\dot{m}_{ref\_in} > 0 \tag{4. 34}$$

4.1.7 Void Fraction Model

Alternative void faction models to the Zivi correlation those used by Li and Alleyne [28] were discussed in Chapter 2, Section 2.7 Page 20. Although the Lockhart–Martinelli and the Rouhani-Axelsson models both predicted HFC databases with greater accuracy there was little information on how well they performed for CO_2 and they were both more complex models than the Zivi correlation. With this in mind it was decided that there was insufficient benefit to be gained in changing the moving boundary evaporator model to include either of these correlations and the Zivi correlation was retained.

4.1.8 Pressure Drop

The coil outlet pressure is an important parameter when modeling the open cycle system. In some models developed for vapour compression systems an assumption is made that there is negligible pressure drop along the length of the evaporator coil [28,39,52]. This assumption allows for a significant reduction in the complexity of the model as the effects of momentum can be ignored. While this is valid for vapour compression systems with multi-pass evaporator coils it cannot be assumed to be the case for open cycle, single pass CO_2 evaporator coils where the pressure drop along the length of the coil can be up to 30% of the inlet pressure. To avoid adding too much complexity, which would slow down the model, it was decided not to try and integrate the coil pressure drop into the governing equations of the model but to calculate the pressure drop separately at each time step. This approach has been used before in literature to simplify the modelling by Qiao et al. [53] and Tian & Li [76] as discussed in Chapter 2 Section 2.5 Page 18.

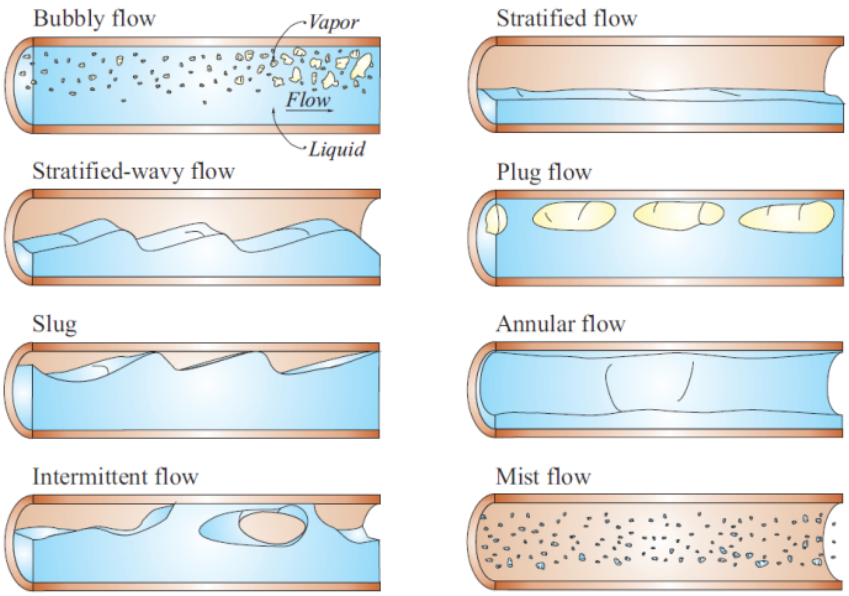

Figure 58: Flow Pattern Map [57]

To calculate the pressure drop in the two-phase region a model developed for vapour compression systems by Da Silva Lima [57] is adopted since it includes the effects of u-bends. A flow pattern map, Figure 58, categorizes the different types of flow within the two-phase region of the evaporator coil and then calculates the pressure drop for both the straight sections and the u-bends within the coil. A combination of the mass flux and the quality of the refrigerant is used to calculate which flow pattern applies and this in turn determines the equations for pressure drop along the straight and the u-bend sections. For this investigation the mass flux was high enough to discount stratified and bubbly flow models, however all the other flow patterns, shown in Figure 58, were included.

The refrigerant pressure in the governing equations is assumed to be the average pressure in the two-phase zone and a linear assumption is then used to calculate the inlet and outlet pressures of the two-phase zone based on the calculated pressure drop. The pressure drop for the superheat zone, which also takes into account flow in u-bends, is calculated from the same work by Da Silva Lima [57]. It is subtracted from the two-phase outlet pressure to determine the coil outlet pressure and hence the inlet pressure to the BPR.

4.1.9 Refrigerant Side Heat Transfer Coefficient

CO_2 tends to exhibit a much higher heat transfer coefficient than conventional refrigerant like R404A [47] as discussed in Chapter 2 Section 2.4 Page 18. As a result the heat transfer

correlation used by Li and Alleyne [28] did not accurately predict the heat transfer for the open cycle CO_2 system. A review of the state of the art for CO_2 heat transfer coefficients [49,77] suggested that the most accurate correlation for CO_2 was from Fang [78]. However the temperature at the tube inner wall was required as an input for this correlation which was not possible to calculate accurately using the moving boundary model. Instead the next best option was adopted where the two-phase heat transfer coefficient was based on a flow pattern based correlation proposed by Cheng et al. [47] and the superheated heat transfer coefficient is derived from [79]. The two-phase heat transfer coefficient, U_{wet}, is given by:

$$U_{wet} = \left[(SU_{nb})^3 + U_{cb}^3\right]^{1/3} \tag{4. 35}$$

where U_{nb} is the nucleate boiling heat transfer coefficient, S is the nucleate boiling heat transfer suppression factor and U_{cb} is the convective boiling heat transfer coefficient. The values of these terms depend on the flow pattern that is again identified by the quality and mass flux of the fluid.

The vapour heat transfer coefficient, U_v, is given by:

$$U_v = 0.23 Re_v^{0.8} Pr_v^{0.4} \frac{k_v}{D} \tag{4. 36}$$

4.1.10 Superheat Zone Assumptions

Rasmussen [39], Li and Alleyne [28] and Fasl [74] all assume a linear relationship for the enthalpy within the superheated zone as described in Chapter 2 Section 2.6 Page 19.

$$h_{SH} = \frac{h_g + h_{out}}{2} \tag{4. 37}$$

This allows for simpler state equations for the superheated zone enthalpy and does not generate significant error when the length of the superheated zone is short compared to the two-phase zone as is the case with most vapour compression system. However it does cause issues with the calculation for the refrigerant outlet enthalpy and outlet temperature when the zone gets longer as will be demonstrated in Section 4.4.

4.2 Back Pressure Regulator (BPR) Model

A feature of open cycle CO_2 systems is the BPR at the outlet of the evaporator. Consisting of a spring and bellows the BPR maintains the pressure at the outlet of the coil above the triple point of CO_2. As seen in Figure 59 the outlet pressure P3 is exerted against both the bellows effective area and the outlet side of the seat disk. Since the effective area of the bellows is equal to the area of the valve port and outlet pressure forces are cancelled and have no effect on the valve operation. The inlet pressure P1 acts on the valve seat and is opposed by the spring pressure P2. The force exerted by the adjustable spring determined at what pressure the valve opens. Any pressure above this value will increase the valve opening position until it comes into contact with the stop. If the pressure drops again below the force needed to counteract the spring the seat disc will begin to close and will close the valve again when it goes below the original opening inlet pressure.

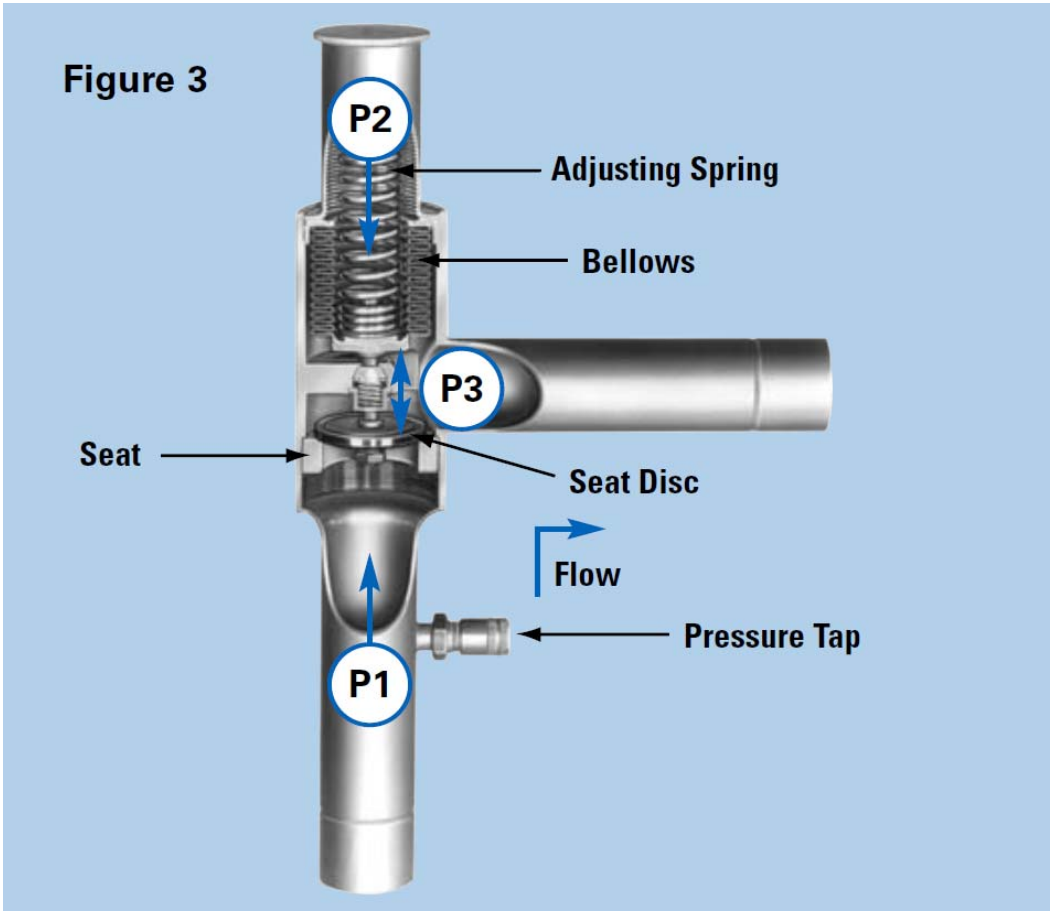

Figure 59: Back Pressure Regulator Representation [80]

In the modelling environment, Simulink, the flow through the valve was calculated using Bernoulli's equation. The valve was set to open at 630 kPa and was fully open at 700 kPa. A non-linear empirical table is used to calculate the valve flow coefficient changes between the initial opening position and the fully open position depending on the inlet pressure.

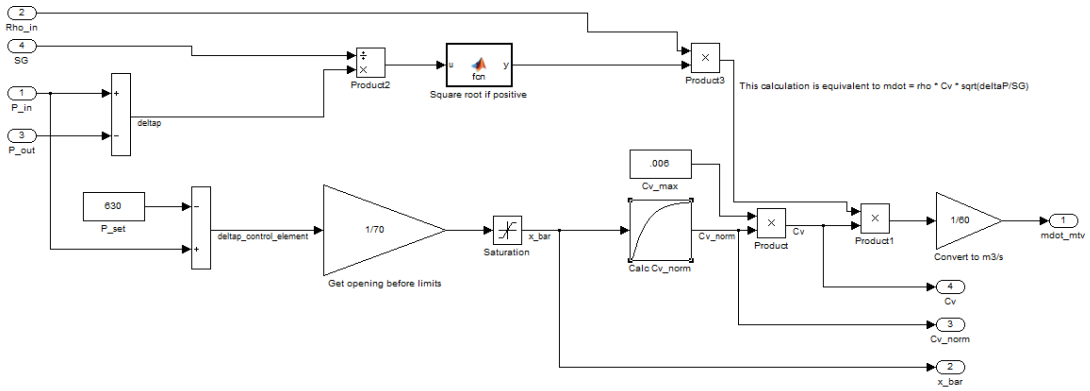

Figure 60: Simulink Back Pressure Regulator Model

For simulation purposes a first order filter was used to model the inertia in the valve to prevent algebraic loops forming. The model of the BPR takes the evaporator coil outlet pressure and density, the specific gravity of CO_2 and the atmospheric pressure as an inputs and calculates the mass flow rate through the BPR that is then used as an input to the evaporator coil model for the next iteration step.

4.3 Evaporator Fan Model

A model of the evaporator fan was also added to improve the accuracy of the model for the dynamic results in particular. This model was based on the fan laws which state that with a constant blower diameter:

$$Q_1/Q_2 = RPM_1/RPM_2 \quad (4.\ 38)$$

$$\Delta P_1/\Delta P_2 = (RPM_1/RPM_2)^2 \quad (4.\ 39)$$

$$P_1/P_2 = (RPM_1/RPM_2)^3 \quad (4.\ 40)$$

Reference values for the volumetric flow rate, Q, the pressure drop, ΔP, and the power, P were measured experimentally in Chapter 3, Section 3.2 Page 27 and from these the mass flow rate of the air for variation in ambient temperature and RPM was calculated. The effects of the changes in ambient temperature on the electric motor in the blower was also included using some adjustment factors calculated from the experimental testing. The fan model is included in Model 1 for which results are presented in Section 4.4 below.

4.4 Results for Baseline Model 1

4.4.1 Static Results

At first it was decided to compare the moving boundary model with the experimental conditions at static conditions to see if there were substantial issues with the models performance for open cycle CO_2 system. The first comparison of the model to the experimental results is shown in Table 4. The evaporator air inlet temperature, the refrigerant mass flow-rate and the EEV inlet enthalpy, measured in Chapter 3, were used as inputs to the model for three distinct EAIT values.

The values calculated by the model for EAOT are close to those measured in experimental testing. With a counter cross flow heat exchanger the EAOT passes the two-phase zone of the coil last so this parameter is dominated in the model by the wall temperature in the two-phase zone and the air side heat transfer. The wall temperature term depends on the temperature and pressure of the liquid CO_2. Some errors are expected with the liquid saturation temperature due to the assumption of constant pressure along the length of the coil. As discussed in Chapter 3, Section 3.5, Page 33 measuring EAOT that is equivalent to the model is also difficult. With these factors in mind the small error shown between the model and the experimental results for this parameter indicate that the air side heat transfer portion of the model gave good correlation for the open cycle CO_2 system.

The same cannot be said of the correlation between the model and the experimental results for the EROT. Large errors exist with EROT exceeding EAIT, for all three cases, which is not physically possible for a counter cross flow heat exchanger where EAIT flows across EROT. The model takes no account of the relationship between EAIT and EROT instead relying on an assumption that there is a linear relationship between the saturated vapour enthalpy, h_v, and the calculated superheated enthalpy, h_{TP}, to give an outlet enthalpy, h_{out}, and hence calculate an EROT. This assumption that the enthalpy and the temperature vary linearly along the length of the two-phase region is the source of the large error and needs further improvement for the model to be useful.

The length of the two-phase zone, ζ, is under predicted by the model in all three cases with the error growing for lower values of EAIT. The cause of this under prediction in the model is an over estimation of the heat transfer between the refrigerant and the air. As it has already been concluded that the air side heat transfer model gives good correlation the solution for this issue will be to further investigate the refrigerant side heat transfer equations. The increase in error for longer values of ζ would suggest that the error is dominated by the two-phase heat transfer co-efficient.

The model tended to over predict the pressure drop in the evaporator coil with errors of 21%, 24% and 36% for the three tests. The ΔP measurements from the experimental testing appear to be largely independent of the EAIT and length of ζ with some correlation to the mass flow rate of CO_2 as this is related to EEVIP. However the model predictions of ΔP are related to the length of ζ as calculated pressure drop in the two-phase region is significantly more than in the superheated region as discussed in Chapter 2, Section 2.5, Page 18. However the error does not present significant difficulties for the model in its current form as the outlet pressure is controlled by the back pressure regulator model and the inlet pressure is not used as an input to any other part of the model. It would present issue if the inlet pressure was used as an input to an EEV model for calculating the mass flow rate through the evaporator coil. Keeping in mind that larger errors in two-phase pressure drop are not uncommon [57] achieving a model of the two-phase pressure drop that could give an accurate inlet pressure was considered to be outside the scope of this project.

The final variable to be compared in these static results was the cooling capacity of the system. The experimental testing had a relatively high margin of error for this variable due to the test method employed where it was difficult to maintain stable refrigerant pressures as discussed in Chapter 3, Section 3.7, Page 37. Taking this into account the correlation between the model and

the experimental testing is reasonably good. Other factors such as vapour in the liquid line before the EEV and frosting of the coils could account for the remaining error.

Table 4: Static results comparison for Model 1

Test 1		
	Exp Results	**Model 1**
Air Inlet Temperature (EAIT) (°C)	4.4± 1.0	
Average Ref Mass Flow rate (kg s-1)	0.0215± 0.25%	
EEV Inlet Enthalpy (kJ kg-1)	114 ± 3.5	
Two-phase Zone Length (ζ)	0.33± 0.04	0.26
Ref Outlet Temp (EROT) (°C)	0.6 ± 1.0	35.41
Air Outlet Temp (EAOT) (°C)	-13.8 ± 1.0	-9.88
Av. Pressure Drop (ΔP) (kPa)	193 ± 2.5	248
Cooling Capacity (kW)	7.7 ± 0.25	8.52
Test 2		
	Exp Results	**Model 1**
Air Inlet Temperature (EAIT) (°C)	-9.5± 1.0	
Average Ref Mass Flow rate (kg s-1)	0.0216± 0.25%	
EEV Inlet Enthalpy (kJ kg-1)	113± 3.5	
Two-phase Zone Length (ζ)	0.5 ± 0.04	0.36
Ref Outlet Temp (EROT) (°C)	-14.2 ± 1.0	10.78
Air Outlet Temp (EAOT) (°C)	-23.3 ± 1.0	-22.23
Av. Pressure Drop (ΔP) (kPa)	192 ± 2.5	264
Cooling Capacity (kW)	8.1 ± 0.25	8.11
Test 3		
	Exp Results	**Model 1**
Air Inlet Temperature (EAIT) (°C)	-12.96± 1.0	
Average Ref Mass Flow rate (kg s-1)	0.0252± 0.25%	
EEV Inlet Enthalpy (kJ kg-1)	116± 3.5	
Two-phase Zone Length (ζ)	0.79 ± 0.04	0.54
Ref Outlet Temp (EROT) (°C)	-21.99 ± 1.0	-0.85
Air Outlet Temp (EAOT) (°C)	-31.11 ± 1.0	-27.60
Av. Pressure Drop (ΔP) (kPa)	221 ± 2.5	344
Cooling Capacity (kW)	7.9 ± 0.25	9.12

4.4.2 Dynamic Results

An evaluation of how Model 1 performed in a dynamic situation was also performed by comparing the pull-down testing results from Chapter 3, Section 3.9, Page 52 to the model outputs. The results are shown in Figure 61 for EAOT, Figure 62 for EROT, Figure 63 for ECIP and ECOP, and Figure 64 for ζ. The test had a mass flow-rate of CO_2 of 0.0243 kg s^{-1} and an average inlet enthalpy of 116 kJ kg^{-1}. EAIT from Section 3.8 is used as an input to the model.

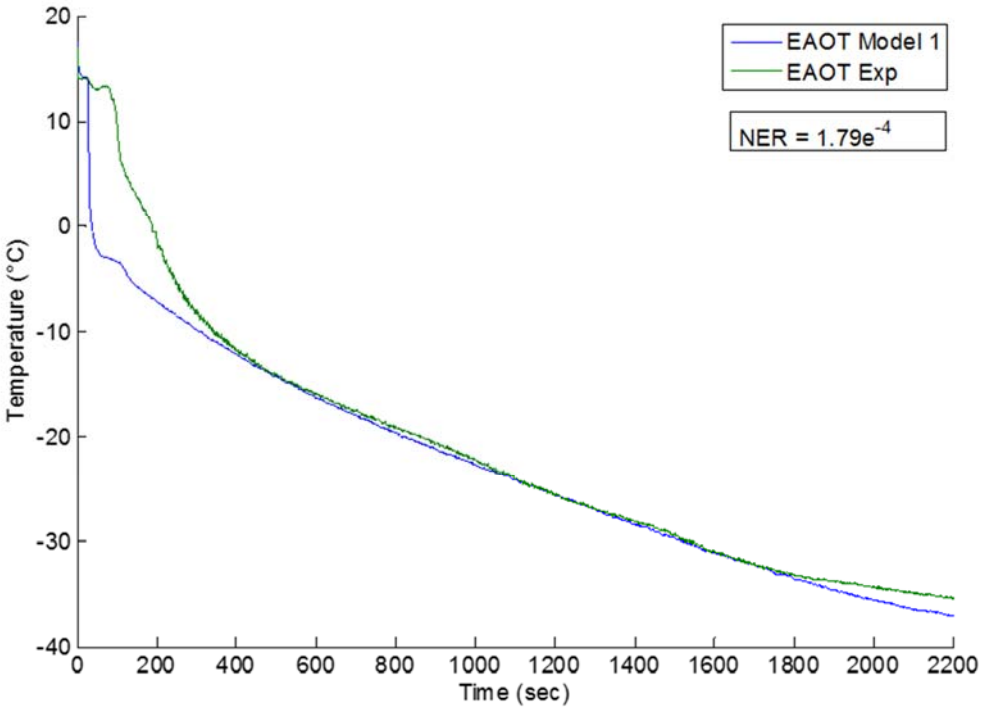

Figure 61: Dynamic Pull-down EAOT Comparison for Model 1 with Experimental Result

A quantitative analysis was performed on the dynamic results using the normalized error residual (NER) discussed in Chapter 2 Section 2.2.2, Page 13. The EAOT and EROT results were calculated in Kelvin to avoid the issue of over inflating error where the mean of the experimental result was close to 0°C. The NER is only useful as a comparison of parameters with the same units and with similar magnitude.

For EAOT there was some initial error as the model reacted quicker to the opening of the EEV than it should. The majority of the delayed response seen in the experimental results can be attributed to the time taken for the liquid to travel the length of the pipe from the CO_2 tank to the EEV and coil inlet. There was also a small deviation from the experimental results towards the end of the pull-down which appears to start at the same time the two-phase zone reaches the outlet of the coil as shown in Figure 62 and Figure 64. The cause of this deviation can be linked to the still increasing volume of two-phase refrigerant in the model compared to the volume in the experimental system that has reached its maximum. The NER for EAOT was small at $1.79e^{-4}$ which agrees with the qualitative observations that the model matches the experimental results well.

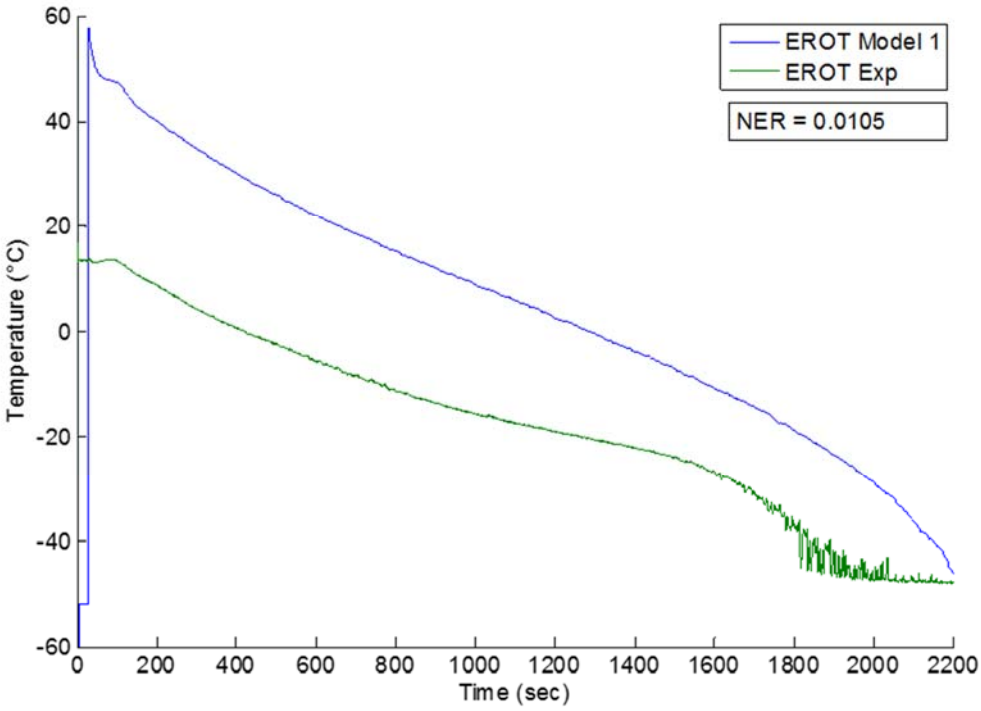

Figure 62: Dynamic Pull-down EROT Comparison for Model 1 with Experimental Results

As noted in the static results in Section 4.4.1, EROT is not well predicted by Model 1. This is also evident in the dynamic pull-down comparison with large errors until the model has two-phase fluid at the outlet of the coil. The NER at 0.0105 is 58 times higher than the value calculated for EAOT with the same model. Significant improvements are needed in this area.

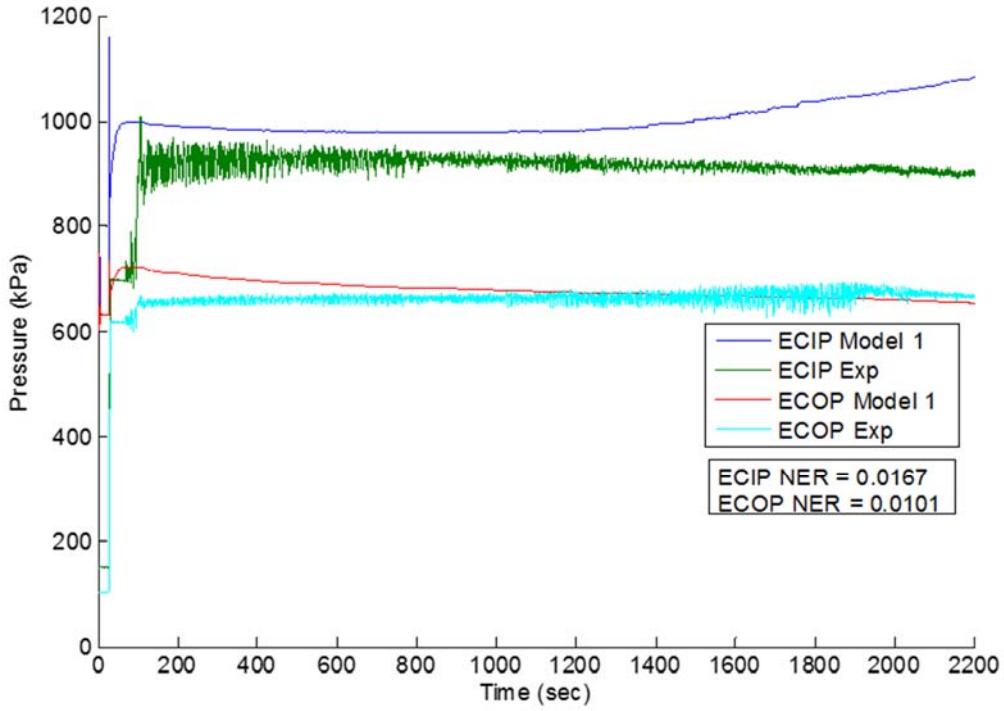

Figure 63: Dynamic Pull-down Pressure Comparison for Model 1 with Experimental Results

The comparison of the coil inlet and outlet pressure in Figure 63 once again shows the model reacting differently than the experimental results. In this case an immediate response to the EEV opening can be seen in the experimental results but the pressures do not reach their steady state values until there is liquid CO_2 present. Once steady state is reached there is generally good agreement between ECOP for the model and the experimental results. The model tends to overestimate ECIP compared to the experimental results and the error increases as the length of the two-phase zone increases. This is consistent with the static results in Section 4.4.1. The high frequency oscillations present in the experimental results are not replicated in the model as there is no attempt to capture the dynamics of the system at this level with the lumped parameter moving boundary model.

The quantitative analysis with NER shows that the model replicates ECOP with a greater level of accuracy than ECIP with ECOP calculated to have 40% less error.

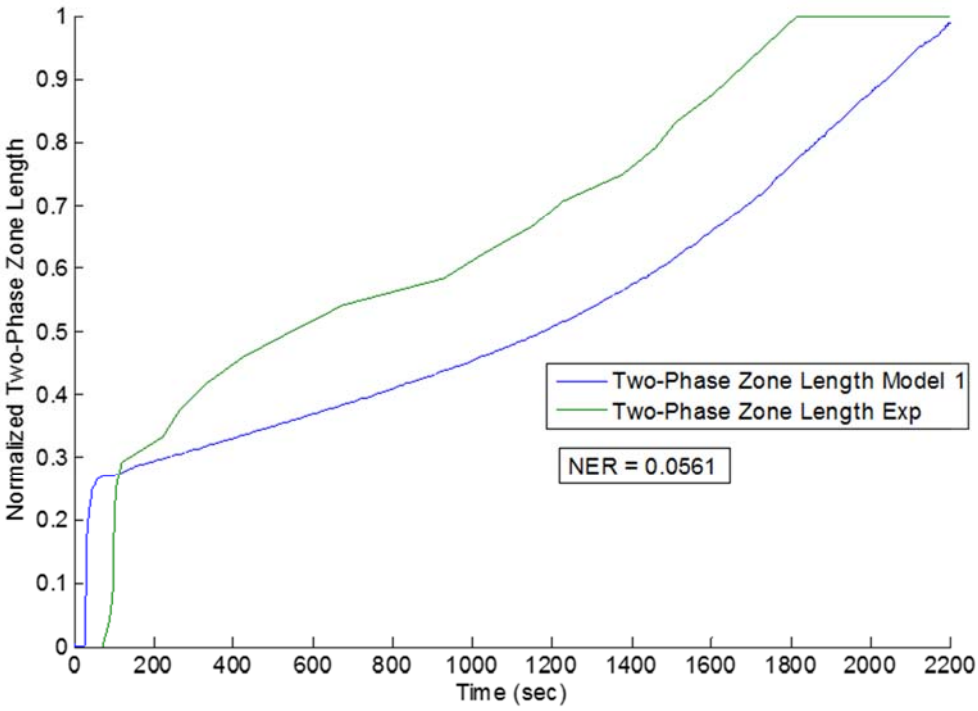

Figure 64: Dynamic Pull-down ζ Comparison for Model 1 with Experimental Results

The shape of the graph for ζ for Model 1 shows good agreement in Figure 64 when compared to the experimental results. This indicates that the good agreement should be possible if the offsets seen in the initial period up to 100 seconds and the error in the time needed for the two-phase boundary to reach the end of the coil can be eliminated. The NER of 0.0561 is already low but will be used as a baseline in the next sections to demonstrate the improvements in accuracy of the model.

4.5 New Calculation of Refrigerant Outlet Temperature

As outlined in Section 4.4 the correlation of Model 1 with experimental results for EROT is poor. One of the major differences between previously modelled standard vapour compression systems and the open cycle CO_2 system was the significance of the superheated region within the evaporator coil. In vapour compression systems, the majority of heat transfer in an evaporator occurs in the two-phase region and control algorithms attempt to minimize the length of the superheated region without making it go to zero completely. For this reason the

modelling of the superheated zone has often been simplified to a model that assumes the temperature and enthalpy vary linearly across this region [28,52,59]. With the open cycle CO_2 system there can often be superheated regions that are 50-60% of the length of the coil. In this case a linear assumption can lead to an error in the heat transfer to the superheated refrigerant from the air and a significant error for the outlet temperature of the refrigerant leaving the superheated zone.

The error in the heat transfer for the superheated zone is not too problematic as the heat transfer in the two-phase zone dominates but the error in the refrigerant outlet temperature is an issue as this is used in the system, along with the outlet pressure, as a control variable for the EEV.

To rectify this, a new model was developed based on the ε-NTU method [61] that describes the heat transfer rate between a hot fluid and a cold fluid for steady state conditions,

$$q = \varepsilon C_{\min}\left(T_{h,i} - T_{c,i}\right) \tag{4. 41}$$

where ε is the effectiveness of the heat exchanger, $C_{\min}$ is the lower heat capacity rate of either the hotter or the colder fluid, $T_{h,i}$ is the hot fluid inlet temperature and $T_{c,i}$ is the cold fluid inlet temperature.

This type of ε-NTU method has been used previously by McKinley [52] and Li [29] to calculate the air outlet temperature in a moving boundary model considering the heat transfer between the tube wall and the air. In this case the heat transfer between the refrigerant and the tube wall is considered and therefore the following assumptions are made. $T_{c,i}$ can be substituted by the refrigerant outlet temperature of the two-phase region which is the fluid saturation temperature T_{sat}. The moving boundary technique calculates lumped parameters and therefore the average wall temperature in the superheated region T_{wall_SH} is used in place of $T_{h,i}$. The heat capacity rate of the refrigerant, C_{ref} is much less than that of the wall. These assumptions give

$$q = \varepsilon C_{\text{ref}}\left(T_{wall\_SH} - T_{sat}\right) \tag{4. 42}$$

Since

$$q = C_{ref}(T_{ref,o} - T_{ref,i}) \tag{4. 43}$$

one obtains

$$T_{ref,o} = T_{wall\_SH} + \varepsilon\left(T_{wall\_SH} - T_{sat}\right) \tag{4. 44}$$

The effectiveness in our model can be assumed to be the same as that used for an evaporator as the thermal capacitance of the wall is extremely large compared with the refrigerant and thus the wall temperature can be assumed to be constant during the time step for the calculation. Therefore

$$\varepsilon = (1 - e^{-NTU}) \tag{4. 45}$$

and

$$NTU = \frac{U_v A}{C_{ref}} \tag{4. 46}$$

where U_v is the heat transfer coefficient and A is the heat transfer area.

Section 4.6 below details the improvements seen with Model 2 which includes this ε-NTU method for calculating the refrigerant outlet temperature.

4.6 Results comparison for Model 2

4.6.1 Static Results

A comparison was made with the experimental results and the new Model 2 with the updated calculation for EROT. The results are shown in Table 5 and all three cases show a significant improvement in the correlation of EROT with Test 1 being within the measurement error. The largest error is in Test 3 where the error in ζ is most significant as the boundary is closer to the coil outlet. There is also an improvement in the correlation for the cooling capacity as the more

realistic change in temperature in the superheated zone gives a lower value for that zones cooling capacity. None of the other variables are significantly affected by the change.

Table 5: Static Results for new EROT Equation

Test 1		
	Exp Results	**Model 2**
Air Inlet Temperature (EAIT) (°C)	4.4± 1.0	
Average Ref Mass Flow rate (kg s-1)	0.0215± 0.25%	
EEV Inlet Enthalpy (kJ kg-1)	114 ± 3.5	
Two-phase Zone Length (ζ)	0.33± 0.04	0.27
Ref Outlet Temp (EROT) (°C)	0.6 ± 1.0	-0.16
Air Outlet Temp (EAOT) (°C)	-13.8 ± 1.0	-9.86
Av. Pressure Drop (ΔP) (kPa)	193 ± 2.5	243
Cooling Capacity (kW)	7.7 ± 0.25	7.79
Test 2		
	Exp Results	**Model 2**
Air Inlet Temperature (EAIT) (°C)	-9.5± 1.0	
Average Ref Mass Flow rate (kg s-1)	0.0216± 0.25%	
EEV Inlet Enthalpy (kJ kg-1)	113± 3.5	
Two-phase Zone Length (ζ)	0.5 ± 0.04	0.39
Ref Outlet Temp (EROT) (°C)	-14.2 ± 1.0	-13.05
Air Outlet Temp (EAOT) (°C)	-23.3 ± 1.0	-22.58
Av. Pressure Drop (ΔP) (kPa)	192 ± 2.5	253
Cooling Capacity (kW)	8.1 ± 0.25	7.60
Test 3		
	Exp Results	**Model 2**
Air Inlet Temperature (EAIT) (°C)	-12.96± 1.0	
Average Ref Mass Flow rate (kg s-1)	0.0252± 0.25%	
EEV Inlet Enthalpy (kJ kg-1)	116± 3.5	
Two-phase Zone Length (ζ)	0.79 ± 0.04	0.57
Ref Outlet Temp (EROT) (°C)	-21.99 ± 1.0	-17.15
Air Outlet Temp (EAOT) (°C)	-31.11 ± 1.0	-27.53
Av. Pressure Drop (ΔP) (kPa)	221 ± 2.5	344
Cooling Capacity (kW)	7.9 ± 0.25	8.69

4.6.2 Dynamic Results

The dynamic pull-down results also show a large improvement in the correlation of the EROT model output with the experimental results, Figure 65. The NER is 11 times smaller than that which was present for Model 1 at $9.35e^{-4}$. Qualitatively it can be seen that error remains during the initial pull-down until 600 seconds due to the response time of the model. After 600 seconds the model over-estimates EROT due to the length of the two-phase zone being under-estimated as seen in Figure 64 for Model 1. The issue with the length of ζ will be addressed in Section 4.7 and should have a positive effect on the remaining error shown here for EROT.

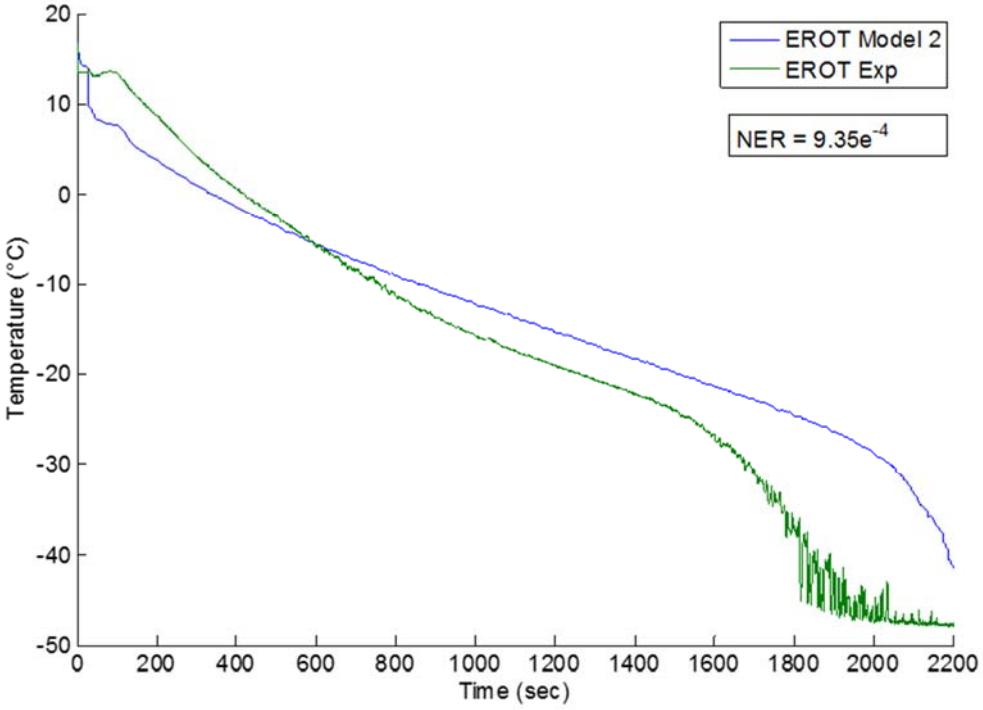

Figure 65: Dynamic Pull-down EROT Comparison for Model 2 with Experimental Results

The improvement in EROT also had an effect on the ECIP and ECOP correlation in the dynamic results, see Figure 66. The lower temperatures resulted in lower pressures in the early part of the pull-down which improved the correlation with the experimental results. NER for ECIP reduced by 14% to 0.0147 and NER for ECOP reduced by 16% to 0.0087.

There are no significant changes for EAOT or ζ as a result of the new EROT calculation so no results for those parameters are displayed for Model 2.

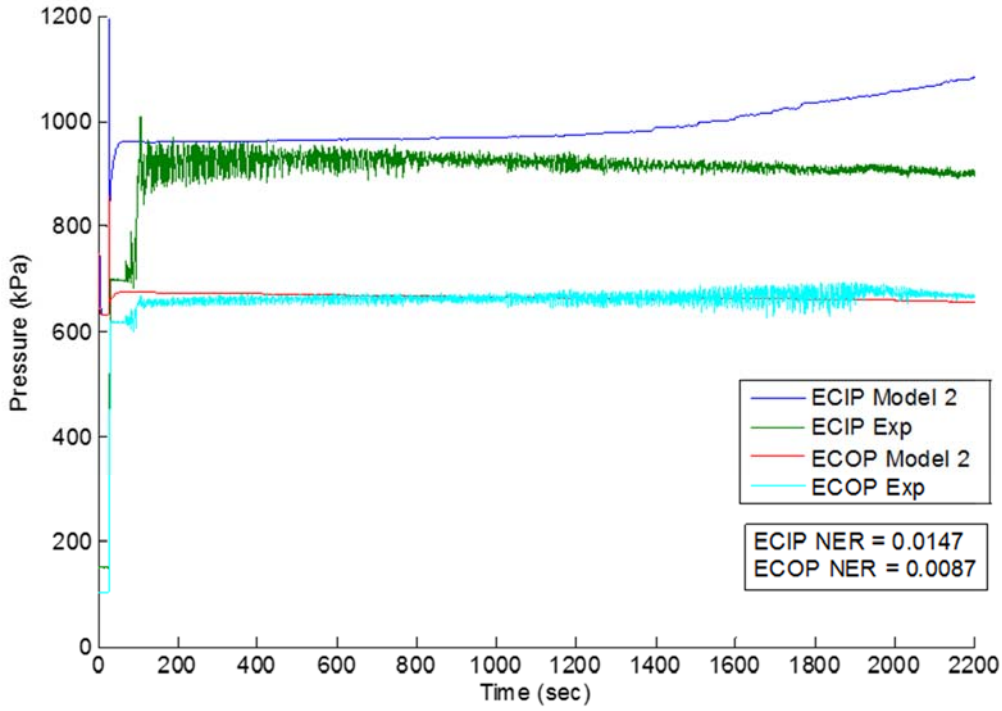

Figure 66: Dynamic Pull-down Pressure Comparison for Model 2 with Experimental Results

4.7 Performance Adjustment Factor

One of the parameters that did not change significantly with the new EROT calculation was the two-phase zone length ζ. This parameter is primarily affected by the two-phase and air side heat transfer rates. Since the air side heat transfer is also involved in the calculation for the air outlet temperature, and that parameter has showing reasonable accuracy, it was decided to focus on the two-phase heat transfer to resolve the error in ζ.

Although the heat transfer calculations from Cheng et al. [47] outlined in Section 4.1.9, Page 85 were more accurate for CO_2 than those previously employed in the Thermosys toolbox they were not an exact correlation and were developed for systems where the saturation temperatures were between -28°C and 25°C and the reduced pressure was only down as far as 0.21 for a small portion of their data. The saturation temperatures in the open cycle CO_2 system are between -53°C and -45°C with reduced pressures of between 0.08 and 0.11. As outlined in Chapter 2, Section 2.4, Page 18 reduced pressures have been shown to have a significant effect on the heat transfer coefficient of a refrigerant. This, along with simple modelling of frosting of the coils could explain the error in ζ.

To correct this error a performance adjustment factor (PAF), used extensively in industry for making models match real life applications [31,81], was utilized as a multiplier to the two-phase heat transfer coefficient. A sensitivity analysis was carried out with values ranging from 0.15 to 0.35 to determine the best value to use. A value of 0.2 was selected as it brought the error of ζ to zero for Test 3 where it was longest and had the most influence of other parameters such as EROT but also maintained reasonable accuracy for the length of ζ and EROT in the other tests. Section 4.8 below details the results of Model 3 with the PAF included.

4.8 Results comparison for Model 3

4.8.1 Static Results

The addition of the PAF of 0.2 for Model 3 brought the ζ value within measurement error range for both Test 1 and Test 3 with Test 2 only being marginally outside with an error of 0.06. For Test 1 and 2 the effect on the other variables was insignificant. For Test 3 having ζ at the correct value also increased the accuracy of EROT but it had a detrimental effect on the pressure drop due to the issues with the two-phase zone pressure drop calculations discussed in Section 4.4.1.

Table 6: Static Test Results using a PAF on the Two-Phase Heat Transfer Coefficient

Test 1						
	Exp Results	**Model 3**				
EAIT (°C)	4.4± 1.0					
$\dot{m}$ (kg s^{-1})	0.0215± 0.25%					
Inlet Enthalpy (kJ kg^{-1})	114 ± 3.5					
PAF	N/A	0.15	0.20	0.25	0.3	0.35
ζ	0.33± 0.04	0.43	0.38	0.36	0.34	0.32
EROT (°C)	0.6 ± 1.0	-0.81	-0.59	-0.47	-0.39	-0.34
EAOT (°C)	-13.8 ± 1.0	-9.77	-9.80	-9.82	-9.83	-9.83
Pressure Drop (kPa)	170-216 ± 2.5	248	247	246	246	245
Cooling Capacity (kW)	7.7 ± 0.25	7.78	7.78	7.78	7.78	7.78
Test 2						
	Exp Results	**Model 3**				
EAIT (°C)	-9.5± 1.0					
$\dot{m}$ (kg s^{-1})	0.0216± 0.25%					
Inlet Enthalpy (kJ kg^{-1})	113± 3.5					
PAF	N/A	0.15	0.20	0.25	0.3	0.35
ζ	0.5 ± 0.04	0.63	0.56	0.52	0.49	0.47
EROT (°C)	-14.2 ± 1.0	-14.16	-13.74	-13.53	-13.41	-13.33
EAOT (°C)	-23.3 ± 1.0	-22.41	-22.48	-22.51	-22.53	-22.54
Pressure Drop (kPa)	169-214 ± 2.5	278	264	260	258	258
Cooling Capacity (kW)	8.1 ± 0.25	7.58	7.58	7.59	7.59	7.59
Test 3						
	Exp Results	**Model 3**				
EAIT (°C)	-12.96± 1.0					
$\dot{m}$ (kg s^{-1})	0.0252± 0.25%					
Inlet Enthalpy (kJ kg^{-1})	116± 3.5					
PAF	N/A	0.15	0.20	0.25	0.3	0.35
ζ	0.79 ± 0.04	0.87	0.79	0.74	0.70	0.68
EROT (°C)	-21.99 ± 1.0	-22.01	-19.25	-18.47	-18.07	-17.83
EAOT (°C)	-31.11 ± 1.0	-26.90	-27.18	-27.29	-27.36	-27.41
Pressure Drop (kPa)	198-244 ± 2.5	414	398	391	379	368
Cooling Capacity (kW)	7.9 ± 0.25	8.58	8.65	8.66	8.67	8.68

4.8.2 Dynamic Results

For the dynamic results the PAF of 0.2 on the two-phase heat transfer coefficient was also used. The addition had a beneficial effect on the model correlation with all the measured parameters. Figure 67 shows that EAOT for Model 3 matches closely to the experimental results now from 1800 seconds to 2200 seconds where previously there was an error. This was due to the error in the length of ζ which has now been addressed by the PAF. This improvement results in a 3% improvement in NER to 1.73e^{-4}.

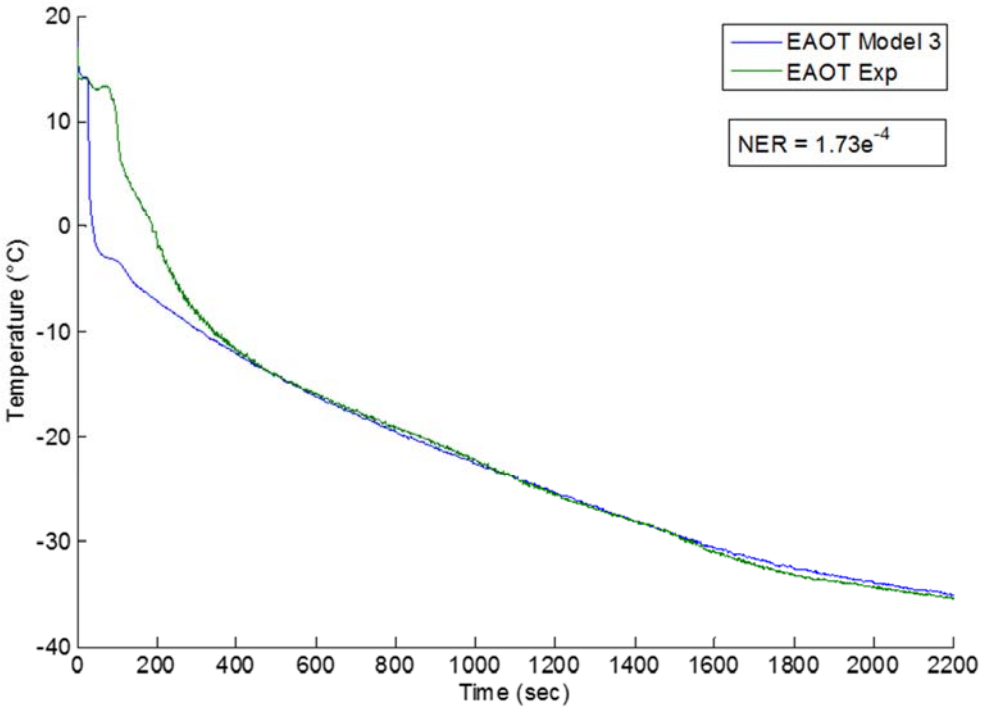

Figure 67: Dynamic Pull-down EAOT Comparison for Model 3 with Experimental Results

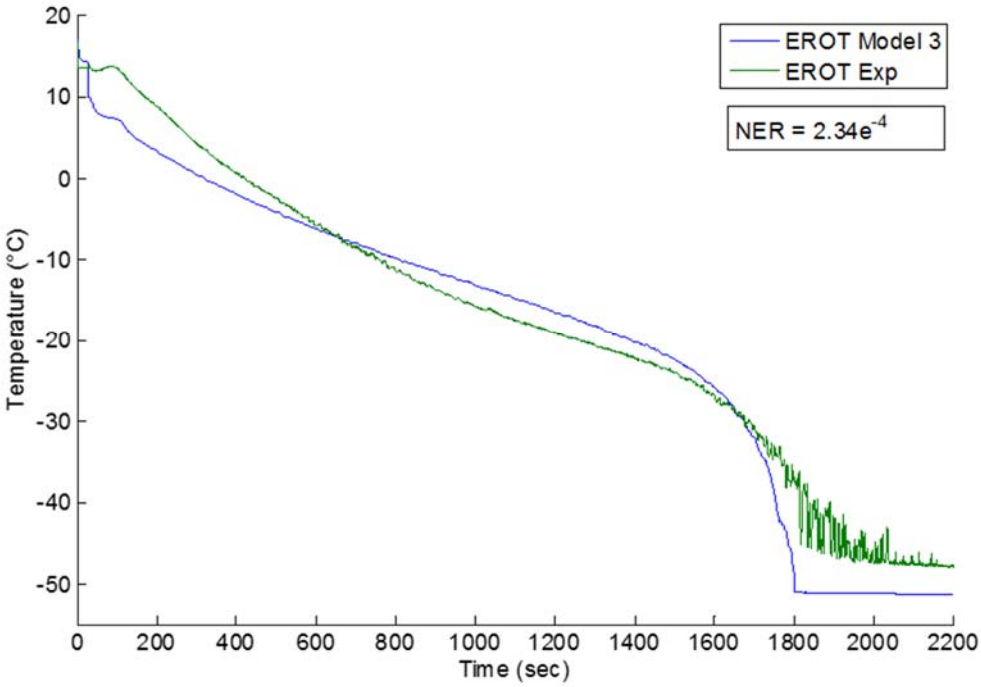

Figure 68: Dynamic Pull-down EROT Comparison for Model 3 with Experimental Results

The correlation for EROT, Figure 68, also shows an improvement from 1800 s onwards as the two-phase boundary if now at the correct distance from the coil outlet leading to greater accuracy in the calculation of EROT. As discussed above in Section 4.4.1 the fast dynamics of the system are not captured by the model so the oscillations for EROT seen in the experimental results are not present but the model goes to the saturation temperature at the same time the two-phase region reaches the outlet of the coil. There is an offset between the saturation temperature seen for the model and the experimental results as the copper at the coil outlet needs time to soak at the saturation temperature and the measurement of the outside of the copper tube will always be slightly warmer than the actual fluid temperature. The NER for EROT is four times lower than for Model 2 at $2.34e^{-4}$.

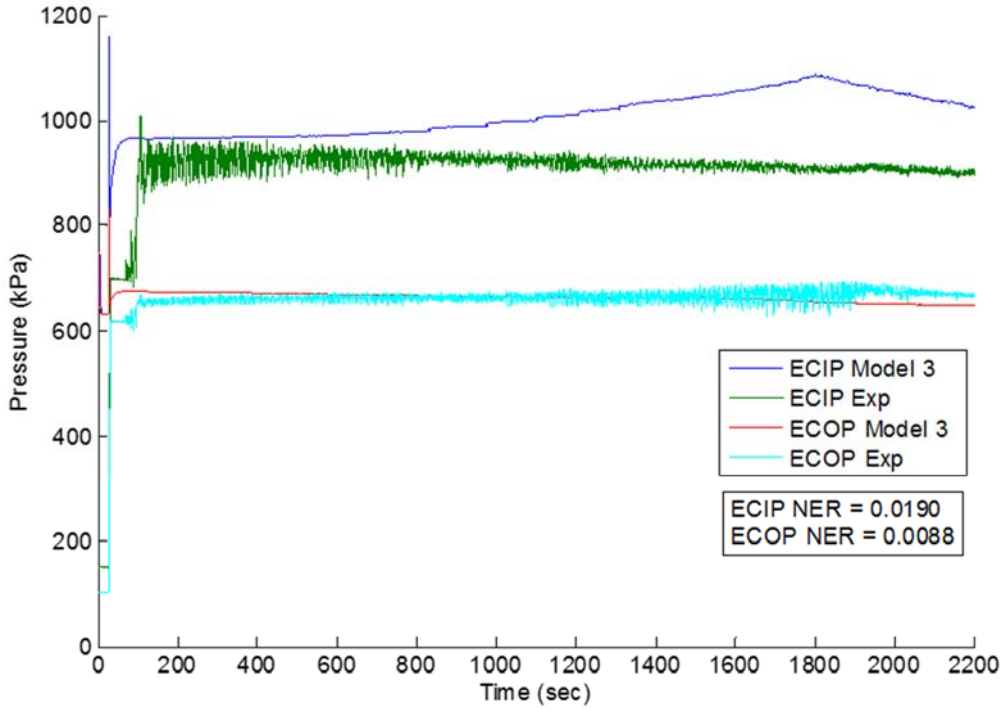

Figure 69: Dynamic Pull-down Pressure Comparison for Model 3 with Experimental Results

ECIP and ECOP for Model 3 in Figure 69 are very similar to the previous model until the two-phase boundary reaches the outlet of the coil at 1800s. At this point ECOP starts to decrease. Although this does bring it back towards the results seen in the experimental testing the shape of the curve is significantly different to the experimental results which show no significant change at this time. The change in ECIP in the model is due to the shift to a single zone two-

phase only representation and the subsequent new calculation of the outlet quality, as opposed to the assumption that the quality is equal to 1 due to the presence of the superheated zone. This in turn affects the values of the void fraction γ and the average pressure calculated for the two-phase zone. These changes result in an increase of ECIP NER of 23% to 0.0190 and a marginal increase in NER for ECOP to 0.0088.

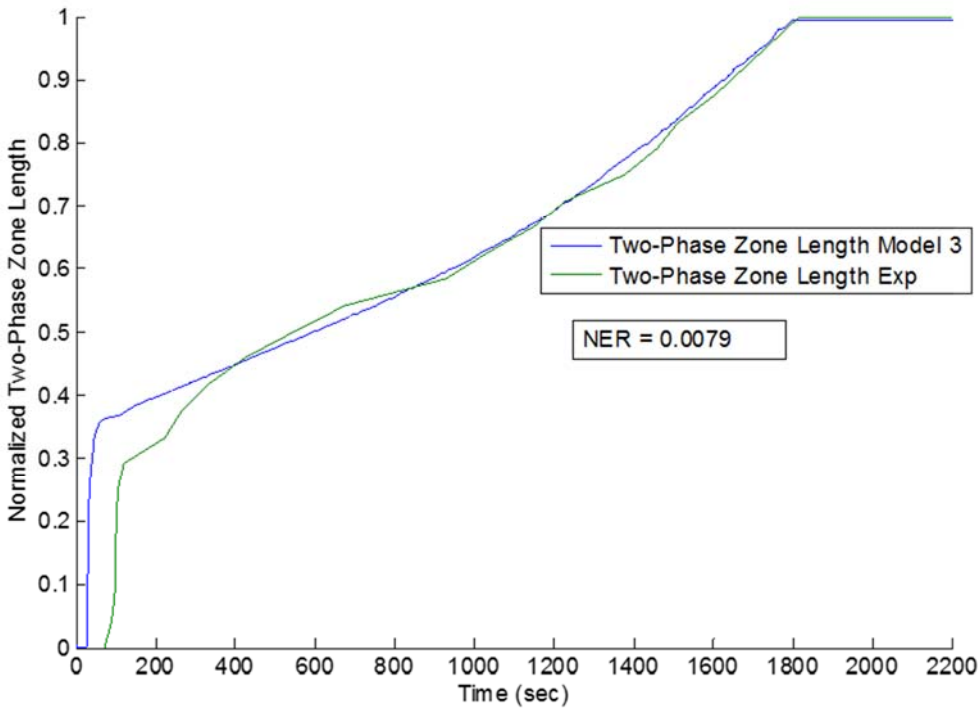

Figure 70: Dynamic Pull-down ζ Comparison for Model 3 with Experimental Results

Figure 70 shows improved results for ζ where the addition of the PAF to Model 3 has the expected effect of correcting the offset seen in ζ in Figure 64 from 400s onwards. Figure 70 shows that after the initial period, where the transport properties of the fluid have a significant effect, the error between the model and experimental test results becomes negligible. NER for the two-phase zone length reduces by factor of 7 compared to Model 1 to 0.0079.

4.9 Transport Delays

The last significant source of error in the model is the initial response to the EEV opening to take account of the time needed for the liquid CO_2 to travel the length of the pipe to the EEV and coil inlet. This delay was calculated to be an average of 40 s for the seven dynamic tests outlined in Chapter 3, Sections 3.8-3.10. Since the time taken is a function of the CO_2 tank pressure, which was not included in the model, it was decided to add this parameter to the model by delaying the opening of the EEV until liquid had reached the valve as indicated by the increase in ECIP for each test. The comparison to experimental result for Model 4, which adds this delay to Model 3, is detailed below in Section 4.10.

4.10 Results for Model 4

4.10.1 Dynamic Results

No static results are presented for Model 4 as the transport delay only affects the dynamics of the system. With the introduction of the delayed EEV opening the comparison of the EAOT output for the model to the experimental results in Figure 71 show a closer correlation in the initial 400 s. The model now reacts at roughly the same time as the experimental test results to the liquid at the EEV but the response it still quicker than it should be. This can be explained by two effects, first the momentum is not taken into account in the model. Secondly the lumped parameter nature of the moving boundary model allows for the outlet properties of the model to react instantly to the model inputs whereas in reality time is needed for the liquid CO_2 to travel along the length of the coil. The remaining NER for EAOT is cut by an additional factor of 1.8 to $9.5e^{-5}$.

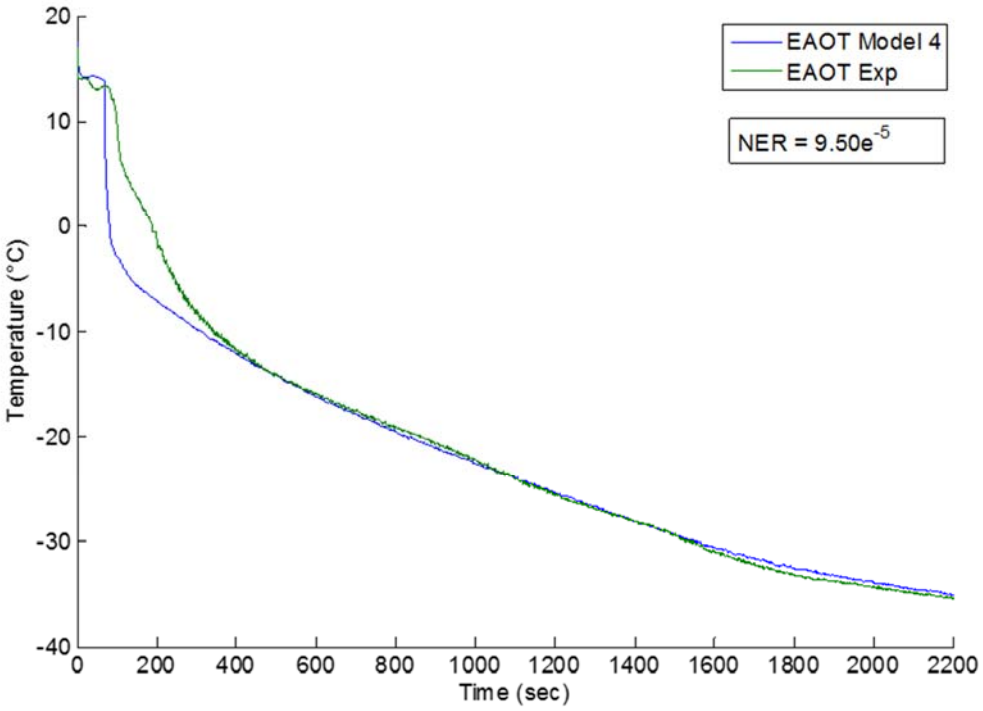

Figure 71: Dynamic Pull-down EAOT Comparison for Model 4 with Experimental Results

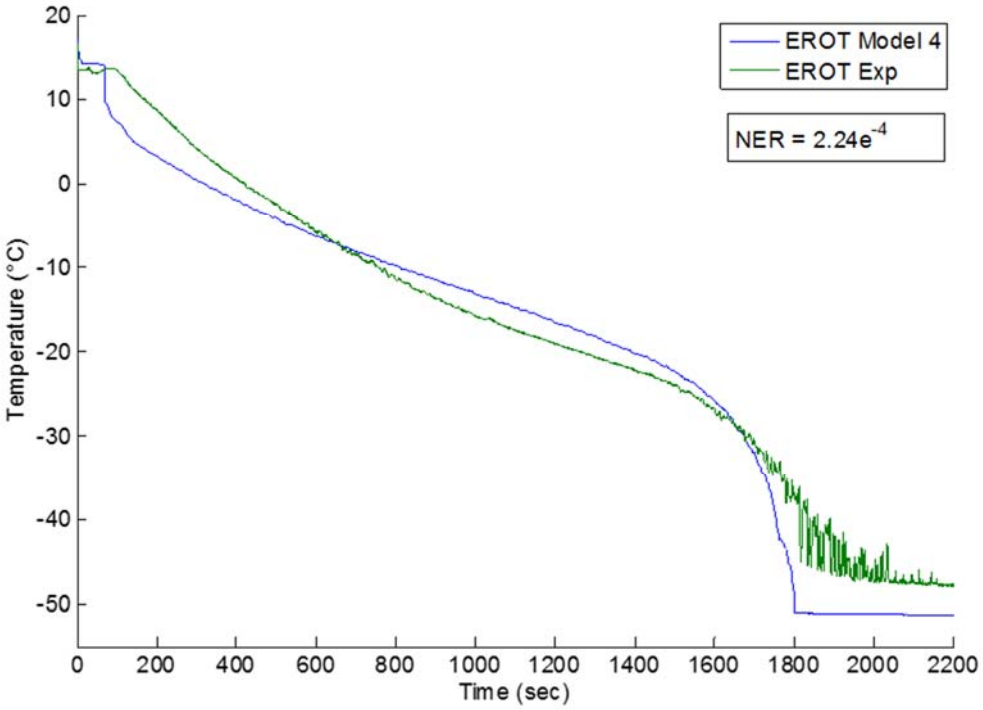

Figure 72: Dynamic Pull-down EROT Comparison for Model 4 with Experimental Results

This faster response is also evident in the model for EROT in Figure 72 where an NER reduction of 4% to 2.24e^{-4} is seen and in Figure 73 where ECIP and ECOP also show improvements in NER of 10% and 1% respectively to 0.0172 and 0.0086.

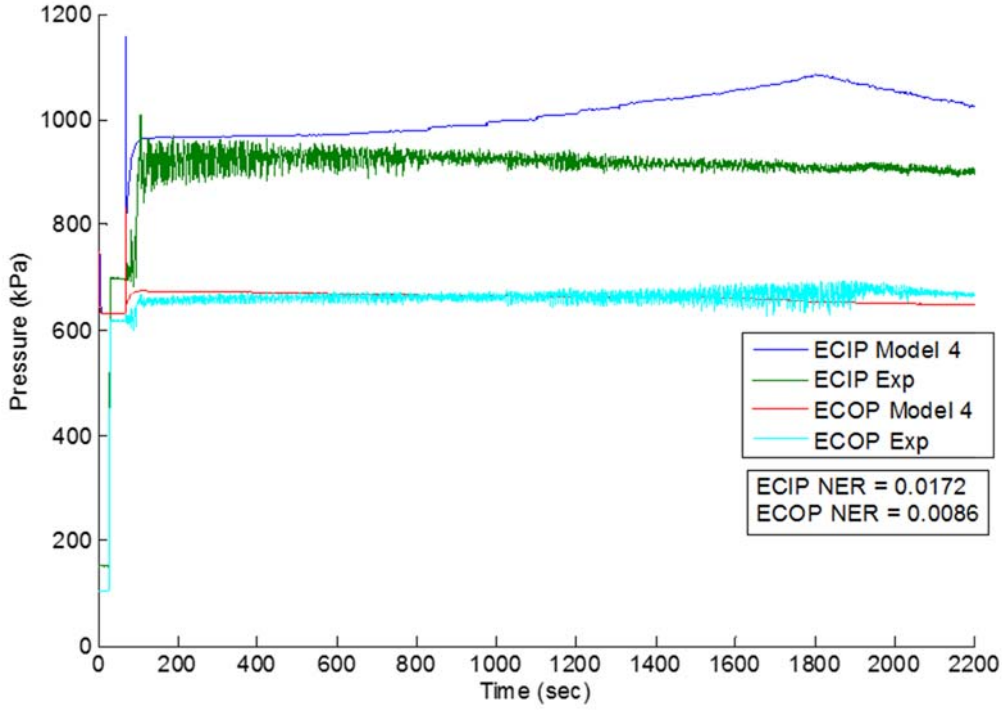

Figure 73: Dynamic Pull-down Pressure Comparison for Model 4 with Experimental Results

In the case of ζ in Figure 74 the faster response has a substantial impact on the NER, reducing it by an additional factor of 2.7 to 0.0029. The remaining error can be attributed to the same lack of momentum in the model that causes the error in EAOT.

In the case of ζ in Figure 74 the faster response has a substantial impact on the NER, reducing it by an additional factor of 2.7 to 0.0029. The remaining error can be attributed to the same lack of momentum in the model that causes the error in EAOT.

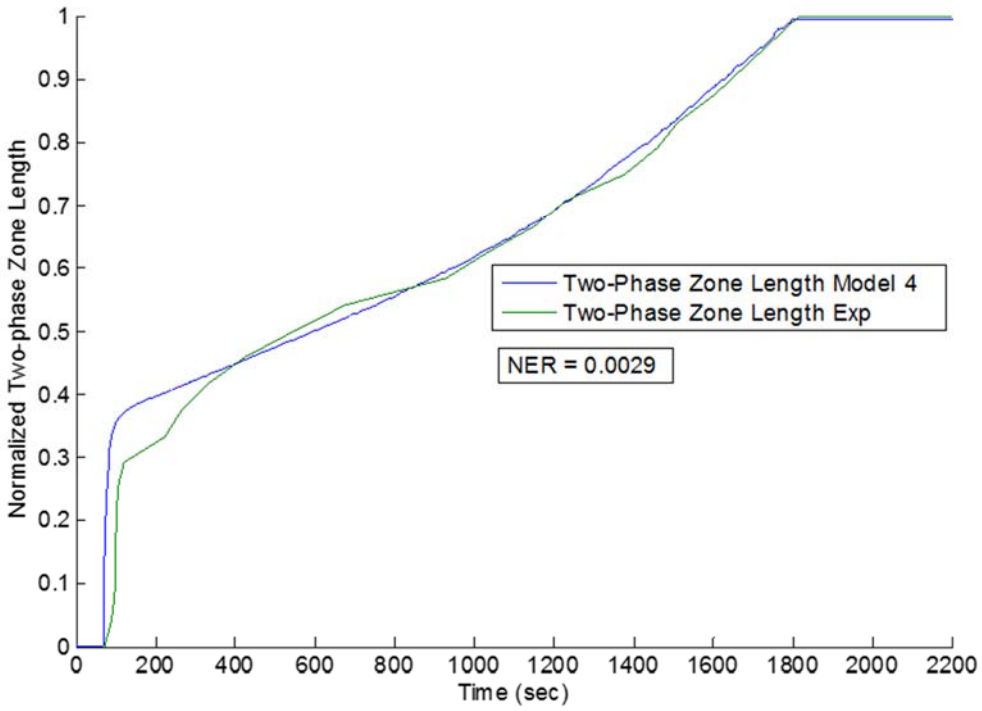

Figure 74: Dynamic Pull-down ζ Comparison for Model 4 with Experimental Results

4.11 Summary

In this chapter the modelling techniques identified in Chapter 2 for vapour compression systems were utilized to model an open cycle CO_2 system. A switched moving boundary model was used as the base model for the evaporator. Additions such as the back pressure regulator model, the evaporator fan model and the introduction of pressure drop within the evaporator coil as well as changes to the refrigerant properties and the two-phase heat transfer coefficients were necessary to get the model to work correctly for the open-cycle CO_2 system.

Once a comparison was made to experimental results further changes were made to improve the correlation of the main model outputs; EAOT, EROT, ECIP, ECOP and ζ. A change to how the refrigerant outlet temperature was calculated led to a large reduction in the normalized error residual for EROT and some smaller improvements to ECIP and ECOP. The addition of a PAF to the two-phase heat transfer coefficient resulted in large improvements in the correlation for the length of ζ, further improvements to EROT and small improvements to EAOT. The final Model 4 utilized a delay in the EEV opening to simulate the time taken for CO_2 to reach the EEV and the evaporator coil inlet. This change led to additional improvements in all the variables.

The final model produced showed good agreement to both the static and dynamic pull-down experimental results with only small errors still present due to the lack of momentum considerations leading to a quicker model response and the lumped parameter nature of the model being unable to replicate the fast dynamics of the EROT, ECIP and ECOP outputs.

With this model it is now possible to examine the dynamic response for the system for the continuous and cycle-sentry modes that customers use at both fresh and frozen set-points. Comparisons of the Model 4 to the experimental results will be presented in the next Chapter.

Chapter 5 Dynamic Model Validation & Optimization

This chapter examines how well the model developed in Chapter 4 correlates to real world customer usage of the open cycle CO_2 transport refrigeration system. It compares model outputs to experimental results from Chapter 3 for both continuous and cycle-sentry control and looks at how well the model correlates once the EEV starts pulsing for both superheat and temperature control. It also looks at how well the model deals with the EEV closing for extended periods of time with and without evaporator fan airflow. The chapter is broken up into sections of continuous control and cycle-sentry control with discussions on the EEV pulsing and EEV Null periods for each type of control.

5.1 Continuous Control

5.1.1 Fresh Set-point of 0°C

Figure 75 shows the EROT comparison for the pull-down to set-point and temperature control for continuous control at a fresh set-point of 0°C. The unit pulls down until the unit EAIT sensor reaches the 0°C set-point at 503 s as detailed in Chapter 3, Section 3.10.1, Page 56. The response during this pull-down section is similar to that seen in Section 4.10.1.

Once the EEV closes at 503 s the model output drop sharply before recovering. This is caused by the pressure drop which also decreases the liquid saturation temperature used in the calculation of EROT. The model response is too quick to propagate this temperature change to the coil outlet causing the error. The experimental results display no sharp drop in temperature at the coil outlet but such drops can be seen closer to the coil inlet where the drop in pressure is more immediate.

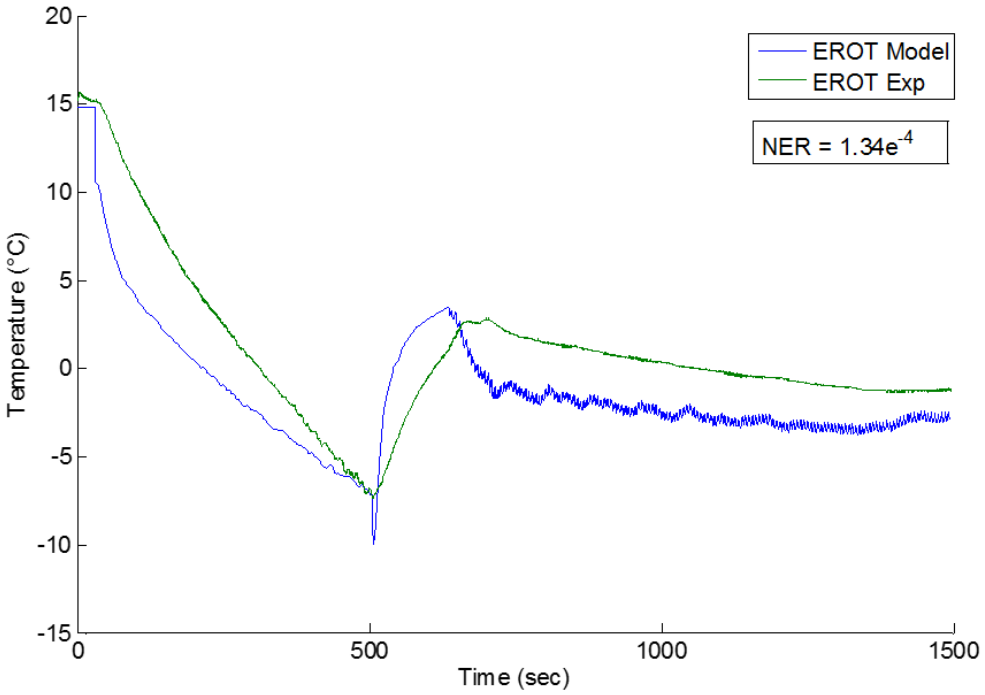

Figure 75: EROT Comparison for Fresh Continuous Control at 0°C Set-point. Mass flow rate of CO_2 for 100% EEV Duty Cycle: 0.0248 kg s^{-1}

During the period of time when the EEV is closed from 503 s to 630 s and after the EEV opens again the model again reacts too quickly for the same reasons that have been discussed in Section 4.10.1. Once the valve starts to pulse the model displays small amplitude oscillations in the EROT output which correspond to the EEV pulsing. These are no evidence of these pulsations in the experimental results with the two-phase boundary so far away from the coil exit but similar pulsations can be seen for the frozen tests in later sections where the two-phase boundary is closer to the coil exit.

During the period of time where the EEV is pulsing for temperature control there is an offset between the model output and the experimental results for EROT. This is seen to gradually reduce and it is likely that it would reduce to the levels seen in the static testing if sufficient time was allowed for the unit to soak at the set-point temperature.

Although the error in Figure 75 appears larger than the error in EROT for the dynamic pull-down for Model 4 in Chapter 4, Section 4.10.1, Page 106 the NER value is lower by 68%. This apparent inconsistency is due to the different temperature scale used in the two graphs and shows the value of employing a quantitative analysis when comparing results.

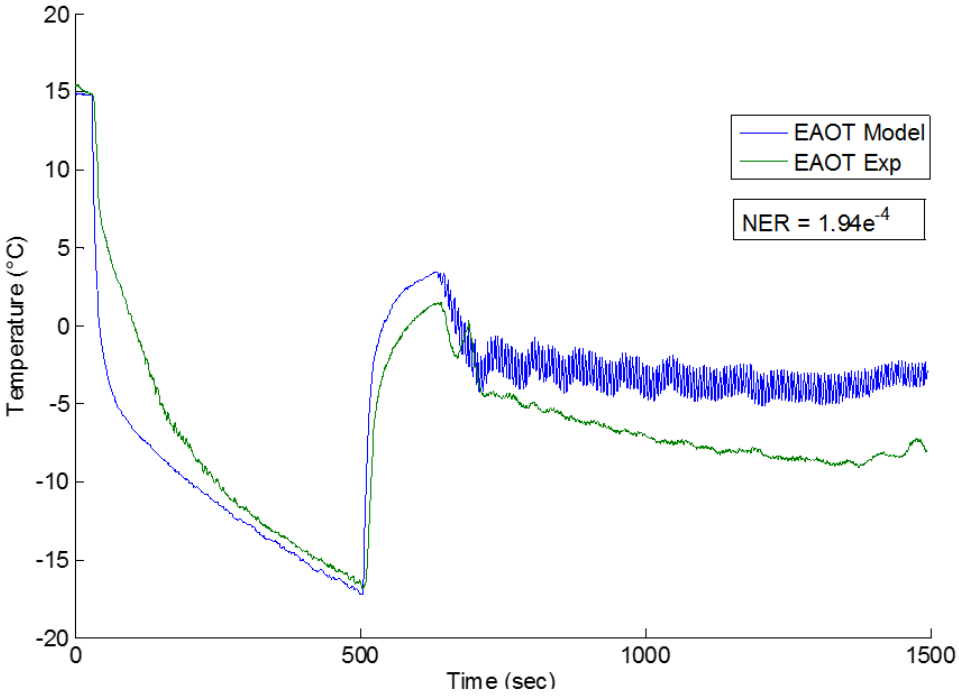

Figure 76: EAOT Comparison for Fresh Continuous Control at 0°C Set-point. Mass flow rate of CO_2 for 100% EEV Duty Cycle: 0.0248 kg s^{-1}

The results for EAOT shown in Figure 76 are similar to those for EROT in the quicker response for the pull-down, EEV closing and EEV opening. There is no sharp drop in temperature for the EEV closing for EAOT as the temperature change is buffered by the thermal mass of the copper tubing. Once again there is high frequency fluctuations for the EEV pulsing section, this time of a slightly larger amplitude. The reason for this is that ζ is very close to the coil inlet during this period and, with the cross-flow heat exchanger, EAOT passes the inlet of the coil. The effect is compounded by the large amplitude of the ζ fluctuations displayed in Figure 78 caused by the quicker model response.

There is also an offset evident in Figure 76 for EAOT during the EEV pulsing section and it this case it appears to have stabilised at the end of the test at roughly 4°C which is similar in magnitude to the error seen in the static test results in Chapter 4, Section 4.8.1, Page 101.

The NER in this case is larger than the EAOT results from Chapter 4, Section 4.10.1, Page 106 due to the offset between the model and the experimental results during temperature control.

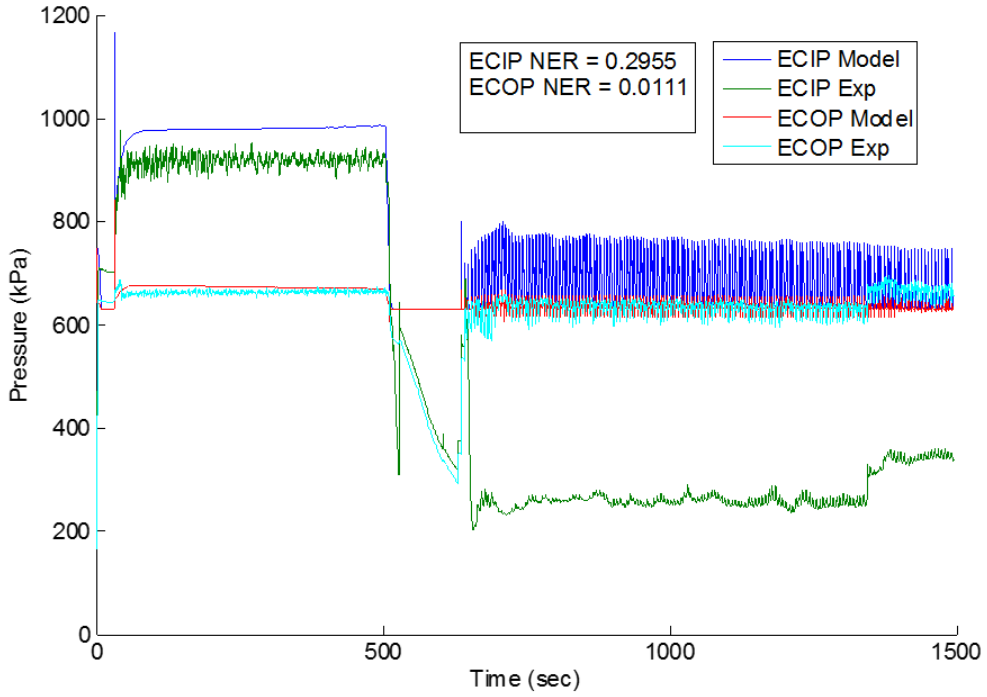

Figure 77: Inlet and Outlet Pressure Comparison for Fresh Continuous Control at 0°C Set-point. Mass flow rate of CO_2 for 100% EEV Duty Cycle: 0.0248 kg s^{-1}

For ECIP and ECOP Figure 77 shows similar behaviour for the pull-down time period to the pull-down tests in Chapter 4. When the EEV shuts both pressures in the model drop until they reach the BPR set pressure and stop decreasing there. In reality the BPR does not seal fully so the pressure seen in the experimental results gradually falls after the EEV and BPR valves close. Adding this behaviour to the model would cause issues once the EEV opened again as the pressure would be below the triple point of CO_2 and the fluid property routines are unable to calculate properties in this region as the CO_2 can be in the solid phase.

Once the EEV opens again ECOP stays at the BPR set-point and displays high frequency oscillations matching the EEV pulsing. In this case these oscillations are also visible in the experimental results as the pressure response is much quicker than the temperature response. ECIP also increases to a value of approximately 100 kPa above the BPR setting but displays fluctuations of +/- 100 kPa. It is difficult to know how accurate these values are due to the difficulty in measuring ECIP for these conditions as described in Chapter 3, Section 3.10, Page 55. However it is reasonable to presume that the dry ice discussed as a possible cause of the measurement difficulties might be formed under the conditions shown in the model where the

pressure is fluctuating close to or below the triple point. It is also reasonable to assume the amplitude of the fluctuations seen would be much large than those seen at the outlet of the coil.

NER for ECOP is comparable with the results seen in Chapter 4, Section 4.10.1, Page 106 but it is effected by the Null period where the model fails to follow the experiment below the BPR setting. The NER for ECIP is an order of magnitude higher than what is seen in the dynamic pull-down results due to the measurement error in ECIP. As a result it is not useful as a comparison.

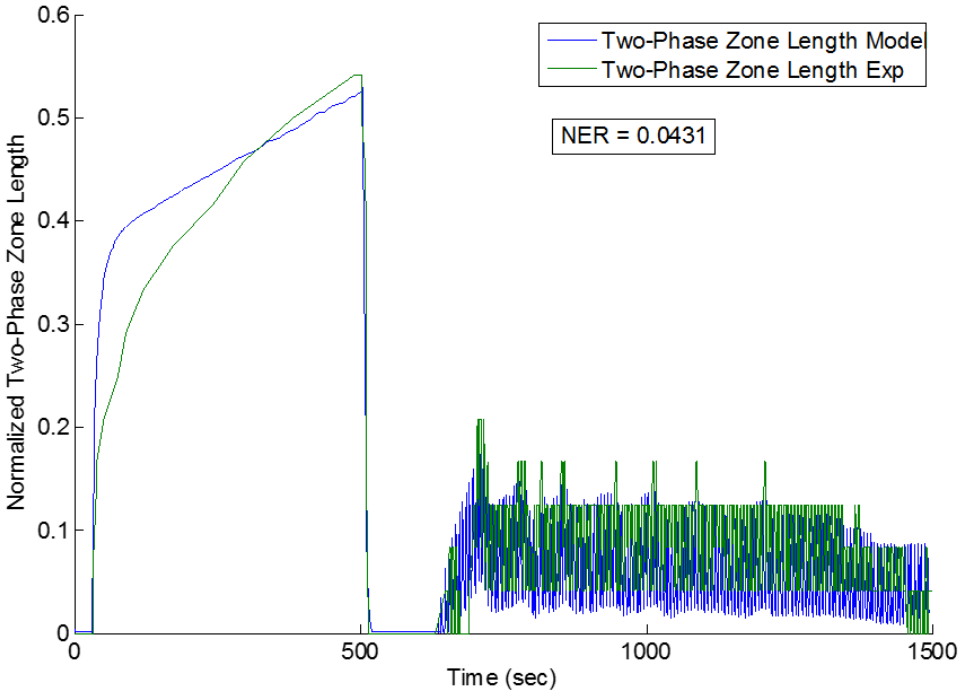

Figure 78: Two-phase Zone Length Comparison for Fresh Continuous at 0°C Set-point. Mass flow rate of CO_2 for 100% EEV Duty Cycle: 0.0248 kg s^{-1}

The comparison of the two-phase zone length output of the model and the measurements from the experimental testing is shown in Figure 78. The transport delays are evident during the start of the pull-down phase and there is a small amount of error as ζ reaches its maximum value. The shutdown stage is well modelled and there is generally good agreement for the period while the EEV pulses for temperature control.

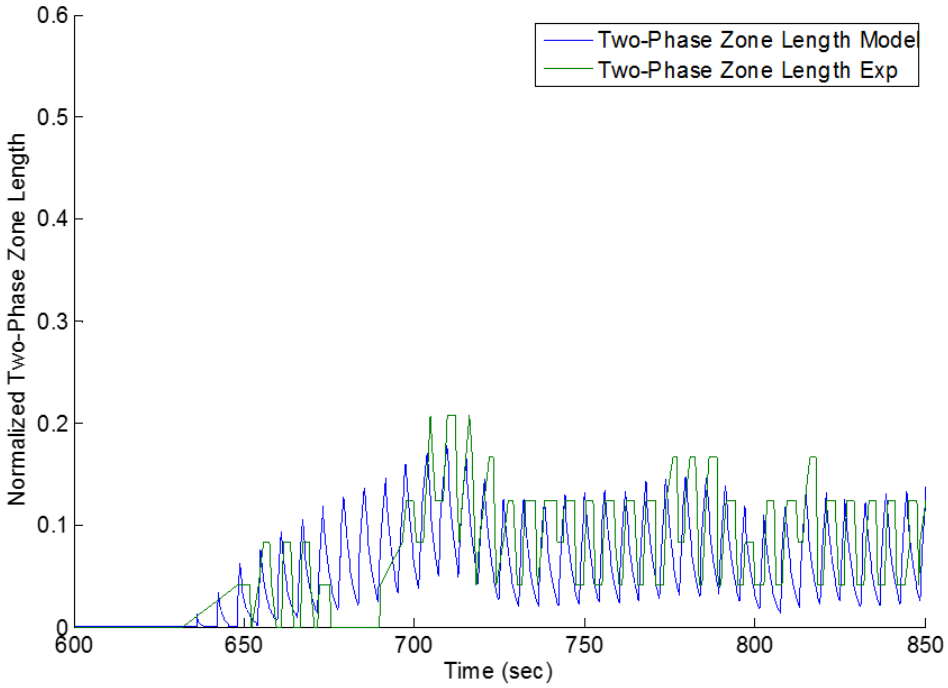

Figure 79: Two-phase Zone Length Comparison with Pulsing of EEV for Fresh Temperature Control. Mass flow rate of CO_2 for 100% EEV Duty Cycle: 0.0248 kg s^{-1}

A more detailed look at the EEV pulsing in shown in Figure 79. It can be seen that ζ starts to increase at the same time but the pulsing in the model is not replicated in the experimental results as the length of ζ for these initial pulses is shorter than the length of distance to the first measurement point on the coil where ζ is equal to 0.0417. The square nature of the pulses for the experimental results can also be attributed to the relatively course measurement resolution. Between 670 s and 680 s the ζ length in the experimental results goes to zero. This is not consistent with the EEV pulsing, nor is there a pressure fluctuation that can explain this occurrence so it is not surprising that the model does not capture it correctly. It is possible that a vapour bubble in the liquid line is responsible for the temperature increase measured on the coil temperatures as discussed in Chapter 3, Section 3.10, Page 55. Otherwise the agreement of the model with the experimental results is good with slight increases and decreases in the ζ length capture although not always at the correct magnitude. The timing of the pulses is also well captured as the ζ length is very short and there is no significant transport delays to model.

The NER value of 0.0431 appears high compared to the 0.0029 calculated for ζ in Chapter 4, Section 4.10.1, Page 106. The different shape of the pulses between the model and the experimental results may be one reason for this. However the biggest factor in this case may be

that the errors between the model and experimental results will always be large relative to the values of the experimental results that are so close to zero. This makes comparisons for the NER results in this Chapter 5 difficult to compare with the values calculated in Section 4.10.1.

5.1.2 Frozen Set-point of -25°C

This section details the dynamic comparisons for frozen continuous control at -25°C box temperature. The unit pulls down with the EEV fully open until 1901 s when EROT reaches the superheat setting and the EEV starts pulsing for superheat control. This continues until EAIT reaches the -25°C set-point at 2531 s as outlined in Chapter 3, Section 3.10.2, Page 59. After this there is a short period where the EEV is off before it begins temperature control at 2621 s.

The pull-down section of the EROT graph in Figure 80 is similar to the pull-down for Model 4 in Chapter 4, Section 4.10.1, Page 106 including the lower temperatures seen once the two-phase refrigerant reaches the coil outlet. However once the unit sensor reaches the superheat setting the EEV begins to pulse. The frequency of the pulses for superheat control is well captured by the model but the amplitude tends to be over-estimated. There is again a quicker response from the model when the EEV closes and when it opens again but once the temperature control stabilizes after 3000 s the correlation between the experimental results and the model is good. The high frequency fluctuations in the model for the temperature control section are not evident in the experimental results but their amplitude is minimal. The NER of $2.94e^{-4}$ is comparable with the error for EROT seen in Section 4.10.1 even though the dynamics captured by the model are much more complex.

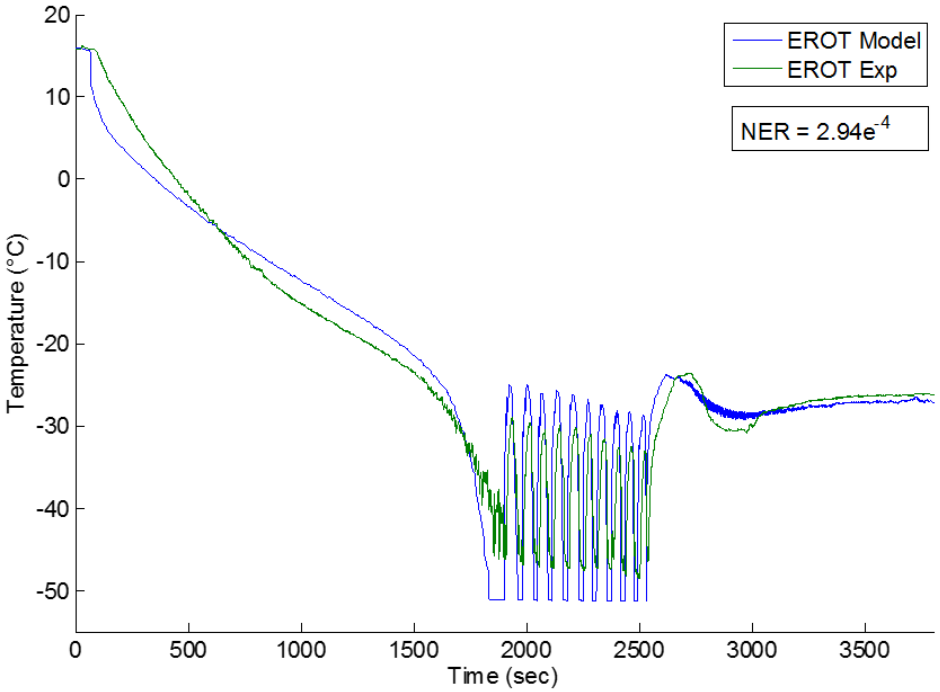

Figure 80: EROT Comparison with Frozen Continuous Control at -25°C Set-point. Mass flow rate of CO_2 for 100% EEV Duty Cycle: 0.0245 kg s^{-1}

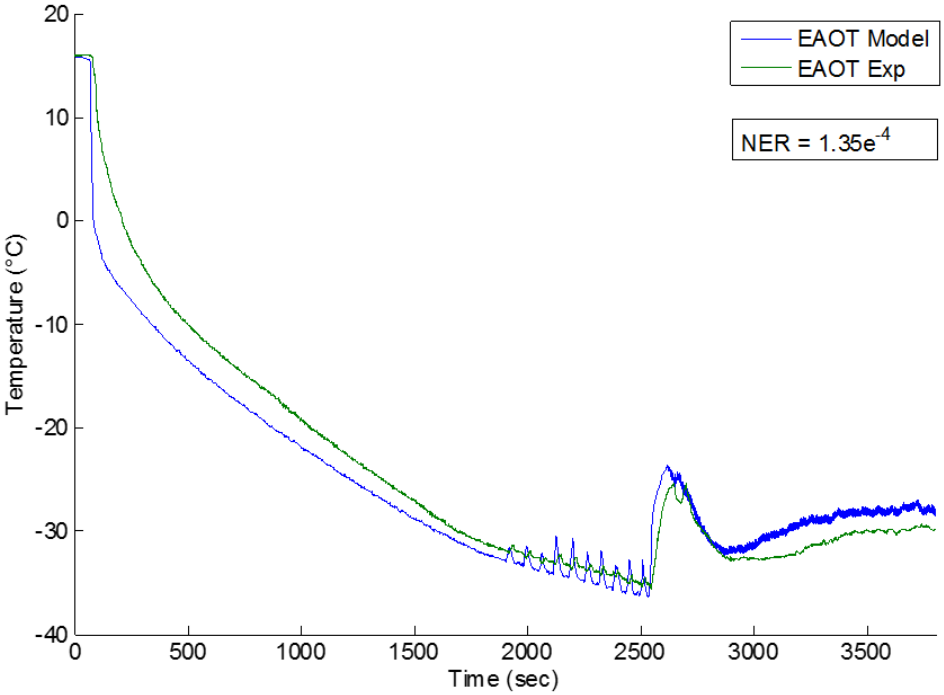

Figure 81: EAOT Comparison for Frozen Continuous Control at -25°C Set-point. Mass flow rate of CO_2 for 100% EEV Duty Cycle: 0.0245 kg s^{-1}

For EAOT the correlation of the model outputs to the experimental results is good. The quicker response of the model causes some error in the initial pull-down, in the amplitude and timing of the temperature spikes during superheat control and the response to the EEV closing and opening. Again there are some high frequency fluctuations in the model which are not replicated in the experimental results but the EEV pulsing does appear to have some effect on the EAOT measurements in this case. The NER is lower than the fresh continuous test at $1.35e^{-4}$ and is 42% higher than the much simpler dynamic pull-down in Section 4.10.1.

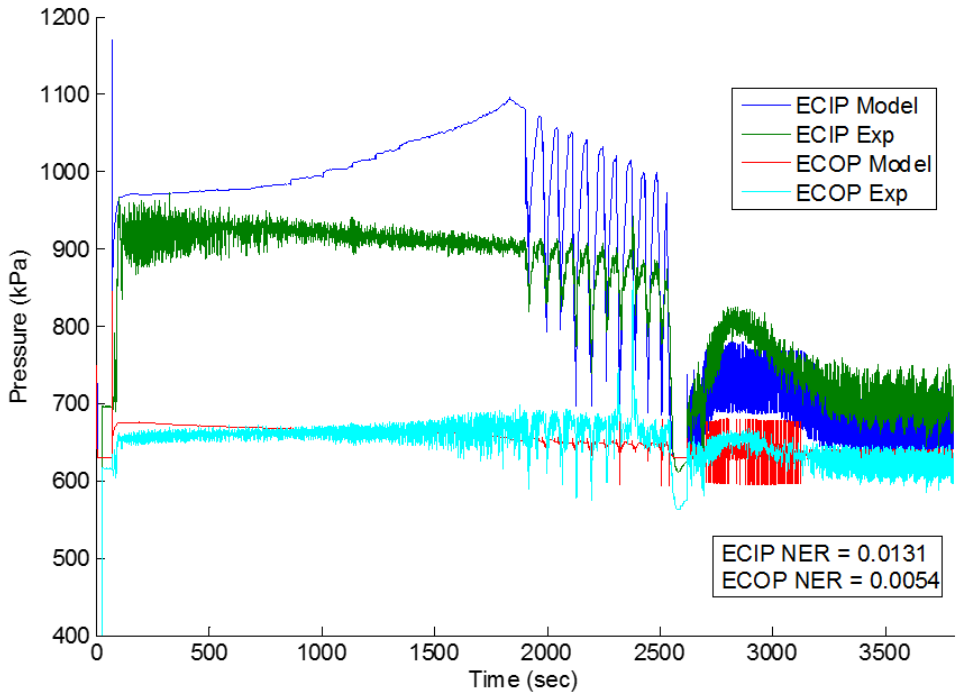

Figure 82: Inlet and Outlet Pressure Comparison for Frozen Continuous Control at -25°C Set-point. Mass flow rate of CO_2 for 100% EEV Duty Cycle: 0.0245 kg s^{-1}

The inlet and outlet pressures are compared in Figure 82 above. For the pull-down section the ECOP output from the model matches closely to the experimental results. However as the EEV starts to pulse for superheat control ECOP in the experimental results starts to oscillate to a larger degree than the model output. For ECIP the opposite is the case where the amplitude of the fluctuations for the model are much larger than those seen in the experimental results. This is compounded by the overestimation of ECIP in the model at this stage.

The EEV opens again at 2621 s and starts pulsing for temperature control. This produces the opposite effect in the ECOP response with larger amplitude fluctuations outputted by the model than seen in the experimental results. These large amplitude fluctuations reduce substantially at approximately 3130 s around the time EAIT and EAOT temperatures stabilize. The ECIP model response during this period matches the shape of the experimental results well although the amplitude of the response and the amplitude of the fluctuations are overestimated.

Overall the NER for ECIP and ECOP is low compared to previous tests, reflecting the lack of issues with the measurements and the general good agreement between model and the experimental results during the temperature control phase.

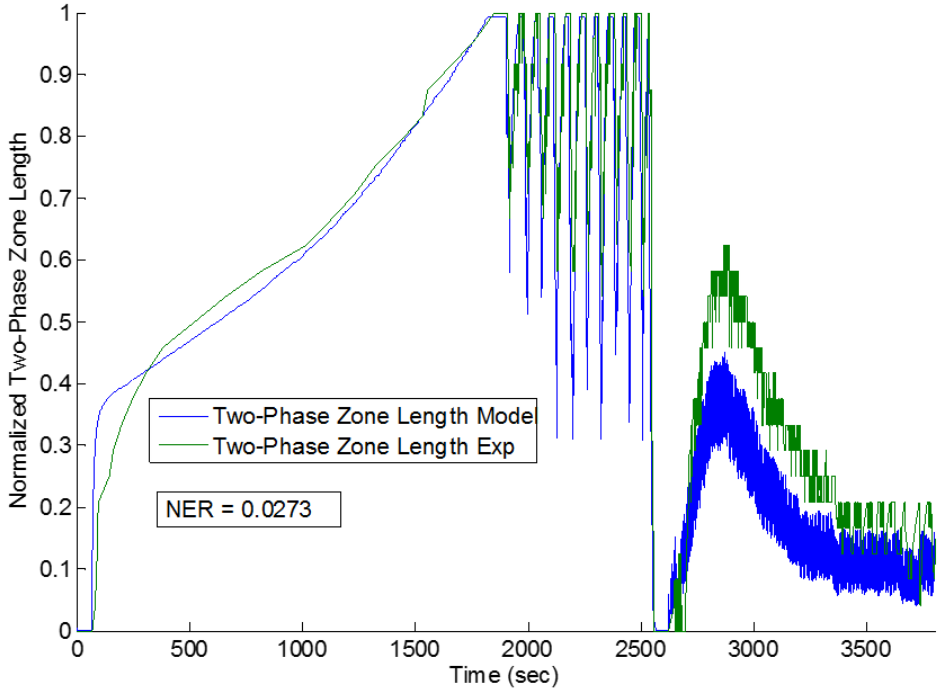

Figure 83: Two-Phase Zone Length Comparison for Frozen Continuous Control at -25°C Set-point. Mass flow rate of CO_2 for 100% EEV Duty Cycle: 0.0245 kg s^{-1}

The comparison for the two-phase zone length is shown in Figure 83. The model reaction time is similar to before for the initial pull-down section. The model output for ζ reaches the coil outlet at approximately the same time as the experimental results. At this point superheat control commences. Figure 84 shows the superheat control section of the graph in more detail. The error in the response of the model to the EEV closing can clearly be seen here with the

model reacting approximately 8-12 s before the experimental results. The model also has a greater amplitude of movement of ζ. The fluctuations in ζ within the larger cycle are present in both experimental and model results but tend not to be in exactly in phase due to the differences in response times.

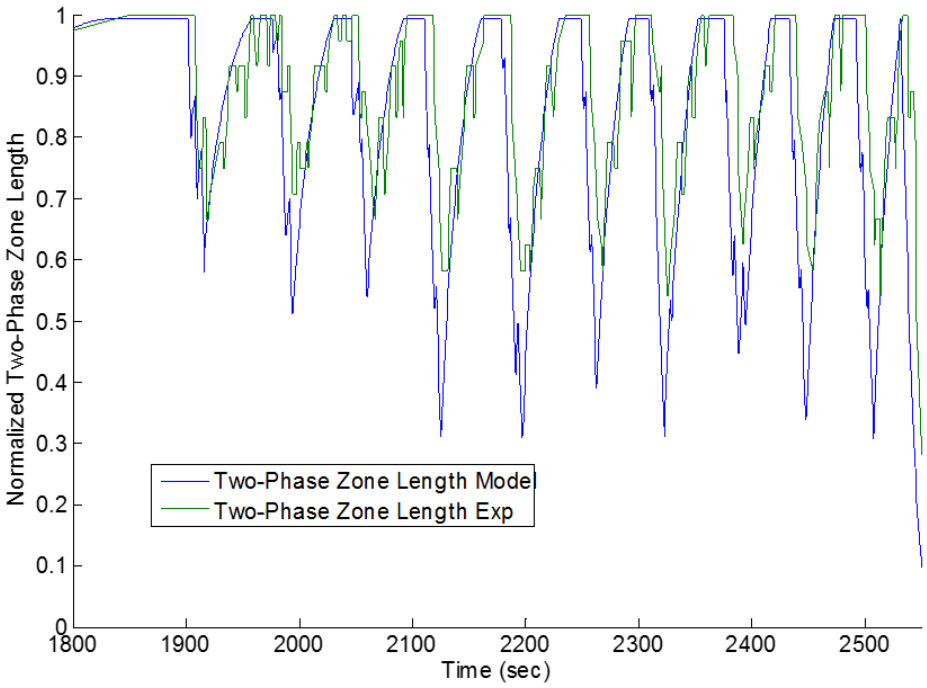

Figure 84: Two-phase Zone Length Comparison with Pulsing of EEV for Frozen Superheat Control. Mass flow rate of CO_2 for 100% EEV Duty Cycle: 0.0245 kg s^{-1}

The ζ comparison for the temperature control section of the graph is shown in Figure 85. The initial pulsing in the model from 2621 s to 2645 s is again not replicated in the experimental results and between 2685 s and 2700 s we once again see ζ going to zero in the experimental results similar to the results for fresh continuous control discussed in Section 5.1.1. The frequency of fluctuations in the model is generally consistent with what was measured in the experimental results and the shape of the ζ graph is also captured well. There is an offset between the average values of approximately 0.2 at the peak at 2700 s which settles out at approximately 0.1 as the two-phase zone length stabilizes. This error is opposite to what we see in the static results where the model tends to overestimate the length of ζ to a small degree in two out of the three test conditions.

NER, displayed in Figure 83, for the frozen continuous test compares well with the fresh continuous test due to the good agreement seen during the pull-down and superheat control pulsing periods as well as the relatively larger values for the experimental results.

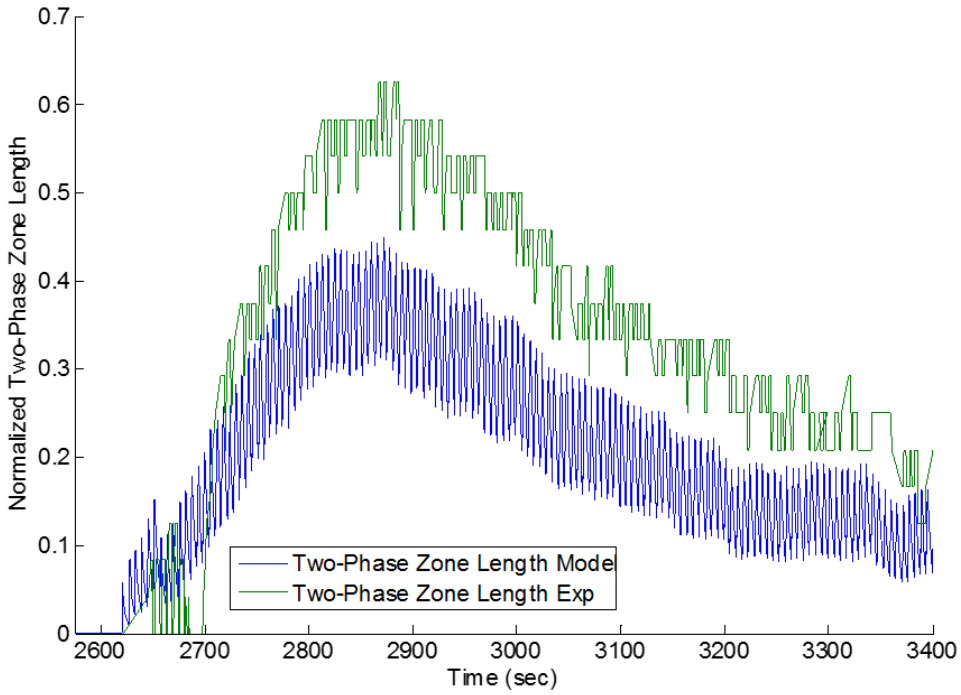

Figure 85: Two-phase Zone Length Comparison with Pulsing of EEV for Frozen Temperature Control. Mass flow rate of CO_2 for 100% EEV Duty Cycle: 0.0245 kg s^{-1}

5.2 Cycle Sentry with Fans On in Null

This section examines the correlation between experimental test results and model outputs for cycle sentry control where the unit pulls down to set-point and switches off the EEV until an EAIT temperature above set-point is reached. The period of time while the EEV is off is known as Null and the fans remain on during this period. EEV pulsing is only used in this mode for superheat control.

5.2.1 Fresh Set-point of 0°C

The first case examined for cycle sentry control is at a fresh set-point of 0°C with the evaporator fans on during Null. The unit pulls-down with the EEV fully open until 1339 s where EAIT reaches the set-point of 0°C. The EEV then closes until 1441 s when EAIT reaches the restart temperature, at which point it opens fully again and pulls back down until EAIT reaches the set-point again at 1581 s. This is cycle of Null and pull-down is repeated twice more within the duration of the test. There is no pulsing of the EEV during this test.

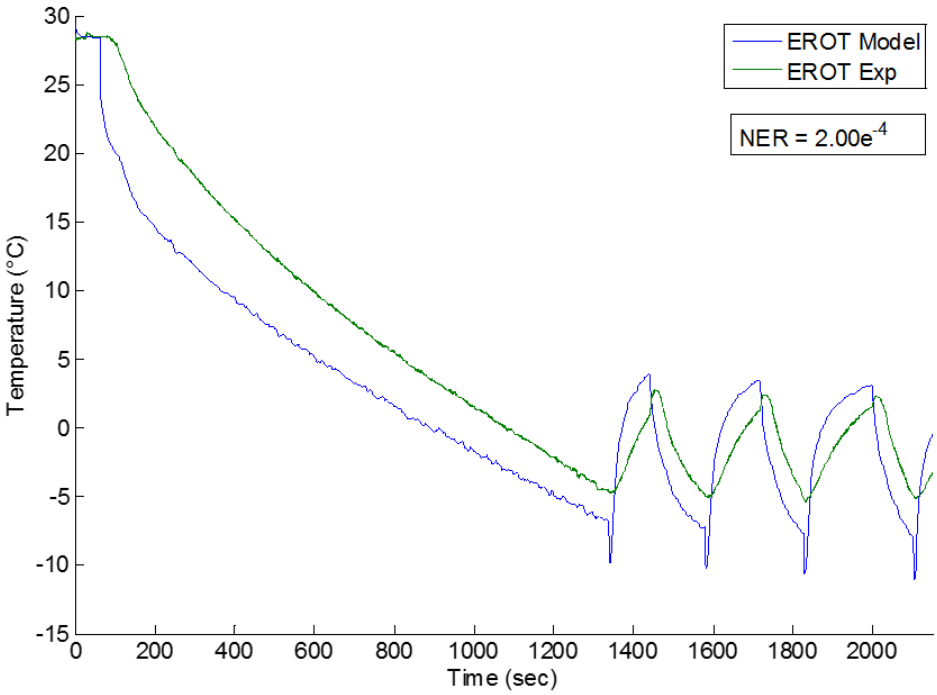

Figure 86: EROT Comparison for Fresh Cycle Sentry Control with Fans On in Null at 0°C Set-point. Mass flow rate of CO_2 for 100% EEV Duty Cycle: 0.0238 kg s^{-1}

The EROT comparison in Figure 86 shows very similar results to the fresh continuous case discussed in Section 5.1.1 for the pull-down and Null periods. Once the EEV opens again after the Null period the response is similar to the initial pull-down with the exception of a short increase in temperature for the experimental results cause by the pressure increase for both ECIP and ECOP. Although there is a corresponding pressure increase in the model the temperature increase is not replicated. The NER of 2.0e^{-4} is higher than that seen for the fresh

continuous case with a larger error evident for both the pull-down and temperature control sections of Figure 86.

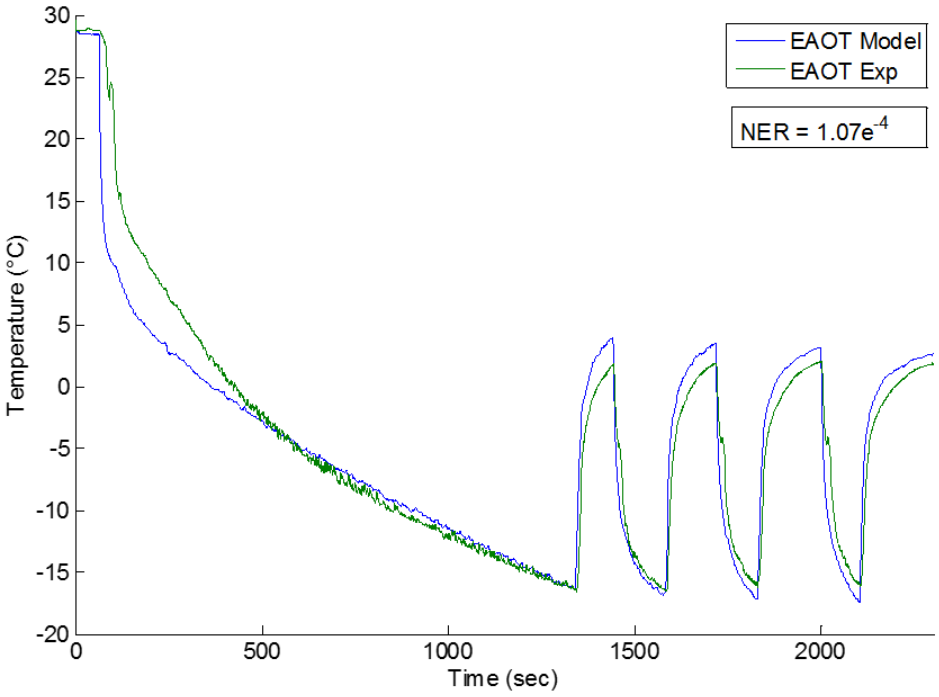

Figure 87: EAOT Comparison for Fresh Cycle Sentry Control with Fans On in Null at 0°C Set-point. Mass flow rate of CO_2 for 100% EEV Duty Cycle: 0.0238 kg s^{-1}

For EAOT the correlation between the experimental results and the model outputs is good and the only error can be related to the speed of the model response. The NER is this case is lower than the fresh continuous test in Section 5.1.1 as the error in the temperature control period of the test is very small.

The pressure outputs of the model also show good correlation with the model outputs for the most part. There are some small changes in ECIP measurements during the pull-down phase which are not replicated in the model due to its lumped-parameter nature. When the EEV closes we see the same response as before where the pressure decay in the experimental results is not replicated. There is also the issue with the measurements of ECIP for the first two Null periods in the experimental results but the third period, which appears to have accurate measurements, shows good correlation with the model outputs. For ECOP the NER is slightly higher than the fresh continuous test with the error discussed during Null periods having the major effect. The NER for ECIP suffers from the measurement error once again.

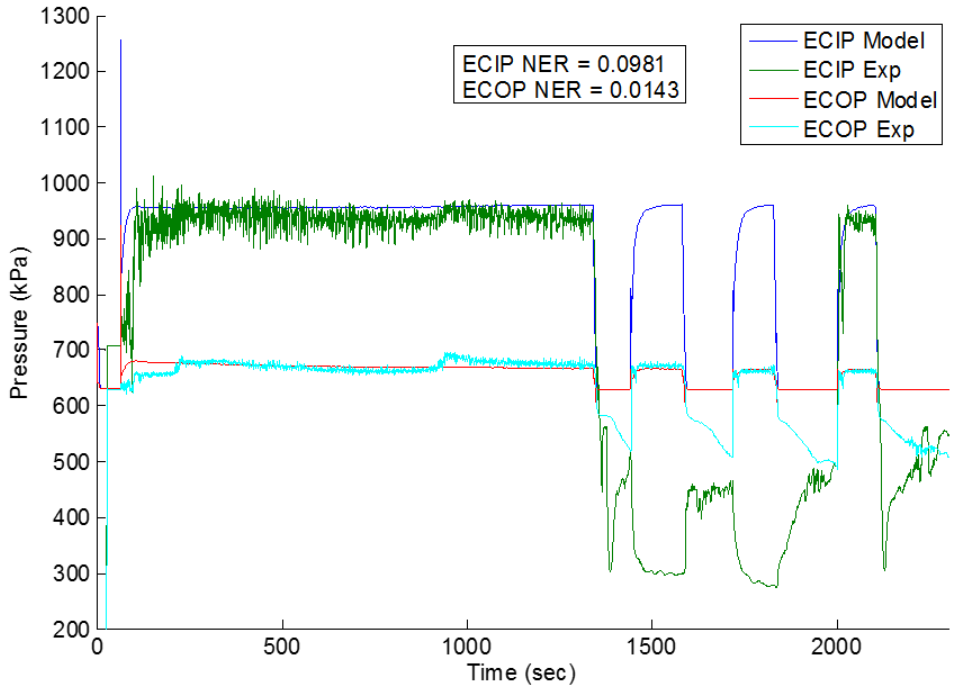

Figure 88: Coil Inlet and Outlet Pressure Comparison for Fresh Cycle Sentry Control with Fans On in Null at 0°C Set-point. Mass flow rate of CO_2 for 100% EEV Duty Cycle: 0.0238 kg s^{-1}

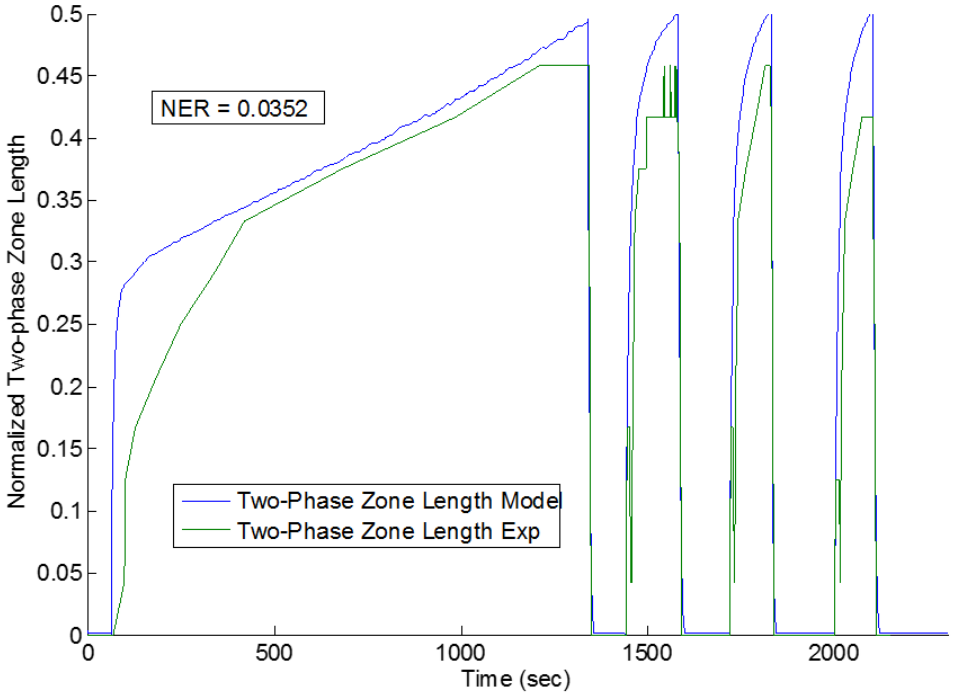

Figure 89: Two-phase Zone Length Comparison for Fresh Cycle Sentry Control with Fans On in Null at 0°C Set-point. Mass flow rate of CO_2 for 100% EEV Duty Cycle: 0.0238 kg s^{-1}

The comparison of the two-phase zone length in Figure 89 follows the same trend as the other outputs for the pull-down and Null periods of the test. Once the valve opens again the experimental results show a slower response and a smaller amplitude for the length of ζ. This is consistent with previous observations and the static results from Chapter 4, Section 4.8.1, Page 101. There are some fluctuations of ζ during the period from 1540 s to 1580 s in the experimental results which are not replicated in the model but the cause for these fluctuations are unclear as the valve does not pulse during this time. It is possible that the two-phase zone boundary is very close to the boundary during this time and temperature measurements are fluctuating slightly as a result. In this case the NER is lower than the fresh continuous test at 0.0352 as the larger changes in ζ are better matched by the model than the short pulsing.

5.2.2 Frozen Set-point of -25°C

The frozen set-point examined for cycle sentry control with the fans on in Null is -25°C. The unit pulls-down with the valve fully open until 1995 s. At this point the EEV starts pulsing for superheat control and this continues until 2444 s when EAIT reaches the set-point temperature of -25°C. The unit then enters a Null period until EAIT reaches the restart temperature at 2558 s at which point the EEV opens. There is a short period of time until 2627 s where the EEV is fully open during the pull-down after which it pulses for superheat control again until EAIT reaches the set-point at 2707 s. This cycle of Null and pull-down is repeated twice more during the duration of the test.

The pull-down portion of the test until EAIT reaches the set-point of -25°C and the EEV closes is very similar to the frozen continuous test outlined in Section 5.1.2.

Once the EEV closes EROT rises until the EAIT re-start temperature is reached and the EEV opens to pull back down to temperature once again. The model response for this section is similar to previous tests with a response faster than the experimental testing but general good agreement for the pull-up, pull-down and pulsing portions. The NER is substantially higher than for the frozen continuous test at $5.82e^{-4}$ as there is a significant amount of time spent with the two-phase boundary at the outlet where the model underestimates the EROT temperature.

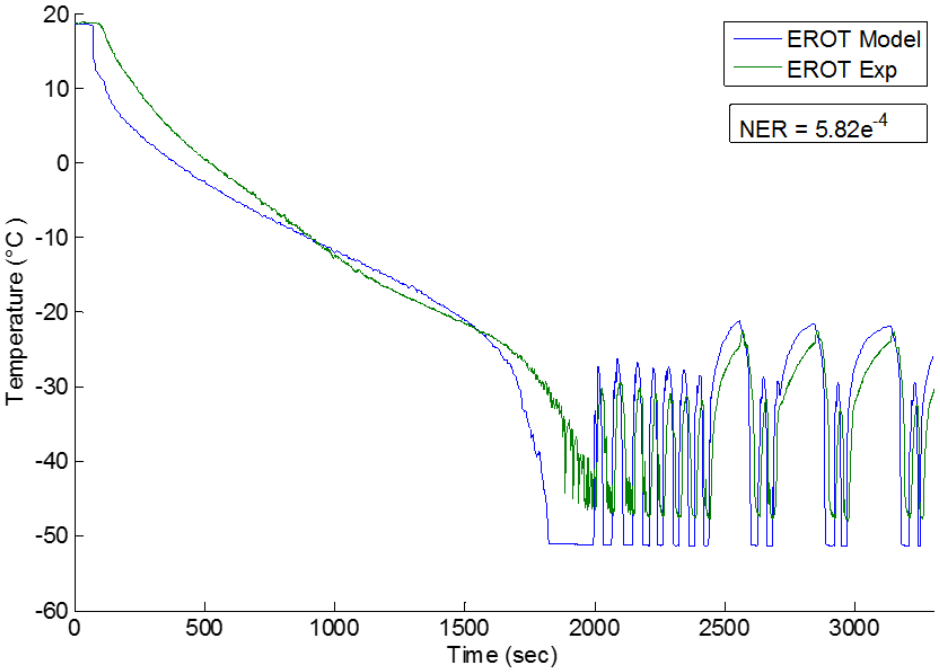

Figure 90: EROT Comparison for Frozen Cycle Sentry Control with Fans On in Null at -25°C Set-point. Mass flow rate of CO_2 for 100% EEV Duty Cycle: 0.0249 kg s^{-1}

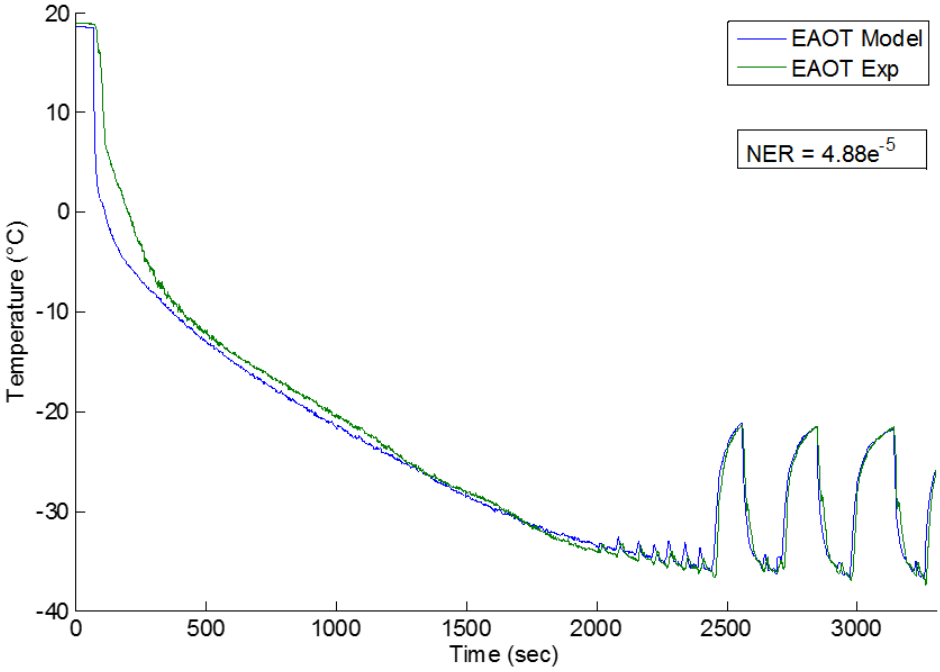

Figure 91: EAOT Comparison for Frozen Cycle Sentry Control with Fans On in Null at -25°C Set-point. Mass flow rate of CO_2 for 100% EEV Duty Cycle: 0.0249 kg s^{-1}

The correlation of the model output for EAOT is excellent with only a small amount of error on the initial pull-down section and good agreement for the superheat pulsing section as well as the Null periods and subsequent pull-ups and pull-downs. This is shown in the value of the NER which at $4.88e^{-5}$ is less than half the value seen for the equivalent frozen test in Section 5.1.2.

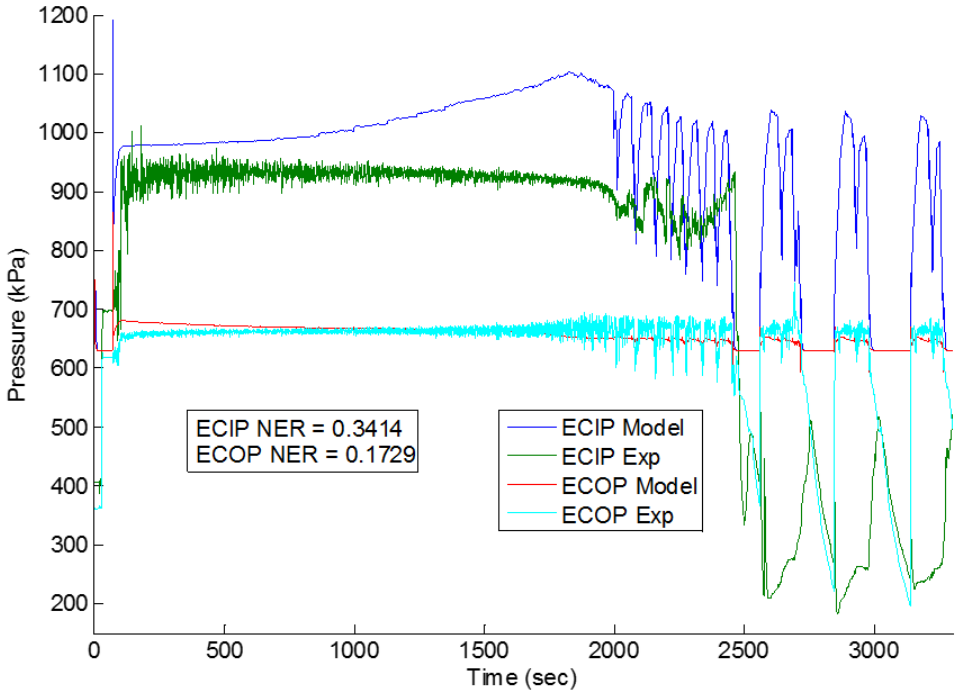

Figure 92: Coil Inlet and Outlet Pressure Comparison for Frozen Cycle Sentry Control with Fans On in Null at -25°C Set-point. Mass flow rate of CO_2 for 100% EEV Duty Cycle: 0.0249 kg s^{-1}

ECOP once again shows good agreement between the model and the experimental results in Figure 92 with similar issues to previous tests for ECIP for both the experimental results and the model output. The valve pulsing in the pull-down periods after the Null periods has an effect on the model output. It can only be assumed that this would be reflected in the experimental results if the sensor readings were correct. As with the fresh cycle sentry test in Section 5.2.1 the values of NER for ECIP and ECOP are effected by the error during the Null periods and the measurement error for ECIP.

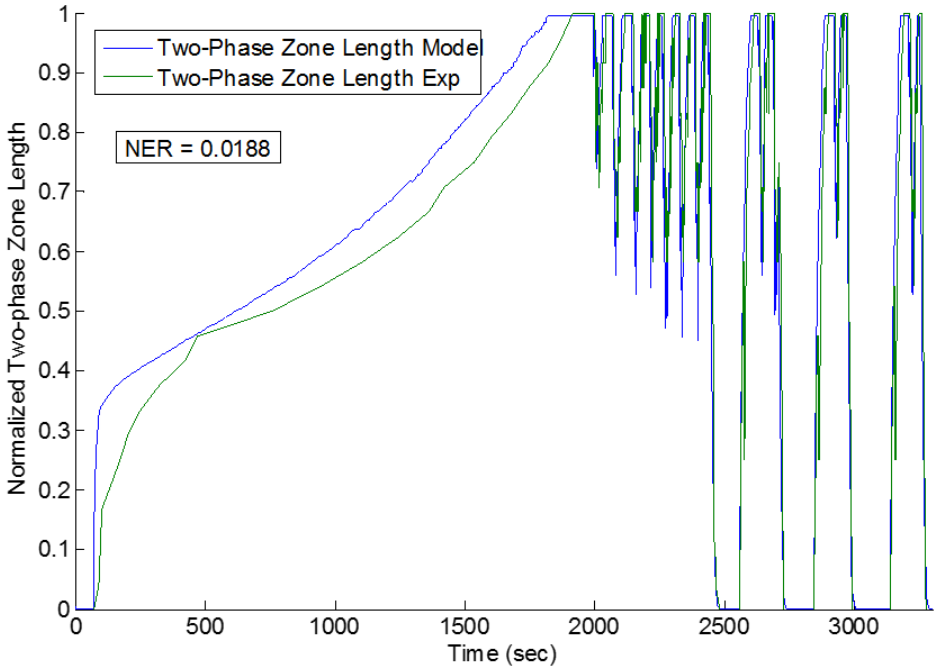

Figure 93: Two-phase Zone Length Comparison for Frozen Cycle Sentry Control with Fans On in Null at -25°C Set-point. Mass flow rate of CO_2 for 100% EEV Duty Cycle: 0.0249 kg s^{-1}

The comparison for ζ in Figure 93 shows some error during the initial pull-down with the model reaching the outlet 92 s before the experimental results. This error has not been present in the other cases where the two-phase boundary reached the end of the coil and shows the limitations for the PAF's in addressing the errors in the heat transfer calculations.

Once the unit starts pulsing for super heat control the model shows good correlation to experimental results once again and continues this into the Null periods and the further superheat control pulsing. A comparison of NER to the frozen continuous results shows that the model is also more capable of replicating the experimental results for ζ with the value of 0.0188 over 30% lower.

5.3 Cycle Sentry with Fans Off in Null

This section looks at the model response for cycle sentry control with the evaporator fans off in Null. The response of the system during the pull-down portion of the test does not deviate

significantly from Section 5.2. However for the Null period there are significant differences which will be discussed.

5.3.1 Fresh Set-point of 0°C

In this test the unit pulls-down with the EEV fully open until EAIT reaches the 0°C set-point. The Null period then last until 1626 s followed by the pull-down back to the set-point until 1796 s. This cycle is repeated twice more over the duration of the test.

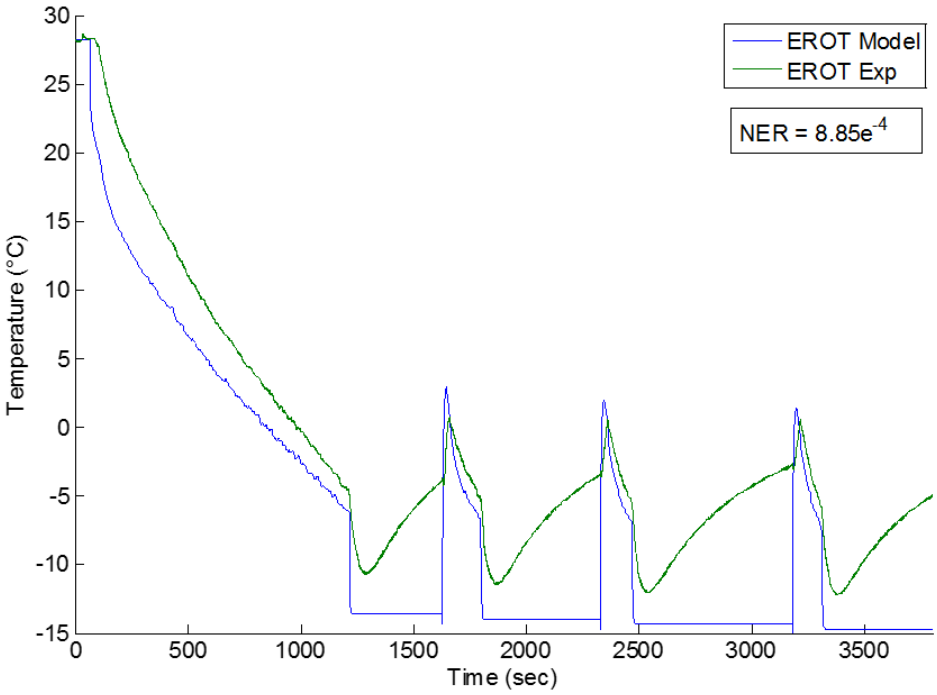

Figure 94: EROT Comparison for Fresh Cycle Sentry Control with Fans Off in Null at 0°C Set-point. Mass flow rate of CO_2 for 100% EEV Duty Cycle: 0.0236 kg s^{-1}

For EROT, shown in Figure 94, the response to the EEV closing is a drop in temperature due to the drop in pressure. This occurred for the model in Section 5.2.1 but not for the experimental results. Here the experimental results also show a drop as there is no airflow across the coil to help to boil the two-phase CO_2 and the heat transfer to the air drops considerably. There is still some refrigerant flow during this period as the pressure decays towards the BPR setting. However the model response is larger than the experimental results and it fails to recover from

the low temperature. The reason for this is that the model heat transfer stops when both the refrigerant flow and the airflow go to zero whereas in reality there is still heat conducted from the air into the refrigerant even without forced airflow. Natural convection and conduction allow heat to be added to the refrigerant during this period and they are neglected in the model. This large error during the Null periods contributes to an NER value over 4 times higher than any of the other fresh tests.

Once the EEV opens and the fans start again the model correlates well with the experimental results.

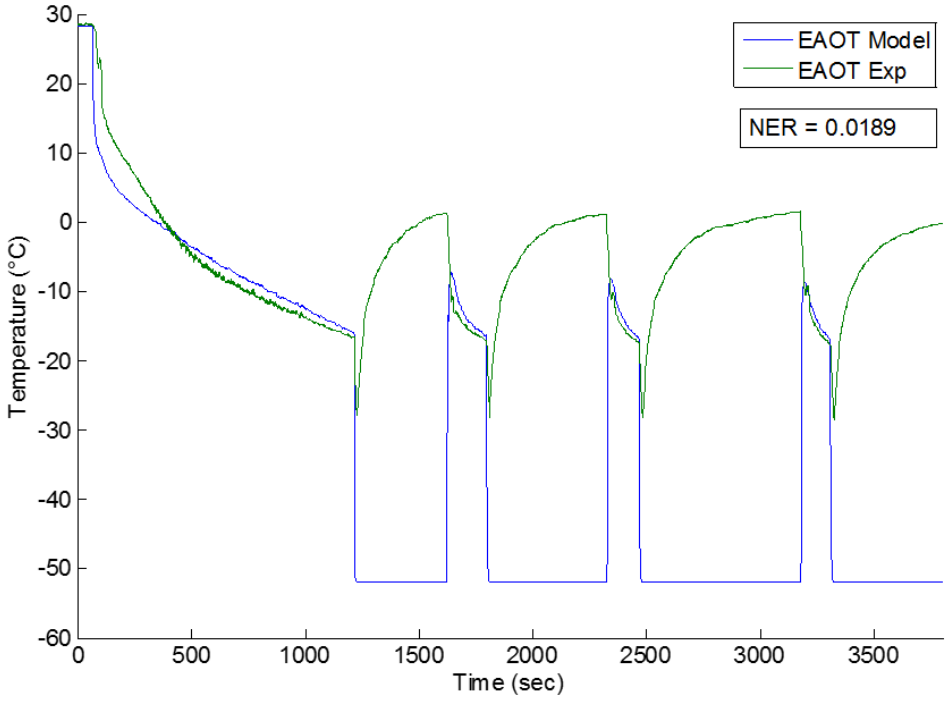

Figure 95: EAOT Comparison for Fresh Cycle Sentry Control with Fans Off in Null at 0°C Set-point. Mass flow rate of CO_2 for 100% EEV Duty Cycle: 0.0236 kg s^{-1}

A similar response to the EEV closing and the shutting off of the fans is seen for EAOT in Figure 95. Once again there is a drop in temperature which was not seen in Section 5.2.1 also due to the drop in pressure at the coil inlet. For this case the error is even larger as without airflow the EAOT temperature is assumed to be the same as the wall temperature which is now at the liquid CO_2 saturation temperature. Again once the EEV opens and the fan airflow returns the correlation improves. The location of the thermocouple 10-15 mm off the face of the coil would

also contribute to the error here between the experimental results and the model outputs as the model output is the air directly after it leaves the coil. However placing the thermocouples any closer would introduce the risk of them contacting the coil and measuring the fin temperature rather than the air temperature. Since EAOT was well correlated for the other fresh tests the NER in this case is several orders of magnitude larger at 0.0189.

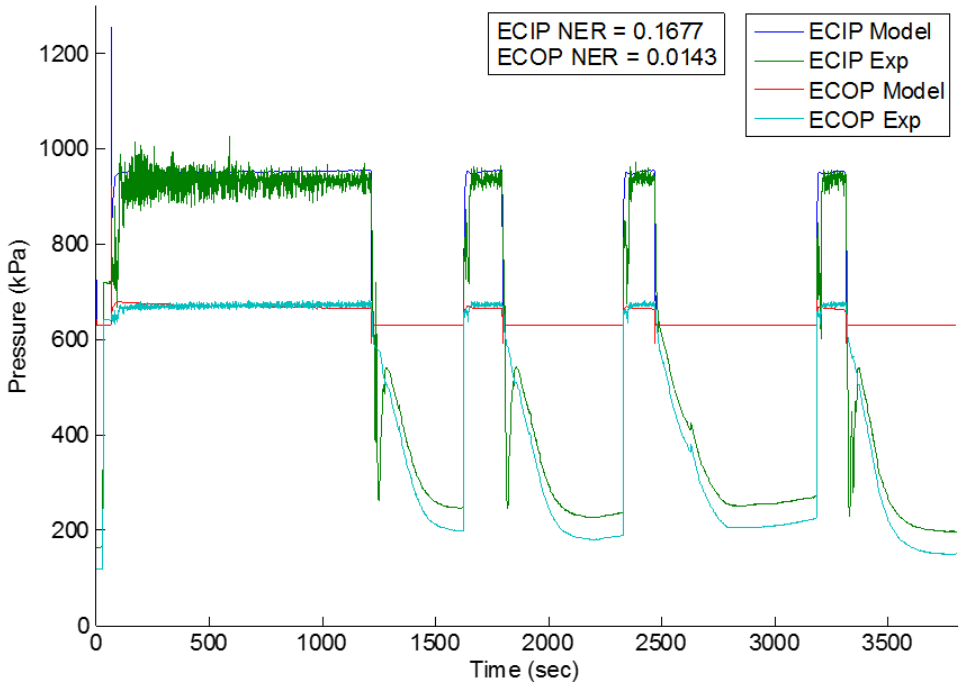

Figure 96: Coil Inlet and Outlet Pressure Comparison for Fresh Cycle Sentry Control with Fans Off in Null at 0°C Set-point. Mass flow rate of CO_2 for 100% EEV Duty Cycle: 0.0236 kg s^{-1}

The ECIP and ECOP pressure comparison in Figure 96 show that the fans turning off during the Null period have little effect on the unit pressure and as a consequence the pressures behave much as they did in Section 5.2.1. It should be noted that the pressure decay seen in the experimental results will also allow for some mass flow of the refrigerant even after the BPR setting is reached. As discussed previously it is not possible to model this due to the limitations of the refrigerant property routines. The NER values for ECIP and ECOP are close to those seen in Section 5.2.1 where the fans were on during the Null period.

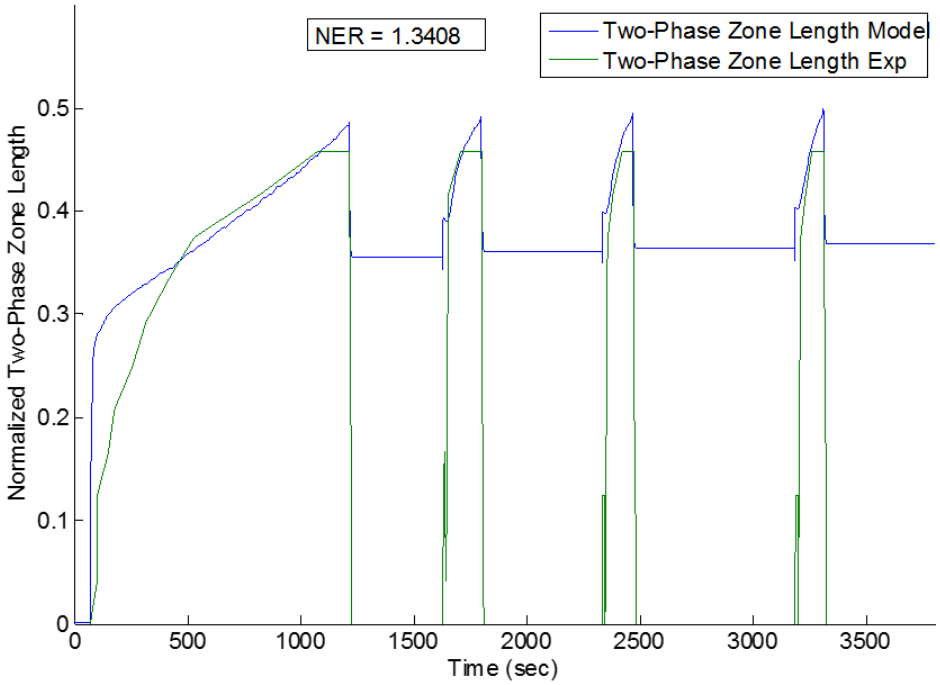

Figure 97: Two-phase Zone Length Comparison for Fresh Cycle Sentry Control with Fans Off in Null at 0°C Set-point. Mass flow rate of CO_2 for 100% EEV Duty Cycle: 0.0236 kg s^{-1}

The comparison for ζ in Figure 97 shows that the two-phase boundary stops moving once the refrigerant flow stops for each Null period. Up until this point the correlation is good and once the refrigerant flow and airflow resume the model matches the experimental results well. The NER suffers considerably from the model error during the Null periods and the value of 1.3408 is 38 times higher than the previous fresh cycle sentry test.

5.3.2 Frozen Set-point of -25°C

For this test the EEV remains fully open until 2181 s, it then pulses in superheat control until EAIT reaches the set-point temperature of -25°C at 2739 s. The subsequent Null period last until 3702 s at which point the EEV opens again. It remains open fully until 3801 s and then pulses in superheat control until 4031 s when EAIT once again reaches the set-point. One more cycle of Null period and pull-down occurs during the test.

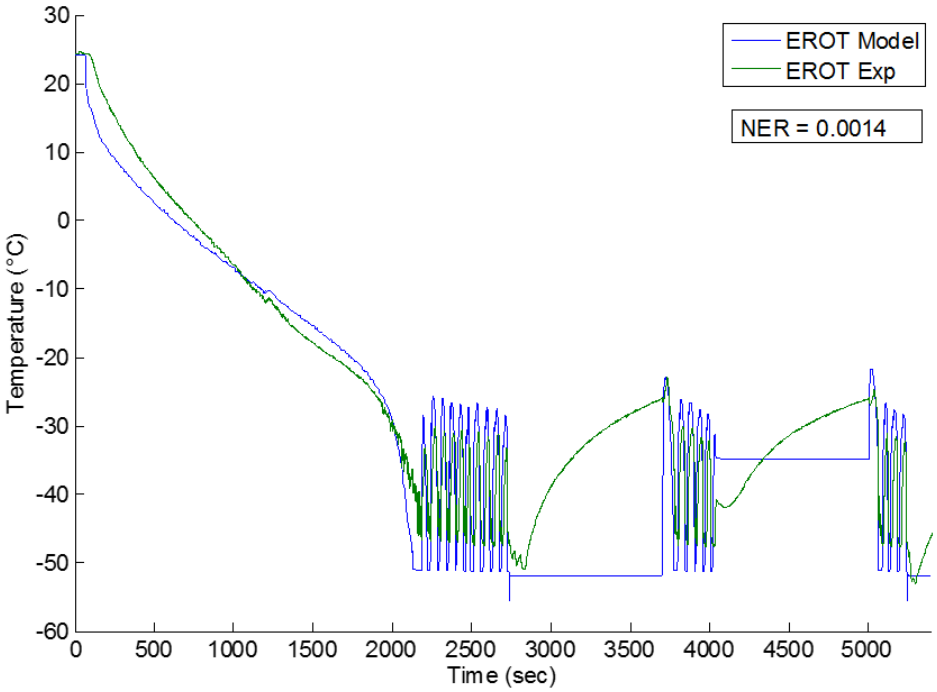

Figure 98: EROT Comparison for Frozen Cycle Sentry Control with Fans Off in Null at -25°C Set-point. Mass flow rate of CO_2 for 100% EEV Duty Cycle: 0.0245 kg s^{-1}

For the frozen -25°C set-point case the trend of large deviations for the Null period continues. Again there is a drop in temperature for EROT, Figure 98, once the EEV closes. For the model this is very sharp and short lived before it settles at very close to the saturation temperature for the duration of the Null period as the two-phase boundary is very close to the coil outlet. Once again the model correlation improves once the EEV opens and it shows good agreement for the pull-down periods with the valve fully open and with it pulsing. The NER value is significantly affected once again by the large errors during the Null periods.

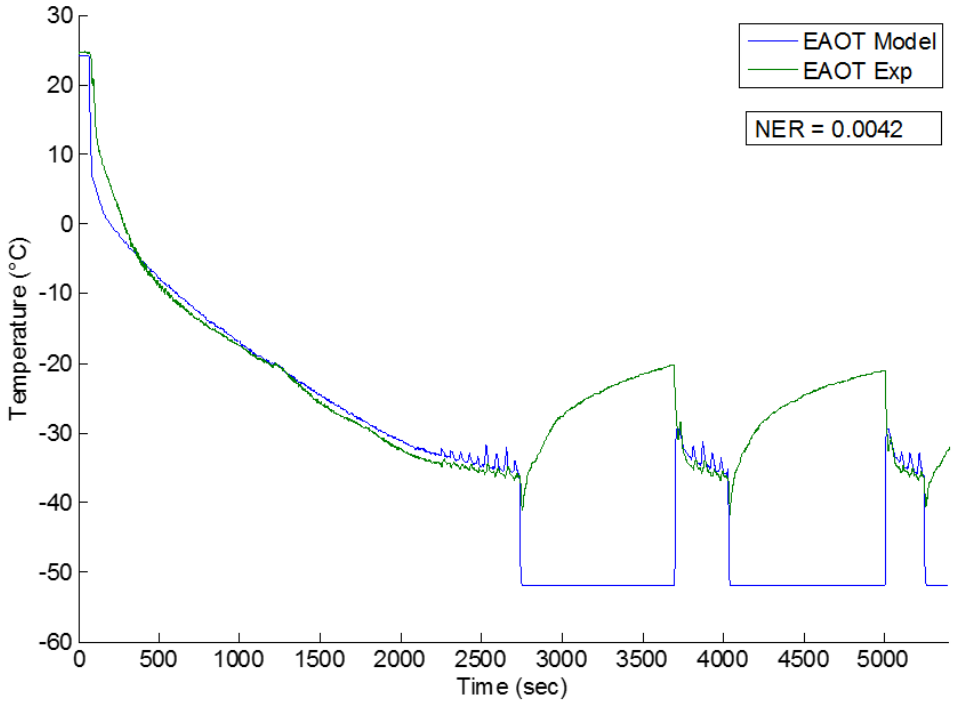

Figure 99: EAOT Comparison for Frozen Cycle Sentry Control with Fans Off in Null at -25°C Set-point. Mass flow rate of CO_2 for 100% EEV Duty Cycle: 0.0245 kg s^{-1}

The EAOT model response for the Null period for the frozen condition is almost identical to the fresh condition discussed in Section 5.3.1 although the magnitude of the error is diminished as the experimental results for EAOT in this case are closer to the liquid CO_2 saturation temperature. The NER value reflect the smaller magnitude of the error during the Null periods although it is still 100 higher than those seen in the cycle sentry tests with fans on during Null.

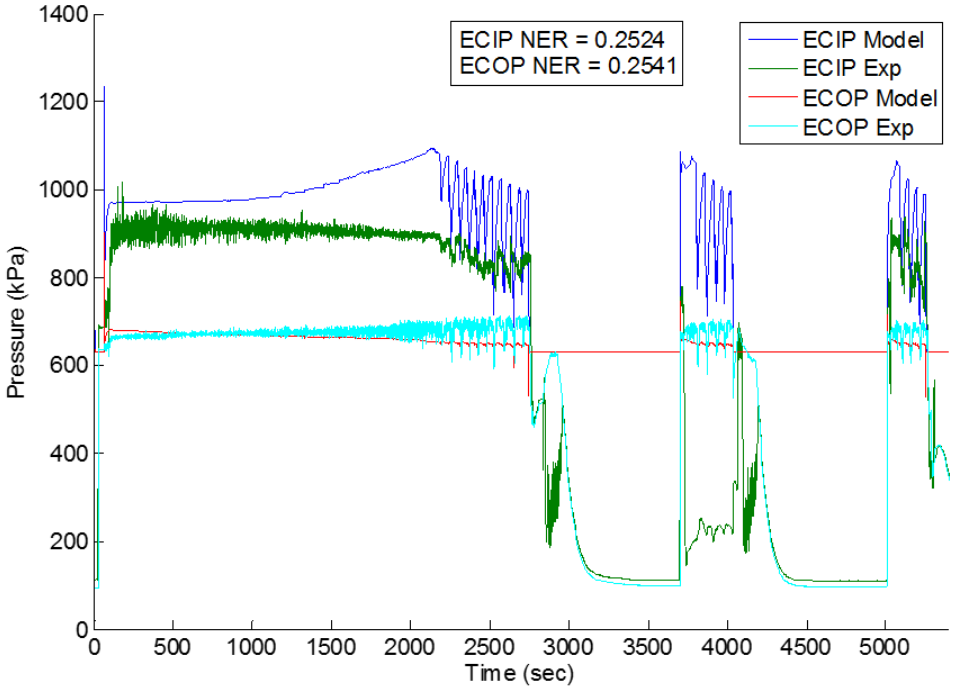

Figure 100: Coil Inlet and Outlet Pressure Comparison for Frozen Cycle Sentry Control with Fans Off in Null at -25°C Set-point. Mass flow rate of CO_2 for 100% EEV Duty Cycle: 0.0245 kg s^{-1}

The ECIP and ECOP outputs are very similar to the results from Section 5.2.2 where the fans are on in Null although the NER value for ECIP is slightly lower due to the experimental results for the 2nd temperature control cycle being correct. The value for ECOP is higher than the fans on test as the Null periods where the significant error occurs are longer.

The ζ model response for this case is shown in Figure 101 and is quite different for the two Null periods shown. For the first Null period the ζ value remain at the maximum while the EEV is off and only drops once the EEV opens again reacting to the changes in the other parameters. This occurs directly after a period where the EEV is open for 34 s. For the 2nd Null period the ζ drops to 0.564, similar to what happened for the fresh case in Section 5.3.1, and remains at that level until the valve opens and it again reacts to the change in conditions. In this case the EEV is only open for 2 s prior to the Null period. The differences between the response for the two Null periods is related to how long the model has been in the single zone two-phase only representation and whether it can switch to the two zone two-phase and superheated representation before the mass flow rate of CO_2 stops and causes the heat transfer to cease in

the model. The large errors during Null periods have a similar effect on the NER as the fresh test resulting in a value 44 times higher than the test with fans on during the Null periods.

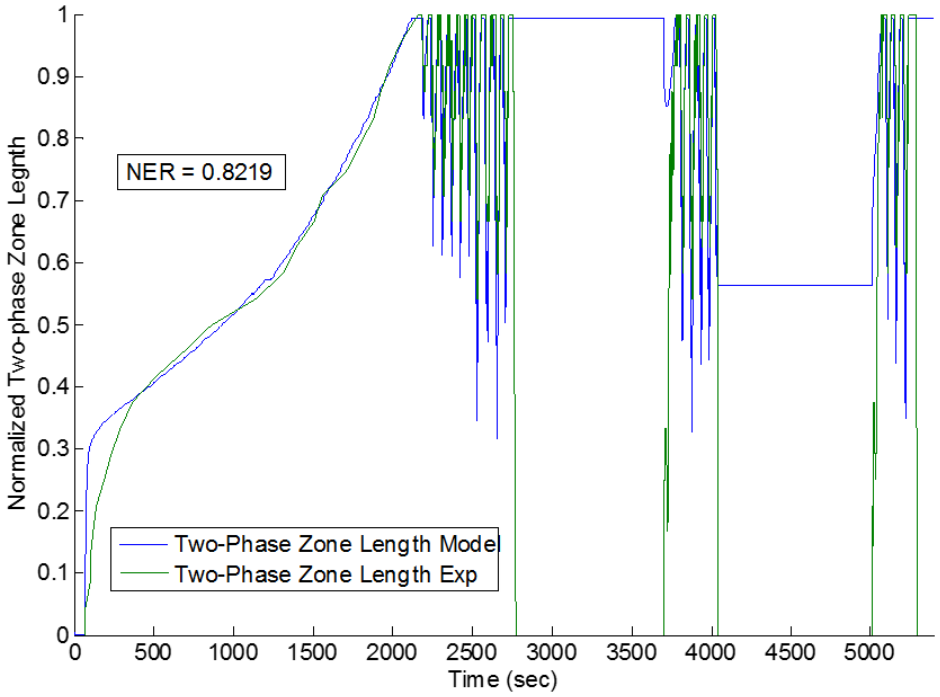

Figure 101: Two-phase Zone Length Comparison for Frozen Cycle Sentry Control with Fans Off in Null at -25°C Set-point. Mass flow rate of CO_2 for 100% EEV Duty Cycle: 0.0245 kg s^{-1}

5.4 Superheat Control Optimization

The results of the frozen tests for both cycle sentry and continuous control in Chapter 3, Section 3.10, Page 55, showed that the superheat control of the open cycle CO_2 system was not achieving its purpose of preventing the two-phase fluid reaching the outlet of the evaporator coil. In the case of the frozen cycle sentry with fans on in Null test ζ was equal to one for 44% of the time the unit was in superheat control during the initial pull-down to the -25°C set-point. Using the model it was attempted to eliminate the time periods with ζ was equal to one in superheat control while maintaining a fast pull-down time.

To achieve this aim the model was used to determine the duty cycle that resulted in the maximum ζ value of 0.95 for an EAIT range of -19°C to -27°C and a mass flow rate of CO_2 from

0.0235 kg s^{-1} to 0.0255 kg s^{-1}. These conditions were chosen as they spanned the range of temperature and flow rates at which superheat control was observed in the frozen tests in Chapter 3. It was decided to aim for a maximum ζ value of 0.95 to allow for any error between the model and the results on the experimental system. The results of the model are show in Figure 102 and it can be seen that the relationship between duty cycle and temperature appears to be linear and the even spacing of the lines for the different mass flow rates indicates that the relationship between duty cycle and mass flow rate is also likely to be linear.

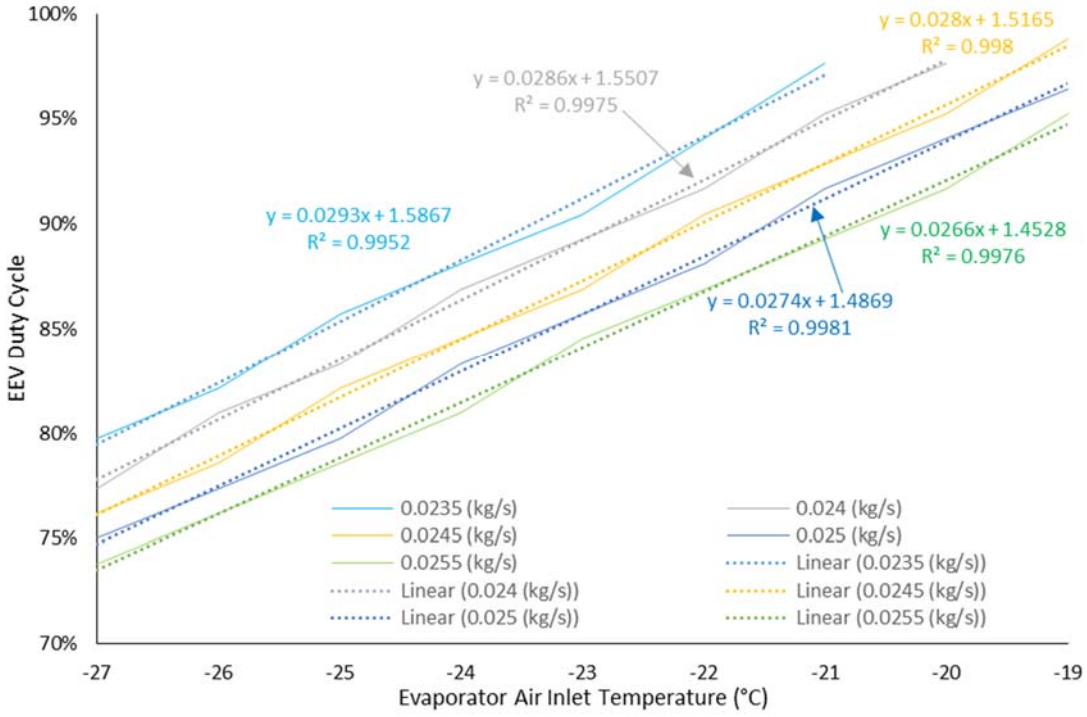

Figure 102: Model Outputs for EEV Duty Cycle Optimization

With the data above a linear regression analysis was performed and a linear fit was found with a maximum error of 1.1%. The equation is given by:

$$EEV\ Duty\ Cycle\ \% = 0.0277.EAIT - 34.4769.\dot{m} + 2.3571 \qquad (5.\ 1)$$

where the duty cycle is limited to 0-100%.

Utilising Equation 5.1 the model for frozen cycle sentry was re-run with an optimized EEV duty cycle for the superheat control period of the initial pull-down. The results in Figure 103 show that the aim of keeping ζ at a maximum of 0.95 was achieved. A comparison of the superheat control periods shows that the EEV was open 89% of the time for the original test and was open 87% of the time for the optimized model. However when the 44% of the time the original test have a ζ value of 1 is taken into account it can be assumed that the pull-down time for the optimized duty cycle would be at least as fast as the original test.

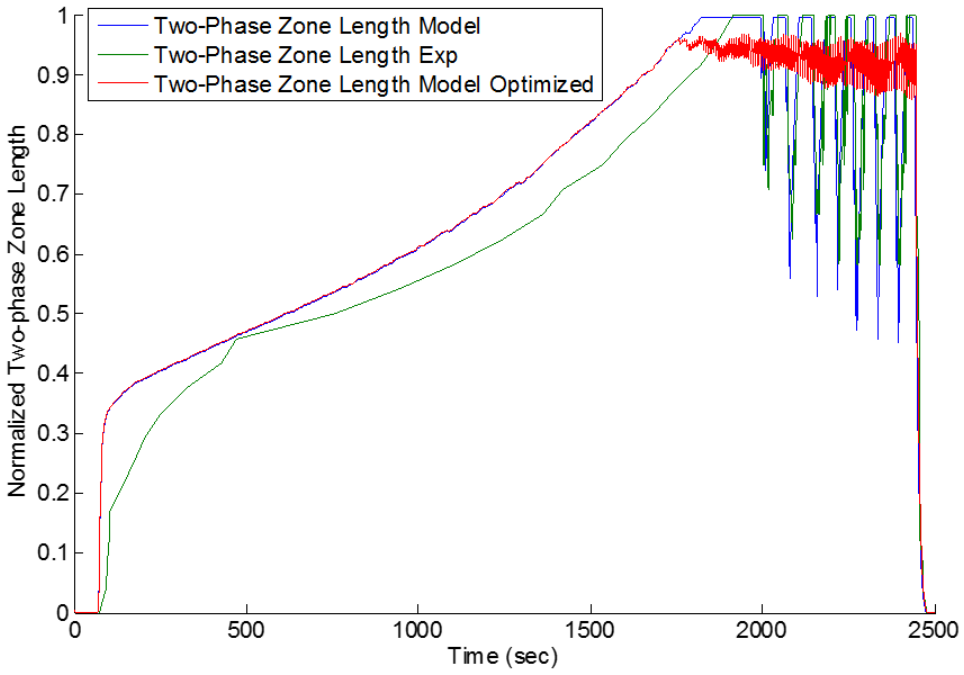

Figure 103: Optimized Two-phase Zone Length Comparison for Frozen Pull-down to -25°C Set-point. Mass flow rate of CO_2: 0.0249 kg s^{-1}

The new control was then trialled experimentally and a comparison with the model output for ζ is shown below in Figure 104. While the correlation with the model during the superheat control section was not without error, the new superheat control from Equation 5.1 achieved a ζ value of less than 1 for 99% of the time the unit was in superheat control and average peak ζ value was close to the target of 0.95 throughout superheat control. The pull-down to -25°C was achieved in 2407 seconds in an average ambient temperature of 26°C which compares favourably with the pull-down times in the frozen tests from Chapter 3 which all took longer in

lower ambient temperatures of 16-17°C with higher mass flow rates of CO_2. This validates the assumption made above that the new control would achieve faster pull-down times.

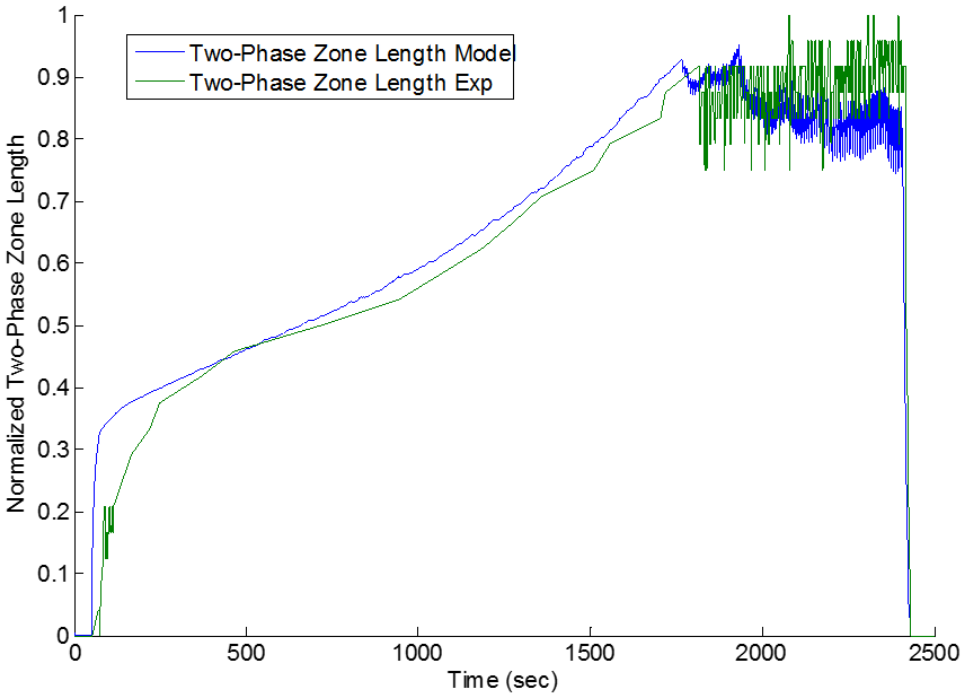

Figure 104: Normalized Two-Phase Zone length comparison for pull-down to -25°C Set-point with optimized superheat control. Mass flow rate of CO_2: 0.0241 kg s^{-1}

5.5 Summary

This chapter achieves the final aims of this work identified in Chapter 1, Section 1.4, Page 8 namely to develop a fully validated model for an open cycle CO_2 system and demonstrate the utility of that model by developing new control to maximize the system efficiency.

In Chapter 2, Section 2.2.2, Page 13 it was identified that studies on moving boundary model are often lacking sufficient validation against experimental results. This chapter presented the validation of the final model developed in Chapter 4, Section 4.9, Page 106 against experimental results for six cases of realistic customer usage; continuous mode, cycle sentry mode with fans on in Null and cycle sentry with fans off in Null all for both fresh and frozen set-points. The data used for the validation covered the expected range of operating temperatures that a typical customer would experience and includes hard transients for start-up, for transitions to

temperature control and for EEV pulsing which were identified in Chapter 2, Section 2.2.2 as important for full validation of moving boundary models.

The correlation of the model for continuous control for both fresh and frozen set-points showed good overall agreement between the model and experiment results with low values of the normalized error residuals for most variables in the dynamic results. All the trends for EROT, EAOT, ECOP and ζ were well represented with only ECIP diverging significantly during the frozen pull-down. The model tended to respond too quickly for all the outputs and some errors remaining especially in the temperature control sections.

In general the fresh and frozen cases of cycle sentry control with fans on in Null showed good correlation of the model with the experimental results. Errors in the speed of the model response were still present but the Null periods and subsequent pull-ups and pull-downs were well captured for all EROT, EAOT and ζ. ECIP and ECOP during the Null periods were not well captured due to the BPR model limitations and these errors are shown in higher NER values for these variables.

Cycle sentry control with fans off showed similar results to the fans on case while the EEV was open but has significant differences for all the model outputs when the EEV closes and the fans turn off due to the lack of heat transfer in the model during this time. In general it was seen that the model is not well correlated to the experimental results for any of the four outputs during Null periods and was not useful for predicting the system outputs. However these errors have no effect on the correlation for the other portions of the test. In this case the qualitative analysis was more useful than the NER comparisons as the large errors during the Null periods dominated and mask the relatively good correlation while the EEV was open.

The utility of the model was then demonstrated by developing a new method of superheat control using the EAIT and the mass flow rate of CO_2 as inputs. The new control was modelled first with one of the frozen tests from Section 5.2.2 and showed good control in terms of limiting the amount of time ζ reached the outlet of the coil without sacrificing the amount of time that the EEV was open to any great degree. Subsequently the control was trialled experimentally and limited the amount of time that ζ reached the coil outlet to only 1% of the total time the unit was in superheat control while still achieving a faster pull-down to the -25°C set-point than any of the other testing outlined in Chapter 5. This new control achieved the aim of maximizing the efficiency of the open cycle CO_2 system during superheat control.

Further aspects of the accuracy and utility of the model are discussed in the next chapter.

Chapter 6 Discussion

The methodology and experimental results from Chapter 3, the model development from Chapter 4 and the model validation and optimization from Chapter 5 are all discussed in this chapter. The experimental testing was compared to the best practice identified in Chapter 2 and the methodology for measuring the two-phase zone length is examined. The performance and efficiency of the open cycle CO_2 system is scrutinised and compared to vapour compression TRU's. The suitability of the system for meeting environmental goals in low emission zones is discussed as well as its advantages over battery powered alternatives. The switched moving boundary model developed is examined with particular attention paid to the changes made to make it function for an open cycle CO_2 system and to additions made to improve the model accuracy. Finally the model utility in terms of speed, accuracy and suitability for other applications is discussed and all of these items are related back to the project motivation from Chapter 1, Section 1.4, Page 8.

6.1 Experimental Setup and Testing

The experimental set-up with the CryoTech CT-15 unit is discussed in this section with some of the unique opportunities and challenges that an open cycle CO_2 system presented being examined.

6.1.1 Measurement of two-phase zone length

The measurement of the two-phase zone length was performed using temperature measurements along the length of the coil to determine when two-phase fluid came in contact with the tube wall. This is similar to a method often employed to measure the superheat in multi-pass evaporator coils although the two-phase boundary is generally static in these situations. The long length of the single pass coil at 32 m in the open cycle CO_2 system allows for reasonably good resolution to be achieved with 25 measurements between the inlet and outlet of the coil, something that is not often possible in multi-pass evaporator coils with shorter pass lengths. No attempt was made in any of the studies examined in Chapter 2, Section 2.2, Page 11 to measure the two-phase zone length.

The measurement of the outside of the copper tube to measure refrigerant temperature had some inherent transient error due to the time taken for the copper to heat and cool but it was not possible to measure the refrigerant directly without effecting the system performance due to the small inner diameter of 8.125 mm of the tubes in the evaporator coil. There was some offset between temperatures measured at adjoining points in the coil after they reached saturation temperature and this was an indication that the soldering of the thermocouples to the tubes may not have been of consistent quality. Regardless of this it was still possible to use these measurements as the change in temperature was more significant than the actual values in identifying the two-phase boundary.

Pressure fluctuations in the coil, with their subsequent temperature fluctuations, also caused issues at times as it was difficult to determine if the source of the temperature fluctuations was from the pressure or from the two-phase boundary passing. Typically pressure fluctuations caused an effect across a large number of measurement points at the same time whereas fluctuations due to the two-phase boundary changes occurred in sequence from one measurement point to the next. This allowed the temperature fluctuations from the pressure changes to be disregarded.

The proposed methodology for measuring the length of the two-phase zone proved successful for both static and dynamic testing. The success in capturing two-phase zone length fluctuations at the correct frequency while the EEV pulsed, Chapter 3, Section 3.8.3, Page 49 demonstrates that this methodology for measuring the length of ζ has a high degree of accuracy even when the two-phase boundary changes direction over short time steps.

6.1.2 Measurement of Cooling Capacity

Measurements of the cooling capacity of the system were carried out as per the procedures developed for the ATP agreement on the International Carriage of Perishable Foodstuffs. The only deviation was that the box was not placed in a fully temperature controlled calorimeter but the ambient temperature variance during the testing was small. The heat applied by the electric heaters to balance the refrigeration load was controlled manually. This is allowed per the test procedure but it is difficult to exactly match the cooling load and a small increase or decrease in the box temperature over the duration of the test resulted.

However the main issue in the testing was attempting to address the drop off in pressure in the CO_2 tank as the liquid was drawn from the tank as this caused a decrease in the mass flow rate

of CO_2 and a subsequent decrease in the cooling capacity. This issue was also identified by the French ATP agency Cemafroid after the last ATP testing was performed on the open cycle CO_2 system with alternative proposals being made to the WP11 2014/16 working group in the UN to attempt to address the issue. In this testing an external cylinder of CO_2 with a pressure regulator was utilized to stabilize the tank pressure. This was only partially successful as the pressure still tended to drop over the duration of the test but it allowed for enough stability to gain an accurate measurement over 1000 s for two of the static test points and over 500 s for the third one and these measurements were used to validate the model.

6.1.3 Measurement of Mass Flow-rate of CO_2

The measurement of the mass flow-rate of CO_2 was performed by measuring the mass of the tank over the duration of the pull-down to set-point while the EEV was fully open and determining the rate of change of the mass during that time. The R^2 values of greater than 0.99 when compared with the linear trend lines and the calculated accuracy of +/- 0.25 % showed that this method for measuring the mass flow rate was valid. However it did rely on the assumption of constant flow-rate being maintained over the duration of the test and it had the limitation that it was not possible to measure the instantaneous mass flow-rate of the CO_2 during EEV pulsing.

An alternative method that was investigated was the use of a coriolis mass flow meter. Initially it was installed in the liquid line between the tank and the EEV but it proved to be inaccurate due to the presence of vapour in the liquid line as these type of mass flow meters are only accurate with single phase flow. An alternative location in the exhaust of the coil where single phase vapour flow was guaranteed also failed as the flow meter caused too great a restriction in the outlet affecting the back pressure regulator and raising ECOP.

Potential solutions for the vapour in the liquid line are better insulation on the CO_2 tank manifold, on the lines to the flow meter and on the flow meter itself though eliminating vapour in the liquid line completely would be difficult.

6.1.4 Measurement of Evaporator Air Outlet Temperature

As discussed in Chapter 3, Section 3.5, Page 33 the measurement of EAOT varied significantly depending on the distance from the face of the evaporator coil and across the surface area of the evaporator coil. There was a temperature difference of 14.8°C measured between a point

approximately 30 mm from the surface of the coil and a point directly in line with it 100 mm further out when the two-phase zone was less than half the length of the coil. This temperature difference indicates that there is a significant amount of mixing of the air coming off the cold tubes in the coil with the air coming off the warmer tubes of the coil in a short amount of space. The shape of the ducting at the air outlet of the coil encourages this mixing by containing the airflow path. This is beneficial to the customer in that it minimizes the risk of extremely cold air freezing produce that is close to the outlet. However the temperature closest to the coil is what is most representative of the model EAOT and that is what is compared with the model in Chapters 4 & 5.

Across the face of the coil the EAOT measurement points saw a maximum difference of 3.2°C. This contributed to some uncertainty as to the correct measurement location to compare with the model outputs. In this case the likely case of the deviation is the layout of the coil which includes tubes 1-4 of the refrigeration circuit as well as tubes 10 and 11 on the first row of the coil. The air coming off tubes 10 and 11 would be warmer than the air off tubes 1-4 in the case where the two-phase region boundary is before row 10 and 11. After the two-phase boundary passed this point the temperature deviation reduced to under 2.1°C until ζ reaches the coil outlet. Since the thermocouple wire used to measure the air temperature was quite flexible it was difficult to precisely locate the measurement point in front of row 1 of the coil which would be the most comparable location to the EAOT for the counter flow heat exchanged used in the model. It is also possible that the thermocouple wire moved around in the airflow generated by the evaporator fans. As a result it was determined that the average of the three EAOT measurement points just off the right, middle and left header plates of the coil positioned in front of row 1 was the most accurate measurement to validate the model.

6.2 System Performance

Using the data obtained with the experimental test rig in Chapter 3, Section 3.7 - 3.11, Pages 37 - 72 it was possible to analyse the performance of the open cycle CO_2 system and make some comparisons to vapour compression TRU's.

6.2.1 Cooling Capacity

The system was designed in such a way that the evaporator coil over-sized for fresh set-points in the region of 0°C. As can be seen in the measurements of the two-phase zone length in Chapter 3 only about half of the coil is utilized in the pull-down to set-point for these conditions and less than 20% is used during fresh continuous modulation. While this would seem to be a waste of resources it does allow for a large capacity to be realized for frozen conditions where the temperature difference between the air and the refrigerant is less. The experimental results in Chapter 3, Section 3.7, Page 37 shows that there is little difference between the refrigeration capacity at 4°C and -13°C box temperatures and this should hold true as long as ζ remains less than 1. The model indicates that ζ would reach the coil outlet at an EAIT temperature of -19°C for the mass flow rate of 0.0252 kg s^{-1} used for Test 3 in Chapter 3 and that the capacity would remain at approximately 8 kW. At temperature below this the system would start to exhaust two-phase CO_2 or pulse the EEV for superheat control and the capacity would start to decrease. This is a large advantage over the capacity figures for traditional vapour compression systems where the refrigeration capacity can drop by over 40% for frozen set-points [82] resulting in much faster pull-downs for open cycle CO_2 systems with similar size coils and fresh refrigeration capacity figures.

The open cycle CO_2 system is extremely efficient at converting the latent heat in the CO_2 into cooling capacity. Apart from the loss in enthalpy from the liquid boiling in the pipe while it travels from the tank to the inside of the insulated box and the pressure drop along that pipe all the latent energy from the liquid CO_2 ends up inside the box when the two-phase region is less than the full length of the coil. In Chapter 3, Section 3.3, Page 29 it was shown that poor insulation of the liquid line can result in vapour quality increases of up to 4% but a well-insulated liquid line could reduce this to only 1%. There is also some loss of sensible heat of the vapour CO_2 at the exhaust as the refrigerant temperature never matches the air temperature exactly. For the three static tests in Chapter 3, Section 3.7, Page 37 the efficiencies are shown below in Table 7.

Table 7: Open Cycle CO_2 system Efficiencies

Test #	**1**	**2**	**3**
EAIT	4.4	-9.5	-12.96
CO_2 Tank Enthalpy	112	112	115
Enthalpy at EEV	114	113	116
Enthalpy at ζ=1	432	432	432
Enthalpy at Coil Exit	479	466	459
Enthalpy if EROT = EAIT	482	470	467
Total Enthalpy Loss	5	5	9
Efficiency	99%	99%	97%

The dynamic tests with frozen set-points where the unit is in superheat control would have lower efficiency numbers as they exhaust two-phase CO_2 at times but if this could be eliminated the efficiency numbers would be similar to the static results presented above. In any case improvements to the system efficiency should be concentrated on liquid line insulation during the unit installation and on improving the superheat control to prevent two-phase CO_2 being exhausted.

6.2.2 Discharge air temperature control

Discharge temperatures below freezing can be an issue when transporting sensitive produce such as flowers or fresh fruit and vegetables. As a result it is important to be able to control the EAOT especially for fresh set-points. With evaporating temperatures as low as - 51°C in the open cycle CO_2 system this would appear to be a difficult task. However the short length of ζ for fresh set-points limits the effects of these low evaporating temperatures and result in EAOT temperature that are in the region of 15-18°C colder than EAIT during pull-downs. This air is then mixed with warmer air from other parts of the coil before it reaches the produce to a temperature not more than 13°C lower than EAIT as described in Section 6.1.4. If this 13°C difference is still too much, the customers also have an option to select a mode which limits the EAOT temperature to floor limit below the set-point, defaulted to 2.2°C, during pull-down just as it does in temperature control mode. This selection limits the cooling capacity of the system when the floor limit is reached for EAOT and therefore has the knock on effect of increasing the pull-down time to set-point but offers sufficient protection from freezing temperatures for sensitive produce.

6.2.3 Air Inlet Temperature control

The system controls the EAIT to the set-point to within +/-0.25°C in continuous control once EEV pulsing starts and the temperatures settle for both fresh and frozen set-points. Comparable control can be achieved on vapour compression systems for fresh set-points with an electronic throttling valve (ETV) [82] but, as the valve is generally fully open for frozen set-points, tight control at these box temperature is not possible. For this reason heat/cool cycles are used in that case for continuous temperature control and result in substantially higher temperature swings than the +/-0.25°C achieved at -25°C for the open cycle CO_2.

The transition from pull-down to temperature control results in an increase in EAIT which is not ideal but is driven by the requirement to keep EAOT to less than 2.2°C below the set-point in this type of control. However EAOT appears to increase by more than this so further improvements could be made here to optimize temperature control by removing the overshoot of the 2.2°C limit.

In cycle sentry control there tends to be some overshoot of the set-point and the re-start temperature that occur after the EEV closes and again after it opens. For the case where the fans are off in Null mode this overshoot once the EEV opens again is considerable. Anticipating the overshoot and closing or opening the EEV early would be one way to counter this. However the factors that affected the overshoot would need to be studied in detail to make sure the timing of this is correct.

Overall the control of EAIT to the set-point for the open cycle CO_2 system is comparable with vapour compression systems for cycle sentry and continuous fresh modes and is substantially better for the continuous frozen mode.

6.2.4 Superheat Control

The function of superheat control in the open cycle CO_2 system was to prevent two-phase CO_2 from exiting the evaporator coil and in this regard the present control is only partially successful. In one example 44% of the time when the EEV was pulsing during superheat control, ζ was measured to be 1. It appears that the PI controller that was used has not been tuned correctly and that the lack of a derivative term results in oscillations around the superheat set-point. The significant delay between the opening and closing of the EEV and the response at the outlet of the coil could also be a factor.

Solutions to the superheat control problems seen in experimental testing in Chapter 3 have been devised using the system model and will be discussed in Section 6.4.3.

6.2.5 Suitability for LEZ's

As mentioned in Chapter 1, Section 1.1, Page 1 many cities in Europe and throughout the world are introducing LEZ's to help address the effects of NO_x and CO_2 pollution. The majority target diesel engines and several cities have announced that they will be banning diesel cars in the near future. If these bans also affect HDV's and their TRU's then open cycle CO_2 systems are a potential solution.

It is interesting then to compare them to one potential alternative solution, a battery powered vapour compression system. In essence the tank full of liquid CO_2 and the battery serve the same purpose, they store energy for their refrigeration system. While Li-ion batteries pack more energy per kg than liquid CO_2 at, 110-160 W h kg^{-1} vs 63-92 W h kg^{-1}, liquid CO_2 has other advantages. Even with the vacuum insulated tank the cost is lower for CO_2 systems, which makes them comparable in cost to diesel TRU's, although this advantage may not remain for long due to the rapidly decreasing cost of Li-ion batteries. The re-charge time for CO_2 is a fraction of what is needed for batteries as a 430L tank can be filled in under 15 minutes whereas recharging batteries sufficient to power a TRU would take hours. Since the CO_2 is exhausted to atmosphere the weight of the tank also reduces throughout the day unlike batteries. Finally the open cycle CO_2 system is a proven technology which has been scaled as needed for use from small vans to full length articulated trailers. Currently only the smallest vans have vapour compression systems that are capable of being powered only from a battery. It is likely that the battery technology will improve and compete with open cycle CO_2 systems in time but until they are proven and readily available open cycle CO_2 systems are the one of the only option for LEZ's whe re diesel TRU's are not allowed.

6.3 Model Development

The approach used in this work was to develop a model of the open cycle CO_2 system from modelling techniques used by others and compare with experimental results to identify problem areas within the model for further development. The original techniques and the

improvements made based on the comparisons to experimental testing are discussed in this section.

6.3.1 Baseline Model

The switch moving boundary technique was chosen to model the open cycle transport refrigeration system under study. It was selected as it had been successfully used in the past to model transport refrigeration systems and because it was faster than the alternative finite difference technique. Alternative void fraction models were examined in Chapter 2, Section 2.7, Page 20 to determine if more accurate correlations could be implemented but it was determined that there was insufficient benefit for the increased complexity of either the Lockhart–Martinelli or the Rouhani-Axelsson models and the Zivi correlation was retained for the moving boundary evaporator model.

An additional superheated only representation was added to the evaporator model to deal with the two-phase zone length going to zero on closing or pulsing of the EEV. Without this the model tended to slow-down considerably with decreasing time-steps during the time period when very short ζ lengths were present. The switching criteria for this new evaporator representation were taken from similar mode transitions used in switched moving boundary condenser coils [74]. The new superheated only resolved the issues with short ζ lengths resulting in fast computation during cycle sentry Null periods.

6.3.2 Model Additions and Accuracy

Pressure Drop

The pressure drop correlation was introduced to calculate a realistic evaporator coil outlet pressure which could be then used as an input to the back pressure regulator model. The average pressure in the evaporator was still used for the calculation of the heat transfer in the coil but the calculated outlet pressure was also used in the calculation of the refrigerant outlet temperature.

In general ECOP was controlled well by the BPR model but the pressure drop correlation tended to over-estimate the total pressure drop in the coil. This resulted in higher ECIP values in the model than were measured in the experimental results for the pull-down tests in Chapter 3, Section 3.9, Page 52. This error tended to increase with the length of ζ indicating that the error was primarily in the calculation for the two-phase region. While these errors in ECIP were

significant they were not unexpected as the correlation used was developed for HFC refrigerants and the Da Silva Lima [57] acknowledged that errors in calculations of two-phase pressure drop can be as large as 50%. The correlation was chosen primarily due to its inclusion of the effects of u-bends in the two-phase pressure drop but further work to update it for CO_2 at the reduced pressures typical of an open cycle CO_2 system would lead to greater accuracy.

For both ECIP and ECOP more significant errors were seen during the temperature control portions of the tests in Chapter 5. In some cases the ECIP measurements were determined to be faulty due to blockages of the sensors caused by low pressures close to the coil inlet and the formation of dry-ice. For the cycle sentry tests the issues were as a result of the models failure to accurately allow the pressure to drop below the BPR setting during the Null periods.

The normalized error residual for the pressures were consistent with the qualitative analysis for the pull-down portions of the test but became less useful when large errors occurred during the temperature control periods. The large magnitude of the NER where either the experimental results or the model results were faulty prevented any useful conclusions being drawn for sections where the correlation between the experiments and the model was good. For these tests the qualitative analysis was more valuable. Where the NER did prove useful was in comparing variables of similar magnitudes which were presented on different scales as was the case for some of the temperature results.

While large errors were seen in some cases due to issues with both the model and the experimental testing the main objective of obtaining an accurate ECOP for the model was achieved.

Refrigerant Property routines

The replacement of the look-up tables for calculating refrigerant properties with a DLL to obtain the correction refrigerant properties directly from RefProp was a significant improvement on the stability and accuracy of the model. This negated the risk of linear interpolation across the saturation curve where the refrigerant properties behave in a non-linear way due to the latent heat. However using the DLL still has limitations as it is unable to calculate fluid properties below the triple point were solid CO_2 forms. As a result it was not possible to drop the pressure in the evaporator below 518 kPa and this limited the accuracy of the pressure correlations during cycle sentry Null periods.

Refrigerant heat transfer coefficient and PAF's

The original refrigerant side heat transfer coefficient model that were used for HFC refrigerants gave rise to unrealistic values for the two-phase heat transfer coefficients causing the model to become unstable. A review of the literature determined that the correlations by Cheng et al. [54] were the best available that would work with a moving boundary model CO_2 model. When introduced they gave more realistic values solving the stability issue. However comparisons of the model to the results from the experimental testing indicated that the correlation still had significant error for an open cycle CO_2 system in real world conditions and a performance adjustment factor (PAF) was used to good effect to address these differences.

The differences between the data set used to develop the correlation, where the saturation temperatures were between -28°C and +25°C and the reduced pressure was only down as far as 0.21 for a small portion of their data, compared to saturation temperatures in the open cycle CO_2 system of between -53°C and -45°C with reduced pressures of between 0.08 and 0.11, are likely to have been significant factors in the error. The averaging of the calculated values for the different flow regions within the two-phase region would also have created some error as there are large differences between annular, stratified, mist flow and dry-out region values. The reduced pressures for the open cycle CO_2 system are more comparable with standard vapour compression systems so it is reasonable to assume that lower values of the two-phase heat transfer coefficient would result and this, along with the averaging of the flow regime values, could account for up to 50% of the PAF value used.

The simple J factor correlation to model the effects of frost build-up on the evaporator coil would also have been be a source of error. Frost can have a complex effect on heat transfer as it can increase effective heat transfer area while also insulating the copper tube from the air. The effects depend on humidity levels, EAIT temperatures and coil temperatures and can change over time as the frost density changes. Due to the low evaporating temperature, frost on the open cycle CO_2 coil was more prevalent than with vapour compression systems with higher evaporating temperatures. Due to the complexity, modeling these effects was deemed beyond the scope for the project and instead the PAF on the two-phase heat transfer coefficient was used to address this error. This error could account for another 25% of the PAF used.

Although it was determined in Section 4.7 Page 100 that the air side heat transfer was not the main source of error in the length of ζ, the complex 3D geometry of the counter cross-flow heat exchanger used for the evaporator in the open cycle CO_2 system when compared with the

assumption of single pass cross flow arrangement would likely have been a source of error and could account for the remaining 25% of the PAF utilized.

With the PAF it was possible to account for the majority of the error but, as a significant portion of the error was not due to the two-phase heat transfer, differences between model and experimental data were still present.

Calculation for EROT

In the initial model (Model 1) comparisons between measured and simulated results made in Chapter 4, Section 4.4, Page 89 showed large errors for EROT with values far exceeding EAIT which is not physically possible in a counter flow heat exchanger. The baseline model used a very simple assumption that the enthalpy varied linearly along the length of the two-phase zone and hence the enthalpy at the outlet was based on the calculated average enthalpy in the zone and saturated liquid enthalpy at the two-phase region boundary. The temperature was then calculated based on this outlet enthalpy and the pressure. In reality the refrigerant outlet temperature is linked to the air that flows over this part of the coil which in a counter flow heat exchanger is the inlet air. With this in mind a new calculation of EROT was developed based on the same ε-NTU method that was used for the air outlet temperature calculation. This correlation was developed for static models so some adjustments were needed to the model to allow for the heat transfer to be made between the refrigerant and the tube wall rather than to the air to make it suitable for the dynamic moving boundary model.

Results with the new calculation were significantly better with small amounts of error in the final model (Model 4) for the static tests, good qualitative agreement for the EROT parameter during dynamic pull-down testing comparisons and an NER that was a factor of 45 lower than Model 1. For the customer duty cycles in Chapter 5 the fresh tests for the most part showed comparable accuracy to the simpler pull-down in terms of NER. By comparison the frozen tests demonstrated larger values of NER when compared to simulated results due to error that was present once ζ reached the coil outlet as the two-phase fluid was at the saturation temperature and the experimental measurement was of the outside wall temperature of the tube. The fluctuations in temperatures as a result of the liquid droplets in the mist flow region of the two-phase region hitting the tube wall as the two-phase boundary approached were also not captured in the model due to the lumped parameter moving boundary model which averaged the outputs in the two-phase and superheated zones.

The exception to the high level of accuracy for both fresh and frozen conditions was the testing with fans off in Null periods where the NER was substantially higher than the other cases. This is due to the model being unable to take account of the heat transfer without mass flow of air and refrigerant.

Transport Delays

One simple addition that had a big impact on the model accuracy was the implementation of a delay to the EEV opening to simulate the time needed for the liquid CO_2 to travel from the tank to the EEV and coil inlet. While this delay was not strictly correct, the only parameters it had a negative effect on were the inlet and outlet pressures and these were not modelled correctly with only vapour in the liquid line in any case. The delay introduced was only for start-up as this was when the liquid had the longest time to travel from the tank. However long periods of time with the EEV off such as cycle sentry Null should also see some impact. The vapour bubble seen in the experimental results which causes ζ to go to zero shortly after the EEV opens again after a Null periods may be a related event. A more complex model that accounts for the transporting of the liquid in the pipe and includes heat transfer through the pipe walls could accounts for both of these phenomenon as well as the increase in enthalpy discussed in Section 6.2.1.

Evaporator Air Outlet Temperature

No changes were deemed necessary to the model with regards to the air outlet temperature as the correlation of the model from the start with the experimental results was reasonably good. Taking into account the variability in the measurements of EAOT in the experimental results discussed in Section 6.1.4 and the good correlation of the shape of this parameter in the dynamic results comparison it was determined that no further improvements could be made. The only significant error occurred with the model predictions in cycle sentry null periods with the fans off. In this case the model assumed that the EAOT was equal to the wall temperature in the two-phase zone resulting in substantial NER values which were several orders of magnitude larger than any other test.

Normalized Two-Phase Length Correlation

This work presented validation of the two-phase zone length for a moving boundary model against experimental results for the first time in literature. Some issues with regards to the experimental measurements were discussed in Section 6.1.1 but the potential inaccuracies as a result are small so the comparison to the model was still valid. The length of ζ proved to be a useful parameter in tuning the model to get better correlation for other outputs such as EROT and cooling capacity. Once the tuning was completed the final model showed good agreement for ζ for the static and dynamic testing. The NER decreased substantially from 0.0561 to 0.0029 during the model development in Chapter 4. In Chapter 5 the NER for the fresh tests tended to be higher than the frozen tests as the absolute values of the experimental results were close to zero resulting in a very small denominator in the calculation. However both fresh and frozen results showed good qualitative agreement between the model and the experimental results even with EEV pulsing for superheat and temperature control. Cycle sentry null periods with fans on were well correlated but Null periods with fans off were once again affected significantly by the failure of the model to predict the heat transfer in these situations.

The use of experimental testing to validate the length of the two-phase zone for a moving boundary model proved to be of benefit and could be useful in other applications with long coils that allow for sufficient measurements along length of the coil to be made.

6.3.2 Model Response Time

The model response time was effected by the assumption that the momentum equations could be neglected in the moving boundary model. The result was a model that responded instantaneous to EEV opening and closing events along the full length of the coil. In the experimental testing results delays of up to 20 s were seen between valve openings and parameters such as the refrigerant outlet temperature reacting. Valve closing events tended to have a shorter lag close to 10 s. The reaction times for the two-phase zone length measurements tended to vary based on the location of the two-phase boundary as would be expected. When ζ was short it exhibited little or no lag with the EEV closing but when ζ was close or equal to 1 the lag tended to be similar to that seen for the refrigerant outlet temperature.

During pulsing of the EEV the model response error was most significant particularly for temperature control since the time periods of the pulses were only 6 s in duration. Superheat control pulsations tend to be longer due to the issues with oscillations discussed in Section 6.2.4 and the impact here was limited to the start of the ζ oscillation.

The instantaneous response of the model also affects the accuracy of the magnitude of the simulated output parameters since the physical system took time to respond to changes.

The overall effects of the response error for the model correlation to the experimental results is small and it does not have a significant effect on the NER value for any of the parameters.

6.4 Model Utility

This section discusses how useful the model developed in Chapter 4 is for predicting system behaviour and developing system control as well as how easily it could be extended to work for other systems.

6.4.1 Suitability for predicting system behaviour

The model in its current form gives reasonably good cooling capacity predictions which would be useful in determining if the system has enough cooling capacity to maintain temperature for different cargo box types and ambient temperature ranges. The NER values show that the predications of the EAOT for a pull-down to set-point where the EEV is fully open have only small errors so would also be suitable for use in predicting effects like top-freezing of produce that can occur. The EROT predictions are also well correlated with the experimental results for the final Model 4 with low values of NER in most cases. This is important as EROT and ECOP are often used for superheat control.

The issues with the model response time limit the utility of the model once the EEV starts pulsing for either superheat or temperature control but EROT and EAOT are still predicted reasonably well during these control modes and could again be useful.

ECOP is well predicted throughout, with the exception of cycle sentry Null periods, but the error in the two-phase zone pressure drop mean that ECIP could not be used with any confidence.

6.4.2 Model Speed

As mentioned in Chapter 2, Section 2.3.2, Page 16 model speed is one of the advantages that the moving boundary model is determined to have over the finite difference method. For this model, running on a PC with an Intel i7 6820HQ CPU running at 2.70 GHz with 16.0 GB of RAM, speed were significantly quicker than real time in most cases. For the dynamic pull-down and for the cycle sentry comparisons the model ran between 2.1 and 5.4 times faster than real time

with the pulsing for superheat control slowing down the frozen cycle sentry models. The continuous fresh models ran slower at 1.5 times faster than real time. However the frozen continuous model was 1.9 times slower than real time due to the larger amount of EEV pulsing in superheat and temperature control. The EEV pulsing results in smaller time steps needing to be taken by the variable step solver used which results in the slower times.

These run times do depend on the load from other applications on the PC but the fact that the models can be run substantially faster than real time in most cases increases its usefulness when compared to experimental testing.

6.4.3 Suitability for control algorithm development

The comparison between experimental test results and the model outputs show that EAOT is well correlated. In its current form EAIT is an input to the model but a cargo box model from the Thermosys library could be added to allow for it to be modelled also and it is likely that similar accuracy to EAOT could be achieved. Doing so would make the model suitable for developing temperature control algorithms that depend on the EAOT and EAIT measurements.

The use of the model to develop a new method of superheat control based on EAIT and the mass flow rate of CO_2 in Chapter 5, Section 5.4, Page 137 showed that the model can be used successfully to create control algorithms. The new superheat control resulted in two phase CO_2 exiting from the evaporator coil outlet less than 1% of time compared with 44% of the time for the previous control algorithm. This improvement was achieved while still maintaining the refrigeration capacity to pull-down the cargo to the -25°C set-point. When the higher heat load from the higher temperature difference between ambient and box temperatures in the optimized test is compared with the original test and that effect is combined with the lower mass flow rate of CO_2 in the optimized test, it can be concluded that the new method of superheat control is significantly more efficient in terms of CO_2 consumption than the previous superheat control and would result in quicker pull-down times to set-points below -20°C.

The utility of the numerical model came to the fore when developing the new superheat control algorithms when design iterations were easily performed over a wide range of EAIT's and mass flow rates.

6.4.4 Suitability of model for other applications

The model is easily adaptable to the different size evaporator coils that are utilized in the CryoTech range or future designs which may be planned. Different size EEV's and evaporator fans could be accommodated through the introduction of different mass flow rates of refrigerant and air respectively. Some tuning of the PAF is likely to be necessary, though this could be performed with little effort by completing a dynamic pull-down test and matching the time taken for ζ to reach the coil outlet.

Modelling other refrigerants such as N_2 in an open cycle would take more effort as the refrigerant heat transfer coefficients would not be suitable and the refrigerant property routines do not currently support this refrigerant. The back pressure regulator would also not be needed in this case.

Some of the improvements to the model such as the superheat only single zone representation, the pressure drop model and the refrigerant outlet temperature calculation would be beneficial if re-worked into the original model for HFC refrigerants.

6.5 Summary

The main aims of this work, as outlined in Chapter 1, Section 1.4, Page 8 were to examine the characteristics of the open cycle CO_2 transport refrigeration system in detail, to analyse the system efficiency, to develop a validated model of the system to utilize for maximizing that system efficiency and to provide a tool for future system development. In these aims the work has been a success.

An experimental test rig was developed that measured main system outputs; EROT, EAIT, EAOT, ECIP, ECOP, mass flow-rate of CO_2 and cooling capacity, based on best practices from other studies outlined in Chapter 2, Section 2.2, Page 11. The two-phase zone length was determined experimentally for the first time in such a system by measuring the temperatures at the u-bends along the coil and interpreting these measurements to indicate where the boundary was at any given time.

Experimental tests were carried out at both static conditions and for real world dynamic system modes that would be used by customers in the field. These tests allowed for the performance of the system to be analysed including its efficiency at using the liquid CO_2 to cool the cargo space, the ability of the system to control EAIT and EAOT, and the superheat control which was

to prevent two-phase fluid being lost out the exhaust. In all of these bar the superheat control the open cycle CO_2 system was demonstrated to have comparable or better performance than vapour compression TRU systems.

A switched moving boundary model of the system was developed from a baseline model developed for vapour compression systems. Additions such as evaporator pressure drop, a new method for obtaining the refrigerant properties, a back pressure regulator model, new refrigerant heat transfer coefficient correlations and a superheated only single zone representation were needed to get the model to work correctly. Further developments took the form of a new calculation for the refrigerant outlet temperature, the addition of a performance adjustment factor (PAF) to correct for heat transfer errors and the introduction of a transport delay for the EEV. These improved the accuracy, resulting in a model that was closely correlated to the experimental results for both static and dynamic models.

The resultant model was validated using the data from the experimental testing for dynamic conditions including hard transients such as start-up and shutdown. The model was analysed quantitatively by comparing the static results and the normalized error residual for the dynamic results. The shape of the outputs for the dynamic results were also analysed qualitatively and this proved to be more useful in situations where large errors for certain portions of the test masked the correlation for the other periods of the test. An example of this was presented for the cycle Null tests where issues were identified with the correlation during Null with fans off.

In general it was found that the model was well correlated to the experimental testing for the static and dynamic results with the exception of cycle sentry Null periods and the issues identified with the model response time after EEV opening and closing events. As a result the model is useful for predicting the slow dynamics of the system such as the EROT and EAOT temperatures but is less useful for the faster dynamics that occur after the EEV starts pulsing. The speed of the model also allows for faster than real time simulations to be performed for most types of control.

The model would be easily adapted to work with other sizes of evaporator coils in an open cycle CO_2 system. A change of refrigerant to N_2 would require further model development. Models of vapour compression systems could benefit from some of the model improvements made during this work.

Chapter 7 Conclusions

The aims for this study were to examine an open cycle CO_2 system in detail in order to characterize performance and efficiency and to accurately model the system dynamics with a view to improving control and maximize system efficiency. To these ends the project has been successful. A comprehensive analysis of the system performance has demonstrated the benefits over other TRU's, the high efficiency of the system when ζ remains less than 1 but also the short comings of the system in terms of superheat control. This analysis was followed by the development of a model which showed good accuracy for the majority of operating modes. Only the model outputs for cycle sentry Null mode with fans off showed significant deviations from measured experimental results. The final task of exploiting the model to improve system efficiency was achieved by significantly reducing the periods when ζ reached unity during superheat control. This resulted in faster pull-down times to the -25°C set-point temperature while consuming less CO_2.

7.1 Summary of Work

The experimental analysis of the open cycle CO_2 system was performed on a Thermo King CryoTech CT-15 with an S-3 CT remote evaporator. The system was instrumented with thermocouples, pressure transducers, load cells and a power meter to measure EAIT, EAOT, EROT, coil temperatures, EEVIP, ECIP, ECOP, mass flow rate of CO_2 and refrigeration capacity. These measurements were used to characterise the system in both static and dynamic tests typical of customer applications.

Through these measurements the system was analysed and the efficiency of the system in utilizing the latent and sensible heat in the liquid CO_2 for the three static tests was determined to be 97% or greater. Discussions on temperature control determined that the control of the discharge air temperatures was sufficient to protect loads from top freezing where necessary and that the control of the EAIT was as good as or better than anything else available on the market especially for the frozen continuous modes of operation.

The systems suitability for LEZ's, in terms of PM, NO_x and noise emissions was discussed. The benefits over battery power vapour compression systems in terms of technological maturity, refuelling times, cost, scalability and weight were also highlighted.

The development of a switched moving boundary model was presented with additions to the model such as a back pressure regulator model, pressure drop within the evaporator coil, updated refrigerant heat transfer coefficient calculations and a new method of obtaining the refrigerant properties, all of which were needed to make the model suitable for the open cycle CO^2 system. Further enhancements were then added to improve the model based on the correlation of the model outputs with the results from experimental testing. The improvements included a new calculation for the refrigeration outlet temperature, the addition of PAF's to improve the correlation of the two-phase refrigerant heat transfer coefficients and the addition of a transport delay on system start-up.

With the final model (Model 4) further comparisons between simulated and experimental data were made for dynamic system tests typical of real world customer usage. Good correlation was shown for EAOT, EROT, ECIP, ECOP and ζ for continuous control and for cycle sentry control with fans on in Null mode at a fresh set-point of 0°C and a frozen set-point of -25°C. Some issues with the model were identified for cycle sentry control with fans off in Null mode as the model failed to correctly model the system once refrigerant and air mass flows ceased.

Optimization of the superheat control, which had been identified as an issue in Chapter 3, was performed using Model 4. Using linear regression analysis, a direct relationship between EAIT and mass flow rate when ζ reached 0.95 was established. This equation was then incorporated into the control in numerical simulations of the frozen cycle sentry tests before testing on the actual system. The results from the experimental testing corroborated the numerical simulation results, showing a reduction from 44% to 1% in the amount of time the two-phase boundary spent at the coil outlet. In addition both the pull-down time to achieve set-point and CO_2 consumption were reduced.

7.2 Recommendations for Future Work

Future work on the simulation of the open cycle CO_2 system should focus on extending the model to the smaller S-2 remote evaporator to analyse the scalability of the model. Multi-

temperature systems which utilize more than one remote evaporator could also be investigated to determine the effects of supplying CO_2 to evaporators in parallel.

The utility of the model could be improved by modelling the other aspects of the system such as the EEV, the CO_2 tank and the cargo box so that less input data is required by the user upfront. Improvements in the correlation of the evaporator coil two-phase pressure drop would be needed to obtain the correct outlet pressure at the EEV as discussed in Chapter 6, Section 6.3.2, Page 150. A CO_2 specific correlation that took into account u-bends should show improvements in this accuracy.

The heat transfer that occurs in the evaporator coil with no mass transfer of air or refrigerant could be examined to address the errors shown in Chapter 5, Section 5.3, Page 129 for the cycle sentry with fans off in Null mode case. Further improvements to the two-phase refrigerant heat transfer coefficient correlation would lessen the need to rely on PAF's for accurate results although it is likely that some error would still remain due to the other sources such as the lumped parameter nature of the moving boundary model.

References

[1] Urban Access Regulations in Europe, http://urbanaccessregulations.eu/overview-of-lezs, accessed 30-May-2018.

[2] Volkswagen Clean Air Act Civil Settlement, https://www.epa.gov/enforcement/volkswagen-clean-air-act-civil-settlement, accessed June 2018.

[3] Griffin A.: Rome to ban diesel cars to combat air pollution by 2024, Independent Newpaper, 2018.

[4] London's 'Low Emission Zone' for non-road mobile machinery, http://nrmm.london/, accessed June 2018.

[5] European Commission: Regulation (EU) 2016/1628 of the European Parliament and of the Council of 14 September 2016 on requirements relating to gaseous and particulate pollutant emission limits and type-approval for internal combustion engines for non-road mobile machinery, 2016, 1628.

[6] Reducing CO_2 emissions from Heavy-Duty Vehicles, https://ec.europa.eu/clima/policies/transport/vehicles/heavy_en#tab-0-0, accessed 04/03 2018.

[7] European Commission: Regulation (EU) No 517/2014 of the European Parliament and of the Council of 16 April 2014 on fluorinated greenhouse gases, 2014, 517.

[8] European Commission: Directive 2006/40/EC of the European Parliament and of the Council of 17 May 2006 relating to emissions from air conditioning systems in motor vehicles, 2006, 40.

[9] PIEK, http://www.piek-international.com/english/, accessed May 2018.

[10] Public Consultation on an evaluation and possible revision of the Outdoor Noise Directive 2000/14/EC, https://ec.europa.eu/info/consultations/public-consultation-evaluation-and-possible-revision-outdoor-noise-directive-2000-14-ec_en, accessed June 2018.

[11] Engberg P., Widheden J., Eriksson E., Hallberg L.: Life Cycle Analysis of temperature controlled foods by truck transport, 2002.

[12] Jones F.M., Numero J.A.: Air conditioner for vehicles. Patent US2303857 A 1942.

[13] Tassou S.A., De-Lille G., Ge Y.T.: Food transport refrigeration – Approaches to reduce energy consumption and environmental impacts of road transport, Applied Thermal Engineering, 2009, 29, (8), pp. 1467-1477.

[14] Kane J.J., Matter A.P.: In transit Liquefied Gas Refrigeration System. Patent US3287925 A 1966.

[15] Nielsen D.M.: Refrigeration system with carbon dioxide injector. Patent US4399658 A 1983.

[16] Martin P., Moody B.: Refrigeration apparatus. Patent US3802212 A 1972.

[17] Tyree L.J.: CO_2 Cooling of Vehicles. Patent US4045972 A 1977.

[18] The Friendly Side of CO_2Sustainable CO_2 technologies help the environment. , http://www.r744.com/files/pdf_417.pdf, accessed 04/11 2017.

[19] Sustainable Freight: Pathways to Zero and Near-Zero Emissions– A Discussion Document. , https://www.arb.ca.gov/gmp/sfti, accessed 04/11 2017.

[20] Rai A., Tassou S.A.: Environmental impacts of vapour compression and cryogenic transport refrigeration technologies for temperature controlled food distribution, Energy Conversion and Management, 2017, 150, pp. 914-923.

[21] Environmental Impacts of carbon dioxide and dry ice production. , http://ecojetinc.com/ecopress/wp-content/uploads/2012/10/EIGA-Environmental-Impact.pdf, accessed 04/011 2017.

[22] United Nations: Agreement of the International Carriage of Perishable Foodstuffs and on the Special Equipment to be Used for such Carriage, 2015.

[23] Jia X., Tso C.P., Jolly P., Wong Y.W.: Distributed steady and dynamic modelling of dry-expansion evaporators: Modèlisation du régime stable et du régime transitoire des évaporateurs à détente sèche, International Journal of Refrigeration, 1999, 22, (2), pp. 126-136.

[24] Donnellan W.: Investigation and Optimization of Demand Defrost Strategies for Transport Refrigeration Systems. Ph. D, Galway Mayo Institute of Technology, 2007.

[25] Jain N.: Dynamic Modeling and Validation of a Commercial Transport Refrigeration System. M. Sc, University of Illinois at Urbana-Champaign, 2006.

[26] Rasmussen B.P.: Dynamic modeling for vapor compression systems—Part I: Literature review, HVAC&R Research, 2012, 18, (5), pp. 934-955.

[27] Rasmussen B.P., Shenoy B.: Dynamic modeling for vapor compression systems—Part II: Simulation tutorial, HVAC&R Research, 2012, 18, (5), pp. 956-973.

[28] Li B., Alleyne A.G.: A dynamic model of a vapor compression cycle with shut-down and start-up operations, Int. J. Refrig., 2010, 33, (3), pp. 538-552.

[29] Li B.: Dynamic Modelling and Control of Vapor Compression Cycle Systems with Shut-down and Start-up Operations. M. Sc, University of Illinois at Urbana-Champaign, 2004.

[30] Yao Y., Wang W., Huang M.: A state-space dynamic model for vapor compression refrigeration system based on moving-boundary formulation, International Journal of Refrigeration, 2015, 60, pp. 174-189.

[31] Pangborn H., Alleyne A.G., Wu N.: A comparison between finite volume and switched moving boundary approaches for dynamic vapor compression system modeling, Int. J. Refrig., 2015, 53, pp. 101-14.

[32] Schurt L.C., Hermes C.J.L., Neto A.T.: A model-driven multivariable controller for vapor compression refrigeration systems, International Journal of Refrigeration, 2009, 32, (7), pp. 1672-1682.

[33] Zhang W., Zhang C.: A generalized moving-boundary model for transient simulation of dry-expansion evaporators under larger disturbances, Int. J. Refrig., 2006, 29, (7), pp. 1119-1127.

[34] Sulc V., Berge J.: Characteristics of refrigeration systems: extension of the graphical-analytical method, Proceedings of the Institution of Mechanical Engineers, Part E (Journal of Process Mechanical Engineering), 2008, 222, pp. 225-40.

[35] von Dosky S., Heinze D., Wolf J.: Numerical simulation of a refrigeration cycle for scaling towards small geometries, Int. J. Refrig., 2008, 31, (8), pp. 1384-1390.

[36] Bendapudi S., Braun J.E., Groll E.A.: A comparison of moving-boundary and finite-volume formulations for transients in centrifugal chillers, Int. J. Refrig., 2008, 31, (8), pp. 1437-1452.

[37] Pfafferott T., Schmitz G.: Numeric Simulation of an Integrated CO_2 Cooling System. Proc. Modelica Workshop 2000Lund. Sweden, pp. 89-92.

[38] Shah R.: Dynamic Modeling and Control of single and multi-evaporator subcritical vapour compression systems. M.Sc, University of Illinois at Urbana-Champaign, 2003.

[39] Rasmussen B.P.: Dynamic Modeling and Advanced Control of Air Conditioning and Refrigeration Systems. PhD, University of Illinois at Urbana-Champaign, 2005.

[40] Rodriguez E., Rasmussen B.: A comparison of modeling paradigms for dynamic evaporator simulations with variable fluid phases, Applied Thermal Engineering, 2017, 112, pp. 1326-1342.

[41] Eldredge B.: Improving the Accuracy and Scope of Control-Oriented Vapor Compression Cycle System Models. M. Sc, University of Illinois Urbana-Champaign, 2004.

[42] Iragorry J., Tao Y., Jia S.: A critical review of properties and models for frost formation analysis, HVAC and R Research, 2004, 10, (4), pp. 393-420.

[43] Tso C.P., Cheng Y.C., Lai A.C.K.: Dynamic behavior of a direct expansion evaporator under frosting condition. Part I. Distributed model, Int. J. Refrig., 2006, 29, (4), pp. 611-23.

[44] Gnielinski V.: New equations for heat and mass-transfer in turbulent pipe and channel flow, International Journal of Chemical Engineering, 1967, 16, pp. 359-368.

[45] Patiño J., Llopis R., Sánchez D., Sanz-Kock C., Cabello R., Torrella E.: A comparative analysis of a CO_2 evaporator model using experimental heat transfer correlations and a flow pattern map, International Journal of Heat and Mass Transfer, 2014, 71, pp. 361-375.

[46] Wojtan L., Ursenbacher T., Thome J.R.: Investigation of flow boiling in horizontal tubes: Part I—A new diabatic two-phase flow pattern map, International Journal of Heat and Mass Transfer, 2005, 48, (14), pp. 2955-2969.

[47] Cheng L., Ribatski G., Thome J.R.: New prediction methods for CO_2 evaporation inside tubes: Part II—An updated general flow boiling heat transfer model based on flow patterns, International Journal of Heat & Mass Transfer, 2008, 51, (1), pp. 125-135.

[48] Thome J.R., El Hajal J.: Flow boiling heat transfer to carbon dioxide: general prediction method, International Journal of Refrigeration, 2004, 27, (3), pp. 294-301.

[49] Thome J.R., Ribatski G.: State-of-the-art of two-phase flow and flow boiling heat transfer and pressure drop of CO_2 in macro- and micro-channels, International Journal of Refrigeration, 2005, 28, (8), pp. 1149-1168.

[50] Yuan S., Cheng W., Nian Y., Zhong Q., Fan Y., He J.: Evaluation of prediction methods for heat transfer coefficient of annular flow and a novel correlation, Applied Thermal Engineering, 2017, 114, pp. 10-23.

[51] Mastrullo R., Mauro A.W., Thome J.R., Toto D., Vanoli G.P.: Flow pattern maps for convective boiling of CO_2 and R410A in a horizontal smooth tube: Experiments and new correlations analyzing the effect of the reduced pressure, International Journal of Heat and Mass Transfer, 2012, 55, (5), pp. 1519-1528.

[52] McKinley T.L., Alleyne A.G.: An advanced nonlinear switched heat exchanger model for vapor compression cycles using the moving-boundary method, Int. J. Refrig., 2008, 31, (7), pp. 1253-1264.

[53] Qiao H., Aute V., Radermacher R.: An Improved Moving Boundary Heat Exchanger model with Pressure Drop. International Refrigeration and Air Conditioning Conference.

[54] Cheng L., Ribatski G., Moreno Quibén J., Thome J.R.: New prediction methods for CO_2 evaporation inside tubes: Part I – A two-phase flow pattern map and a flow pattern based phenomenological model for two-phase flow frictional pressure drops, International Journal of Heat and Mass Transfer, 2008, 51, (1), pp. 111-124.

[55] Mastrullo R., Mauro A.W., Rosato A., Vanoli G.P.: Carbon dioxide heat transfer coefficients and pressure drops during flow boiling: Assessment of predictive methods, International Journal of Refrigeration, 2010, 33, (6), pp. 1068-1085.

[56] Wu J., Koettig T., Franke C*., et al*.: Investigation of heat transfer and pressure drop of CO_2 two-phase flow in a horizontal minichannel, International Journal of Heat and Mass Transfer, 2011, 54, (9), pp. 2154-2162.

[57] Da Silva Lima, R. J.: Two-Phase Pressure Drops and Flow Patterns in U-bends for R-134a and R404a. PhD, École Polytechnique Fédérale de Lausanne (EPFL), 2011.

[58] Moreno Quibén J., Thome J.R.: Flow pattern based two-phase frictional pressure drop model for horizontal tubes, Part II: New phenomenological model, International Journal of Heat and Fluid Flow, 2007, 28, (5), pp. 1060-1072.

[59] Cecchinato L., Mancini F.: An intrinsically mass conservative switched evaporator model adopting the moving-boundary method, Int. J. Refrig., 2012, 35, (2), pp. 349-64.

[60] Huang L., Aute V., Radermacher R.: A finite volume coaxial heat exchanger model with moving boundaries and modifications to correlations for two-phase flow in fluted annuli, International Journal of Refrigeration, 2014, 40, pp. 11-23.

[61] Shah R.K., Sekulic D.P.: Basic Thermal Design Theory for Recuperators: Fundamentals of Heat Exchanger Design (John Wiley & Sons, 2003, pp. 97-98-132.

[62] Cavallini A., Censi G., Del Col D*., et al*.: Condensation inside and outside smooth and enhanced tubes — a review of recent research, International Journal of Refrigeration, 2003, 26, (4), pp. 373-392.

[63] Thome J.R., El Hajal J., Cavallini A.: Condensation in horizontal tubes, part 2: new heat transfer model based on flow regimes, International Journal of Heat and Mass Transfer, 2003, 46, (18), pp. 3365-3387.

[64] Jassim E.W., Newell T.A., Chato J.C.: Prediction of refrigerant void fraction in horizontal tubes using probabilistic flow regime maps, Experimental Thermal and Fluid Science, 2008, 32, (5), pp. 1141-1155.

[65] Zivi S.M.: Estimation of steady-state steam void-fraction by means of the principle of minimum entropy production, Journal of Heat Transfer, 1964, 86, pp. 247-252.

[66] Kim Y.J., Jang J., Hrnjak P.S., Kim M.S.: Adiabatic Horizontal and Vertical Pressure Drop of Carbon Dioxide Inside Smooth and Microfin Tubes at Low Temperatures, Journal of Heat Transfer, 2008, 130, (11).

[67] Lockhart R.W., Martinelli R.C.:
Proposed correlation of data for isothermal two-phase, two-component flow in pipes, Chemical, 1949, 1, pp. 39-48.

[68] Wattelet J.P.: Heat Transfer Flow Regimes of Refrigerants in a Horizontal-tube Evaporator, 1994, ACRC TR-55.

[69] Tandon T.N., Varma H.K., Gupta C.P.: A void fraction model for annular two-phase flow, International Journal of Heat and Mass Transfer, 1985, 28, (1), pp. 191-198.

[70] Yashar D.A., Wilson M.J., Kopke H.R., Graham D.M., Chato J.C.: An investigation of refrigerant void fraction in horizontal, microfin tubes, HVAC & R Research, 2001, 7, pp. 67-82.

[71] Jorgensen R., Adamski S., Bohanon H.R., Cermak J., Coward C.W., Fragnito D.: Laboratory Methods for Testing Fans for Aerodynamic Performance Rating, ACMA, 1999, 210.

[72] Lemmon E.W., Huber M.L., McLinden M.O.: NIST Standard Reference Database 23: Reference Fluid Thermodynamic and Transportation Properties - REFPROP, 2013, 9.1.

[73] Rice C.K.: Effect of Void Fraction Correlation and Heat Flux Assumption on Refrigerant Charge Inventory Predictions. ASHRAE Transactions: Technical and Symposium Papers Presented at the 1987 Winter Meeting, pp. 341-367.

[74] Fasl J.M.: Modeling and Control of Hybrid Vapor Compression Cycles. M. Sc, University of Illinois at Urbana-Champaign, 2013.

[75] Ding G., Wu Z., Liu J., Inagaki T., Wang K., Fukaya M.: An implicit curve-fitting method for fast calculation of thermal properties of pure and mixed refrigerants, International Journal of Refrigeration, 2005, 28, (6), pp. 921-932.

[76] Tian C., Li X.: Transient behavior evaluation of an automotive air conditioning system with a variable displacement compressor, Applied Thermal Engineering, 2005, 25, (13), pp. 1922-1948.

[77] Fang X., Zhou Z., Li D.: Review of correlations of flow boiling heat transfer coefficients for carbon dioxide, International Journal of Refrigeration, 2013, 36, (8), pp. 2017-2039.

[78] Fang X.: A new correlation of flow boiling heat transfer coefficients for carbon dioxide, International Journal of Heat and Mass Transfer, 2013, 64, pp. 802-807.

[79] Dittus F.W., Boelter L.M.K.: Heat transfer in an automobile radiator of the tubular type, University of California Publication Engineering, 1930, 2, pp. 443-461.

[80] Sporlan: Evaporator Pressure Regulating Valves for Evaporator Temperature Control, 2007, 90-20.

[81] Dhiman S., Yavuzkurt S.: Film cooling calculations with an iterative conjugate heat transfer approach using empirical heat transfer coefficient corrections. ASME Turbo Expo 2010: Power for Land, Sea, and Air, GT 2010, June 14, 2010 - June 18, 2010, pp. 1607-1616.

[82] SLXe Single and Multi Temperature Refrigeration Systems for Trailers, http://www.thermoking.no/uploads/2/4/8/5/24859428/slxe.pdf, accessed May 2018.

Appendix A

Matlab Functions Code

A.1 Evaporator Model Code

```
function Outputs(block)

global AirProp cRfgLib

%Block Parameter Callbacks
Dh_ref          = block.DialogPrm(1).Data;
L_ref           = block.DialogPrm(2).Data;
Ac_air          = block.DialogPrm(3).Data;
As_air          = block.DialogPrm(4).Data;
As_ref          = block.DialogPrm(5).Data;
Ac_ref          = block.DialogPrm(6).Data;
N               = block.DialogPrm(9).Data;
PAF_AIR         = block.DialogPrm(10).Data(3);
R_ubend         = block.DialogPrm(18).Data;
N_ubend         = block.DialogPrm(19).Data;
Ubend_h         = block.DialogPrm(20).Data;
Ubend_vu        = block.DialogPrm(21).Data;
Ubend_vd        = block.DialogPrm(22).Data;
Ubend_vu45      = block.DialogPrm(23).Data;
Ubend_vd45      = block.DialogPrm(24).Data;

%Input Callbacks
Massflow_air_in     = block.InputPort(1).Data/N;
T_air_in            = block.InputPort(2).Data;
Massflow_ref_in     = block.InputPort(3).Data/N;
Massflow_ref_out    = block.InputPort(4).Data/N;
H_ref_in            = block.InputPort(5).Data;

%State Callbacks
Zeta1           = block.ContStates.Data(1);
if Zeta1 <=0
   Zeta1 = 0.001;
end
P_ref           = block.ContStates.Data(2);
```

```
H2              = block.ContStates.Data(3);
Gamma           = block.ContStates.Data(4);
T_wall1         = block.ContStates.Data(5);
T_wall2         = block.ContStates.Data(6);
Zeta2           = 1.0 - Zeta1;
%%%%%%%%%%%%%%%%%%%%%%%%%%%%%%%%%%%%%%%%%%%%%%%%%%%%%%%%%%%%%%%%%%%%%%%%%%%%
% Calculate Necessary Properties
%%%%%%%%%%%%%%%%%%%%%%%%%%%%%%%%%%%%%%%%%%%%%%%%%%%%%%%%%%%%%%%%%%%%%%%%%%%%


%Use cRfgLib DLL for calculating refrigerant parameters
[Rhog] = Rho_Px(P_ref, 1);
[Rhof] = Rho_Px(P_ref, 0);

[Hg]    = H_Px(P_ref, 1);
[Hf]    = H_Px(P_ref, 0);


%Superheat Parameters

[~, ~, Cp_r2, Mu_g, Mu_f K_r2] = Ref_Props(P_ref, H2);
C_SH = Massflow_ref_out * Cp_r2;

%Air Side Parameters
Beta_air            = qminterp1(AirProp.T, AirProp.Beta_t, T_air_in);
Cp_air              = qminterp1(AirProp.T, AirProp.C_t, T_air_in);
Rho_air             = qminterp1(AirProp.T, AirProp.Rho_t, T_air_in);
Mu_air              = qminterp1(AirProp.T, AirProp.Mu_t, T_air_in);
K_air               = qminterp1(AirProp.T, AirProp.K_t, T_air_in);
Thermal_Diff_air    = K_air/(Rho_air*Cp_air);
Nu_air              = Mu_air/Rho_air;
Pr_air              = Nu_air/Thermal_Diff_air;

%%%%%%%%%%%%%%%%%%%%%%%%%%%%%%%%%%%%%%%%%%%%%%%%%%%%%%%%%%%%%%%%%%%%%%%%%%%%
% Calculate Heat Transfer Coefficients from Subroutines
%%%%%%%%%%%%%%%%%%%%%%%%%%%%%%%%%%%%%%%%%%%%%%%%%%%%%%%%%%%%%%%%%%%%%%%%%%%%
G_ro        = (Massflow_ref_out)/Ac_ref;
```

```
%Calculate heat transfer coefficients from Cheng et al. 2008 "New prediction methods for CO2 evaporation inside tubes"
if Zeta1 > 0.005;
     [DeltaP_TP DeltaP_SH] = Press_Drop(P_ref, H_ref_in, Hg, Hf, Zeta1, G_ro, Rhog, Rhof, Mu_f, Mu_g, Dh_ref, R_ubend, N_ubend,Ubend_h, Ubend_vu, Ubend_vd, Ubend_vu45, Ubend_vd45, Gamma, Ac_ref, L_ref);
else
   DeltaP_TP = 0;
   [~, DeltaP_SH] = Press_Drop(P_ref, H_ref_in, Hg, Hf, Zeta1, G_ro, Rhog, Rhof, Mu_f, Mu_g, Dh_ref, R_ubend, N_ubend,Ubend_h, Ubend_vu, Ubend_vd, Ubend_vu45, Ubend_vd45, Gamma, Ac_ref, L_ref);
end

P_out_TP = P_ref - (DeltaP_TP/2);
P_out = P_out_TP-DeltaP_SH;
P_in = P_ref + (DeltaP_TP/2);
if P_out < 10
   P_out = 10;
end

Tsat = (calllib(cRfgLib, 'tdrp', 'R744', P_out_TP/6.89475729) - 32)/1.8;
% Saturation pressure at outlet of Two-phase region


%Air Side Subroutine Evaluations
if Massflow_air_in == 0

   Ra_D_SH = 9.81 * Beta_air * (abs(T_wall2 -  T_air_in)) * Dh_ref^3/(Nu_air * Thermal_Diff_air);
   Ra_D_TP = 9.81 * Beta_air * (abs(T_wall1 - T_air_in)) * Dh_ref^3/(Nu_air * Thermal_Diff_air);

   Nu_D_SH = max([1 ((.6  +  .387 * (Ra_D_SH)^(1/6)/((1+(.559/Pr_air)^(9/16))^(8/27)))^2)]);
   Nu_D_TP = max([1 ((.6 + .387 * (Ra_D_TP)^(1/6)/((1+(.559/Pr_air)^(9/16))^(8/27)))^2)]);

   Alpha_air_SH = Nu_D_SH*K_air/Dh_ref;

   Alpha_air_TP = Nu_D_TP*K_air/Dh_ref;

else
   Alpha_air_SH = H_COLBURN_FACTOR(29, Massflow_air_in, Ac_air, Mu_air, Cp_air, Pr_air)*PAF_AIR;
   Alpha_air_TP = H_COLBURN_FACTOR(29, Massflow_air_in, Ac_air, Mu_air, Cp_air, Pr_air)*PAF_AIR;
```

```
end


%Calculate SH heat transfer coefficient from Cheng et al. 2008 "New prediction
methods for CO2 evaporation inside tubes"

Re_v =                  (G_ro*Dh_ref)/(Mu_g);
Pr_v    =               Cp_r2*Mu_g/K_r2;
Alpha_ref_SH =          0.023*(Re_v^0.8)*(Pr_v^0.4)*(K_r2/Dh_ref);
UA_SH =                 Alpha_ref_SH * Zeta2 * As_ref;


if block.Dwork(1).Data == 2;
    Xin  = (H_ref_in-Hf)/(Hg-Hf);
    Xout = getOutletQuality(Rhog, Rhof, (Rhof/Rhog)^(1/3), Xin, Gamma, 1);
    if Xout >1
       Xout =1;
    end
    H_ref_out = Xout*Hg+(1-Xout)*Hf;
    T_ref_out = (calllib(cRfgLib, 'tdrp', 'R744', P_out/6.89475729) - 32)/1.8;
    %Saturation temperature at outlet pressure
    Rho_out = Rho_Px(P_out, Xout);
else
   %H_ref_out = 2*H2-Hg; % Use for Model 1
   %   Calculate Tout based on an e(-NTU) relationship for the SH region.

   if C_SH <= 0.002 * UA_SH
      T_ref_out =       T_wall2;
   else
      NTU_SH =          UA_SH / C_SH;
      T_ref_out =       T_wall2 + (Tsat - T_wall2) * exp(-NTU_SH);

   end
   H_ref_out =          H_vap(P_out, T_ref_out);
  %[Rho_out T_ref_out] = Ref_Props(P_out, H_ref_out); % Use for model 1
   Rho_out =            Ref_Props(P_out, H_ref_out);

end
```

```
%%%%%%%%%%%%%%%%%%%%%%%%%%%%%%%%%%%%%%%%%%%%%%%%%%%%%%%%%%%%%%%%%%%%%%%%%%%%
%  Calculate Heat Transfer Rates
%%%%%%%%%%%%%%%%%%%%%%%%%%%%%%%%%%%%%%%%%%%%%%%%%%%%%%%%%%%%%%%%%%%%%%%%%%%%

% Base condition on whether mass flow is sufficient to allow
% division without blowing up.
C_air = Massflow_air_in * Cp_air;

%
% Air passes the superheated section first.
% If it is not active, it has no effect on air temperature.
%
if block.Dwork(1).Data == 2
    % No superheated section: no change of temperature,
  % no heat transfer from wall.
  Tin_air_TP = T_air_in;
else
   UA_air_SH = Alpha_air_SH * (Zeta2 * As_air) * 0.972;
  % If mass flow is low enough that effectiveness approaches 100%,
  % avoid dividing by C_air.  This is approximated by NTU > 5.
  if ( C_air > (0.2 * UA_air_SH) )
    NTU =                UA_air_SH / C_air;
    eff =                1 - exp( -NTU );
    Q_air_SH =           eff * C_air * (T_wall2 - T_air_in);
    Tout_air_SH =        T_air_in + (Q_air_SH / C_air);
  else
    % Effectiveness = 100%
    Tout_air_SH =        T_wall2;
  end
  Tin_air_TP =           Tout_air_SH;

end

%
% Next, air passes the two-phase section
% The "inlet" air temp for this section is the exit temp from
% the superheated section.
%
UA_air_TP = Alpha_air_TP * (Zeta1 * As_air) * 0.972;
% If mass flow is low enough that effectiveness approaches 100%,
% avoid dividing by C_air.  This is approximated by NTU > 5.
if ( C_air > (0.2 * UA_air_TP) )
  NTU =          UA_air_TP / C_air;
  eff =          1 - exp( -NTU );
  Q_air_TP =     eff * C_air * (T_wall1 - Tin_air_TP);
```

```
  Tout_air_TP = Tin_air_TP + (Q_air_TP / C_air);
else
  % Effectiveness = 100%
  Tout_air_TP = T_wall1;
end

% Air passes through the two-phase section last, so its exit temp is
% the overall exit temperature.

if block.Dwork(1).Data == 3
   T_air_out = Tout_air_SH;
else
   T_air_out = Tout_air_TP;
end

TotCap = N*(Massflow_ref_out*H_ref_out - Massflow_ref_in*H_ref_in);

block.OutputPort(1).Data      = block.ContStates.Data(2);%P_ref
block.OutputPort(2).Data      = H_ref_out;
block.OutputPort(3).Data      = T_ref_out;
block.OutputPort(4).Data      = T_air_out;
block.OutputPort(5).Data(1)   = block.ContStates.Data(5); %T_wall1
block.OutputPort(5).Data(2)   = block.ContStates.Data(6); %T_wall2
block.OutputPort(6).Data(1)   = block.ContStates.Data(1); %Zeta1
block.OutputPort(6).Data(2)   = 1.0 - block.ContStates.Data(1); %Zeta2
block.OutputPort(7).Data      = Gamma;%Vol_ref*(Rho1*Zeta1+Rho2*Zeta2)*N;
block.OutputPort(8).Data      = TotCap;
block.OutputPort(9).Data      = P_in; %Inlet Pressure
block.OutputPort(10).Data     = P_out; %Outlet Pressure
block.OutputPort(11).Data     = Rho_out; %Outlet Density

end

function Update(block)

%global cRfgLib

%Input Callbacks
Massflow_ref_in       = block.InputPort(3).Data;
H_ref_in              = block.InputPort(5).Data;

%State Callbacks
Zeta1                 = block.ContStates.Data(1);
if Zeta1 < 0
   Zeta1 = 0;
end
```

```
P_ref          = block.ContStates.Data(2);
Gamma          = block.ContStates.Data(4);
Zeta2          = 1.0 - Zeta1;

[Rhog]         = Rho_Px(P_ref, 1);
[Rhof]         = Rho_Px(P_ref, 0);

[Hg]           = H_Px(P_ref, 1);
[Hf]           = H_Px(P_ref, 0);
Xin            = (H_ref_in-Hf)/(Hg-Hf);
Rho1           = Gamma * Rhog + (1.0 - Gamma) * Rhof;

if( block.Dwork(1).Data == 1 )
    if( Zeta2 < 0.005 && block.Dwork(2).Data(1) > 0.0 ) % Zeta2 is smaller than the
minimum value and zeta1 is increasing
        disp(['Switching from 2-zone to 1-zone (two-phase) representation in Evaporator
at time = ', num2str(block.CurrentTime), ' seconds.']);
        block.Dwork(1).Data = 2;
    elseif( Zeta1 < 0.005 && block.Dwork(2).Data(2) > 0.0 )% Zeta1 is smaller than the
minimum value and gamma is increasing
        disp(['Switching from 2-zone to 1-zone(Superheat) representation in Evaporator
at time = ', num2str(block.CurrentTime), ' seconds.']);
        block.Dwork(1).Data = 3;
    else
        block.Dwork(1).Data = 1;
    end

 elseif( block.Dwork(1).Data == 2 )
    Gamma_Tot = getVoidFrac(Rhog, Rhof, 0, 0, (Rhof/Rhog)^(1/3), Xin, 1);
    if( (Gamma-Gamma_Tot)*Zeta1 > 0.005 && block.Dwork(2).Data(2) > 0.0)%The
vapour in the two-phase zone is above the minimum threshold and is increasing
        block.Dwork(1).Data = 1;
        disp(['Switching from 1-zone (two-phase) to 2-zone representation in Evaporator
at time = ', num2str(block.CurrentTime), ' seconds.']);
    else
        block.Dwork(1).Data = 2;
    end
 elseif( block.Dwork(1).Data == 3 )
    if( Rho1 > 0.99*Rhog && Massflow_ref_in > .0001 ) % If the two-phase density is
greater than the vapour density and the mass flow rate is greater than 0
        disp(['Switching from 1-zone (Superheat) to 2-zone representation in Evaporator
at time = ', num2str(block.CurrentTime), ' seconds.']);
        block.Dwork(1).Data = 1;
    else
        block.Dwork(1).Data = 3;
    end
```

```
end

end

%%%%%%%%%%%%%%%%%%%%%%%%%%%%%%%%%%%%%%%%%%%%%%%%%%%%%%%%%%%%%%%%%%%%%%%
% Derivatives:
%   Functionality    : Called to update derivatives of
%                      continuous states during simulation step
%%%%%%%%%%%%%%%%%%%%%%%%%%%%%%%%%%%%%%%%%%%%%%%%%%%%%%%%%%%%%%%%%%%%%%%

function Derivatives(block)

global AirProp cRfgLib

%Block Parameter Callbacks
Dh_ref          = block.DialogPrm(1).Data;
L_ref           = block.DialogPrm(2).Data;
Ac_air          = block.DialogPrm(3).Data;
As_air          = block.DialogPrm(4).Data;
As_ref          = block.DialogPrm(5).Data;
Ac_ref          = block.DialogPrm(6).Data;
M_wall          = block.DialogPrm(7).Data;
Cp_wall         = block.DialogPrm(8).Data;
N               = block.DialogPrm(9).Data;
PAF_TP          = block.DialogPrm(10).Data(1);
PAF_SH          = block.DialogPrm(10).Data(2);
PAF_AIR         = block.DialogPrm(10).Data(3);

%Input Callbacks
Massflow_air_in     = block.InputPort(1).Data/N;
T_air_in            = block.InputPort(2).Data;
Massflow_ref_in     = block.InputPort(3).Data/N;
Massflow_ref_out    = block.InputPort(4).Data/N;



H_ref_in            = block.InputPort(5).Data;

%State Callbacks
Zeta1               = block.ContStates.Data(1);
if Zeta1 <0
   Zeta1 = 0.001;
end
P_ref               = block.ContStates.Data(2);
H2                  = block.ContStates.Data(3);
```

```
Gamma                   = block.ContStates.Data(4);
T_wall1                 = block.ContStates.Data(5);
T_wall2                 = block.ContStates.Data(6);
Zeta2                   = 1.0 - Zeta1;
[Rhog, dRhog_dP]        = Rho_Px(P_ref, 1);
[Rhof, dRhof_dP]        = Rho_Px(P_ref, 0);
[Hg]                    = H_Px(P_ref, 1);
[Hf]                    = H_Px(P_ref, 0);
Xin                     = (H_ref_in-Hf)/(Hg-Hf);

if ( Xin < 0.0 )
  Xin = 0.0;
elseif ( Xin > 0.99 )
  Xin = 0.99;
end

if Zeta1<0.995
  Xout = 1; %assumption that there is a SH zone.
else
  Xout = getOutletQuality(Rhog, Rhof, (Rhof/Rhog)^(1/3), Xin, Gamma, 1);
  if Xout > 1
    Xout = 1;
  end
end
%%%%%%%%%%%%%%%%%%%%%%%%%%%%%%%%%%%%%%%%%%%%%%%%%%%%%%%%%%%%
%%%%%%%%%%%%%%%%%%%%%%%%%%%%%%
%   Calculate Physical Properties
%%%%%%%%%%%%%%%%%%%%%%%%%%%%%%%%%%%%%%%%%%%%%%%%%%%%%%%%%%%%
%%%%%%%%%%%%%%%%%%%%%%%%%%%%%%

Vol_ref = Ac_ref * L_ref;

%Two-Phase Parameters
Tsat_IP         = calllib(cRfgLib, 'tdrp', 'R744', P_ref/6.89475729);
Tsat            = (Tsat_IP - 32)/1.8;
Pcrit           = calllib(cRfgLib, 'pcrit', 'R744')*6.8947572;
K_f             = calllib(cRfgLib, 'kfrt', 'R744', Tsat_IP)/ 577.79;
Rho1            = Gamma * Rhog + (1.0 - Gamma) * Rhof;
H1              = (Rhog*Hg*Gamma+Rhof*Hf*(1-Gamma))/Rho1;
G_ri            = Massflow_ref_in/Ac_ref;

dRho1_dP                = Gamma * dRhog_dP + (1.0 - Gamma) * dRhof_dP;
dRho1_dGamma            = Rhog - Rhof;
dH1_dGamma              = (Hg - Hf) * Rhog / Rho1 * (1.0 - Gamma * (Rhog - Rhof) / Rho1);
delta                   = 0.005;
Pstar                   = P_ref - delta * P_ref;
[Rho1gstar]             = Rho_Px(Pstar, 1);
```

```
[Rho1fstar]     = Rho_Px(Pstar, 0);
Rho1star        = Gamma * Rho1gstar + (1.0 - Gamma) * Rho1fstar;
Xbarstar        = Gamma * Rho1gstar / Rho1star;
[H1gstar]       = H_Px(Pstar, 1);
[H1fstar]       = H_Px(Pstar, 0);
H1star          = Xbarstar * H1gstar + (1.0 - Xbarstar) * H1fstar;
dH1_dP          = (H1star - H1) / (Pstar - P_ref);
[Rho1, ~, ~, Mu_g_TP, Mu_f_TP K_r1] = Ref_Props(P_ref, H1);
%Superheat Parameters
[Rho2, T2, Cp_r2, Mu_g, ~, K_r2] = Ref_Props(P_ref, H2);
Rhostar         = Ref_Props(Pstar, H2);
dRho2_dP        = (Rhostar - Rho2) / (Pstar - P_ref);

% Simple assumption for dRho2_dH: linear between sat vapour and state (2).
% Matches assumption of how Hg and H2 are used to calculate H_out.
dRho2_dH        = (Rho2-Rhog)/(H2-Hg);

%Air Side Parameters
Beta_air        = qminterp1(AirProp.T, AirProp.Beta_t, T_air_in);
Cp_air          = qminterp1(AirProp.T, AirProp.C_t, T_air_in);
Rho_air         = qminterp1(AirProp.T, AirProp.Rho_t, T_air_in);
Mu_air          = qminterp1(AirProp.T, AirProp.Mu_t, T_air_in);
K_air           = qminterp1(AirProp.T, AirProp.K_t, T_air_in);
Thermal_Diff_air   = K_air/(Rho_air*Cp_air);
Nu_air          = Mu_air/Rho_air;
Pr_air          = Nu_air/Thermal_Diff_air;

%%%%%%%%%%%%%%%%%%%%%%%%%%%%%%%%%%%%%%%%%%%%%%%%%%%%%%%%%%%%%%%%%%%%%%%%%%%%
%   Calculate Outlet Properties
%%%%%%%%%%%%%%%%%%%%%%%%%%%%%%%%%%%%%%%%%%%%%%%%%%%%%%%%%%%%%%%%%%%%%%%%%%%%

if block.Dwork(1).Data == 1
   [Gamma_tot dGamma_dP] = getVoidFrac(Rhog, Rhof, dRhog_dP, dRhof_dP,
(Rhof/Rhog)^(1/3), Xin, 1);
   %H_ref_out = 2*H2-Hg; % for model 1
else
   %H_ref_out = H1; for model 1
end

%%%%%%%%%%%%%%%%%%%%%%%%%%%%%%%%%%%%%%%%%%%%%%%%%%%%%%%%%%%%%%%%%%%%%%%%%%%%
%   Calculate Heat Transfer Coefficients from Subroutines
%%%%%%%%%%%%%%%%%%%%%%%%%%%%%%%%%%%%%%%%%%%%%%%%%%%%%%%%%%%%%%%%%%%%%%%%%%%%
Mol_weight = calllib(cRfgLib, 'MolecularWeight', 'R744');
```

```
%Refrigerant Side Subroutine Evaluations
q = (Massflow_ref_in*(Hg-H_ref_in))/(Zeta1*As_ref); %Heatflux
h_vl = Hg-Hf;

%Calculate heat transfer coefficients from Cheng et al. 2008 "New prediction methods for CO2 evaporation inside tubes"
if block.Dwork(1).Data ==1
   [Alpha_ref_TP, Alpha_ref_SH] = HX_CHENG_THOME_NEW(Dh_ref, G_ri, P_ref, Xin, Xout, q, Mu_g_TP, Mu_g, Mu_f_TP,K_r1*1000, K_r2*1000, K_f*1000, Cp_r2*1000, Rhog, Rhof, Pcrit,Ac_ref,Mol_weight, h_vl);
   Q_ref_TP = Alpha_ref_TP * As_ref * Zeta1 * (T_wall1 - Tsat)*PAF_TP;
   Q_ref_SH = Alpha_ref_SH * As_ref * Zeta2 * (T_wall2 - T2)*PAF_SH;
elseif block.Dwork(1).Data ==2
   [Alpha_ref_TP] = HX_CHENG_THOME_NEW(Dh_ref, G_ri, P_ref, Xin, Xout, q, Mu_g_TP, Mu_g, Mu_f_TP, K_r1*1000, K_r2*1000, K_f*1000, Cp_r2*1000, Rhog, Rhof, Pcrit,Ac_ref,Mol_weight, h_vl);
   Q_ref_TP = Alpha_ref_TP * As_ref * Zeta1 * (T_wall1 - Tsat)*PAF_TP;
else
   [~, Alpha_ref_SH] = HX_CHENG_THOME_NEW(Dh_ref, G_ri, P_ref, Xin, Xout, q, Mu_g_TP, Mu_g, Mu_f_TP, K_r1*1000, K_r2*1000, K_f*1000, Cp_r2*1000, Rhog, Rhof, Pcrit,Ac_ref,Mol_weight, h_vl);
    Q_ref_SH = Alpha_ref_SH * As_ref * Zeta2 * (T_wall2 - T2)*PAF_SH;
end

%Air Side Subroutine Evaluations
if Massflow_air_in == 0

   Ra_D_SH = 9.81 * Beta_air*(abs(T_wall2 - T_air_in)) * Dh_ref^3/(Nu_air * Thermal_Diff_air);
   Ra_D_TP = 9.81*Beta_air*(abs(T_wall1 - T_air_in)) * Dh_ref^3/(Nu_air * Thermal_Diff_air);

   Nu_D_SH = max([1 ((.6 + .387 * (Ra_D_SH)^(1/6)/((1+(.559/Pr_air)^(9/16))^(8/27)))^2)]);
   Nu_D_TP = max([1 ((.6 + .387 * (Ra_D_TP)^(1/6)/((1+(.559/Pr_air)^(9/16))^(8/27)))^2)]);

   Alpha_air_SH = Nu_D_SH*K_air/Dh_ref;
   Alpha_air_TP = Nu_D_TP*K_air/Dh_ref;

else
   Alpha_air_TP = H_COLBURN_FACTOR(29, Massflow_air_in, Ac_air, Mu_air, Cp_air, Pr_air)*PAF_AIR;
   Alpha_air_SH = H_COLBURN_FACTOR(29, Massflow_air_in, Ac_air, Mu_air, Cp_air, Pr_air)*PAF_AIR;
end
```

```
%%%%%%%%%%%%%%%%%%%%%%%%%%%%%%%%%%%%%%%%%%%%%%%%%%%%%%%%%%%%%%%%%%%%%%%
%  Calculate Heat Transfer Rates
%%%%%%%%%%%%%%%%%%%%%%%%%%%%%%%%%%%%%%%%%%%%%%%%%%%%%%%%%%%%%%%%%%%%%%%

% Base condition on whether mass flow is sufficient to allow
% division without blowing up.
C_air = Massflow_air_in * Cp_air;

%
% Air passes the superheated section first.
% If it is not active, it has no effect on air temperature.
%
if block.Dwork(1).Data == 2
  % No superheated section: no change of temperature,
  % no heat transfer from wall.
   Tin_air_TP = T_air_in;
else
  UA_air_SH = Alpha_air_SH * (Zeta2 * As_air) * 0.972;
  % If mass flow is low enough that effectiveness approaches 100%,
  % avoid dividing by C_air.  This is approximated by NTU > 5.
  if ( C_air > (0.2 * UA_air_SH) )
    NTU                 = UA_air_SH / C_air;
    eff                 = 1 - exp( -NTU );
    Q_air_SH            = eff * C_air * (T_wall2 - T_air_in);
    Tout_air_SH         = T_air_in + (Q_air_SH / C_air);
  else
    % Effectiveness = 100%
    Tout_air_SH         = T_wall2;
    Q_air_SH            = C_air * ( T_wall2 - T_air_in );
  end
  Tin_air_TP            = Tout_air_SH;

end

%
% Next, air passes the two-phase section
% The "inlet" air temp for this section is the exit temp from
% the superheated section.
%
UA_air_TP = Alpha_air_TP * (Zeta1 * As_air) * 0.972;
% If mass flow is low enough that effectiveness approaches 100%,
% avoid dividing by C_air.  This is approximated by NTU > 5.
```

```
if ( C_air > (0.2 * UA_air_TP) )
  NTU           = UA_air_TP / C_air;
  eff           = 1 - exp( -NTU );
  Q_air_TP      = eff * C_air * (T_wall1 - Tin_air_TP);
else
  % Effectiveness = 100%
  Q_air_TP      = C_air * ( T_wall1 - Tin_air_TP );
end

% Air passes through the two-phase section last, so its exit temp is
% the overall exit temperature.


%%%%%%%%%%%%%%%%%%%%%%%%%%%%%%%%%%%%%%%%%%%%%%%%%%%%%%%%%%%%%%%%%%%%%%%
%%%%%%%%%%%%%%%%%%%%%%%%%%
%   Calculate Coupled Refrigerant Mass / Energy Equations
%%%%%%%%%%%%%%%%%%%%%%%%%%%%%%%%%%%%%%%%%%%%%%%%%%%%%%%%%%%%%%%%%%%%%%%
%%%%%%%%%%%%%%%%%%%%%%%%%%

%=========================================================================
=====
% First case - Two-Zone (two-phase and superheated)
%=========================================================================
=====

if block.Dwork(1).Data == 1

   %   Continuity equation for the superheated zone
%
     A(1,1)       = 1.0;
     A(1,2)       = - Zeta2 * dRho2_dP / Rho2;
     A(1,3)       = - Zeta2 * dRho2_dH / Rho2;
     A(1,5)       = 1.0 / (Rho2 * Vol_ref);
     y(1)         = Massflow_ref_out / (Rho2 * Vol_ref);
%
% energy equation for the superheated zone
%
     A(2,2)       = - 1.0 / Rho2;
     A(2,3)       = 1.0;
     A(2,5)       = (H2 - Hg) / (Rho2 * Vol_ref * Zeta2);
     y(2)         = (Q_ref_SH + Massflow_ref_out * (Hg - H2)) / (Rho2 * Vol_ref * Zeta2);
%
% Continuity equation for the two-phase zone
%
     A(3,1)       = 1.0;
     A(3,2)       = Zeta1 * dRho1_dP / Rho1;
     A(3,4)       = Zeta1 * dRho1_dGamma / Rho1;
```

```
    A(3,5)      = 1.0 / (Rho1 * Vol_ref);
    y(3)        = Massflow_ref_in / (Rho1 * Vol_ref);
%
% Energy equation for the two-phase zone
%
    A(4,2)      = dH1_dP - 1.0/Rho1;
    A(4,4)      = dH1_dGamma;
    A(4,5)      = (Hg - H1) / (Rho1 * Vol_ref * Zeta1);
    y(4)        = (Q_ref_TP + Massflow_ref_in * (H_ref_in - H1)) / (Rho1 * Vol_ref *
                  Zeta1);
%
% Observer dynamics for mean void fraction
%
    A(5,2)      = dGamma_dP;
    A(5,4)      = -1.0;
    K_Gamma     = 5.0;
    y(5)        = K_Gamma * (Gamma - Gamma_tot);
%
% invert the equations (solve for state derivatives and flows from one
% zone to another

    x = A\y';

    Zeta1_dot  = x(1);
    P_ref_dot  = x(2);
    H2_dot     = x(3);
    Gamma_dot  = x(4);
    mdot_12    = x(5);

%%%%%%%%%%%%%%%%%%%%%%%%%%%%%%%%%%%%%%%%%%%%%%%%%%%%%%%%%%%%%%%%%%%%%%%%%%%%
%   Calculate Change in Wall Temperatures
%%%%%%%%%%%%%%%%%%%%%%%%%%%%%%%%%%%%%%%%%%%%%%%%%%%%%%%%%%%%%%%%%%%%%%%%%%%%
    if( Zeta1_dot > 0.0 )
       T_r1 = T_wall2;
    else
       T_r1 = T_wall1;
    end

    T_wall1_dot = ( -(Q_ref_TP + Q_air_TP)/(Cp_wall * M_wall) + (T_r1 - T_wall1)*
Zeta1_dot) / Zeta1;
    T_wall2_dot = ( -(Q_ref_SH + Q_air_SH)/(Cp_wall * M_wall) + (T_wall2 - T_r1) *
Zeta1_dot) / Zeta2;
```

```
%  Set Derivatives
   block.Derivatives.Data(1)    = Zeta1_dot; %Zeta_1_dot
   block.Derivatives.Data(2)    = P_ref_dot; %P_dot
   block.Derivatives.Data(3)    = H2_dot; %H2_dot
   if Massflow_ref_out <= .00001
      block.Derivatives.Data(3) = 0;
   end
   block.Derivatives.Data(4)    = Gamma_dot; %Gamma_dot

%   Calculate and Set Temperature Derivatives
   block.Derivatives.Data(5)    = T_wall1_dot; %TwallTP_dot
   block.Derivatives.Data(6)    = T_wall2_dot; %TwallSH_dot
   block.Derivatives.Data(7)    = mdot_12;  %
   block.Dwork(2).Data          = [Zeta1_dot, Gamma_dot];

%=========================================================================
=====
% Second case - one zone (two-phase)
%=========================================================================
=====

elseif( block.Dwork(1).Data == 2 )

    A = zeros(2,2);

   Xin  = (H_ref_in-Hf)/(Hg-Hf);
   Xout = getOutletQuality(Rhog, Rhof, (Rhof/Rhog)^(1/3), Xin, Gamma, 1);
   if Xout > 1
      Xout = 1;
   end

   H_ref_out = Xout*Hg+(1-Xout)*Hf;

% Continuity equation for the two-phase zone
%
    A(1,1)       = Zeta1 * dRho1_dP / Rho1;
    A(1,2)       = Zeta1 * dRho1_dGamma / Rho1;
    y(1)         = (Massflow_ref_in - Massflow_ref_out) / (Rho1 * Vol_ref);
%
% Energy equation for the two-phase zone
%
    A(2,1)       = dH1_dP - 1.0/Rho1;
    A(2,2)       = dH1_dGamma;
    y(2)         = (Q_ref_TP - Massflow_ref_out * (H_ref_out - H1) + Massflow_ref_in *
                   (H_ref_in - H1)) / (Rho1 * Vol_ref * Zeta1);
%
```

```
% invert the equations (solve for state derivatives and flows from one
% zone to another
    x = A\y';

    P_ref_dot           = x(1);
    Gamma_dot           = x(2);

    Zeta1_dot           = 0.0;

    K_H2                = 5.0;
    H2_dot              = K_H2 * (Hg - H2);

%%%%%%%%%%%%%%%%%%%%%%%%%%%%%%%%%%%%%%%%%%%%%%%%%%%%%%%%%%%%%%%%%%%%%%%
%%%%%%%%%%%%%%%%%%%%%%%%%%
%   Calculate Change in Wall Temperatures
%%%%%%%%%%%%%%%%%%%%%%%%%%%%%%%%%%%%%%%%%%%%%%%%%%%%%%%%%%%%%%%%%%%%%%%
%%%%%%%%%%%%%%%%%%%%%%%%%%
%
    T_wall1_dot         =  -(Q_ref_TP + Q_air_TP) / (Cp_wall * M_wall) ;

    K_Twall             = 5.0;
    T_wall2_dot         = K_Twall * (T_wall1 - T_wall2);

%   Set Derivatives

   block.Derivatives.Data(1)   = Zeta1_dot;      %Zeta_1_dot
   block.Derivatives.Data(2)   = P_ref_dot;       %P_dot
   block.Derivatives.Data(3)   = H2_dot;         %H2_dot
   block.Derivatives.Data(4)   = Gamma_dot;          %Gamma_dot
   block.Derivatives.Data(5)   = T_wall1_dot;          %TwallTP_dot
   block.Derivatives.Data(6)   = T_wall2_dot;  %TwallSH_dot
   block.Dwork(2).Data         = [0, Gamma_dot];


elseif( block.Dwork(1).Data == 3)
%
% third case - single zone (superheated)
%
     A = zeros(2,2);
%
% Continuity equation for the superheated zone
%
    A(1,1)       = dRho2_dP;
    A(1,2)       = dRho2_dH;
    y(1)         = (Massflow_ref_in - Massflow_ref_out) / (Vol_ref * Zeta2);
%
```

```
% Energy equation for the superheated zone
%
    H_ref_out  = 2.0* H2- Hg;
    A(2,1)     = -1.0 / Rho2;
    A(2,2)     = 1.0;
    y(2)       = (Q_ref_SH + Massflow_ref_in * (Hg - H2) - Massflow_ref_out *
                 (H_ref_out - H2)) / (Rho2 * Vol_ref * Zeta2);
%
% invert the equations
%
    x = A\y';

    P_ref_dot  = x(1);
    H2_dot     = x(2);

    Zeta1_dot  = 5*(.001-Zeta1);

%%%%%%%%%%%%%%%%%%%%%%%%%%%%%%%%%%%%%%%%%%%%%%%%%%%%%%%%%%%%%%%%%%%%%%%%%%%%
%   Calculate Change in Wall Temperatures
%%%%%%%%%%%%%%%%%%%%%%%%%%%%%%%%%%%%%%%%%%%%%%%%%%%%%%%%%%%%%%%%%%%%%%%%%%%%
%
    T_wall2_dot      = ( -(Q_ref_SH + Q_air_SH) / (Cp_wall * M_wall) );

    K_Twall          = 5.0;
    T_wall1_dot      = K_Twall * (T_wall2 - T_wall1);


%   Set Derivatives

   block.Derivatives.Data(1)   = Zeta1_dot;      %Zeta_1_dot
   block.Derivatives.Data(2)   = P_ref_dot;      %P_dot
   block.Derivatives.Data(3)   = H2_dot;         %H2_dot
   block.Derivatives.Data(4)   = 5*(.9999-Gamma); %Gamma_dot
   block.Derivatives.Data(5)   = T_wall1_dot;    %TwallTP_dot
   block.Derivatives.Data(6)    = T_wall2_dot;    %TwallSH_dot
   block.Dwork(2).Data          = [0, 0];


end
end
```

A.2 Pressure Drop Model Code

```
function [DeltaP_TP DeltaP_SH] = Press_Drop(P_ref, H_ref_in, Hg, Hf, Zeta1, G_ro,
Rhog, Rhof, Mu_f, Mu_g, Dh_ref, R_ubend, N_ubend,Ubend_h, Ubend_vu, Ubend_vd,
Ubend_vu45, Ubend_vd45, Gamma, Ac_ref, L_ref)


% Calculated Pressure Drop within the evap coil
% Based on "Experimental Evaluation and Prediction of Two Phase Pressure
% Drops and Flow Patterns in U-bends for R404a and R134a". R.J. Da Silva
% Lima and J. R. Thome.

if G_ro >0

Xin  = (H_ref_in-Hf)/(Hg-Hf); % Inlet Quality

if Zeta1<0.995
   Xout = 1; % assumption that there is a SH zone.
else
   Xout= getOutletQuality(Rhog, Rhof, (Rhof/Rhog)^(1/3), Xin, Gamma, 1);
   if Xout >1
      Xout = 1;
   end
end


X_av = (Xout-Xin)/2; % Average Quality
X_ia = ((0.34^(1/0.875)*(Rhog/Rhof)^(-1/1.75)*(Mu_f/Mu_g)^(-1/7))+1)^-1;
% Intermittent to Annular Transition boundary
X_slug_int = (X_ia-Xin)/2; % Quality for Slug Intermittent Flow
X_anr = ((Xout-X_ia)/2)+X_ia; % Quality for Annular Flow


ALd = (Ac_ref*(1-Gamma))/Dh_ref^2; % Dimensionless Cross sectional area of liquid
AVd = (Ac_ref*Gamma)/Dh_ref^2; % Dimensionless Cross sectional area of vapour

L_TP = L_ref*Zeta1;% Length of Two Phase Zone
L_SH = L_ref-L_TP; % Length of SH zone
L_slg_int = (X_ia/(Xout-Xin))*L_TP;
% Length of two phase region with slug intermittent flow
L_anr = L_TP-L_slg_int; % Length of two phase region with annular flow

N_ubend_TP = fix(N_ubend*Zeta1);
%Calculate number of u-bends in Two-Phase region
N_ubend_slg_int = fix(N_ubend_TP*(X_ia/(Xout-Xin)));
%Number of u-bends with slug/intermittant flow
```

```
N_ubend_anr = N_ubend_TP-N_ubend_slg_int;
% Number of u-bends with annular flow

%Frg = (G_ro^2)/((Rhog^2)*9.81*Dh_ref); %Vapour Froude Number (not required
Frf = (G_ro^2)/((Rhof^2)*9.81*Dh_ref); %Liquid Froude Number

Sigma = (-0.000007*P_ref) + 0.0198; % Linear Approx. of Surface Tension with
Pressure

Wef = ((G_ro^2)*Dh_ref)/(Rhof*Sigma); % Liquid Webber Number

De_v0 = ((G_ro*Dh_ref)/(Mu_g))*(Dh_ref/(R_ubend*2))^0.5;% Vapour Deans Number


Re_lo = G_ro*Dh_ref/Mu_f; %Single Phase liquid Reynolds number
De_lo = ((G_ro*Dh_ref)/Mu_f)*(Dh_ref/(R_ubend*2))^0.5;
%Single Phase liquid Deans number

Ug = (G_ro*X_av)/(Rhog*Gamma); %Vapour true mean velocity
Uf = (G_ro*(1-X_av))/(Rhof*(1-Gamma)); %Liquid true mean velocity

U_lo = G_ro/Rhof;   %Liquid Single Phase Velocity
U_vo = G_ro/Rhog;   %Vapour Single Phase Velocity


Re_g = (G_ro*Dh_ref)/(Mu_g);%Reynolds number for vapour


Fst_v = 0.079/(Re_g^0.25); %Vapour Friction factor

if Re_g > 2000
   f = 4/((1.58*log(Re_g))-3.28)^2;

else
   f = 64/Re_g;
end


%Friction factors for vapour flow in u-bends
Fuh_go = Fst_v*(1+(5102000*((Dh_ref/(R_ubend*2))^1.109)*(De_v0^(-1.222))));
Fuvd_go = Fst_v*(1+(8.39*((Dh_ref/(R_ubend*2))^1.278)*(De_v0^0.057)));
Fuvu_go = Fst_v*(1+(47100*((Dh_ref/(R_ubend*2))^2.707)*(De_v0^(-0.057))));

% calculate Stratification angle
Theta_strat = 2*pi -2*(pi*(1-Gamma) + ((3*pi/2)^(1/3))*(1-2*(1-Gamma)+((1-
Gamma)^(1/3))-(Gamma^(1/3)))-(1/200)*(1-Gamma)*Gamma*(1-2*(1-
Gamma))*(1+4*((1-Gamma)^2+Gamma^2)));
```

```
hLd = 0.5*(1-cos(((2*pi)-Theta_strat)/2)); % Liquid Reference Level

% Calculate G_wavy(Xia)
Gamma_ia = getVoidFraction(Rhog, Rhof, 0, 0, (Rhof/Rhog)^(1/3), X_ia, X_ia);
% Void Fraction at the Intermittent to Annular Transition boundary
Theta_strat_ia = 2*pi -2*(pi*(1-Gamma_ia) + ((3*pi/2)^(1/3))*(1-2*(1-Gamma_ia)+((1-
Gamma_ia)^(1/3))-(Gamma_ia^(1/3)))-(1/200)*(1-Gamma_ia)*Gamma_ia*(1-2*(1-
Gamma_ia))*(1+4*((1-Gamma_ia)^2+Gamma_ia^2)));
hLd_ia = 0.5*(1-cos(((2*pi)-Theta_strat_ia)/2)); %Liquid Reference Level
AVd_ia = (Ac_ref*Gamma_ia)/Dh_ref^2; % Dimensionless Cross sectional area of
vapour
G_wavy_xia = ((((16*(AVd_ia^(1/3))*9.81*Dh_ref*Rhof*Rhog)/((X_ia^2)*(pi^2)*((1-
((2*hLd_ia)-1)^2)^0.5)))*(((pi^2)/(25*(hLd_ia^2)))*(((Wef/Frf)^(-1)))+1))^0.5)+50;

%Calculations for slug/intermittent Flow Region
if(G_ro > G_wavy_xia && Xin < X_ia)
   Gamma_slug_int = getVoidFraction(Rhog, Rhof, 0, 0, (Rhof/Rhog)^(1/3), Xin, X_ia);
% Void Fraction at the Intermittent to Annular Transition boundary
   Deg_si =
((G_ro*Dh_ref*X_slug_int)/(Mu_g*Gamma_slug_int))*(Dh_ref/(R_ubend*2))^0.5;
%Vapour Deans Number
   Ug_si = (G_ro*X_slug_int)/(Rhog*Gamma_slug_int); %Vapour true mean velocity
   Uf_si = (G_ro*(1-X_slug_int))/(Rhof*(1-Gamma_slug_int)); %Liquid true mean
velocity

   Theta_dry_si = 0; %Dry angle for annular, slug and intermittent flow i.e. no dry zone.

   AL_si = Ac_ref*(1-Gamma_slug_int);
   % Liquid thickness can't physically be greater than half the pipe diameter
   delta_si = (Dh_ref/2)-((Dh_ref/2)^2-((2*AL_si)/((2*pi)-Theta_dry_si)))^0.5;
%Liquid Thickness
   if delta_si > Dh_ref/2
      delta_si = Dh_ref/2;
   end

   Fr_2delta_si = Uf_si^2/(9.81*2*delta_si);
%Froude number with reference to liquid thickness
   Re_2delta_si = (2*G_ro*(1-X_slug_int)*delta_si)/(Uf_si*(1-Gamma_slug_int));
%Reynolds number with reference to liquid thickness
   %Friction factor annular flow
   Fst_anr_si = 0.215*(delta_si/(Dh_ref-(2*delta_si)))^0.515*(((Rhof-
Rhog)*9.81*Dh_ref^2)/(Sigma))^(-
0.298)*(Mu_f/Mu_g)^0.285*((Rhof*Uf_si^2)/(Rhog*Ug_si^2))^(-0.044);

   DeltaP_st_anr_si = 4*Fst_anr_si*(L_slg_int/Dh_ref)*((Rhog*(Ug_si^2))/2);
% Two Phase Pressure Drop for annular flow in straight tubes
```

```
   %Friction factors for annular flow in u-bends
   Fuh_anr_si = Fst_anr_si*(1+(0.2*(Dh_ref/(R_ubend*2))^1.313*Deg_si^0.358));
   Fuvd_anr_si = Fst_anr_si*(1+0.5*(Dh_ref/(R_ubend*2))^1.339*Fr_2delta_si^(-
0.193)*Re_2delta_si^0.555);
   Fuvu_anr_si =
Fst_anr_si*(1+(8*(Dh_ref/(R_ubend*2))^1.178*Fr_2delta_si^0.196*((Uf_si^2*Rhog)/(
Ug_si^2*Rhof))^0.106));


   %Two Phase Pressure Drop for annular flow in u-bends
   DeltaP_uh_anr_si = 4*Fuh_anr_si*((R_ubend*pi*Rhog*Ug_si^2)/(Dh_ref*2));
   DeltaP_uvd_anr_si = 4*Fuvd_anr_si*((R_ubend*pi*Rhog*Ug_si^2)/(Dh_ref*2));
   DeltaP_uvu_anr_si = 4*Fuvu_anr_si*((R_ubend*pi*Rhog*Ug_si^2)/(Dh_ref*2));

   Fst_lo = 0.79/Re_lo^0.25; %Liquid Friction Factor

   DeltaP_st_lo = 4*Fst_lo*(L_slg_int/Dh_ref)*((Rhof*U_lo^2)/2);
%Liquid Friction Pressure Drop for straight tubes

   DeltaP_st_slg_int = (DeltaP_st_lo*(1-
(Gamma_slug_int/Gamma_ia))^0.25)+(DeltaP_st_anr_si*(Gamma_slug_int/Gamma_ia
))^0.25; %Two Phase Pressure Drop for slug/intermittent flow for straight tubes

   % All liquid single phase friction factors for u-bends
   Fuh_lo = Fst_lo*(1+(103.19*10^3*(Dh_ref/(R_ubend*2))^2.405*De_lo^(-0.653)));
   Fuvd_lo = Fst_lo*(1+(717.7*10^5*(Dh_ref/(R_ubend*2))^1.244*De_lo^(-1.461)));
   Fuvu_lo = Fst_lo*(1+(4.09*10^3*(Dh_ref/(R_ubend*2))^1.002*De_lo^(-0.381)));

   % All liquid single phase pressure drop for u-bends
   DeltaP_uh_lo = 4*Fuh_lo*((R_ubend*pi*Rhof*U_lo^2)/(Dh_ref*2));
   DeltaP_uvd_lo = 4*Fuvd_lo*((R_ubend*pi*Rhof*U_lo^2)/(Dh_ref*2));
   DeltaP_uvu_lo = 4*Fuvu_lo*((R_ubend*pi*Rhof*U_lo^2)/(Dh_ref*2));

   % Two phase pressure drop for slug intermittent flow in u-bends
   DeltaP_uh_slg_int = (DeltaP_uh_lo*(1-
(Gamma_slug_int/Gamma_ia))^0.25)+(DeltaP_uh_anr_si*(Gamma_slug_int/Gamma_i
a)^.25);
   DeltaP_uvd_slg_int = (DeltaP_uvd_lo*(1-
(Gamma_slug_int/Gamma_ia))^0.25)+(DeltaP_uvd_anr_si*(Gamma_slug_int/Gamma
_ia)^.25);
   DeltaP_uvu_slg_int = (DeltaP_uvu_lo*(1-
(Gamma_slug_int/Gamma_ia))^0.25)+(DeltaP_uvu_anr_si*(Gamma_slug_int/Gamma
_ia)^.25);

   N_ubend_h_si= 0;
```

```
if Ubend_h == 0
   N_ubend_h_si = 0;
else
   for r =1:length(Ubend_h)
      if Ubend_h(r) <= N_ubend_slg_int
         N_ubend_h_si = N_ubend_h_si+1;
      end
   end
end

   DeltaP_uh_slg_int_total = DeltaP_uh_slg_int*N_ubend_h_si;
% Multiply press drop in horizontal u-bends by number of horizontal u-bends in TP
region

   N_Ubend_vd_si = 0;

   if Ubend_vd == 0
      N_Ubend_vd_si= 0;
   else
      for r =1:length(Ubend_vd)
         if Ubend_vd(r) <= N_ubend_slg_int
            N_Ubend_vd_si = N_Ubend_vd_si+1;
         end
      end
   end

   DeltaP_uvd_slg_int_total = DeltaP_uvd_slg_int*N_Ubend_vd_si;
% Multiply press drop in vertical down u-bends by number of horizontal u-bends in TP
region

   N_Ubend_vu_si = 0;

   if Ubend_vu == 0
      N_Ubend_vu_si = 0;
   else
      for r =1:length(Ubend_vu)
         if Ubend_vu(r) <= N_ubend_slg_int
            N_Ubend_vu_si = N_Ubend_vu_si+1;
         end
      end
   end

   DeltaP_uvu_slg_int_total = DeltaP_uvu_slg_int*N_Ubend_vu_si;
% Multiply press drop in vertical up u-bends by number of horizontal u-bends in TP
region

   N_Ubend_vd45_si = 0;
```

```
  if Ubend_vd45 == 0
    N_Ubend_vd45_si = 0;
  else
    for r =1:length(Ubend_vd45)
      if Ubend_vd45(r) <= N_ubend_slg_int
        N_Ubend_vd45_si = N_Ubend_vd45_si+1;
      end
    end
  end

  DeltaP_uvd45_slg_int_total =
(DeltaP_uvd_slg_int*N_Ubend_vd45_si+DeltaP_uh_slg_int*N_Ubend_vd45_si)/2;
% Multiply press drop in vertical down 45 degree u-bends by number of horizontal u-
bends in TP region

  N_Ubend_vu45_si = 0;

  if Ubend_vu45 == 0
    N_Ubend_vu45_si = 0;
  else
    for r =1:length(Ubend_vu45)
      if Ubend_vu45(r) <= N_ubend_slg_int
        N_Ubend_vu45_si = N_Ubend_vu45_si+1;
      end
    end
  end

  DeltaP_uvu45_slg_int_total =
(DeltaP_uvu_slg_int*N_Ubend_vu45_si+DeltaP_uh_slg_int*N_Ubend_vu45_si)/2;
% Multiply press drop in vertical up 45 degree u-bends by number of horizontal u-
bends in TP region

  DeltaP_ubend_slg_int_total = DeltaP_uh_slg_int_total + DeltaP_uvd_slg_int_total +
DeltaP_uvu_slg_int_total + DeltaP_uvd45_slg_int_total + DeltaP_uvu45_slg_int_total;

  DeltaP_slg_int_total = DeltaP_ubend_slg_int_total + DeltaP_st_slg_int;
else
  DeltaP_slg_int_total = 0;

end

%Stratified Wavy/Intermittent to Annular boundary
Gamma_anr = getVoidFraction(Rhog, Rhof, 0, 0, (Rhof/Rhog)^(1/3), X_ia, Xout);
% Void Fraction at the Intermittent to Annular Transition boundary
Theta_strat_anr = 2*pi -2*(pi*(1-Gamma_anr) + ((3*pi/2)^(1/3))*(1-2*(1-
Gamma_anr)+((1-Gamma_anr)^(1/3))-(Gamma_anr^(1/3)))-(1/200)*(1-
```

```
Gamma_anr)*Gamma_anr*(1-2*(1-Gamma_anr))*(1+4*((1-
Gamma_anr)^2+Gamma_anr^2)));
hLd_anr = 0.5*(1-cos(((2*pi)-Theta_strat_anr)/2)); %Liquid Reference Level
AVd_anr = (Ac_ref*Gamma_anr)/Dh_ref^2; % Dimensionless Cross sectional area of
vapour

G_wavy_anr =
((((16*(AVd_anr^(1/3))*9.81*Dh_ref*Rhof*Rhog)/((X_anr^2)*(pi^2)*((1-((2*hLd_anr)-
1)^2)^0.5)))*(((pi^2)/(25*(hLd_anr^2)))*(((Wef/Frf)^(-1)))+1))^0.5)+50;

if G_ro > G_wavy_anr
   Theta_dry_anr = 0;
   Deg_anr = ((G_ro*Dh_ref*X_anr)/(Mu_g*Gamma_anr))*(Dh_ref/(R_ubend*2))^0.5;
%Vapour Deans Number
   Ug_anr = (G_ro*X_anr)/(Rhog*Gamma_anr); %Vapour true mean velocity
   Uf_anr = (G_ro*(1-X_anr))/(Rhof*(1-Gamma_anr)); %Liquid true mean velocity

   AL_anr = Ac_ref*(1-Gamma_anr);
   delta_anr = (Dh_ref/2)-((Dh_ref/2)^2-((2*AL_anr)/((2*pi)-Theta_dry_anr)))^0.5;
%Liquid Thickness
   % Liquid thickness can't physically be greater than half the pipe diameter
   if delta_anr > Dh_ref/2
      delta_anr = Dh_ref/2;
   end

   Fr_2delta_anr = Uf_anr^2/(9.81*2*delta_anr);
%Froude number with reference to liquid thickness

   Re_2delta_anr = (2*G_ro*(1-X_anr)*delta_anr)/(Uf_anr*(1-Gamma_anr));
%Reynolds number with reference to liquid thickness

   %Friction factor annular flow
   Fst_anr = 0.215*(delta_anr/(Dh_ref-(2*delta_anr)))^0.515*(((Rhof-
Rhog)*9.81*Dh_ref^2)/(Sigma))^(-
0.298)*(Mu_f/Mu_g)^0.285*((Rhof*Uf_anr^2)/(Rhog*Ug_anr^2))^(-0.044);
   DeltaP_st_anr = 4*Fst_anr*(L_anr/Dh_ref)*((Rhog*Ug_anr^2)/2);
%Two Phase Pressure Drop for annular flow in straight tubes

   %Friction factors for annular flow in u-bends
   Fuh_anr = Fst_anr*(1+0.2*(Dh_ref/(R_ubend*2))^1.313*Deg_anr^0.358);
   Fuvd_anr = Fst_anr*(1+0.5*(Dh_ref/(R_ubend*2))^1.339*Fr_2delta_anr^(-
0.193)*Re_2delta_anr^0.555);
   Fuvu_anr =
Fst_anr*(1+8*(Dh_ref/(R_ubend*2))^1.178*Fr_2delta_anr^0.196*((Uf_anr^2*Rhog)/(
Ug_anr^2*Rhof))^0.106);

   %Two Phase Pressure Drop for annular flow in u-bends
```

```
   DeltaP_uh_anr = 4*Fuh_anr*((R_ubend*pi*Rhog*Ug_anr^2)/(Dh_ref*2));
   DeltaP_uvd_anr = 4*Fuvd_anr*((R_ubend*pi*Rhog*Ug_anr^2)/(Dh_ref*2));
   DeltaP_uvu_anr = 4*Fuvu_anr*((R_ubend*pi*Rhog*Ug_anr^2)/(Dh_ref*2));

      N_ubend_h_anr= 0;

      if Ubend_h == 0
         N_ubend_h_anr = 0;
      else
         for r =1:length(Ubend_h)
            if (Ubend_h(r) <= (N_ubend_anr+N_ubend_slg_int) && Ubend_h(r) >
N_ubend_slg_int)
               N_ubend_h_anr = N_ubend_h_anr+1;
            end
         end
      end

      DeltaP_uh_anr = DeltaP_uh_anr*N_ubend_h_anr;
% Multiply press drop in horizontal u-bends by number of horizontal u-bends in TP
region

      N_Ubend_vd_anr = 0;

      if Ubend_vd == 0
         N_Ubend_vd_anr= 0;
      else
         for r =1:length(Ubend_vd)
            if (Ubend_vd(r) <= (N_ubend_anr+N_ubend_slg_int) && Ubend_vd(r) >
N_ubend_slg_int)
               N_Ubend_vd_anr = N_Ubend_vd_anr+1;
            end
         end
      end

      DeltaP_uvd_anr = DeltaP_uvd_anr*N_Ubend_vd_anr;
% Multiply press drop in vertical down u-bends by number of horizontal u-bends in TP
region

      N_Ubend_vu_anr = 0;

      if Ubend_vu == 0
         N_Ubend_vu_anr = 0;
      else
         for r =1:length(Ubend_vu)
            if (Ubend_vu(r) <= (N_ubend_anr+N_ubend_slg_int) && Ubend_vu(r) >
N_ubend_slg_int)
               N_Ubend_vu_anr = N_Ubend_vu_anr+1;
```

```
        end
      end
    end

    DeltaP_uvu_anr = DeltaP_uvu_anr*N_Ubend_vu_anr;
% Multiply press drop in vertical up u-bends by number of horizontal u-bends in TP
region

    N_Ubend_vd45_anr = 0;

    if Ubend_vd45 == 0
      N_Ubend_vd45_anr = 0;
    else
      for r =1:length(Ubend_vd45)
        if (Ubend_vd45(r) <= (N_ubend_anr+N_ubend_slg_int) && Ubend_vd45(r) >
N_ubend_slg_int)
          N_Ubend_vd45_anr = N_Ubend_vd45_anr+1;
        end
      end
    end

    DeltaP_uvd45_anr =
(DeltaP_uvd_anr*N_Ubend_vd45_anr+DeltaP_uh_anr*N_Ubend_vd45_anr)/2;
% Multiply press drop in vertical down 45 degree u-bends by number of horizontal u-
bends in TP region

    N_Ubend_vu45_anr = 0;

    if Ubend_vu45 == 0
      N_Ubend_vu45_anr = 0;
    else
      for r =1:length(Ubend_vu45)
        if (Ubend_vu45(r) <= (N_ubend_anr+N_ubend_slg_int) && Ubend_vu45(r) >
N_ubend_slg_int)
          N_Ubend_vu45_anr = N_Ubend_vu45_anr+1;
        end
      end
    end

    DeltaP_uvu45_anr =
(DeltaP_uvu_anr*N_Ubend_vu45_anr+DeltaP_uh_anr*N_Ubend_vu45_anr)/2;
% Multiply press drop in vertical up 45 degree u-bends by number of horizontal u-
bends in TP region


    DeltaP_ubend_anr = DeltaP_uh_anr + DeltaP_uvd_anr + DeltaP_uvu_anr +
DeltaP_uvd45_anr + DeltaP_uvu45_anr;
```

```
      DeltaP_anr_total = DeltaP_ubend_anr + DeltaP_st_anr;
else
   DeltaP_anr_total = 0;
end


G_wavy = ((((16*(AVd^(1/3))*9.81*Dh_ref*Rhof*Rhog)/((X_av^2)*(pi^2)*((1-((2*hLd)-
1)^2)^0.5)))*(((pi^2)/(25*(hLd^2)))*(((Wef/Frf)^(-1)))+1))^0.5)+50;


G_strat = ((226.3^2*ALd*AVd^2*Rhog*(Rhof-Rhog)*9.81*Mu_f)/(X_av^2*(1-
X_av)*pi^3))^(1/3);%Stratified to Stratified/Wavy boundary

if G_wavy > G_ro
   Deg = ((G_ro*Dh_ref*X_av)/(Mu_g*Gamma))*(Dh_ref/(R_ubend*2))^0.5;
%Vapour Deans Number

   Theta_dry = (((G_wavy-G_ro)/(G_wavy-G_strat))^0.61)*Theta_strat;
% Dry Angle for stratified wavy flow
   AL = Ac_ref*(1-Gamma);
   delta = (Dh_ref/2)-((Dh_ref/2)^2-((2*AL)/((2*pi)-Theta_dry)))^0.5;
%Liquid Thickness
   % Liquid thickness can't physically be greater than half the pipe diameter
   if delta > Dh_ref/2
      delta = Dh_ref/2;
   end

   Fr_2delta = Uf^2/(9.81*2*delta); %Froude number with reference to liquid thickness

   Re_2delta = (2*G_ro*(1-X_av))/(Uf*(1-Gamma));
%Reynolds number with reference to liquid thickness

   %Friction factor annular flow
   Fst_anr = 0.215*(delta/(Dh_ref-(2*delta)))^0.515*(((Rhof-
Rhog)*9.81*Dh_ref^2)/(Sigma))^(-
0.298)*(Mu_f/Mu_g)^0.285*((Rhof*Uf^2)/(Rhog*Ug^2))^(-0.044);
   %Relative Dry Angle
   Theta_dry_star = Theta_strat/(2*pi);
   %Friction factor stratified wavy flow
   Fst_stw = (Theta_dry_star*Fst_v) + ((1-Theta_dry_star)*Fst_anr);
   DeltaP_st_stw = 4*Fst_stw*(L_TP/Dh_ref)*((Rhog*Ug^2)/2);
% Two Phase Pressure Drop for stratified wavy flow in straight tubes

   %Friction factors for annular flow in ubends
   Fuh_anr = Fst_anr*(1+(0.2*(Dh_ref/(R_ubend*2))^1.313*Deg^0.358));
```

```
   Fuvd_anr = Fst_anr*(1+(0.5*(Dh_ref/R_ubend*2)^1.339*Fr_2delta^(-
0.193)*Re_2delta^0.555));
   Fuvu_anr =
Fst_anr*(1+(8*(Dh_ref/R_ubend*2)^1.178*Fr_2delta^0.196*((Uf^2*Rhof)/(Ug^2*Rho
g))^0.106));

   %Friction factors for stratified wavy flow in u-bends
   Fuh_stw = (Theta_dry_star*Fuh_go)+((1-Theta_dry_star)*Fuh_anr);
   Fuvd_stw = (Theta_dry_star*Fuvd_go)+((1-Theta_dry_star)*Fuvd_anr);
   Fuvu_stw = (Theta_dry_star*Fuvu_go)+((1-Theta_dry_star)*Fuvu_anr);

   % Two Phase Pressure Drop for stratified wavy flow in ubends
   DeltaP_uh_stw = 4*Fuh_stw*((R_ubend*pi*Rhog*Ug^2)/(Dh_ref*2));
   DeltaP_uvd_stw = 4*Fuvd_stw*((R_ubend*pi*Rhog*Ug^2)/(Dh_ref*2));
   DeltaP_uvu_stw = 4*Fuvu_stw*((R_ubend*pi*Rhog*Ug^2)/(Dh_ref*2));

   N_ubend_h_stw = 0;

   if Ubend_h == 0
      N_ubend_h_stw = 0;
   else
      for r =1:length(Ubend_h)
         if Ubend_h(r) <= N_ubend_TP
            N_ubend_h_stw = N_ubend_h_stw+1;
         end
      end
   end

   DeltaP_uh_total = DeltaP_uh_stw*N_ubend_h_stw;
% Multiply press drop in horizontal u-bends by number of horizontal u-bends in TP
region

   N_Ubend_vd_stw = 0;

   if Ubend_vd == 0
      N_Ubend_vd_stw = 0;
   else
      for r =1:length(Ubend_vd)
         if Ubend_vd(r) <= N_ubend_TP
            N_Ubend_vd_stw = N_Ubend_vd_stw+1;
         end
      end
   end

   DeltaP_uvd_total = DeltaP_uvd_stw*N_Ubend_vd_stw;
% Multiply press drop in vertical down u-bends by number of horizontal u-bends in TP
region
```

```
   N_Ubend_vu_stw = 0;

   if Ubend_vu == 0
      N_Ubend_vu_stw = 0;
   else
      for r =1:length(Ubend_vu)
         if Ubend_vu(r) <= N_ubend_TP
            N_Ubend_vu_stw = N_Ubend_vu_stw+1;
         end
      end
   end

   DeltaP_uvu_total = DeltaP_uvu_stw*N_Ubend_vu_stw;
% Multiply press drop in vertical up u-bends by number of horizontal u-bends in TP
region

   N_Ubend_vd45_stw = 0;

   if Ubend_vd45 == 0
      N_Ubend_vd45_stw = 0;
   else
      for r =1:length(Ubend_vd45)
         if Ubend_vd45(r) <= N_ubend_TP
            N_Ubend_vd45_stw = N_Ubend_vd45_stw+1;
         end
      end
   end

   DeltaP_uvd45_total =
(DeltaP_uvd_stw*N_Ubend_vd45_stw+DeltaP_uh_stw*N_Ubend_vd45_stw)/2;
% Multiply press drop in vertical down 45 degree u-bends by number of horizontal u-
bends in TP region

   N_Ubend_vu45_stw = 0;

   if Ubend_vu45 == 0
      N_Ubend_vu45_stw = 0;
   else
      for r =1:length(Ubend_vu45)
         if Ubend_vu45(r) <= N_ubend_TP
            N_Ubend_vu45_stw= N_Ubend_vu45_stw+1;
         end
      end
   end
```

```
   DeltaP_uvu45_total =
(DeltaP_uvu_stw*N_Ubend_vu45_stw+DeltaP_uh_stw*N_Ubend_vu45_stw)/2;
% Multiply press drop in vertical up 45 degree u-bends by number of horizontal u-
bends in TP region
   DeltaP_ubend_total = DeltaP_uh_total + DeltaP_uvd_total + DeltaP_uvu_total +
DeltaP_uvd45_total + DeltaP_uvu45_total;
   DeltaP_stw_wavy_total = DeltaP_ubend_total + DeltaP_st_stw;
else
   DeltaP_stw_wavy_total = 0;
end


if( Zeta1 < 0.995)
   DeltaP_st_v = 4*Fst_v*(L_SH/Dh_ref)*((Rhog*U_vo^2)/2);
   % Single Phase Pressure Drop for vapour flow in u-bends
   DeltaP_ubend_SH_new = ((G_ro^2)/(2*Rhog))*(((f*R_ubend*pi)/Dh_ref)+0.15);
   N_ubend_SH = N_ubend - N_ubend_TP;

   DeltaP_ubend_SH = DeltaP_ubend_SH_new*N_ubend_SH;
   DeltaP_SH = (DeltaP_ubend_SH + DeltaP_st_v)/1000;

else
   DeltaP_SH =0;
end

if (Zeta1 > 0.005)
   DeltaP_TP = (DeltaP_stw_wavy_total + DeltaP_anr_total +
DeltaP_slg_int_total)/1000;

else
   DeltaP_TP = 0;
end

else
   DeltaP_SH =0;
   DeltaP_TP = 0;
end


end
```

A.3 Heat Transfer Coefficient Model Code

```
function [h_wet h_vap] = HX_CHENG_THOME_NEW(Dh_ref, G, P, Xin, Xout, q,
mu_v_TP, mu_v_SH,mu_l, k_v_TP, k_v_SH, k_l, cp_v_SH, Rho_v, Rho_l,
P_crit,Ac_ref,Mol_weight, h_vl)

global FluidProp

%%%%%%%%%%%%%%%%%%%%%%%%%%%%%%%%%%%%%%%%%%%%%%%%%%%%%%%%%%%%%%%%%%%%%%%
% Calculate the Heat Transfer Coefficient
%%%%%%%%%%%%%%%%%%%%%%%%%%%%%%%%%%%%%%%%%%%%%%%%%%%%%%%%%%%%%%%%%%%%%%%

cp_l   = qminterp1(FluidProp.Psat, FluidProp.Cpf, P)*1000;
%multiply by 1000 to convert to J/Kg.K

Re_v = (G*Dh_ref)/(mu_v_SH); % Vapour Reynolds Number
Pr_v    = cp_v_SH*mu_v_SH/k_v_SH; % Vapour Prandtls Number
h_vap = (0.023*(Re_v^0.8)*(Pr_v^0.4)*(k_v_SH/Dh_ref))/1000;

if G >= 110 % This keep us above the slug/SW boundary and allows us to have
Theta_dry=0.

Pr_l    = cp_l*mu_l/k_l; % Liquid Prandtls Number

Sigma = (-0.000007*P) + 0.0198; %Linear Approx of Surface Tension with Pressure

We_v = ((G^2)*Dh_ref)/(Rho_v*Sigma); %Vapour Webber Number

Fr_vm = G^2/(Rho_v*(Rho_l-Rho_v)*9.81*Dh_ref); %vapor Froude number

q_crit = (0.131*Rho_v^0.5*h_vl*1000*(9.81*Sigma*(Rho_l-Rho_v))^0.25);
% Critical heat flux

X_di = 0.58*exp(0.52-
0.236*We_v^0.17*Fr_vm^0.17*(Rho_v/Rho_l)^0.25*(q/q_crit)^0.27);
%Quality at dryout inception

X_de = 0.61*exp(0.57-0.502*We_v^0.16*Fr_vm^0.15*(Rho_v/Rho_l)^(-
0.09)*(q/q_crit)^0.72); %Quality at dryout completion

if X_de>0.999 || X_de<X_di
   X_de = 0.999; % Dry out completion should happen before quality is equal to 1
end
```

```
X_ia = ((0.34^(1/0.875)*(Rho_v/Rho_l)^(-1/1.75)*(mu_l/mu_v_TP)^(-1/7))+1)^-1;
%Intermittent to Annular Transition boundary

X_slug_int = (X_ia-Xin)/2;

X_anr = ((X_di-X_ia)/2)+X_ia;

X_dry = ((X_de-X_di)/2)+X_di;

X_mist = ((Xout-X_de)/2)+X_de;

L_slg_int = X_ia/(Xout-Xin); % Length of two phase region with slug intermittant flow

L_anr = (X_di-X_ia)/(Xout-Xin);% Length of two phase region with annular flow

L_dry = (X_de-X_di)/(Xout-Xin); % Length of two phase region in dry out region

L_mist = (Xout-X_de)/(Xout-Xin); % Length of two phase region in mist flow region

pr = P/P_crit; % Reduced Pressure
a = pr^-0.0063;
b = (-log10(pr))^-0.55;
c = Mol_weight^-0.5;
d = q^0.58;

h_nb = 131*a*b*c*d; %nucleate boiling heat transfer coefficient


%Calculate heat transfer coefficient for the Slug Intermittent Region%
   S_slug_int = 1;
%nucleate boiling suppression factor is equal to 1 for slug intermittent flow
   Gamma_slug_int = getVoidFraction_RA(Rho_v, Rho_l,X_slug_int, Sigma, G);
% void fraction for slug intermittent flow
   Al_slug_int = Ac_ref*(1-Gamma_slug_int);
%Cross sectional area occupied by liquid phase
   if Dh_ref > 0.00753
      D_eq = 0.00753;
   else
      D_eq = Dh_ref;
   end
   delta_slug_int = (D_eq/2)-((D_eq/2)^2-((2*Al_slug_int)/(2*pi)))^0.5;
%Liquid Thickness
   if delta_slug_int > Dh_ref/2
      delta_slug_int = Dh_ref/2;
% If liquid thickness is greater than half the diameter set it to half the diameter
   end
```

```
   Re_delta_slg_int = (4*G*(1-X_slug_int)*delta_slug_int)/(mu_l*(1-
Gamma_slug_int)); %Liquid film reynolds number
   h_cb_slug_int = 0.0133*Re_delta_slg_int^0.69*Pr_l^0.4*(k_l/delta_slug_int);
%Convective boling heat transfer coefficient
   h_wet_slg_int = ((S_slug_int*h_nb)^3+h_cb_slug_int^3)^(1/3);
% heat tranfer coefficient for slug intermittent flow


 %Calculate heat transfer coefficient for the Annular Region%
   Gamma_ia = getVoidFraction_RA(Rho_v, Rho_l,X_ia, Sigma, G);
% Void Fraction at slug/intermittent to annular boundary
   Al_ia = Ac_ref*(1-Gamma_ia); % cross-sectional area occupied by liquid-phase
   delta_ia = (D_eq/2)-((D_eq/2)^2-((2*Al_ia)/(2*pi)))^0.5; %Liquid Thickness
   if delta_ia > Dh_ref/2
      delta_ia = Dh_ref/2; % If liquid thickness is greater than half the diameter set it to
half the diameter
   end
   Gamma_anr = getVoidFraction_RA(Rho_v, Rho_l,X_anr, Sigma, G);
% Void Fraction for Annular flow
   Al_anr = Ac_ref*(1-Gamma_anr);
   delta_anr = (Dh_ref/2)-((Dh_ref/2)^2-((2*Al_anr)/(2*pi)))^0.5; %Liquid Thickness
   if delta_anr > Dh_ref/2
      delta_anr = Dh_ref/2;
% If liquid thickness is greater than half the diameter set it to half the diameter
   end
   Re_delta_anr = (4*G*(1-X_anr)*delta_anr)/(mu_l*(1-Gamma_anr));
%Liquid film reynolds number
   h_cb_anr = 0.0133*Re_delta_anr^0.69*Pr_l^0.4*(k_l/delta_anr);
%Convective boling heat transfer coefficient
   S_anr = 1 - 1.14*(D_eq/0.00753)^2*(1-delta_anr/delta_ia)^2.2;
%nucleate boiling suppression factor
   h_wet_anr = ((S_anr*h_nb)^3+h_cb_anr^3)^(1/3);
%heat transfer coefficient for annular flow

 %Calculate heat transfer coefficient for the Dry Out Region%


   Gamma_de = getVoidFraction_RA(Rho_v, Rho_l,X_dry, Sigma, G);
%void faction at at dryout completion
   Al_de = Ac_ref*(1-Gamma_de); % cross-sectional area occupied by liquid-phase
   delta_de = (D_eq/2)-((D_eq/2)^2-((2*Al_de)/(2*pi)))^0.5; %Liquid Thickness
   if delta_de > Dh_ref/2
      delta_de = Dh_ref/2;
% If liquid thickness is greater than half the diameter set it to half the diameter
   end
   Re_delta_de = (4*G*(1-X_dry)*delta_de)/(mu_l*(1-Gamma_de));
%Liquid film reynolds number
   h_cb_wet = 0.0133*Re_delta_de^0.69*Pr_l^0.4*(k_l/delta_de);
```

```
%Convective boling heat transfer coefficient
   S_de = 1 - 1.14*(D_eq/0.00753)^2*(1-delta_de/delta_ia)^2.2;
%nucleate boiling suppression factor
   h_wet_de = ((S_de*h_nb)^3+h_cb_wet^3)^(1/3);
% heat transfer coefficient at dry out completion

   Re_h_dry = (G*Dh_ref*(X_dry+(Rho_v/Rho_l)*(1-X_dry)))/mu_v_TP;
%homogeneous Reynolds number

   Y_dry = 1-0.1*(((Rho_l/Rho_v)-1)*(1-X_dry))^0.4; % dry out correction factor

   h_m_dry = 2*10^-8*Re_h_dry^1.97*Pr_v^1.06*Y_dry^-1.83*(k_v_TP/Dh_ref);
%heat transfer coefficient mist flow

   h_dry = h_wet_de -((X_dry-X_di)*(h_wet_de-h_m_dry))/(X_de-X_di);
%heat transfer coefficient for dry out region

 %Calculate heat transfer coefficient for the Mist Flow Region if one exists
if Xout > X_de
   Re_h_mist = (G*Dh_ref*(X_mist+(Rho_v/Rho_l)*(1-X_mist)))/mu_v_TP;
%homogeneous Reynolds number

   Y_mist = 1-0.1*(((Rho_l/Rho_v)-1)*(1-X_mist))^0.4; % dry out correction factor

   h_mist = 2*10^-8*Re_h_mist^1.97*Pr_v^1.06*Y_mist^-1.83*(k_v_TP/Dh_ref);
%heat transfer coefficient mist flow
else
   h_mist = 0;
   L_dry = (Xout-X_di)/(Xout-Xin);
end

h_wet = (h_wet_slg_int*L_slg_int + h_wet_anr*L_anr + h_dry*L_dry +
h_mist*L_mist)/1000; % Two-phase heat transfer coefficient

else
   warning('G:Slug_SW', 'Massflux below slug/SW boundary. Constant estimate for
heat transfer coefficient will be used')
   h_wet = 10;
end

return
```

Appendix B

Experimental System Parameters

Table B1: Evaporator Physical Parameters

Parameter	Value
Hydraulic Diameter (m)	0.008125
Length of Refrigerant Circuit (m)	31.857
Air Side Cross Sectional Area (m^2)	0.159422
Air Side Surface Area (m^2)	7.5
Refrigerant Side Cross Sectional Area (m^2)	5.18E-05
Refrigerant Side Surface Area (m^2)	0.6181
Wall Mass (kg)	3.45
Wall Specific Heat ($kJ.kg^{-1}.K^{-1}$)	0.594082399
U-bend Radius (m)	0.0127
Number of u-bends	23
Vertical u-bends with flow upwards	[1 2 3 13 14 15 16]
Vertical u-bends with flow downwards	[5 6 7 8 10 18 19 20 21 22]
U-bend at 45° with flow upwards	[4 11 12 17]
U-bend at 45° with flow downwards	[9 23]